

# Theoretical Biophysics

**Prof. Dr. Ulrich Schwarz**

Heidelberg University, Institute for Theoretical Physics

Email: [schwarz@thphys.uni-heidelberg.de](mailto:schwarz@thphys.uni-heidelberg.de)

Homepage: <http://www.thphys.uni-heidelberg.de/~biophys/>

Summer term 2021

Last update: May 12, 2021





# Contents

Important numbers . . . . .	7
Some history . . . . .	8
<b>1 Review of some basic physics</b>	<b>11</b>
1.1 Statistical mechanics . . . . .	11
1.1.1 The microcanonical ensemble . . . . .	11
1.1.2 The canonical ensemble . . . . .	11
1.1.3 The grandcanonical ensemble . . . . .	12
1.1.4 The harmonic system . . . . .	13
1.1.5 The ideal gas . . . . .	14
1.1.6 The law of mass action . . . . .	16
1.1.7 Phase transitions . . . . .	16
1.2 Electrostatics . . . . .	20
1.2.1 Electrostatic potential . . . . .	20
1.2.2 Multipolar expansion . . . . .	21
<b>2 Biomolecular interactions and dynamics</b>	<b>23</b>
2.1 The importance of thermal energy . . . . .	23
2.2 Review of biomolecular interactions . . . . .	26
2.2.1 Covalent ("chemical") bonding . . . . .	26
2.2.2 Coulomb ("ionic") interaction . . . . .	26
2.2.3 Dipolar and van der Waals interactions . . . . .	28
2.2.4 Hydrophilic and hydrophobic interactions . . . . .	31
2.2.5 Protein folding . . . . .	33
2.2.6 Steric interactions . . . . .	35
2.3 Phase separation . . . . .	36
2.4 Molecular dynamics . . . . .	37
2.5 Brownian dynamics . . . . .	40

<b>3</b>	<b>Electrostatics and genome packing</b>	<b>45</b>
3.1	Role of geometry . . . . .	45
3.2	The membrane as a parallel plate capacitor . . . . .	47
3.3	Charged wall in different limits . . . . .	49
3.4	Poisson-Boltzmann theory . . . . .	52
3.5	Debye-Hückel theory . . . . .	53
3.6	Strong coupling limit . . . . .	55
3.7	Two charged walls . . . . .	55
3.7.1	Poisson-Boltzmann solution . . . . .	55
3.7.2	Debye-Hückel solution . . . . .	57
3.7.3	Strong coupling limit . . . . .	58
3.8	Electrostatics of viruses . . . . .	59
3.8.1	The line charge density of DNA . . . . .	59
3.8.2	DNA packing in $\phi 29$ bacteriophage . . . . .	60
3.8.3	Electrostatics of viral capsid assembly . . . . .	63
<b>4</b>	<b>Binding and assembly</b>	<b>67</b>
4.1	Binding polynomial . . . . .	67
4.2	Micelle assembly . . . . .	70
4.3	Virus capsid assembly . . . . .	71
4.4	Growth of cytoskeletal filaments . . . . .	74
<b>5</b>	<b>Physics of membranes and red blood cells</b>	<b>77</b>
5.1	A primer of differential geometry . . . . .	78
5.1.1	Curves in 3D . . . . .	78
5.1.2	Surfaces in 3D . . . . .	81
5.2	Curvature energy and minimal energy shapes . . . . .	87
5.2.1	Bending Hamiltonian . . . . .	87
5.2.2	Tether pulling . . . . .	90
5.2.3	Particle uptake . . . . .	91
5.2.4	Minimal energy shapes for vesicles . . . . .	96
5.3	Shape of red blood cells . . . . .	99
5.4	Membrane fluctuations . . . . .	104
5.4.1	Thermal roughening of a flat membrane . . . . .	104
5.4.2	Steric (Helfrich) interactions . . . . .	108
5.4.3	Flickering spectroscopy for red blood cells . . . . .	111

<b>6</b>	<b>Physics of polymers</b>	<b>113</b>
6.1	General introduction to polymers . . . . .	114
6.2	Basic models for polymers . . . . .	116
6.2.1	Freely jointed chain (FJC) . . . . .	116
6.2.2	Freely rotating chain (FRC) . . . . .	118
6.2.3	Worm-like chain (WLC) . . . . .	120
6.2.4	Radius of gyration . . . . .	121
6.2.5	Gaussian Chain model (GCM) . . . . .	123
6.3	Stretching polymers . . . . .	127
6.3.1	Stretching the FJC . . . . .	127
6.3.2	Stretching the WLC . . . . .	130
6.4	Interacting polymers . . . . .	137
6.4.1	Self-avoidance and Flory theory . . . . .	137
6.4.2	Semiflexible polymer networks . . . . .	139
<b>7</b>	<b>Molecular motors</b>	<b>141</b>
7.1	Classification . . . . .	142
7.2	One-state model . . . . .	143
7.3	Force dependence . . . . .	144
7.4	ATP dependence . . . . .	145
7.5	Two-state model . . . . .	148
7.6	Ratchet model for single motors . . . . .	150
7.7	Ratchet model for motor ensembles . . . . .	154
7.8	Master equation approach for motor ensembles . . . . .	157
7.8.1	Without load . . . . .	159
7.8.2	With load . . . . .	160
<b>8</b>	<b>Diffusion</b>	<b>161</b>
8.1	Life at low Reynolds-number . . . . .	161
8.2	Measuring the diffusion constant . . . . .	166
8.2.1	Single particle tracking . . . . .	166
8.2.2	Fluorescence Recovery After Photo-bleaching (FRAP) . . .	166
8.2.3	Fluorescence Correlation Spectroscopy (FCS) . . . . .	170
8.3	Diffusion to capture . . . . .	173
<b>9</b>	<b>Reaction kinetics</b>	<b>183</b>
9.1	Biochemical reaction networks . . . . .	183
9.2	Law of mass action . . . . .	187
9.3	Cooperative binding . . . . .	189

9.4	Ligand-receptor binding . . . . .	191
9.5	Network motifs . . . . .	192
9.5.1	Synthesis and degradation (steady state) . . . . .	193
9.5.2	Phosphorylation and dephosphorylation (buzzer) . . . . .	193
9.5.3	Adaptation (sniffer) . . . . .	195
9.5.4	Positive feedback (toggle switch) . . . . .	195
9.5.5	Negative feedback without delay (homeostasis) . . . . .	196
9.5.6	Negative feedback with delay (blinker) . . . . .	197
9.6	Enzyme kinetics . . . . .	198
9.6.1	Standard treatment . . . . .	199
9.6.2	Rigorous treatment . . . . .	200
9.7	Basics of non-linear dynamics . . . . .	203
9.7.1	One-dimensional systems . . . . .	205
9.7.2	Bifurcations . . . . .	207
9.7.2.1	Saddle-node bifurcation . . . . .	208
9.7.2.2	Transcritical bifurcation . . . . .	208
9.7.2.3	Supercritical pitchfork bifurcation . . . . .	208
9.7.2.4	Subcritical pitchfork bifurcation . . . . .	209
9.7.3	Two-dimensional systems . . . . .	210
9.7.4	Stable limit cycles . . . . .	212
9.8	Biological examples . . . . .	214
9.8.1	Revisiting bistability . . . . .	214
9.8.2	Stability of an adhesion cluster . . . . .	215
9.8.3	Genetic switch . . . . .	217
9.8.4	Glycolysis oscillator . . . . .	219
9.9	Excitable membranes and action potentials . . . . .	222
9.9.1	Channels and pumps . . . . .	222
9.9.2	Hodgkin-Huxley model of excitation . . . . .	223
9.9.3	The FitzHugh-Nagumo model . . . . .	227
9.9.4	The cable equation . . . . .	230
9.9.5	Neuronal dynamics and neural networks . . . . .	231
9.10	Reaction-diffusion systems and the Turing instability . . . . .	233

## Important numbers

Quantity	Meaning	Value
$N_A$	Avogadro's number	$1 \text{ mol} = 6.022 \times 10^{23}$
Da	mass of hydrogen atom	$1 \text{ g/mol} = 1.6 \times 10^{-24} \text{ g}$
M	molar	$\text{mol/l} \approx 1/\text{nm}^3$
nM	nanomolar	$\approx 1/\mu\text{m}^3$
	water density	55 M
	cellular ATP / ADP / $P_i$ conc	mM / 10 $\mu\text{M}$ / mM
$c_S$	physiological salt concentration	100 mM
pH	pH in human cell	7.34
$\lambda$	de Broglie or thermal wavelength	0.1 $\text{\AA}$
$l_{DH}$	Debye Hückel screening length	1 nm
$k_B T$	thermal energy	$4.1 \times 10^{-21} \text{ J} = 2.5 \text{ kJ/mol} = 0.6 \text{ kcal/mol} = 4.1 \text{ pNnm} = 25 \text{ meV} = eV/40$
$\Delta V$	voltage difference	$k_B T/e = 25 \text{ mV}$
$\hbar\omega$	red photon (700 nm)	$70 k_B T$
$\hbar\omega$	blue photon (450 nm)	$110 k_B T$
	ATP-hydrolysis	$20 - 30 k_B T$
	work in motor cycle	$8 \text{ nm} \times 5 \text{ pN} = 10 k_B T$
	metabolism of glucose	30 ATP molecules
	number of cells human	$3 \times 10^{13}$
	exchange rate cells human	$10^7 \text{ Hz}$
	human metabolic rate	90 W = 2.000 kcal / day
	size of human genome	3.2 Gbp
	length of human genome	$2 \times 3.2 \text{ G} \times 0.34 \text{ nm} = 2 \text{ m}$
	mutation rate per bp humans	$10^{-8}$
	mutation rate per bp HIV	$3 \times 10^{-5}$
D	diffusion constant small protein	$(10 \mu\text{m})^2/\text{s}$
v	molecular motor	$\mu\text{m}/\text{s}$
	blood flow	0.3 mm/s (capillaries) - 0.4 m/s (aorta)
	action potential	10-100 m/s
	thickness plasma membrane	4 nm
	tension plasma membrane	$300 \text{ pN}/\mu\text{m} = 0.3 \text{ mN/m}$
	cortical tension	$2 \text{ nN}/\mu\text{m} = 2 \text{ mN/m}$
	bending stiffness plasma membrane	$20 k_B T$
	$d / l_p$ DNA	2 nm / 50 nm
	$d / l_p$ actin	7 nm / 17 $\mu\text{m}$
	$d / l_p$ microtubule	25 nm / 1 mm

## Some history (NP = Nobel Prize)

1827	thermal motion of microscopic particles observed by Brown
1873	Plateau experiments on soap films
1905	Einstein paper on Brownian motion (NP 1921)
1906	Smoluchowski theory on Brownian motion
1908	Langevin equation
1910	Perrin experiments on colloids and Avogadro's number (NP 1926)
1917	Fokker-Planck equation
1920	Staudinger shows that polymers are chain molecules (NP 1953)
1940	Kramers' reaction-rate theory
1941	DLVO theory for colloids
1944	Onsager solution of the 2D Ising model (NP 1968)
1952	Hodgkin and Huxley papers on action potentials (NP 1963)
1953	structure of DNA by Watson and Crick (NP 1962)
1954	Huxley sliding filament hypothesis for muscle (could have earned him a second NP)
1958	central dogma by Crick
1959	X-ray structure of hemoglobin by Perutz and Kendrew (NP 1962)
1960	FitzHugh and (later) Nagumo phase plane analysis of Hodgkin Huxley model
1965	Density functional theory by Walter Kohn (NP 1998)
1969	Israelachvili surface force apparatus
1970	Canham curvature elasticity explains discocyte shape
1972	Warshel and Karplus molecular dynamics of biomolecules (NP 2013)
1973	Helfrich Hamiltonian with spontaneous curvature
1976	Neher and Sakmann Nature paper on patch clamp technique for ion channels (NP 1991)
1978	Helfrich interaction between membranes
1978	Doi and Edwards reptation model for polymer melts
1979	book <i>Scaling Concepts in Polymer Physics</i> by de Gennes (NP 1991)
1981	Evans micropipette aspiration of red blood cells
1982	de Gennes and Taupin persistence length of membranes
1983	Howard Berg book on <i>Random Walks in Biology</i>
1985	Peliti and Leibler renormalization of bending rigidity
1986	Safinya and Roux X-ray on membranes
1986	Lipowsky and Leibler unbinding transition of membranes
1986	book <i>The Theory of Polymer Dynamics</i> by Doi and Edwards



1990	Seifert and Lipowsky paper on vesicle adhesion
1991	spontaneous curvature phase diagram of vesicles (Seifert et al.)
1994	book <i>Statistical Thermodynamics of Surfaces, Interfaces, and Membranes</i> by Safran
1994	area difference elasticity (ADE) model for vesicles (Miao et al.)
1995	Marko and Siggia model for stretching the WLC
1997	NP physics 1997 for laser cooling includes Steven Chu, who also works on biomolecules
1997	RMP review by Jülicher, Armand and Prost on molecular motors
1998	MacKinnon Science paper on the structure of the $K^+$ channel (NP 2003)
2002	Lim et al. PNAS paper on shape of red blood cells
2014	NP chemistry for super-resolution microscopy to Eric Betzig, Stefan Hell and Bill Moerner
2016	NP chemistry for the synthetic molecular motors (still missing is one on biological molecular motors)
2018	NP physics for optical tweezers to Arthur Ashkin



# Chapter 1

## Review of some basic physics

In this script on theoretical biophysics we will make use of concepts and methods from many different fields of physics, which we will introduce when they are needed. However, there are two parts of basic physics which we will need right from the start, and therefore we briefly review them in this chapter. The first one is statistical mechanics, and the second one is electrostatics.

### 1.1 Statistical mechanics

#### 1.1.1 The microcanonical ensemble

The most basic principle of statistical physics is the fundamental postulate that states that a closed system maximizes its entropy. One way to arrive at this conclusion is by starting from information theory. This approach to statistical mechanics has been pioneered by Claude Shannon (founder of information theory) and Edwin Jaynes (inventor of the maximum entropy principle). We start from the Shannon entropy

$$S = - \sum_i p_i \ln p_i \quad (1.1)$$

where  $i$  numbers all states of the system and  $p_i$  is the probability of a state with  $\sum_i p_i = 1$ . By multiplying with  $k_B$ , we would get the physical (or Gibbs) entropy  $S$ . For the microcanonical ensemble, we would have  $p_i = 1/\Omega$  being constant ( $\Omega$  is the number of states) and thus  $S = k_B \ln \Omega$ , the famous Boltzmann formula. One can show that entropy  $S$  is a unique measure for the disorder or information content in the probability distribution  $\{p_i\}$ . From a more physics point of view, it is a measure for phase space volume that is additive over subsystems. A system that explores all possible states to an equal extent has maximal entropy. The microcanonical ensemble assumes that a physical system at equilibrium has exactly this property.

#### 1.1.2 The canonical ensemble

In general, biological systems are not in equilibrium and driven by energy that is supplied by the environment (food, light, etc). However, often state variables

change only slowly and therefore the system can be described by the laws of thermodynamics and statistical physics, albeit often only on local and temporary scales. Biological systems operate at relatively high and constant (body or room) temperature and therefore the canonical ensemble is relevant.

We now want to maximize entropy under the constraint of constant average energy,  $U = \sum_i E_i p_i$ . We add normalization and average energy condition with Lagrange multipliers to the Shannon entropy:

$$\delta S = - \sum_i (\ln p_i + 1 + \alpha + \beta E_i) \delta p_i = 0 \quad (1.2)$$

leading to

$$p_i = e^{-(1+\alpha+\beta E_i)} \quad (1.3)$$

From the normalization we get

$$e^{-(1+\alpha)} = \text{const} = \frac{1}{Z} \quad (1.4)$$

with

$$Z = \sum_i e^{-\beta E_i} \quad (1.5)$$

From the average condition  $U = (1/Z) \sum_i E_i e^{-\beta E_i}$  we get that  $\beta$  should be a function of  $U$ . We can make the connection to temperature  $T$  and identify  $\beta = k_B T$ . Now we have the Boltzmann distribution:

$$p_i = \frac{1}{Z} e^{-\beta E_i} \quad (1.6)$$

where  $Z$  is the partition sum. For a continuous state space, we would replace the sum over states by an integral over states. We conclude that the canonical distribution is the one that maximizes entropy under the condition that the average energy has a fixed (observed) value.

### 1.1.3 The grandcanonical ensemble

We now generalize to the case of particle exchange with a reservoir, for example molecules in a bulk fluid that can adsorb or bind to a surface. Another example might be the molecules in an open beer bottle lying on the floor of a lake. We now have a second side constraint, namely for the average number of particles,  $N = \sum_i N_i p_i$ . Variation of the entropy gives

$$\delta S = - \sum_i (\ln p_i + 1 + \alpha + \beta E_i + \gamma N_i) \delta p_i = 0 \quad (1.7)$$

where we have introduced a third Lagrange parameter  $\gamma$ . With the same arguments as above, we can identify  $\gamma = -\beta\mu$  with the chemical potential  $\mu$ . We then get

$$Z_G = \sum_i e^{-\beta(E_i - \mu N_i)} \quad (1.8)$$

for the grandcanonical partition sum and

$$p_i = \frac{1}{Z_G} e^{-\beta(E_i - \mu N_i)} \quad (1.9)$$

for the grandcanonical distribution.

### 1.1.4 The harmonic system

We now consider a system with one harmonic degree of freedom at constant temperature. This could be for example a particle in a one-dimensional laser trap with a harmonic potential  $E = \frac{1}{2}kx^2$ , where  $k$  is the spring constant (trap stiffness) and  $x$  is the one-dimensional state space coordinate (position). The corresponding partition sum is

$$Z = \int_{-\infty}^{\infty} dx \exp(-\beta E) = \int_{-\infty}^{\infty} dx \exp(-\beta \frac{1}{2}kx^2) = \left( \frac{2\pi k_B T}{k} \right)^{\frac{1}{2}} \quad (1.10)$$

where  $\beta = 1/(k_B T)$  and we have evaluated the Gaussian integral  $\int dx e^{-ax^2} = (\pi/a)^{1/2}$ . The corresponding correlation function is the mean squared displacement (MSD):

$$\langle x^2 \rangle = \frac{1}{Z} \int dx x^2 \exp(-\beta \frac{k}{2}x^2) \quad (1.11)$$

$$= \frac{1}{Z} \frac{-2}{\beta} \partial_k Z = \frac{-2}{\beta} \partial_k \ln Z = \frac{k_B T}{k} \quad (1.12)$$

Thus the larger temperature  $T$  and the smaller trap stiffness  $k$ , the larger the excursions of the particle. In fact this relation is used to calibrate laser traps:

$$k = \frac{k_B T}{\langle x^2 \rangle} \quad (1.13)$$

Because  $\langle x \rangle = 0$ , the variance of position is

$$\sigma_x^2 = \langle (x - \langle x \rangle)^2 \rangle = \langle (x^2 - 2x \langle x \rangle + \langle x \rangle^2) \rangle \quad (1.14)$$

$$= \langle x^2 \rangle - \langle x \rangle^2 = \langle x^2 \rangle = \frac{k_B T}{k} \quad (1.15)$$

The average energy is

$$\langle E \rangle = \frac{1}{Z} \int dx E \exp(-\beta E) = \frac{-1}{Z} \partial_\beta Z = -\partial_\beta \ln Z = \frac{k_B T}{2} \quad (1.16)$$

This is the famous equipartition theorem: every harmonic degree of freedom carries an energy of  $k_B T/2$ . Here we have one degree of freedom, for a harmonic oscillator it would be two (potential and kinetic energy) and for an ideal gas with  $N$  particles it would be  $3N$  (only kinetic energy, but  $N$  particles in three dimensions). The specific heat is constant:

$$c_V = \partial_T \langle E \rangle = \frac{k_B}{2} \quad (1.17)$$

For the variance of the energy we find

$$\sigma_E^2 = \langle E^2 \rangle - \langle E \rangle^2 = \frac{1}{Z} \partial_\beta^2 Z - \left( \frac{1}{Z} \partial_\beta Z \right)^2 \quad (1.18)$$

$$= \partial_\beta^2 \ln Z = -\partial_\beta \langle E \rangle = \frac{(k_B T)^2}{2} \quad (1.19)$$

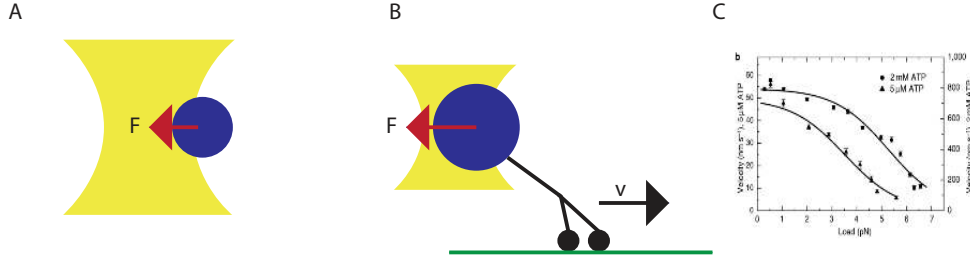


Figure 1.1: (A) A dielectric bead is attracted to the center of the laser beam. The force  $F$  is proportional to the distance from the center. This is the principle of the optical tweezer as developed in the 1970s by Arthur Ashkin at Bell Labs (Nobel prize physics 2018). (B) The optical tweezer can be used e.g. to measure the force-velocity relation of a molecular motor. Using a feedback system that keeps force  $F$  constant, one can measure the corresponding velocity  $v$  of the motor. For calibration of trap stiffness  $k$ , one uses the relation  $\langle x^2 \rangle = k_B T / k$  for a harmonic system. (C) Force-velocity relation for the molecular motor kinesin (from Mark J. Schnitzer, Koen Visscher and Steven M. Block, Force production by single kinesin motors, Nature Cell Biology 2, 718 - 723, 2000). The larger  $F$ , the smaller  $v$ : eventually the motor gets stalled ( $v = 0$ ) at high forces. The higher ATP-concentration, the faster the motor.

For the harmonic system, the free energy follows as

$$F = -k_B T \ln Z = \frac{k_B T}{2} \ln\left(\frac{k}{2\pi k_B T}\right) = \frac{-k_B T}{2} \ln(2\pi \langle x^2 \rangle) \quad (1.20)$$

In field theory, this corresponds to the free energy of a Gaussian theory.

The harmonic system is the simplest approximation for a bound system and we will encounter it frequently in this script.

### 1.1.5 The ideal gas

Biomolecules are always in solution and if their concentration is low, the solution is diluted and can be described as an ideal gas. We consider  $N$  point particles in a volume  $V$  at temperature  $T$  (canonical ensemble). The partition sum is

$$Z = \frac{1}{N! h^{3N}} \prod_{i=1}^N \int d\vec{p}_i d\vec{q}_i e^{-\beta H(\vec{p}, \vec{r})} = \frac{z^N}{N!} \quad (1.21)$$

where  $H = \sum_i \vec{p}_i^2 / 2m$  is the ideal gas Hamiltonian (only kinetic energy),  $\vec{p}_i$  and  $\vec{q}_i$  are momenta and positions, respectively, of the different particles ( $1 \leq i \leq N$ ).  $h$  is Planck's constant. It enters here because the different possible states are assumed to be squeezed together in phase space as closely as permitted by Heisenberg's uncertainty principle,  $\Delta p \Delta q \geq h$ . The factor  $N!$  accounts for the indistinguishability of the particles.  $z$  is the partition sum for one particle and again it is simply a Gauss integral:

$$z = \int \frac{d\vec{p} d\vec{q}}{h^3} e^{-\beta \frac{\vec{p}^2}{2m}} = \frac{V}{h^3} (2\pi k_B T m)^{3/2} = \frac{V}{\lambda^3} \quad (1.22)$$

where

$$\lambda = \sqrt{\frac{h^2}{2\pi m k_B T}} \quad (1.23)$$

is the *thermal (de Broglie) wavelength*. A typical value for an atom is 0.1 Angstrom and below this scale, quantum mechanics become relevant. The free energy follows with the help of Stirling's formula  $\ln N! \approx N \ln N - N$  for large  $N$  as

$$F = -k_B T \ln Z = -k_B T \ln \left( \frac{z^N}{N!} \right) = -k_B T N \left( \ln \left( \frac{V}{\lambda^3 N} \right) + 1 \right) \quad (1.24)$$

The Euler fundamental form for the Helmholtz free energy  $F = F(N, V, T)$  is

$$dF = -SdT - pdV + \mu N \quad (1.25)$$

From the statistical mechanics result for the free energy  $F = F(N, V, T)$ , we can thus now calculate the pressure  $p$  as

$$p = -\partial_V F = k_B T \frac{N}{V} \Rightarrow pV = Nk_B T \quad (1.26)$$

The result is known as the *thermal equation of state* or simply as the *ideal gas law*.

The average energy is the *caloric equation of state*:

$$\langle E \rangle = -\partial_\beta \ln Z = -N \partial_\beta \ln \beta^{-3/2} = \frac{3N}{2} k_B T \quad (1.27)$$

which is another example of the equipartition theorem (3N harmonic degrees of freedom).

Finally we calculate the chemical potential as

$$\mu = \partial_N F = k_B T \ln \left( \frac{\lambda^3 N}{V} \right) = k_B T \ln \left( \frac{p}{p_0} \right) \quad (1.28)$$

with  $p_0 = k_B T / \lambda^3$  (note that from the three terms, two have canceled each other). Thus chemical potential and pressure are related logarithmically.

We can write our fundamental equation  $F(T, V, N)$  and the three equations of state in a very compact way using density  $\rho = N/V$ :

$$f = \frac{F}{V} = k_B T \rho \left( \ln(\rho \lambda^3) - 1 \right) \quad (1.29)$$

$$p = \rho k_B T \quad (1.30)$$

$$e = \frac{\langle E \rangle}{V} = \frac{3}{2} \rho k_B T \quad (1.31)$$

$$\mu = k_B T \ln(\rho \lambda^3) \quad (1.32)$$

### 1.1.6 The law of mass action

From the ideal gas, we get for the chemical potential of species  $i$  in dilute solution:

$$\mu_i = \mu_{i0} + k_B T \ln \left( \frac{c_i}{c_{i0}} \right) \quad (1.33)$$

Thus the change in Gibbs free energy at constant  $T$  and constant  $p$  is

$$\Delta G = \sum_i \frac{\partial G}{\partial N_i} \Delta N_i = \sum_i \mu_i \Delta N_i = \sum_i \mu_i \nu_i \Delta N \quad (1.34)$$

where  $\nu_i$  are the stoichiometric coefficients of the reaction and  $\Delta N$  is the reaction coordinate. At equilibrium,  $\Delta G = 0$  and  $\Delta N$  drops out:

$$0 = \sum_i \nu_i \left( \mu_{i0} + k_B T \ln \left( \frac{c_{i,eq}}{c_{i0}} \right) \right) \quad (1.35)$$

From this we get the law of mass action:

$$\prod_i c_{i,eq}^{\nu_i} = \left( \prod_i c_{i0}^{\nu_i} \right) e^{-\beta \sum_i \nu_i \mu_{i0}} = \text{const} = K_{eq} \quad (1.36)$$

where we have defined the equilibrium constant  $K_{eq}$ .

We next consider a reaction with  $\Delta N = 1$ . The corresponding change in Gibbs free energy is

$$\Delta G = k_B T \ln \left( \frac{\prod_i c_i^{\nu_i}}{\prod_i c_{i,eq}^{\nu_i}} \right) \quad (1.37)$$

This leads to

$$\Delta G = \Delta G_0 + k_B T \ln (\prod_i c_i^{\nu_i}) , \quad \Delta G_0 = -k_B T \ln K_{eq} \quad (1.38)$$

with the understanding that to get a dimensionless argument of the logarithm, we might have to insert some reference concentration (typically 1 M).

A very important example is ATP-hydrolysis, for which we have  $\nu_{ATP} = -1$ ,  $\nu_{ADP} = +1$  and  $\nu_{P_i} = +1$ . Thus we get

$$\Delta G = \Delta G_0 + k_B T \ln \left( \frac{[ADP][P_i]}{[ATP]} \right) \quad (1.39)$$

With a reference concentration of 1M, the first term is  $-12.5k_B T$ . For cellular concentrations ( $[ADP] = 10\mu M$ ,  $[P_i] = mM$ ,  $[ATP] = mM$ ), the second term is  $-11.5k_B T$ , so together we have  $\Delta G = -24k_B T$ .

### 1.1.7 Phase transitions

If the concentration of a solution increases, the particles start to interact and form a real gas. We briefly discuss the van der Waals gas as the most prominent



example of a real gas that is undergoing phase transitions. For particles interacting through some potential  $U$ , the partition sum can be divided into an ideal part and an interaction part:

$$Z = Z_{ideal} Z_{inter} \quad (1.40)$$

where

$$Z_{ideal} = \frac{V^N}{N! \lambda^{3N}} \quad (1.41)$$

as above and

$$Z_{inter} = \frac{1}{V^N} \prod_{i=1}^N \int d\vec{q}_i e^{-\beta U(\{\vec{q}_i\})} \quad (1.42)$$

This term does not factor into single particle functions because the potential  $U$  couples all coordinates. Yet all thermodynamic quantities separate into an ideal gas part and a correction due to the interactions. In particular, we have

$$F = -k_B T \ln Z = F_{ideal} + F_{inter} \quad (1.43)$$

$$p = -\partial_V F = p_{ideal} + p_{inter} \quad (1.44)$$

The formulae for the ideal expressions have been given above. For the pressure, one expects that the correction terms should scale at least in second order in  $\rho$ , because two particles have to meet in order to give a contribution to this term. This suggests to make the following ansatz of a Taylor expansion in  $\rho$ , the so-called *virial expansion*:

$$p_{inter} = k_B T \sum_{i=2}^{\infty} B_i(T) \rho^i \quad (1.45)$$

where the  $B_i(T)$  are called *virial coefficients*. For many purposes, it is sufficient to consider only the first term in this expansion, that is the second virial coefficient  $B_2(T)$ . We then have

$$F = N k_B T \left[ \ln(\rho \lambda^3) - 1 + B_2 \rho \right] \quad (1.46)$$

$$p = \rho k_B T [1 + B_2 \rho] \quad (1.47)$$

For pairwise additive potentials, one can show

$$B_2(T) = -\frac{1}{2} \int d\vec{r} \left( e^{-\beta u(\vec{r})} - 1 \right) \quad (1.48)$$

For the van der Waals model, one considers two effects: a hard core repulsion with particle diameter  $d$  and a square well attractive potential with an interaction range  $\delta$  and a depth  $\epsilon$ . Then one gets

$$B_2(T) = \frac{2\pi}{3} d^3 - 2\pi(d^2 \delta) \frac{\epsilon}{k_B T} = b - \frac{a}{k_B T} \quad (1.49)$$

where we have introduced two positive constants  $b$  (four times the repulsive eigen-volume) and  $a$  (representing the attractive part). This general form of  $B_2(T)$  has

been confirmed experimentally for many real gases. It now allows to rewrite the gas law in the following way:

$$pV = Nk_B T \left(1 + B_2 \frac{N}{V}\right) \quad (1.50)$$

$$= Nk_B T \left(1 + b \frac{N}{V}\right) - \frac{N^2 a}{V} \quad (1.51)$$

$$\approx \frac{Nk_B T}{1 - b \frac{N}{V}} - \frac{N^2 a}{V} \quad (1.52)$$

thus

$$p = \frac{k_B T}{(v - b)} - \frac{a}{v^2} \quad (1.53)$$

where  $v = V/N = 1/\rho$  is the volume per particle. This is the *van der Waals equation of state*: the volume per particle is reduced from  $v$  to  $v - b$  due to excluded volume, and pressure is reduced by the attractive interaction, that is less momentum is transferred onto the walls due to the cohesive energy.

The van der Waals equation of state (1.53) is characterized by an instability. For a stable system, if a fluctuation occurs to higher density (smaller volume), then a larger pressure should result, which can counteract the fluctuation. Therefore thermodynamic stability requires

$$\frac{\partial p}{\partial V} < 0 \quad (1.54)$$

However, below the critical temperature  $T_c = (8a)/(27bk)$  the van der Waals isotherms from (1.53) have sections in which this stability criterion is violated. This indicates a fluid-fluid phase transition. The transition region can be calculated by the Maxwell construction from thermodynamics. The van der Waals gas thus predicts the fluid-fluid (gas-liquid) phase coexistence observed at low temperatures.

Interacting systems also show a phase transition to a solid at high densities. Together, one gets the generic phase diagram for a one-component fluid. It fits nicely to the experimental results for simple fluids such as carbon dioxide ( $CO_2$ ). However, the phase diagram for water is different, as we will see later.

The physics of phase transitions is important to understand how water molecules, lipids and proteins behave as collectives. Traditionally, it has been thought that biological systems tend to avoid phase transitions and that their appearance is a sign of disease (like gall and bile stones). In recent years, it has become clear however that biology uses phase transitions to create membrane-free compartments, e.g. P-granules<sup>1</sup>. A related and very important subject are rafts, which are phase-separated but kinetically trapped domains in biological membranes<sup>2</sup>.

---

<sup>1</sup>For a recent review, compare Hyman, Anthony A., Christoph A. Weber, and Frank Juelicher, "Liquid-liquid phase separation in biology", Annual review of cell and developmental biology 30 (2014): 39-58.

<sup>2</sup>For a review, compare Lingwood, Daniel, and Kai Simons, "Lipid rafts as a membrane-organizing principle", Science 327.5961 (2010): 46-50.

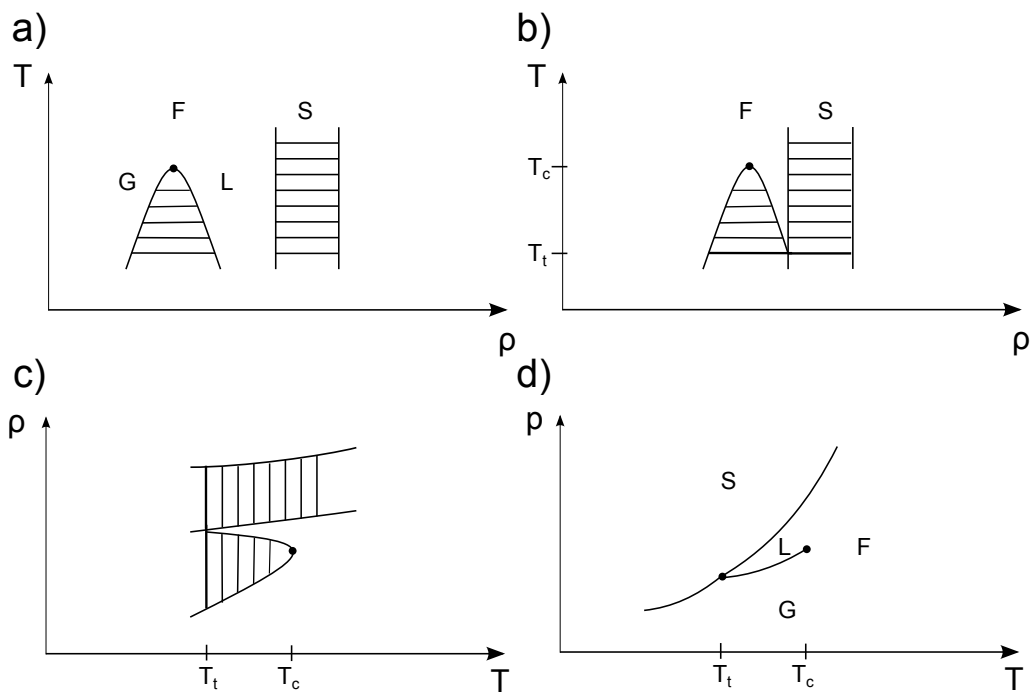


Figure 1.2: Combining the fluid-fluid and the fluid-solid phase transitions in (a), we get the complete phase diagram of a simple one-component system in (b). In (c) we swap  $T$  and  $\rho$  axes. By replacing  $\rho$  by  $p$ , we get the final phase diagram in (d). Two-phase coexistence regions become lines in this representation. Carbon dioxide has a phase diagram like this, but water does not.

## 1.2 Electrostatics

### 1.2.1 Electrostatic potential

In electrostatics, the force on a test particle with charge  $q_2$  is given by Coulomb's law

$$\vec{F} = -\vec{\nabla}U = \frac{q_1 q_2}{4\pi\epsilon_0\epsilon} \cdot \frac{\vec{r}}{r^3} = q_2 \vec{E} = -q_2 \vec{\nabla}\Phi$$

where  $\vec{E}$  and  $\Phi$  are the electrostatic field and the electrostatic potential, respectively, generated by the point charge  $q_1$ . Both are additive quantities (superposition principle), therefore for an arbitrary charge distribution with volume charge density  $\rho(\vec{r})$  we get:

$$\vec{E} = \frac{1}{4\pi\epsilon_0\epsilon} \int d\vec{r}' \rho(\vec{r}') \frac{\vec{r} - \vec{r}'}{|\vec{r} - \vec{r}'|^3} = -\vec{\nabla}\Phi \quad (1.55)$$

$$\Phi(\vec{r}) = \frac{1}{4\pi\epsilon_0\epsilon} \int d\vec{r}' \frac{\rho(\vec{r}')}{|\vec{r} - \vec{r}'|} \quad (1.56)$$

The foundation of electrostatics is formed by the four **Maxwell equations**. For electrostatics, the relevant equations read:

$$\vec{\nabla} \times \vec{E} = 0 \quad (1.57)$$

$$\vec{\nabla} \cdot \vec{E} = -\nabla^2\Phi = \boxed{-\Delta\Phi = \frac{\rho(\vec{r})}{\epsilon_0\epsilon}} \quad \text{Poisson equation} \quad (1.58)$$

The Poisson equation implies that charges are the sources for the electrostatic potential. For instance, the potential of a point charge with volume charge distribution  $\rho(\vec{r}) = Q \cdot \delta(\vec{r})$  can directly be calculated from equation 1.58:

$$\begin{aligned} & \text{spherical} \\ & \text{symmetry} \\ \nabla^2\Phi &= \frac{1}{r} \frac{d^2(r\Phi)}{dr^2} = 0 \\ \Rightarrow \frac{d(r\Phi)}{dr} &= A_1 \quad \Rightarrow \quad \Phi = A_1 + \frac{A_2}{r} \end{aligned}$$

As an appropriate boundary condition we choose  $\Phi(\infty) = 0$ , hence  $A_1 = 0$ . By comparing our result with the Poisson equation, we finally get

$$\Rightarrow \Phi(r) = \frac{Q}{4\pi\epsilon_0\epsilon} \cdot \frac{1}{r}$$

which is the well-known Coulomb law. From a mathematical point of view, the Coulomb law is the Green's function (or propagator) for the Laplace operator in 3D. The given solution can be checked to be true because  $\Delta\left(\frac{1}{r}\right) = -4\pi\delta(r)$ .

Sometimes it is useful to rewrite equation 1.58 in an integral form, using the divergence theorem known from vector calculus:

$$\int_{\partial V} \vec{E} d\vec{A} \stackrel{\text{divergence theorem}}{=} \int_V d\vec{r} \vec{\nabla} \cdot \vec{E} \stackrel{\text{Poisson equation}}{=} \int d\vec{r} \frac{\rho(\vec{r})}{\epsilon_0\epsilon}$$

$$\Rightarrow \boxed{\int_{\partial V} \vec{E} \cdot d\vec{A} = \frac{Q_V}{\epsilon_0 \epsilon}} \quad \text{Gauss law} \quad (1.59)$$

where  $\partial V$  is a closed surface,  $V$  its enclosed volume and  $Q_V$  the enclosed charge. As an example equation 1.59 was used to compute the radial component  $E_r$  of the electric field of rotationally symmetric charge distributions (note that the angular components vanish due to spatial symmetry). For a large sphere the Gauss law reads:

$$\int_{\partial V} \vec{E} \cdot d\vec{A} = 4\pi r^2 E_r = \frac{Q_V}{\epsilon_0 \epsilon} \Rightarrow E_r = \frac{Q_V}{4\pi \epsilon_0 \epsilon r^2}$$

thus we again recover Coulomb's law, as we should.

## 1.2.2 Multipolar expansion

Consider the work to move a charge  $q$  in an electrostatic potential  $\Phi$ :

$$W = - \int_{\vec{r}_1}^{\vec{r}_2} q \vec{E} d\vec{r} = q \int_{\vec{r}_1}^{\vec{r}_2} \vec{\nabla} \Phi d\vec{r} = q [\Phi(\vec{r}_2) - \Phi(\vec{r}_1)]$$

The reference position  $\vec{r}_1$  can be taken to be at infinity, where the potential vanishes. For a continuous charge distribution, we therefore have

$$E_{pot} = \int d\vec{r}' \rho(\vec{r}') \Phi(\vec{r}')$$

We now consider a charge distribution localized around the position  $\vec{r}$  and perform a Taylor expansion around this point:

$$E_{pot} = \int d\vec{r}' \rho(\vec{r}') \left[ \Phi(\vec{r}) + (\vec{r}' - \vec{r}) \cdot \vec{\nabla} \Phi(\vec{r}) + \dots \right] = Q \Phi(\vec{r}) - \vec{p} \cdot \vec{E} + \dots$$

where the monopole  $Q$  is the overall charge and the dipole is defined as

$$\vec{p} = \int d\vec{r}' \rho(\vec{r}') (\vec{r}' - \vec{r})$$

We now write the interaction potential between two charge distributions. For a monopole  $Q_1$  at the origin interacting with a monopole  $Q_2$  at  $\vec{r}$ , we simply get back Coulomb's law:

$$E_{pot} = \frac{Q_1 Q_2}{4\pi \epsilon_0 \epsilon} \frac{1}{r}$$

by using the first term and the potential from a monopole. For a dipole  $\vec{p}$  at  $\vec{r}$  interacting with a monopole  $Q$  at the origin, we use the second term:

$$E_{pot} = -\vec{p} \cdot \vec{E} = \frac{Q}{4\pi \epsilon_0 \epsilon} \frac{\vec{p} \cdot \vec{r}}{r^3}$$

For two dipoles interacting with each other, we first take the potential resulting from a dipole at the origin, which can be read off from the preceding equation:

$$\Phi = \frac{1}{4\pi \epsilon_0 \epsilon} \frac{\vec{p}_1 \cdot \vec{r}}{r^3}$$

We then get for the interaction

$$E_{pot} = -\vec{p}_2 \cdot \vec{E}_1 = \frac{1}{4\pi\epsilon_0\epsilon} \left( \frac{\vec{p}_1 \cdot \vec{p}_2}{r^3} - \frac{3(\vec{p}_1 \cdot \vec{r})(\vec{p}_2 \cdot \vec{r})}{r^5} \right)$$

The dipolar interaction is very prominent in biological systems. In particular, water carries a permanent dipole and thus water molecules interact with this potential function.

## Chapter 2

# Biomolecular interactions and dynamics

From general physics, we know that there are four fundamental forces, but of these only the electrostatic force is relevant for cohesion in biological material. However, it comes in many different forms, as we shall see in this section. We start with a discussion of the mechanical properties of biomaterial and immediately see that we are dealing with very weak interactions on the order of thermal energy  $k_B T$ . We then review the details of these interactions and how they can be used in molecular and Brownian dynamics simulations to predict the behaviour of biomolecules, most prominently of proteins.

### 2.1 The importance of thermal energy

Theoretical biophysics uses mathematical models to study the physics of biological systems. Biophysical length scales cover many orders of magnitude, from biomolecules (nanometer) through cells (micrometer) and tissues (centimeter) to multicellular organisms (meter) and populations (kilometers). Biomolecules form supramolecular assemblies like lipid membranes and the polymer networks of the cytoskeleton. Collectively these materials can be classified as *soft matter*, which is a subfield of condensed matter physics. Soft materials are easily deformed by forces which are sometimes only in the range of thermal forces at room temperature, as we shall see in the following.

In order to measure the mechanical stiffness or rigidity of cells, different stretch experiments have been conceived, two of which are illustrated in figure 2.1. To first order, the mechanical response to a force is an elastic one. A force  $F$  applied over an area  $A$  reversibly stretches the material from length  $L$  to length  $L + \Delta L$  (compare figure 2.2a). From a physics point of view, it is clear that force per area and relative deformation must be the central quantities. We therefore define stress and strain as follows:

$$\begin{array}{llll} \text{cause :} & \text{stress} & \sigma = \frac{F}{A} & [\sigma] = \frac{N}{m^2} = Pa \\ & \text{strain} & \epsilon = \frac{\Delta L}{L} & [\epsilon] = 1 \end{array}$$

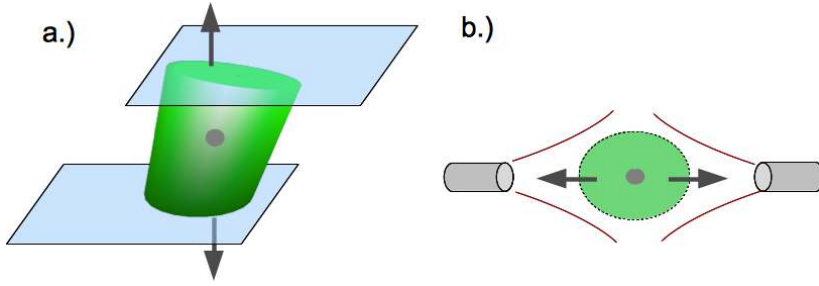


Figure 2.1: Different ways to measure the mechanical rigidity of single cells. (a) Cell stretching between two microplates. A related setup is pulling with an atomic force microscope (AFM). (b) Cell stretching with the optical stretcher. The functional principle is similar to that of optical tweezers.

The simplest possible relation between the two quantities is a linear one:

$$\sigma = E \cdot \epsilon \quad (2.1)$$

where  $E$  is the Young's modulus or rigidity of the material with  $[E] = Pa$ . For cells, this elastic constant is typically in the order of  $10 kPa$ . This is also the typical stiffness of connective tissue, including our skin. In general, tissue stiffness is in this range (on the cellular scale, the softest tissue is brain with 100 Pa, and the stiffest tissue is bone with 50 kPa).

Equation 2.1 might be recognized as Hooke's law, and in fact we can think of the macroscopic deformation as the effect of the stretching of a huge set of microscopic springs which correspond to the elastic elements within the material. Equation 2.1 can be rewritten as

$$F = \frac{E \cdot A}{L} \cdot \Delta L \quad (2.2)$$

thus  $k = E \cdot A/L$  is the "spring constant" of the material.  $EA$  is often called the 1D modulus of the material.

Let us now assume that the system is characterized by one typical energy  $U$  and one typical length  $a$ . A dimensional analysis of  $E$  yields  $E \approx \frac{U}{a^3}$ . As an example a crosslinked polymer gel as illustrated in figure 2.2b can be considered.

The elasticity of cellular material is determined by supramolecular complexes forming the structural elements of the cell with a typical scale  $a = 10 nm$ . Therefore we get for the typical energy

$$U = E \cdot a^3 = 10 kPa \cdot (10 nm)^3 = 10^{-20} J \quad (2.3)$$

This is in the order of the thermal energy at ambient or body temperature (300 K) known from statistical mechanics:

$$k_B T = 1.38 \cdot 10^{-23} \frac{J}{K} \cdot 300 K = 4.1 \cdot 10^{-21} J = 4.1 pN nm \quad (2.4)$$

where  $k_B = 1.38 \cdot 10^{-23} \frac{J}{K}$  is the Boltzmann constant.

In physical chemistry, one usually refers to moles rather than to single molecules:

$$k_B T \cdot N_A = R \cdot T = 2.5 \frac{kJ}{mol} = 0.6 \frac{kcal}{mol} \quad (2.5)$$



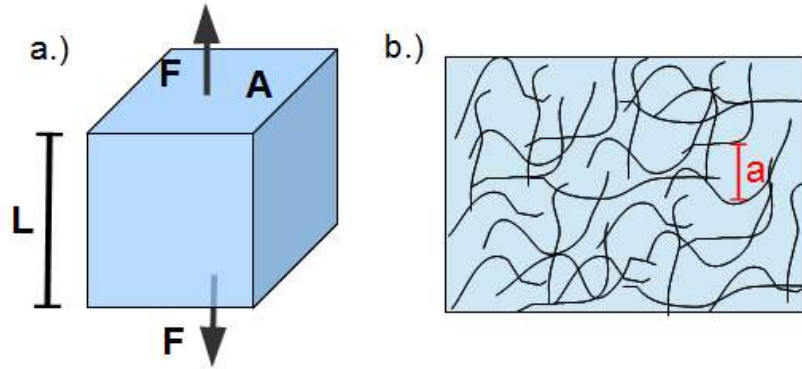


Figure 2.2: (a) A slab of elastic material of length  $L$  and cross sectional area  $A$  is stretched by a force  $F$ . The force acting on the material will result in a deformation. In the case shown here the box will be stretched by the length  $\Delta L$ . (b) Illustration of a polymer gel with a meshsize  $a$  corresponding to a typical length scale. In this example, the typical energy  $U$  is the elastic energy stored in a unit cell.

with  $N_A = 6.002 \cdot 10^{23}$  being Avogadro's number and  $R = N_A \cdot k_B = 8.31 \frac{J}{mol \cdot K}$  being the molar gas constant.

Comparing the Young's modulus of biological material to that of an atomic crystal, it becomes clear why we speak of "soft" matter. The energy scale in a crystal usually is in the range of  $1 eV \approx 40 k_B T$  and it has a typical length  $a$  of a few Å. This yields a Young's modulus in the order of 100 GPa. The most rigid material known today is graphene with a Young's modulus of TPa; therefore it has been suggested to be used for building a space elevator.

From the range of the typical energy in supramolecular structures (compare equation 2.3) it can be concluded that biological material is held together by many weak interactions. However,  $U$  cannot be smaller than  $k_B T$ , because otherwise the entropy of the system would destroy the structure.

Cells are elastic only on the timescale of minutes and later start to flow like viscoelastic material. The constitutive relation of a viscous system is

$$\sigma = \eta \cdot \dot{\epsilon} \quad (2.6)$$

and a typical value for the viscosity of cells is  $\eta$  is  $10^5 Pa s$ , which is 8 orders of magnitude larger than for water. This high viscosity comes from the polymer networks inside the cell. The corresponding time scale is

$$\tau = \eta/E = 10^5 Pa s/kPa = 100s \quad (2.7)$$

and corresponds to the time the system needs to relax from the external perturbations by internal rearrangements. However, these consideration are only relevant on cellular scales. If we make rheological experiments on the scale of molecules, then we are back to the viscosity and relaxation times of water.

Chemical Bond	Bond Energy
$C - C$	$140 k_B T$
$C = C$	$240 k_B T$
$C \equiv C$	$330 k_B T$
$H - CHO$	$144 k_B T$
$H - CN$	$200 k_B T$

Table 2.1: Some chemical bonds and their corresponding bond energies (at  $T \approx 300 K$ )

## 2.2 Review of biomolecular interactions

### 2.2.1 Covalent ("chemical") bonding

Due to the small length scale of a few Å on which covalent interactions occur, one needs quantum mechanics to explain chemical bonding. Usually, calculations concerning chemical bonding are performed using density functional theory (DFT) which was developed by the physicist Walter Kohn in 1965 (he received the Nobel prize in chemistry in 1998).

The energy of chemical bonds is usually in the range of  $\sim 100 k_B T$  (several  $eV = 40 k_B T$ , comparable to energy scales in solids) and does not only depend on the kind of bonding (single bond, double bond,...), but also on the electronic environment (table 2.1).

### 2.2.2 Coulomb ("ionic") interaction

Most interactions on biophysical scales are based on the Coulomb interaction, whose central law is Coulomb's law:

$$U = \frac{q_1 q_2}{4\pi\epsilon_0\epsilon r} \quad \begin{array}{l} \epsilon_0 : \text{permittivity of vacuum} \\ \epsilon : \text{dielectric constant} \end{array} \quad (2.8)$$

with the resulting force

$$F = -\frac{dU}{dr} \sim +\frac{q_1 q_2}{r^2} \quad (2.9)$$

which is repulsive if the two electric charges  $q_1$  and  $q_2$  have the same sign and attractive otherwise.

The Coulomb interaction is a "long-ranged" interaction in 3D. To illustrate this, consider the cohesive energy density of a bulk material of diameter  $L$ :

$$U_{tot} = \int_a^L dr r^2 \frac{1}{r^n} \sim r^{3-n}|_a^L = a^{3-n} \left[ \left(\frac{L}{a}\right)^{3-n} - 1 \right] \quad (2.10)$$

where  $a$  is a microscopic cutoff due to the Born repulsion. Taking the limit  $L \rightarrow \infty$  in equation 2.10 shows that  $U_{tot}$  does not diverge for  $n > 3$ , corresponding to a short-ranged interaction where only the local environment significantly contributes to the force on a point-like object. On the other hand, for  $n < 3$  the

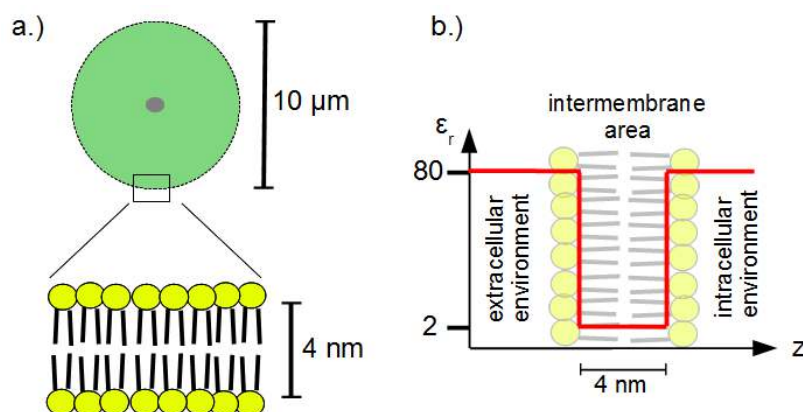


Figure 2.3: (a) Diameter of a typical cell in comparison to the thickness of the biological lipid bilayer membrane. Note the very strong separation of length scales: a very thin oily layer holds together the very large cell. (b) Drop of  $\epsilon$  across the membrane. The situation is similar to two metal sheets separated by plastic. Thus the membrane forms a capacitor.

interaction is long-ranged which means that remote objects cannot be neglected. This is especially true for a pure Coulomb interaction (the situation is even worse for gravitation, which not only has  $n = 1$  like the Coulomb interaction, but moreover does have only positive charges, so there is not cancellation due to opposite charges).

Biological interactions are usually short-ranged for several reasons. One important aspect is that biological systems always operate in water, thus charges such as ions are shielded due to the polarization of the water molecules and, hence, the Coulomb interaction is weakened. This effect is expressed by the large dielectric constant of water ( $\epsilon = 80$ ). Thus the interaction strength is reduced by almost two orders of magnitude in water. Generally, the more polarizable a medium, the larger is its dielectric constant:

$$\epsilon = \begin{cases} 1 & \text{air} \\ 2 & \text{hydrocarbon (oil, fatty acids,...)} \\ 80 & \text{water} \end{cases}$$

Temperature also has an influence on the dielectric constant. With increasing  $T$ , the constant decreases due to the thermal motion which disturbs the order in the surrounding medium. This leads to the surprising effect that the interaction can become effectively stronger at higher temperature because polarization goes down.

Due to the difference in dielectric constant of water and hydrocarbons, biological membranes are natural capacitors. This electrical property forms the basis of electrophysiology and the neurosciences.

Biological systems frequently use metal ions such as  $\text{Ca}^{2+}$ ,  $\text{Mg}^{2+}$  etc. In a solid crystal the ionic interaction is as strong as chemical bonding. For instance, the energy of two neighbouring ions in a sodium ( $\text{Na}^+$ ) chloride ( $\text{Cl}^-$ ) crystal with a lattice constant  $a = 2.81 \text{ \AA}$  is  $U = -200 k_B T$  (equation 2.8 with  $q_1 = -q_2 = e$ ).

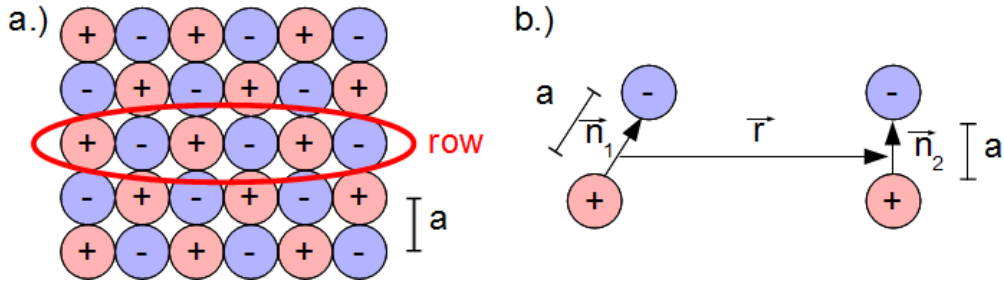


Figure 2.4: (a) Schematic drawing of a simple ionic crystal (such as NaCl). (b) Two dipoles with dipole moments  $\vec{p}_1 = e \cdot a \cdot \vec{n}_1$  and  $\vec{p}_2 = e \cdot a \cdot \vec{n}_2$ , respectively.

For the total energy density of a crystal, one has to sum over all interactions between nearest, next-nearest,... neighbours within the crystal. Let us first consider only one row (compare figure 2.4a).

$$U_{row} = \frac{e^2}{4\pi\epsilon_0 a} \cdot 2 \cdot \left( -1 + \frac{1}{2} - \frac{1}{3} + \dots \right) = -\frac{2e^2}{4\pi\epsilon_0 a} \ln 2 \quad (2.11)$$

Although this summation is mathematically ill-defined (Riemann showed that changing the order of the summation can give any desired value), physically it makes sense. Continuing this calculation to all other rows, we get

$$U_{tot} = - \underbrace{1.747}_{\substack{\text{Madelung} \\ \text{constant}}} \frac{e^2 N}{4\pi\epsilon_0 a} = -206 \frac{\text{kcal}}{\text{mol}} \quad (2.12)$$

From the negative sign of the total energy in equation 2.12 it can be concluded that the crystal is stable. The vaporization energy of a NaCl crystal was experimentally determined to be  $183 \frac{\text{kcal}}{\text{mol}}$ . Hence, although equation 2.12 is the result of strong assumptions, it nevertheless agrees relatively well with the experimental value.

### 2.2.3 Dipolar and van der Waals interactions

Many biomolecules do not have a net charge, but rather a charge distribution. In the sense of a multipolar expansion, the most important contribution is the dipolar interaction. For the interaction of two dipoles like in figure 2.4b, one gets for the interaction energy:

$$U = \frac{(ea)^2}{\epsilon_0 \epsilon_r r^3} \underbrace{\left[ \vec{n}_1 \cdot \vec{n}_2 - 3 \left( \vec{n}_1 \cdot \hat{r} \right) \left( \vec{n}_2 \cdot \hat{r} \right) \right]}_{f(\Theta, \phi, \dots)} \quad (2.13)$$

The factor  $f(\Theta, \phi, \dots)$  does not depend on distance, but on all angles involved. It is thus determined by the geometrical arrangement of the two dipoles and its sign determines whether a certain orientation is favourable or not. Figure

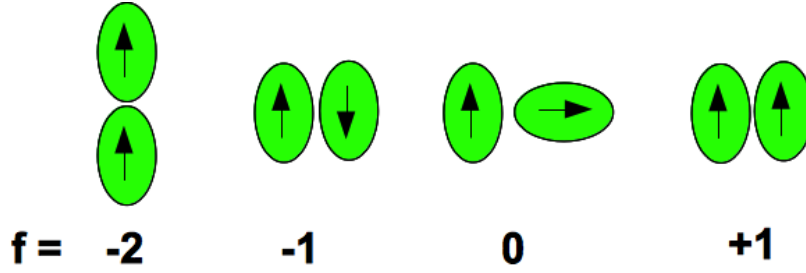


Figure 2.5: f-values of different geometrical arrangements of two dipoles. The more negative the f-value becomes, the more favourable is the arrangement.

2.5 shows some dipole arrangements and their corresponding f-values. The most favorable orientation is a head-tail-alignment. In water, but also in dipolar fluids and ferrofluids, this leads to dipole chains, network formation and spontaneous polarization.

The interaction between charge distributions is further weakened by thermal motion. If the dipoles are free to rotate, the interaction becomes weaker. For example, if a charge  $Q$  is separated by a distance  $r$  from a dipole with dipole moment  $\vec{\mu} = q \cdot a$ , as depicted in figure 2.6, the electrostatic energy of the system is given by

$$U(\vec{r}, \Theta) = \underbrace{\frac{Q\mu}{4\pi\epsilon_0\epsilon r^2}}_{U_0} \cdot \underbrace{\cos(\Theta)}_{\text{orientation factor}} \quad (2.14)$$

The dipole is rotating due to thermal forces, that is why we calculate an effective interaction law by a thermal average weighted with the Boltzmann factor:

$$U(\vec{r}) = \frac{\int_0^\pi \sin(\Theta) d\Theta U(\vec{r}, \Theta) \exp\left(\frac{-U(\vec{r}, \Theta)}{k_B T}\right)}{\int_0^\pi \sin(\Theta) d\Theta \exp\left(\frac{-U(\vec{r}, \Theta)}{k_B T}\right)} \quad (2.15)$$

If we assume that the interaction is weak compared to thermal energy,  $\frac{-U(\vec{r}, \Theta)}{k_B T} \ll 1$ , then we can simplify the above expression:

$$\begin{aligned} U(\vec{r}) &= \frac{\int_0^\pi -d(\cos(\Theta)) U_0 \cos(\Theta) \left(1 - \frac{U_0 \cos(\Theta)}{k_B T}\right)}{\int_0^\pi -d(\cos(\Theta)) \left(1 - \frac{U_0 \cos(\Theta)}{k_B T}\right)} \\ &= -\frac{U_0^2}{3k_B T} = -\frac{1}{3k_B T} \left(\frac{Q\mu}{4\pi\epsilon_0\epsilon}\right)^2 \cdot \frac{1}{r^4} \end{aligned} \quad (2.16)$$

So we see the change in the interaction potential from  $\frac{1}{r^2}$  for a static dipole to  $\frac{1}{r^4}$  for a rotating one. The thermal motion weakens the Coulomb interaction also for dipole-dipole interaction. A similar calculation can be made for dipoles that are free to rotate with a centre-to-centre separation of  $r$ . We then obtain

$$U(\vec{r}) = -\frac{2}{3k_B T} \left(\frac{\mu_1 \mu_2}{4\pi\epsilon_0\epsilon}\right)^2 \cdot \frac{1}{r^6} \quad (2.17)$$

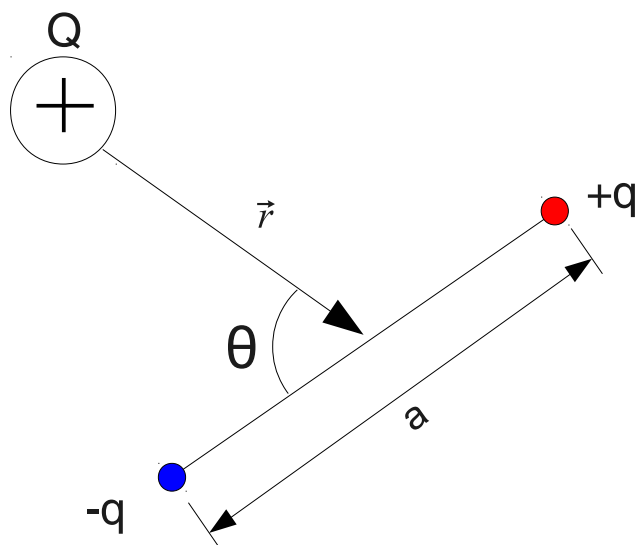


Figure 2.6: Interaction between a single charge and a rotating dipole.

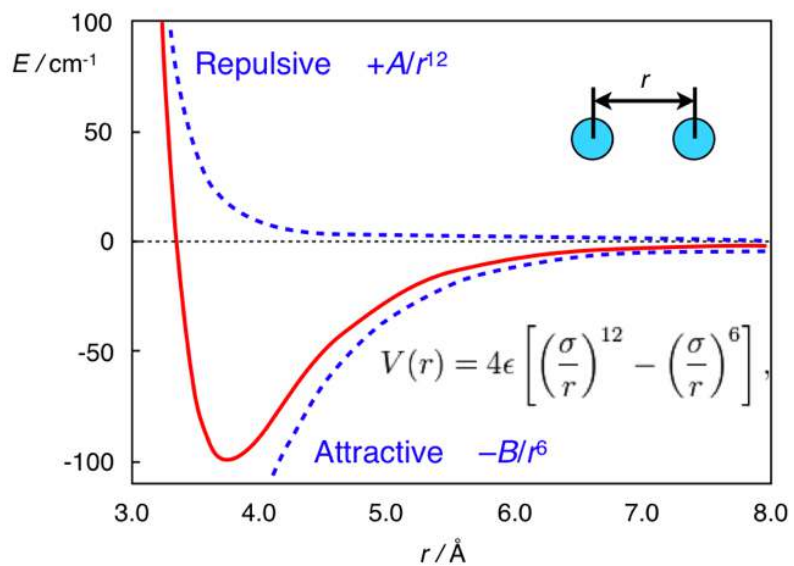


Figure 2.7: Lennard-Jones Potential. Source: <http://homepage.mac.com>

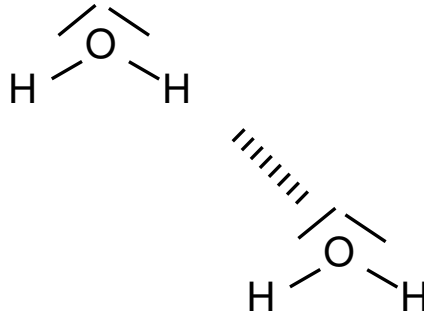


Figure 2.8: Hydrogen bond between two water molecules.

Thus two permanent dipoles interact with an attractive and short-ranged  $1/r^6$  - potential.

A universal and short-ranged  $1/r^6$ -attraction also arises for completely neutral atoms due to quantum fluctuations. A neutral atom can always form a dipole by quantum fluctuations, and this induces another dipole in a near-by atom, with an interaction potential

$$U = -\vec{p}\vec{E} = -\alpha E^2(\vec{r}) \sim -\frac{\alpha}{r^6} \quad (2.18)$$

Here  $\alpha$  is the polarizability and  $E(\vec{r}) \sim \frac{1}{r^3}$  is the electric field of a dipole. Even spherical and uncharged gas atoms like argon condense into liquids at very low temperatures due to these “dispersion forces” (Fritz London 1937).

The different  $\frac{1}{r^6}$ -interactions are collectively called “van der Waals forces”. As a convenient model for these forces one often uses the “Lenard-Jones potential”:

$$U(r) = 4\epsilon \left[ \left(\frac{\sigma}{r}\right)^{12} - \left(\frac{\sigma}{r}\right)^6 \right] \quad (2.19)$$

As one can see in figure 2.7, the interaction between atoms is attractive, if they are situated at distances greater than a certain distance  $\sigma$ . If the two particles come closer and closer together, they start to repel each other due to the Born repulsion. This part of the interaction curve is described by the  $1/r^{12}$  - potential. The 12th power was not measured, but is rather an arbitrary dependency accepted for convenience. For argon, the parameters are  $\epsilon = 0.4 k_B T$  and  $\sigma = 3.4 \text{ \AA}$ .

## 2.2.4 Hydrophilic and hydrophobic interactions

Much of the complexity of biological systems arises from the peculiar properties of water, in particular from its tendency to form hydrogen bonds. In a hydrogen bond a hydrogen atom is situated between two other atoms. An example of this kind of bond is depicted in figure 2.8. Water forms hydrogen bonds with itself, leading to a tetrahedral network structure in ice and liquid water, compare

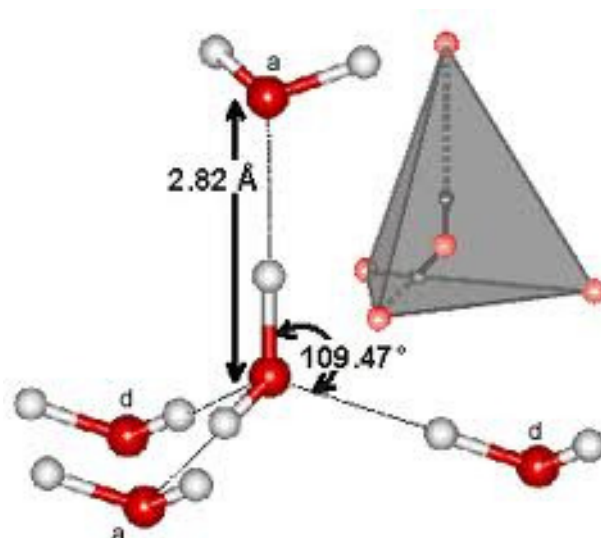


Figure 2.9: Tetrahedral structure of ice and water, due to the hydrogen bonds between the water molecules. Source: [www.lsbu.ac.uk](http://www.lsbu.ac.uk).

figure 2.9. This means that every water molecule has only four neighbors. In comparison, argon atoms have 10 and in close packing structure there are 12.

While the van der Waals interaction tends to condense water molecules, the network of hydrogen bonds creates a more open structure. Because the second effect dominates in ice, it swims on water. This also leads to the maximal density of water at  $4\text{C}^\circ$ . Pressure squeezes the molecules together and usually leads to freezing; in water, it leads to melting. This is part of the explanation why you can skate on ice, but not on glass. The feature of water is demonstrated in figure 2.10, where the phase diagrams of water and carbon dioxide are compared.

In summary water should not be considered as a normal liquid but rather as a network of fluctuating and cooperative hydrogen bonds. Other hydrogen-bonded liquids are hydrogen fluoride HF, hydrogen peroxide  $\text{H}_2\text{O}_2$ , hydrogen cyanide HCN.

Water is also a very special solvent. It is ordered by the presence of the solutes. For a hydrophobic solute, water molecules point their H-bonds away from the solute. This decreases the entropy and therefore makes solution unfavorable (measured by calorimetry, the effect is the strongest at  $25\text{C}^\circ$ ). Because of the “hydrophobic effect” water and oil do not mix. Non-polar solutes attract each other in water and this phenomenon is called the “hydrophobic interaction”.

The large energy stored in the network of hydrogen bonds results in large values for the surface tension, melting and boiling temperatures, heat capacity, etc. Because the network of hydrogen bonds is easily polarized, water has a very high dielectric constant ( $\epsilon = 80$ ). It is also important to remember that polar solutes prefer polar solvents due to the low self-energy. In analogy to the previous paragraph this effect is called “hydrophilic interaction”.



## The Phase Diagrams of H<sub>2</sub>O and CO<sub>2</sub>

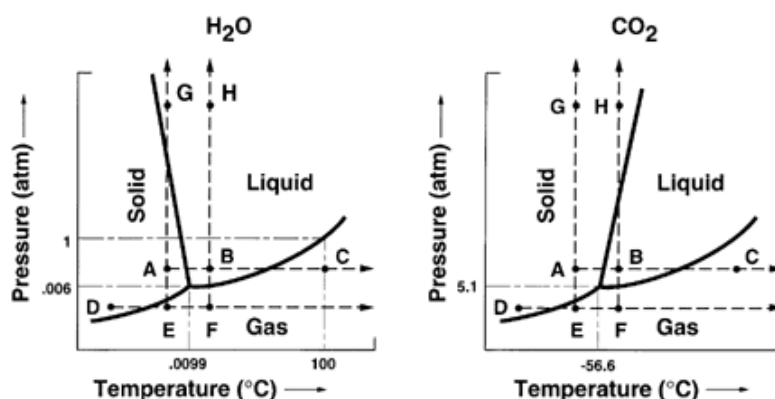


Figure 2.10: Phase diagrams of water on the left and of carbon dioxide on the right. Source: [www.astrosociety.org](http://www.astrosociety.org).

### 2.2.5 Protein folding

The special properties of water are not only the basis of membrane assembly, but also of protein folding. A standard method for studying and analyzing protein folding is the HP-model by Ken Dill. It has been extensively studied on the lattice by exact enumeration. The standard case is a  $3 \times 3 \times 3$  lattice, which can contain  $2^{27} = 134217721$  sequences and has 103346 possible configurations (this number is non-trivial because one has to figure out all symmetry operations that make two configurations identical in order to avoid overcounting). We pick one configuration and fill it with a given sequence. After finishing the construct on the lattice, for every amino acid positioned on the outside of the lattice an extra P is added. After that every unfavorable H-P contact is assigned a free energy penalty  $\epsilon$ . This is repeated for all configurations and at the end we look for the one with the lowest energy for a given sequence. If this ground state is unique, we call it “native structure” and the sequence is “protein-like”.

The HP-model is a very useful toy model for protein folding. We now consider a simpler variant. This time we have a  $2 \times 3$  lattice with  $2^6$  sequences and 3 different configurations. The solvent molecules surrounding the lattice pattern are assumed to be P-monomers. We now try to fit two different sequences on this lattice — HPHPHP and PHPPHP. In figure 2.12 all possible configurations for both sequences are shown.

While the first sequence (HPHPHP) is degenerated, the second (PHPPHP) has a unique ground state. The sequence is therefore protein-like. The probability to find the chain in the native structure as function of temperature is given by a sigmoidal function, see figure 2.12:

$$P_{\text{fold}} = \frac{\exp(-2\beta\epsilon)}{\exp(-2\beta\epsilon) + 2\exp(-4\beta\epsilon)} \quad (2.20)$$

where  $\beta = 1/k_B T$  as always.

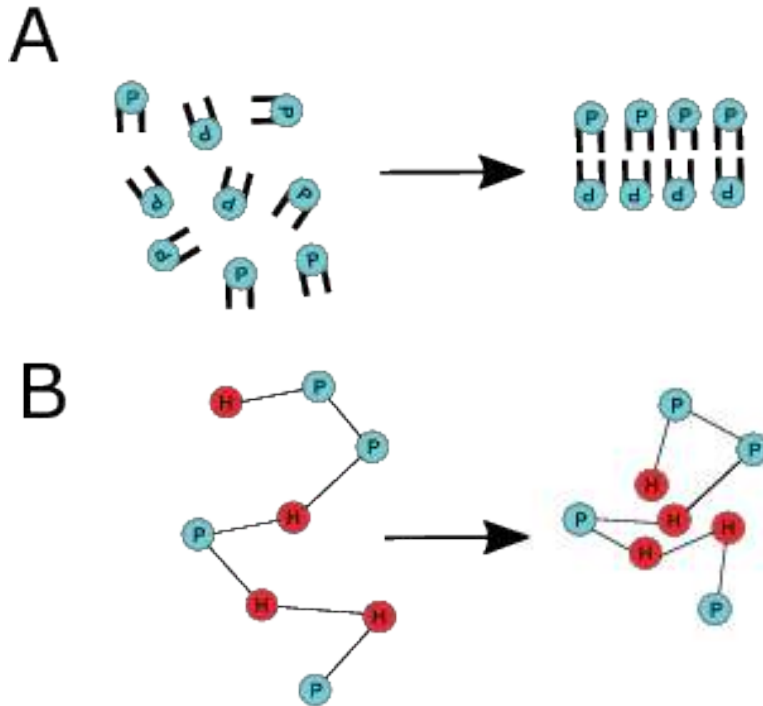


Figure 2.11: The two most important consequences of the hydrophobic effect in biological systems. (A) Lipids form bilayers to shield the hydrophobic tails from the surrounding water. (B) Proteins fold into a native conformation to shield the hydrophobic amino acids from the surrounding water.

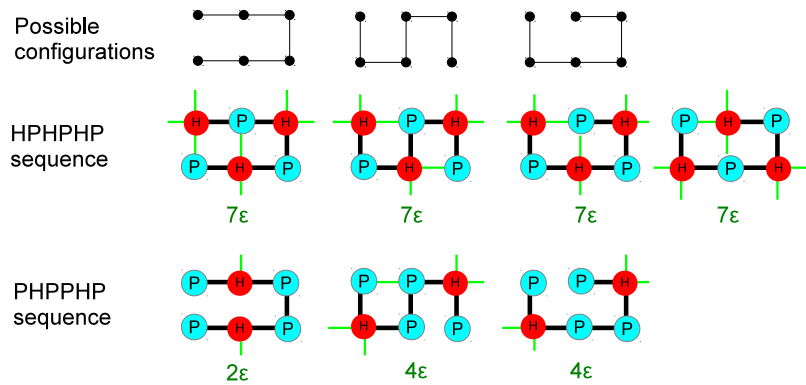


Figure 2.12: HP-model on a  $3 \times 2$  - lattice. The upper panel shows the possible configurations on this lattice. Center panel: Possibilities to arrange the sequence HPHPHP on the lattice. Note, that for the third configuration there exist two possible arrangements. The energy penalty per H-P contact is  $\epsilon$  (denoted as green lines). Recall that the environment of the polymer is polar. Lower panel: PHPPHP sequence on the lattice. The first configuration has a unique lowest energy and therefore forms the ground state.

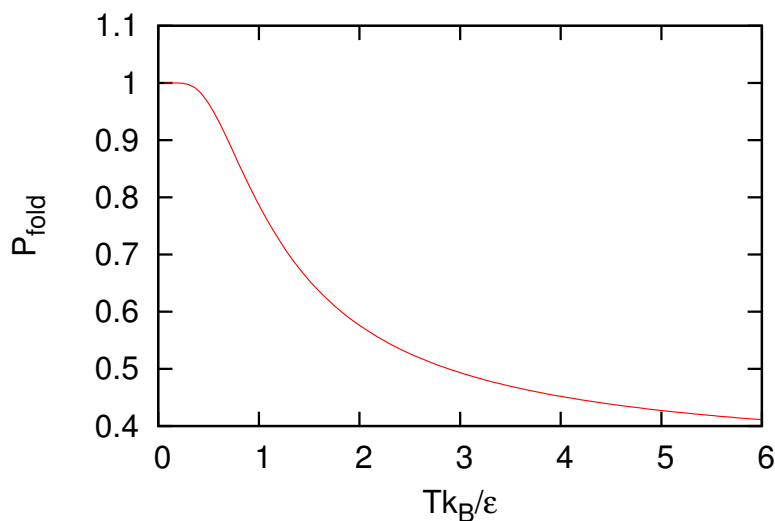


Figure 2.13: The probability to find the native structure as a function of temperature.

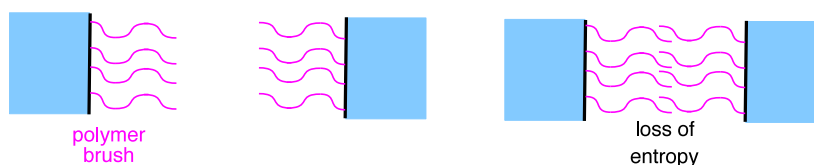


Figure 2.14: Polymer brushes as an example for steric interaction. As the brushes approach each other, the volume available for their motion and hence the entropy is reduced, leading to an effective repulsion.

## 2.2.6 Steric interactions

Another important class of interactions are excluded volume interactions. Because particles cannot overlap, their entropy is reduced and this creates effective interactions. An example of this kind of effects are polymer brushes, shown in figure 2.14. They repel as the chains start to overlap just for entropy reasons. Therefore they are used to stabilize colloidal suspensions like ink, but also in cell-cell interactions. For example polymer brushes on the outside of a cell membrane help avoiding cell attraction. This effect was understood only about 50 years ago because of its complexity and the need of deep knowledge in statistical physics and understanding of entropy.

Another example of steric interactions can be observed between fluctuating membranes. Imagine two membranes coming closer together, as described in figure 2.15. As  $d$  gets smaller the membranes start to perturb each other following the dependency  $V(d) \sim \frac{1}{d^2}$ . Similar considerations apply for two soft particles (e.g. two cells) approaching each other.

The last example given here is the depletion interaction. Imagine two large particles (depicted as large spheres in figure 2.16) that are surrounded by many

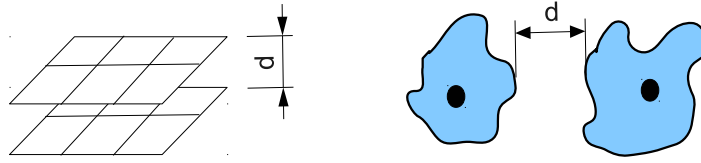


Figure 2.15: The planes on the left side represent two membranes that fluctuate to and away from each other. On the right hand side one can see two whole cells with fluctuating membranes .

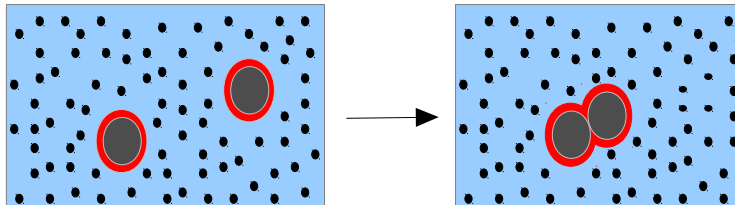


Figure 2.16: Depletion interaction.

small particles. The volume available to the small molecules is marked blue, the excluded volume is marked red. When the two large particles come close together, so that the restricted volumes on their surfaces start to overlap, the entropy of the system increases, because the volume available to the small molecules increases. The system tries to reach a state with higher entropy, that is why the interaction is called entropic attraction.

### 2.3 Phase separation

For a long time, it was thought that biological systems tend to avoid phase separation, in the sense of the one-component phase diagram shown in Fig. 1.2, which has two types of phase separations, fluid-crystal and fluid-fluid.

Crystal formation occurs in the human body, either as calcium phosphate crystals in the bone, which we need, or as gall or bladder stones, which we do not need. Bacteria or viruses sometimes use gene crystals to go into a dormant stage, to survive for a long time under unfavorable conditions. However, all of these examples are rather special and it is believed that usually concentration are not sufficiently high to effect crystal formation. Obviously one artificially cranks up concentration to get the protein crystals needed for structure determination by X-ray diffraction.

Moreover, there was not much evidence for liquid-liquid phase separation (because the proteins are immersed in the cytoplasm, the fluid-fluid phase separation corresponds to low and high density solutions of proteins (and not to gas and liquid), so we call them liquid-liquid in this context.) Recently, this notion has changed completely, because it was realized that many proteins are disordered rather than structured, and that intrinsically disordered proteins (IDPs) tend to undergo liquid-liquid phase separations. Examples include the nucleolus, P-granules and stress granules. It is now realized that liquid-liquid phase separation are a convenient way to establish compartments in the cell, as an alternative to using membranes or protein shells to create closed compartments, like in vesicles or viruses, respectively. With bacterial microcompartments (BMCs), there is even an example which combines both, liquid-liquid phase separation and protein capsid formation.

From the theoretical point of view, one can say that structured and disordered proteins behave as colloids and polymers, respectively. Both phase separate, but large colloids do only crystallize, while polymers only have a liquid-liquid loop. Thus in each case, one of the two transitions from Fig. 1.2 is missing.

## 2.4 Molecular dynamics

Now that we are familiar with the relevant molecular interactions, we have to understand how to combine them in one unifying framework in order to apply them to biomolecules. The structure and dynamics of biomolecules and their interactions can be studied with molecular dynamics (MD) computer simulations. They integrate Newton's equations of motion for atoms interacting through the interaction laws detailed above:

$$m_i \frac{d^2}{dt^2} \vec{r}_i = \vec{F}_i = -\vec{\nabla}_i U(\{\vec{r}_j\}) \quad (2.21)$$

Note that some effects are taken care implicitly (e.g. entropic effects when simulating all particles) and that for some effects one includes effective potentials (e.g. van der Waals interaction). For the energy function we sum all energy contributions as discussed before:

$$\begin{aligned}
 U = & \sum_{\text{covalent bonds}} \underbrace{\frac{k_r}{2}(r - r_0)^2}_{\text{bond stretching}} + \sum_{\text{angles}} \underbrace{\frac{k_\theta}{2}(\theta - \theta_0)^2}_{\text{bond bending}} + \sum_{\text{dihedral angles}} \underbrace{\frac{k_\phi}{2}(\phi - \phi_0)^2}_{\text{torsion}} \\
 & + \sum_{\substack{\text{non-bonded} \\ \text{interactions} \\ \langle ij \rangle}} \underbrace{\left( \frac{a}{r_{ij}^{12}} - \frac{b}{r_{ij}^6} \right)}_{\substack{\text{Lenard-Jones potential} \\ \text{or} \\ \text{van der Waals interactions}}} + \underbrace{\frac{q_i q_j}{4\pi\epsilon_0\epsilon} \cdot \frac{1}{r_{ij}^2}}_{\text{Coulomb interactions}} \quad (2.22)
 \end{aligned}$$

Because MD is a Hamiltonian dynamics, energy should be conserved. If we use an Euler scheme for the integration, we usually see derivations from this expectation,

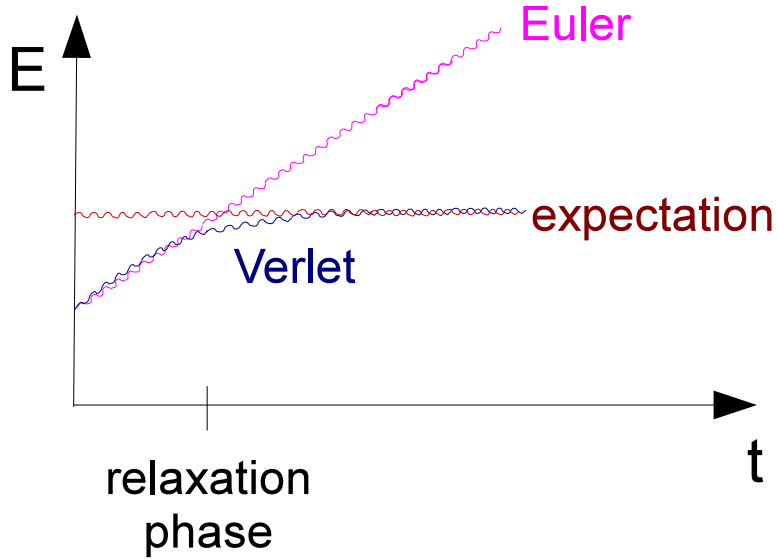


Figure 2.17: Energy distribution over time.

compare figure 2.17. The problem lies in the algorithm:

$$\vec{r}_i(t + \Delta t) \stackrel{\text{Taylor expansion}}{=} \vec{r}_i(t) + \vec{v}_i(t) \cdot \Delta t + \frac{\vec{F}_i(t)}{2m_i} \cdot \Delta t^2 + \mathcal{O}((\Delta t)^3) \quad (2.23)$$

$$\vec{v}_i(t + \Delta t) = \vec{v}_i(t) + \frac{\vec{F}_i(t)}{m_i} \cdot \Delta t + \mathcal{O}((\Delta t)^2) \quad (2.24)$$

This procedure is numerically unstable and does not ensure energy conservation and time reversibility even for small time intervals  $\Delta t$ .

The better solution is the “Verlet algorithm”, also called “leaping frog”:

$$\begin{aligned} \vec{r}_i(t \pm \Delta t) &\stackrel{\text{Taylor Expansion}}{=} \vec{r}_i(t) \pm \frac{d}{dt} \vec{r}_i(t) \cdot \Delta t + \frac{1}{2} \frac{d^2}{dt^2} \vec{r}_i(t) \Delta t^2 \pm \dots \\ \text{now we} &\quad \text{add both} \quad \text{equations and get} \\ \vec{r}_i(t + \Delta t) &= 2\vec{r}_i(t) - \vec{r}_i(t - \Delta t) + \frac{\vec{F}_i(t)}{m_i} \cdot \Delta t^2 \\ &\quad + \mathcal{O}((\Delta t)^4) \end{aligned} \quad (2.25)$$

One advantage is that the odd terms drop out, but more importantly the velocities are not needed and can be calculated independently by

$$\vec{v}_i(t + \Delta t) = \frac{\vec{r}_i(t + \Delta t) - \vec{r}_i(t - \Delta t)}{2\Delta t}$$

Using this algorithm we get results that agree better with our expectations, as can be seen in figure 2.17.

When performing MD-simulations, one has to make sure that one is familiar with the technical pitfalls. If one deals with finite system, in order to avoid surface

effects, one can work with periodic boundary conditions, truncated Lenard-Jones potentials and the appropriate Ewald sum for the Coulomb interaction. The ensemble described here is a NVE ensemble. If the temperature is fixed and the energy fluctuates we have a canonical or NVT ensemble. The standard solution in this case is the Nose-Hoover-thermostat. There are several classical papers and book that describe the details of this important method.

Here is a list of the classical papers on this subject:

- Alder, B. J., and TE Wainwright. "Phase transition for a hard sphere system." *The Journal of Chemical Physics* 27.5 (1957): 1208.
- Rahman, A. "Correlations in the motion of atoms in liquid argon." *Physical Review* 136.2A (1964): A405.
- Warshel, A., and M. Karplus. "Calculation of ground and excited state potential surfaces of conjugated molecules. I. Formulation and parametrization." *Journal of the American Chemical Society* 94.16 (1972): 5612-5625.
- Levitt, Michael, and Arieh Warshel. "Computer simulation of protein folding." *Nature* 253.5494 (1975): 694-698.
- Theoretical studies of enzymic reactions: dielectric, electrostatic and steric stabilization of the carbonium ion in the reaction of lysozyme. Warshel A, Levitt M. *J Mol Biol.* 1976 May 15;103(2):227-49.
- Karplus, Martin. "CHARMM: a program for macromolecular energy, minimization, and dynamics calculations." *Journal of computational chemistry* 4.2,187-217 (1983).
- Car, Richard, and Mark Parrinello. "Unified approach for molecular dynamics and density-functional theory." *Physical review letters* 55.22 (1985): 2471.

In 2013, the Nobel prize for chemistry was awarded to Karplus, Levitt and Warshel for the development of MD.

Books on MD-simulations:

- Daan Frenkel and Berend Smit, *Understanding Molecular Simulation: From Algorithms to Applications*. Academic Press 2001
- DC Rapaport, *The Art of Molecular Dynamics Simulation*, Cambridge University Press 2004
- MP Allan, *Computer Simulation Of Liquids*, Oxford University Press, U.S.A.; Auflage: Reprint (14. September 2006)

Here are some standard software packages:

- GROMACS: GROningen MAchine for Chemical Simulations (Herman Berendsen, Groningen)

- GROMOS: GRONingen MOlecular Simulation computer program package (Wilfred van Gunsteren, Switzerland)
- CHARMM: Chemistry at HARvard Macromolecular Mechanics (Martin Karplus, Harvard)
- NAMD: Not just Another Molecular Dynamics program (Klaus Schulten, Illinois)
- ESPResSo: Extensible Simulation Package for Research on Soft matter (Kurt Kremer and Christian Holm, Mainz and Stuttgart)

Movies on molecular processes (usually based on MD, but in some cases, an artistic component is added):

- Klaus Schulten lab: <http://www.ks.uiuc.edu/Gallery/Movies/>
- Ron Vale lab: <https://valelab.ucsf.edu/external/moviepages/moviesMolecMotors.html>
- DNA learning center: <http://dnalc.org/>
- Biovisions Harvard: <http://multimedia.mcb.harvard.edu/>
- D. E. Shaw Research: <https://www.deshawresearch.com> (private company with very fast code)

## 2.5 Brownian dynamics

Brownian dynamics is an effective or coarse-grained description of how molecules undergo random walks as they constantly collide with other molecules. Like in MD, we start with Newton's equation, for simplicity here for one particle of mass  $m$  in one dimension:

$$m\ddot{x} = m\dot{v} = F = -\nabla U . \quad (2.26)$$

We now add two new terms: a friction term describing energy dissipation into the surrounding medium and a random force (known as the noise term) that continuously kicks the particle:

$$m\dot{v} = F - \xi v + \sigma\eta(t)$$

Note that it is mandatory to add both terms together, because the noise term alone would input too much energy into the system, so the damping is required to balance this effect. This equation is the famous *Langevin equation*. It is a stochastic differential equation (SDE) and conceptually different from an ordinary (ODE) or a partial differential equation (PDE).  $\sigma$  is the amplitude of the noise term and  $\eta$  describes Gaussian white noise which obeys:

1.  $\langle \eta(t) \rangle = 0$
2.  $\langle \eta(t)\eta(t') \rangle = 2\delta(t - t')$



The formal solution is given by:

$$v(t) = e^{-t/t_0} \left( v_0 + \int_0^t ds e^{s/t_0} \frac{\sigma}{m} \eta(s) \right)$$

as one can check easily by insertion into the Langevin equation. Here  $t_0 = m/\xi$  is the characteristic relaxation time of the system.

Obviously  $v$  is defined only through its averages, like the noise itself:

$$\begin{aligned} \langle v(t) \rangle &= v_0 e^{-t/t_0} \\ \langle v(t)v(t') \rangle &= v_0^2 e^{-\frac{t+t'}{t_0}} + \left( \frac{\sigma}{m} \right)^2 e^{-\frac{t+t'}{t_0}} \underbrace{\int_0^t ds \int_0^{t'} ds' e^{\frac{s+s'}{t_0}} 2\delta(s-s')}_{\stackrel{t < t'}{=} \int_0^t ds 2e^{2s/t_0} = t_0(e^{2t/t_0} - 1)} \\ &= e^{-\frac{t+t'}{t_0}} \underbrace{\left( v_0^2 - \frac{\sigma^2}{m\xi} \right)}_{=0 \text{ for } t, t' \gg t_0} + \frac{\sigma^2}{m\xi} e^{(t'-t)/t_0} \\ &\Rightarrow \langle v(t)^2 \rangle = \frac{\sigma^2}{m\xi} \end{aligned}$$

Note that the linear terms in  $\eta$  have dropped out and that the autocorrelation decays exponentially, thus the system is well-behaved.

The equipartition theorem gives us:

$$\begin{aligned} \frac{1}{2} m \langle v^2 \rangle &= \frac{1}{2} k_B T \\ \Rightarrow \boxed{\sigma^2 = \xi k_B T} &\quad \text{fluctuation-dissipation theorem} \end{aligned}$$

The noise amplitude  $\sigma$  (fluctuations) is related to the friction coefficient  $\xi$  (dissipation) through temperature  $T$ . The higher temperature  $T$ , the stronger the noise.

For  $t \gg t_0$ , we can neglect inertia:

$$\begin{aligned} \Rightarrow \xi v &= \sigma \eta(t) = \xi \dot{x} \\ \Rightarrow x(t) &= x_0 + \frac{1}{\xi} \int_0^t dt' \sigma \eta(t') \\ \Rightarrow \langle x(t) \rangle &= x_0 \\ \langle (x(t) - x_0)^2 \rangle &= \frac{1}{\xi^2} \int_0^t dt' \int_0^t dt'' 2\sigma^2 \delta(t' - t'') \\ &= \frac{1}{\xi^2} 2\sigma^2 t \stackrel{!}{=} 2Dt \end{aligned}$$

Here we identified the diffusion constant  $D$  from the one dimensional random walk.

$$\Rightarrow \boxed{D = \frac{\sigma^2}{\xi^2} = \frac{k_B T}{\xi}} \quad \text{Einstein relation}$$

If we use for the friction coefficient Stoke's law from hydrodynamics,  $\xi = 6\pi\eta R$  with viscosity  $\eta$  we get:

$$\Rightarrow \boxed{D = \frac{k_B T}{6\pi\eta R}} \quad \text{Stokes-Einstein relation}$$

Inserting in typical numbers ( $T = 300$  K,  $\eta = 10^{-3}$  Pa s,  $R = 1$  nm), we get  $D = (10 \mu\text{m})^2/\text{s}$  as typical diffusion constant for proteins.

We are now in the position to formulate the basic algorithm for BD-simulations:

$$\frac{dx(t)}{dt} = -M\nabla U + \left(\frac{k_B T}{\xi}\right)^{1/2} \eta \quad (2.27)$$

$$= -D\nabla \left(\frac{U}{k_B T}\right) + D^{1/2}\eta \quad (2.28)$$

Here we have introduced the mobility  $M = 1/\xi$ . Due to the FDT, we only have one relevant parameter, which we take to be  $D$ . The discretized version now reads:

$$x(t + \Delta t) = x(t) - D \frac{d}{dx} \left(\frac{U}{k_B T}\right) \Delta t + \sqrt{2D\Delta t} \mathcal{N}(0, 1) \quad (2.29)$$

where  $\mathcal{N}(0, 1)$  is the Gaussian distribution with vanishing mean and unit variance. In order to be able to work with the standard Gaussian, we now explicitly use the factor of 2 that above we have placed in the definition of the Gaussian white noise. It is straight-forward to generalize this scheme to  $N$  particles with interaction terms in  $U$ .

The BD-community did not yet converge on a few software packages and thus there are many of them. Here are a few examples:

- LAMMPS from Sandia National Labs, started as large-scale parallel MD code, but also includes Langevin, [lammmps.sandia.gov](http://lammmps.sandia.gov)
- HOOMD from Sharon Glotzer's lab, also a MD-code with Langevin mode, <https://hoomd-blue.readthedocs.io>
- ESPResSo from Kurt Kremer Mainz / Christian Holms Stuttgart, coarse-grained MD/BD for soft matter, [www.espresso-pp.de](http://www.espresso-pp.de) / [esspressomd.org/wordpress](http://esspressomd.org/wordpress)
- Smoldyn from Steve Andrews, point particles and arbitrary geometries, many published projects, [www.smoldyn.org](http://www.smoldyn.org)
- MesoRD from Johan Elf, discretized on cubic lattice, diffusion as reaction, Gillespie algorithm, [mesord.sourceforge.net](http://mesord.sourceforge.net)
- Greens Function Reaction Dynamics (GFRD) from Pieter Rein ten Wolde, event-based reactions based on exact solutions to the diffusion equation, [gfrd.org](http://gfrd.org)
- Simulation of diffusional association (SDA) from Rebecca Wade, [mcm.h-its.org/sda](http://mcm.h-its.org/sda)

- BrownDye from Gary Huber (Andrew McCammon group), uses APBS for electrostatics, [browndye.ucsd.edu](http://browndye.ucsd.edu)
- MacroDox from Scott Northrup, reads in PDB-files, [www.cae.tntech.edu/~snorthrup/macrodox/macrodox.html](http://www.cae.tntech.edu/~snorthrup/macrodox/macrodox.html)
- MCell from Terry Sejnowski, Monte Carlo, often used in the neurosciences, [www.mcell.cnl.salk.edu](http://www.mcell.cnl.salk.edu)
- ReaDDy from Frank Noe, includes potentials, combination of MD and BD, [simtk.org/home/readdy](http://simtk.org/home/readdy)
- Cytosim from Francois Nedelec, focus on filament mechanics, [www.cytosim.org](http://www.cytosim.org)
- AFiNeS from Aaron Dinner, active filaments networks, [www.dinner-group.uchicago.edu/-downloads.html](http://www.dinner-group.uchicago.edu/-downloads.html)

We finally note that in BD one deals with an effective solvent that in principle should also mediate hydrodynamic interactions. The importance of hydrodynamics for self-diffusion and molecular interactions is somehow debated and there are many approaches to address this important issue. Because biomolecules and cells are so small, they have a small Reynolds number:

$$Re = \frac{\rho v L}{\eta} \ll 1 \quad (2.30)$$

if we insert typical values for density  $\rho$  and viscosity  $\eta$  of water as well as for velocity  $v$  and size  $L$ . Thus viscous forces dominate over inertial ones and one has to solve the Stokes equation rather than the Navier-Stokes equation. The most common approaches to hydrodynamics in biological systems are

- analytical solutions, including the Oseen and Rotne-Prager tensors
- FEM-implementations of the Stokes equation, e.g. in FEniCS (<https://fenicsproject.org>)
- Lattice Boltzmann Method (LBM)
- Dissipative Particle Dynamics (DPD)
- Multi Particle Collision Dynamics (MPCD)

For a recent review, compare Ulf Schiller et al, Mesoscopic modelling and simulation of soft matter, *Soft Matter* 2018.



## Chapter 3

# Electrostatistics and genome packing

We already discussed that polarizability and thermal rotation weakens the electrostatic interaction between two molecules in the cell. We now consider this issue further for a charged object (an ion, a biomolecule or an assembly of biomolecules) immersed in a sea of other charges. These surrounding charges are counter-ions (balancing the charge on the object) that can be complemented by co-ions (salt). The fact that the counter- and co-ions are highly mobile and under permanent thermal motion creates a cloud of charge distribution that screens and further decreases the electrostatic interaction between the large objects.

### 3.1 Role of geometry

In figure 3.1 we depict two important situations of this kind in the cell, namely the charge distributions around a DNA and around a lipid membrane. For the DNA, the size of a basepair is 0.34 nm and we have  $6 \cdot 10^9$  bp in our genome (counting all chromosome, which come in pairs), thus the DNA in each of our cells amount to a length of 2 m. Now consider that each basepair carries a charge of  $2e^-$  and that the diameter of nuclei are in the order of  $\mu m$ . We therefore must ask the question how the highly charged DNA can be compactified to this small size. The same question arises for bacteria (they typically have one circular chromosome with around 1 Mbp, amounting to a contour length of around 1 mm, packed into a  $\mu m$  large cell body) and for DNA viruses, where the packing density is even higher. As we will see below, the solution to this DNA riddle is provided by theoretical physics in the form of strong coupling theory<sup>1</sup>.

For the lipid bilayer depicted in figure 3.1, the charge distribution is not characterized by a line charge density  $\lambda$ , but by an area charge density  $\sigma$ . Here the

---

<sup>1</sup>For reviews, see Roland Netz, Electrostatistics of counter-ions at and between planar charged walls: From Poisson-Boltzmann to the strong-coupling theory, *Eur. Phys. J. E* 5, 557-574 (2001); and David Andelman, Introduction to electrostatics in soft and biological matter, contribution in collection *Soft condensed matter physics in molecular and cell biology*, editors Wilson Poon and David Andelman, CRC Press, 2006.

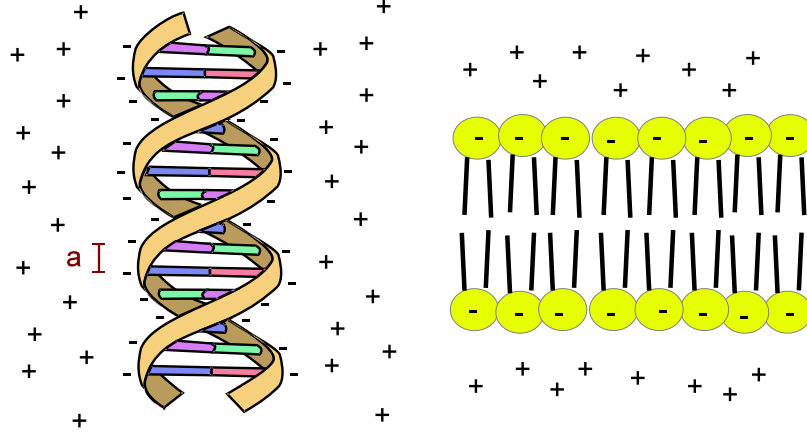


Figure 3.1: Left panel: Polyelectrolyte such as a DNA molecule. Per base pair ( $bp$ , distance between  $bp$   $a = 3.4 \text{ \AA}$ ), the DNA carries a charge of  $2e^-$  and hence a line charge density of  $\lambda = \frac{2e^-}{3.4 \text{ \AA}}$  (image of DNA molecule taken from Wikipedia). Right panel: Negatively charged head groups of the fatty acids in the plasma membrane resulting in an area charge density of  $\sigma = \frac{e^-}{nm^2}$ .

relevant biophysical questions are very different from the case of DNA. Because of the barrier function of the lipid bilayer, we have to ask how charges arrange themselves in its vicinity and how they can cross the bilayer. Obviously the distribution around charged lines and surfaces must be very different for geometrical reasons.

As already mentioned in the beginning of this chapter, a DNA molecule can be seen as a charged line with a linear charge density of  $\lambda = \frac{2e^-}{3.4 \text{ \AA}}$ . To simplify matters, we assume the DNA molecule to be an infinitely long straight line. Then the DNA exhibits a cylindrical symmetry (compare figure 3.2a) and Gauss law can easily be applied to determine the radial component of the electrostatic field:

$$\text{Gauss' law: } E_r \cdot 2\pi r L = \frac{\lambda L}{\epsilon_0 \epsilon}$$

$$\text{Electrostatic field: } E_r = \frac{\lambda}{2\pi \epsilon_0 \epsilon r} \quad (3.1)$$

$$\begin{aligned} \text{Electrostatic potential: } \Phi &= -\int_a^r E_r dr \\ &= -\frac{\lambda}{2\pi \epsilon_0 \epsilon} \ln\left(\frac{r}{a}\right) \end{aligned} \quad (3.2)$$

where a microscopic limit  $a$  was employed. The logarithmic electrostatic potential  $\Phi$  in equation 3.2 diverges for  $r \rightarrow \infty$ . Thus, the boundary condition  $\Phi(\infty) = 0$  cannot be used. One often encounters this logarithmic behavior in 2D systems. For example, this means that one cannot calculate a simple formula for the flow of a fluid around a cylinder (as one can for the flow of a fluid around a sphere in 3D).

For the straight line charge the same result as in equations 3.1 and 3.2 can be obtained from the direct integration of Coulomb's law (equation 1.56) or from

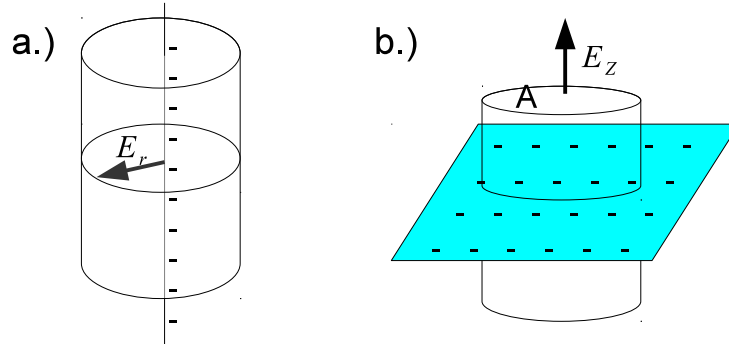


Figure 3.2: Cylindrical symmetry of a.) an infinitely long charged line and b.) an charged plane with infinite surface.

the Poisson equation (equation 1.58) in cylindrical coordinates.

In the cell, the plasma membrane can be seen as a charged plane with an area charge density  $\sigma = \frac{e^-}{nm^2}$ . Again, the electrostatic field can be computed with Gauss law. Restricting oneself to an infinitely large surface with negligible curvature, the cylindrical symmetry of the plane can be made use of (compare figure 3.2):

$$\text{Gauss' law: } E_z \cdot 2A = \frac{A\sigma}{\epsilon_0\epsilon}$$

$$\text{Electrostatic field : } E_z = \frac{\sigma}{2\epsilon_0\epsilon} \quad (3.3)$$

$$\text{Electrostatic potential: } \Phi = -\frac{\sigma z}{2\epsilon_0\epsilon} \quad (3.4)$$

Two comments can be made concerning the results in equations 3.3 and 3.4. Firstly,  $\Phi$  increases linearly with the distance from the charged plane. Secondly, the electric field jumps by  $\sigma/(\epsilon_0\epsilon)$  across the charged plane and does not depend on the distance. As before, the same results can be obtained from explicit integration or from solving the Poisson equation.

### 3.2 The membrane as a parallel plate capacitor

Besides its function as a diffusion barrier, the biomembrane can act as a parallel plate capacitor (compare figure 3.3) if charges are separated to its both sides by active processes such as ion pumps and transporters. Then we are actually dealing with two oppositely charged planes with electric fields according to equation 3.3:

$$E_+ = E_- = \frac{\sigma}{2\epsilon_0\epsilon} \quad (3.5)$$

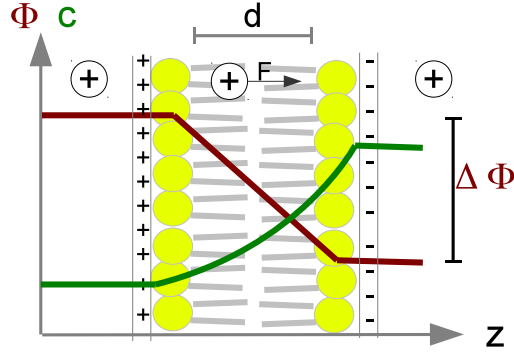


Figure 3.3: Electrostatic potential ( $\Phi$ , labeled in red) and ion concentration ( $c$ , labeled in green) across the plasma membrane which is modeled as a parallel plate capacitor. In the inter-membrane region, the potential decreases linearly whereas the concentration follows  $\sim e^{-q\Delta\Phi/(k_B T)}$  (equation 3.10). Since the electrical field of a charged plane does not depend on the distance from the plane (compare equation 3.3), the net field outside the membrane vanishes. Hence, there is a force on a charged test particle only if it is *within* the lipid bilayer.

Outside the plasma membrane,  $E_+$  and  $E_-$  cancel each other, whereas within the membrane they add up:

$$\text{Electrostatic field: } E_{inside} = E_+ + E_- = \frac{\sigma}{\epsilon_0 \epsilon} \quad (3.6)$$

$$\text{Electrostatic potential difference: } \Delta\Phi = - \int_0^d dz \frac{\sigma}{\epsilon_0 \epsilon} = - \frac{\sigma d}{\epsilon_0 \epsilon} \quad (3.7)$$

From equation 3.7, the capacitance of the plane can be computed:

$$C = \frac{Q}{U} = \frac{A\sigma}{|\Delta\Phi|} = \frac{A\epsilon_0 \epsilon}{d} \quad (3.8)$$

As an example, we choose a myelinated nerve cell membrane with  $\epsilon = 2$  and  $d = 2 \text{ nm}$ . We then obtain for the capacitance of the nerve cell membrane:

$$\frac{C}{A} = \frac{\epsilon_0 \epsilon}{d} \approx \frac{\mu F}{\text{cm}^2}$$

where  $F$  denotes the physical unit Farad. This value membrane capacity has been measured experimentally. Moreover, the measure of  $1 \frac{\mu F}{\text{cm}^2}$  is universally used in experiments to determine the area of any given cell or membrane patch. The concept of the biomembrane being a parallel circuit of a capacitor and an ohmic resistance forms the basis of electrophysiology (theory of action potentials according to Hodgkin and Huxley).

We now consider a single species of mobile ions that is free to distribute along  $z$  (e.g. ions diffusing through the hydrophobic part or through an ion channel of the membrane). At finite temperature  $T$ , there is a competition between electrostatic forces and translational entropy. The concepts of energy stored in the form of



	intracellular (mM)	extracellular (mM)	Nernst potential (mV)
$K^+$	155	4	-98
$Na^+$	12	145	67
$Cl^-$	4	120	-90
$Ca^{2+}$	$10^{-4}$	1.5	130

Table 3.1: Nernst potentials for some important ions in a typical mammalian muscle cell. Because the Nernst potentials of the different ion species differ strongly, this ionic distribution is an out-of-equilibrium situation. Resting potentials of excitable cells are in the range of  $-50$  to  $-90$  mV.

chemical potential  $\mu$  and electrostatic potential  $\Phi$  can be combined in the so-called **electrochemical potential** (compare Eq. 1.28 for the chemical potential of an ideal gas):

$$\mu(z) = k_B T \ln c(z) + Ze\Phi(z) \quad (3.9)$$

where  $Z$  is the valency of the ion species. In equilibrium,  $\mu(z)$  has to be constant:

$$\begin{aligned} \Rightarrow \ln \left( \frac{c(z_1)}{c(z_2)} \right) &= \frac{-Ze(\Phi(z_1) - \Phi(z_2))}{k_B T} \\ \Rightarrow \boxed{c(z_2) = c(z_1) \cdot e^{-Ze\Delta\Phi/(k_B T)}} & \quad \text{Nernst equation} \quad (3.10) \end{aligned}$$

Equation 3.10 was first formulated by the German physical chemist Walter Nernst who won the Nobel prize in chemistry in 1920. It can be seen as Boltzmann's law for charges in an electrostatic potential (compare figure 3.3). In table 3.1 we give experimentally measured values for ion concentrations in a muscle cell. The corresponding Nernst potentials are calculated in the last column. One sees that they differ widely, proving that the distributions are out of equilibrium (ion pumps and channels redistribute them against the thermal forces).

Our discussion showed that mobile charges will lead to concentration profiles that depend on temperature and electrostatic potential. Therefore we now turn to "**electrostatics**", the field that combines these two elements.

### 3.3 Charged wall in different limits

At close approach, each object is locally flat (e.g. a globular protein or a colloid). We therefore start with the planar case as most instructive example. Consider a wall with an area charge density of  $\sigma$  and the corresponding counter-ions, e.g. dissociated groups of the charged object, in solution. Note, that the complete system does not carry a net charge, i.e. it is always charge neutral. Two cases can be distinguished. First a solution containing only counter-ions, and second a solution with additionally added salt, hence also containing co-ions (see figure 3.4). These seemingly simple systems are in fact hard problems in theoretical physics. In the following, we will treat three special cases for the planar geometry:

1. high  $T$  or small charge density  $\sigma$  (no salt): In this case mean field theory (MFT) can be used to derive the **Poisson-Boltzmann theory**.

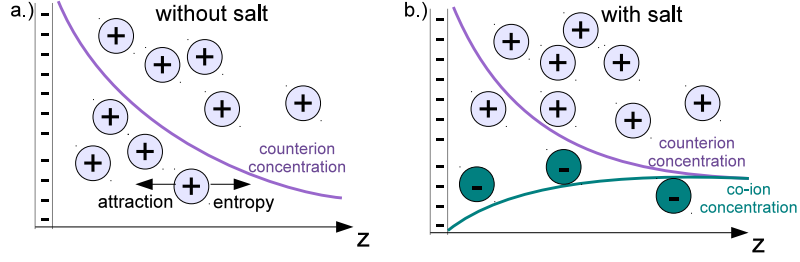


Figure 3.4: Concentration profile of counter-ions (here: positive) and co-ions (here: negative) in a solution (a) without salt and (b) with salt, at a distance  $z$  from the charged wall. For (b), the physiological concentration of additional salt is for instance in the range of  $c_s = 100 \text{ mM}$  (e.g. NaCl).

2. salt,  $c_s \neq 0$ : **Debye-Hückel theory**, will turn out to be a linearized Poisson-Boltzmann theory
3. low  $T$  or high charge density  $\sigma$  (no salt): **strong-coupling limit** (i.e. for DNA condensation)

All other cases are too complicated to be treated analytically and have to be investigated with Monte Carlo simulation.

Because counter-ions and co-ions are mobile, we have to deal with thermal averages. The first step is to formulate the Hamiltonian of the system, therefore we consider  $N$  counter-ions of valency  $Z$  at an oppositely charged wall with area density  $n_{2d}$  (the charge density thus is  $\sigma = en_{2d}$ ):

$$\frac{H}{k_B T} = \sum_{i < j} \underbrace{\frac{Z^2 e^2}{4\pi\epsilon_0\epsilon k_B T \cdot r_{ij}}}_{\text{Coulomb interaction between 2 counter-ions}} + \sum_i \underbrace{\frac{Z e^2 n_{2d} z_i}{2\epsilon_0\epsilon k_B T}}_{\text{Coulomb interaction between one counter-ion and the wall}} \quad (3.11)$$

We introduce two new length scales to write

$$\frac{H}{k_B T} = \sum_{i < j} \frac{Z^2 l_B}{r_{ij}} + \sum_i \frac{z_i}{\mu} \quad (3.12)$$

resulting in the following definitions:

1. The **Bjerrum length**  $l_B = \frac{e^2}{4\pi\epsilon_0\epsilon k_B T}$  is the distance at which two unit charges interact with thermal energy. In water, where  $\epsilon = 80$ , we find  $l_B = 7 \text{ \AA}$ , while in vacuum the value Bjerrum length is  $5.6 \text{ nm}$  (both values computed for  $T = 300 \text{ K}$ ).
2. The **Gouy-Chapman length**  $\mu = (2\pi Z n_{2d} l_B)^{-1}$  marks the distance from a charged wall at which the potential energy of the charge equals  $k_B T$ . Note that in contrast to the definition of the Bjerrum length, we do not use a unit charge, but keep valency  $Z$  in the definition. For  $Z = 1$ , ambient temperature  $T$  and  $n_{2d} = 1/\text{nm}^2$ , one gets  $\mu \approx 1 \text{ nm}$ .

Because we focus on the effect of a wall, we now rescale all distances with  $\mu$ :

$$\frac{H}{k_B T} = \sum_{i < j} \frac{\Xi}{\bar{r}_{ij}} + \sum_i \bar{z}_i \quad (3.13)$$

where

$$\Xi = \frac{Z^2 l_B}{\mu} = 2\pi Z^3 l_B^2 n_{2d} = \frac{Z^3 e^4 n_{2d}}{8\pi(\epsilon_0 \epsilon k_B T)^2} \quad \text{coupling strength} \quad (3.14)$$

In equation 3.13, we rescaled the system such that only one dimensionless parameter, namely the coupling strength (equation 3.14), determines the behavior of the whole system.

At this point, we managed to end up with only one dimensionless parameter, that defines two asymptotic limits of interest<sup>2</sup>:

1.  $\Xi \ll 1$ : This is the case if the system has a low charge density, a low valency and/or a high temperature. One can perform an expansion in small  $\Xi$  (mean-field theory) and ends up with the Poisson-Boltzmann theory.
2.  $\Xi \gg 1$ : In the strong-coupling limit, the system has a high charge density, a high valency and/or is prepared at a low temperature. Here a virial expansion in  $\Xi^{-1}$  can be made.

In order to understand the difference better between the two limits, we use charge neutrality

$$\frac{Ze}{\pi a_{\perp}^2} = \sigma = en_{2d} \quad (3.15)$$

to introduce the typical lateral distance  $a_{\perp}$  between counter-ions. We now rescale this length with the Gouy-Chapman length:

$$\frac{a_{\perp}}{\mu} = \sqrt{\frac{Z}{n_{2d}\pi\mu^2}} = \sqrt{2\Xi} \quad (3.16)$$

This shows that  $\Xi$  determines the ratio between  $a_{\perp}$  and  $\mu$  (compare figure 3.5). For  $\Xi \ll 1$ , the lateral distance between the counter-ions is smaller than their average distance from the wall and they form a 3D cloud that has no structure in the lateral direction; therefore a mean field theory in z-direction is sufficient. For  $\Xi \gg 1$ , the lateral distance between the counter-ions is larger than their average distance from the wall and they form a 2D layer on the wall. For very strong coupling, this condensate can become a crystal.

---

<sup>2</sup>A complete treatment can be given using statistical field theory. For more details, compare the overview in R.R. Netz, European Physical Journal E 5: 557, 2001.

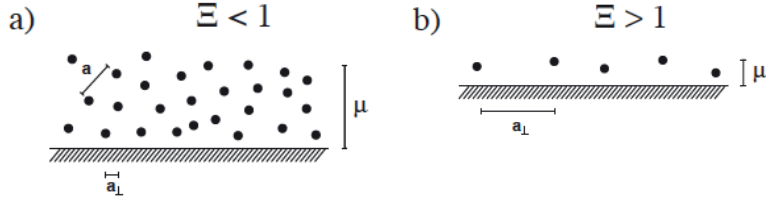


Figure 3.5: The two complementary limits considered here. (a) In the high temperature limit, the lateral distance of the counter-ions is smaller than the vertical extension and thus we get a 3D fluid. This situation is described by a mean field theory in z-direction (Poisson-Boltzmann theory). (b) In the low temperature limit, the lateral distance is larger than the vertical extension and we get a 2D condensate (strong coupling limit).

### 3.4 Poisson-Boltzmann theory

Poisson-Boltzmann theory is a mean field theory that assumes local thermal equilibrium. We start with the Poisson equation from electrostatics (equation 1.58)

$$\Delta\Phi = -\frac{\rho(\vec{r})}{\epsilon_0\epsilon}$$

and combine it with the Boltzmann distribution:

$$\begin{aligned} & \text{for simplicity} \\ \rho(\vec{r}) & \stackrel{Z=1}{=} e \cdot n(\vec{r}) = e \cdot n_0 \cdot \exp\left(\frac{-e\Phi(\vec{r})}{k_B T}\right) \end{aligned} \quad (3.17)$$

This results in

$$\Rightarrow \boxed{\Delta\Phi = -\frac{e}{\epsilon_0\epsilon} \cdot n_0 \cdot \exp\left(-\frac{e\Phi}{k_B T}\right)} \quad \text{Poisson-Boltzmann equation} \quad (3.18)$$

The Poisson-Boltzmann equation (PBE) is a non-linear differential equation of second order which is in general hard to solve analytically. In MD simulations, one usually employs PB-solvers (e.g. DelPhi, APBS, MIBPB, etc). There are only few cases for which it can be solved analytically.

Luckily, this is the case for the example of the charged wall. The boundary conditions are given by the charge neutrality of the whole system and by  $|E(\infty)| = |-\Phi'(\infty)| = 0$ :

$$\begin{aligned} \sigma &= -\int_0^\infty dz \underbrace{\rho(z)}_{\substack{\text{charge density} \\ \text{of counter-ions}}} = \epsilon_0\epsilon \int_0^\infty \Phi'' dz \\ &= \epsilon_0\epsilon \left( \underbrace{\Phi'|_{z=\infty}}_{=0} - \Phi'|_{z=0} \right) \\ &= -E(\infty) = 0 \\ \Rightarrow \Phi'|_{z=0} &= -\frac{\sigma}{\epsilon_0\epsilon} \end{aligned}$$

	point charge	charged wall	with counter-ions (PBT)	with salt (DH)
$\Phi$	$1/r$	$z$	$\ln(z)$	$\exp(-\kappa z)$
$E$	$1/r^2$	<i>const</i>	$1/z$	$\exp(-\kappa z)$

Table 3.2: Distance dependence of the electrostatic potential  $\Phi$  and the electrostatic field  $E$  for different systems. Note that in comparison to a point charge a spatially extended distribution like the charged wall strengthens the interaction, whereas the presence of counter-ions (Poisson-Boltzmann theory) weakens the interactions. If, in addition, salt is added to the solution, the interaction is weakened to an even higher extent.

With the boundary conditions, we get the analytical solution for the charged wall:

$$\text{Electrostatic potential} \quad \Phi(z) = \frac{2k_B T}{e} \ln\left(\frac{z + \mu}{\mu}\right) + \Phi_0 \quad (3.19)$$

$$\text{Counter-ion density} \quad n(z) = \frac{1}{2\pi l_B} \cdot \frac{1}{(z + \mu)^2} \quad (3.20)$$

Recall, that without counter-ions  $\Phi \sim z$  and  $E = \text{const}$  (compare equation 3.2 and equation 3.3; compare also table 3.2). This is now changed to a logarithmic scaling of the potential since a cloud of counter-ions surrounds any charged object and thus weakens the electrostatic potential. In other words, the charged wall is "screened" by the counter-ions. Together with the cloud or layer of counter-ions, the charged wall forms an electrostatic "double layer".

### 3.5 Debye-Hückel theory

Let us once again investigate the charged wall, now with a 1:1 electrolyte (i.e. NaCl) added to the solution. In this system, counter-ions as well as co-ions are present in the solution. Equation 3.17 for the density of the ion species accounts for both counter-ions and co-ions with the same  $n_0$  due to charge neutrality far from the wall. The PBE (equation 3.18) then reads:

$$\begin{aligned} \Delta\Phi &= -\frac{e}{\epsilon_0\epsilon}(n_+ - n_-) \\ &= -\frac{e}{\epsilon_0\epsilon} \left( n_0 \cdot \exp\left(\frac{-e\Phi}{k_B T}\right) - n_0 \cdot \exp\left(\frac{+e\Phi}{k_B T}\right) \right) \end{aligned} \quad (3.21)$$

$$= \frac{2e}{\epsilon_0\epsilon} \cdot n_0 \cdot \sinh\left(\frac{e\Phi}{k_B T}\right) \quad (3.22)$$

Note that the nice mathematical form of this equation arises because of the boundary condition that  $n_0$  is the same for both the plus and minus co-ions at infinity. Interestingly, there exists an analytical solution for this equation. Here however we continue right away with a special case. For small  $e\Phi/(k_B T)$ , we can linearize equation 3.22 by using  $\sinh(x) \approx x$  for small x. We then obtain

$$\boxed{\Delta\Phi = \kappa^2\Phi} \quad \text{Debye-Hückel equation} \quad (3.23)$$

$l_B$	$\mu$	$l_{DH}$
7 Å	1 nm	1 nm

Table 3.3: Values for the three electrostatic length scales Bjerrum length  $l_B$ , Gouy-Chapman length  $\mu$  and Debye-Hückel screening length  $l_{DH}$  at physiological conditions. Note that the three electrostatic lengths are very similar (all around 1 nm).

with the Debye-Hückel screening length

$$l_{DH} = \frac{1}{\kappa} = \left( \frac{\epsilon_0 \epsilon \cdot k_B T}{2e^2 n_0} \right)^{1/2} = (8\pi l_B n_0)^{-1/2} \quad (3.24)$$

$$l_{DH} = \begin{cases} 1 \mu m & \text{pure water, } 10^{-7} M, H_3O^+ : OH^- \\ 10 nm & 1 mM NaCl \\ 1 nm & 100 mM NaCl \text{ (cytoplasm)} \\ 3 \text{ \AA} & 1 M NaCl \end{cases}$$

which adds a third typical length scale to the two (Bjerrum length and Gouy-Chapman length) we already introduced before (see also table 3.3).

The solution of the Debye-Hückel equation for a charged wall is simply

$$\Phi(z) = \frac{\sigma}{\epsilon_0 \epsilon \kappa} e^{-\kappa z} \quad (3.25)$$

where we again employed the boundary condition  $\Phi'(z=0) = -\sigma/(\epsilon_0 \epsilon)$  due to charge neutrality.

In contrast to the result obtained by the PB theory where no salt was added to the solution, equation 3.25 exhibits an exponential decay. Thus, the interaction is short-ranged. In general, the more salt is added to the solution, the smaller is the screening length  $l_{DH}$  and the more the charged wall is screened by the counter-ions.

The DHE (equation 3.23) can also be solved analytically for other geometries than the charged wall, for instance for spherical symmetry. Consider a sphere with radius  $R$  (e.g. an ion, a protein, a micelle, a vesicle, a virus or a cell).

$$\Delta \Phi = \frac{1}{r} \frac{d^2}{dr^2} (r\Phi) = \kappa^2 \Phi$$

$$\Rightarrow \Phi = \frac{R\phi_R}{r} \cdot \exp(-\kappa(r-R)) \quad (3.26)$$

where  $\phi_R$  denotes the surface potential. It follows from Gauss law (equation 1.59) and charge neutrality:

$$E_R = \frac{Q_V}{4\pi\epsilon_0\epsilon R^2} = -\Phi'|_{r=R} = \frac{\phi_R(1+\kappa R)}{R}$$

$$\Rightarrow \phi_R = \frac{Q_V}{4\pi\epsilon_0\epsilon \cdot (1+\kappa R)R} \quad (3.27)$$

Two special cases of equation 3.26 are particularly interesting:

1. No salt added to the solution, hence  $\kappa \rightarrow 0 \Rightarrow \Phi = \frac{Q_V}{4\pi\epsilon_0\epsilon r}$ . This limit results in the well-known Coulomb law.
2. Point charge ( $R \rightarrow 0$ ): Then the potential takes the form

$$\Phi = \frac{Q_V \cdot \exp(-\kappa r)}{4\pi\epsilon_0\epsilon r} \quad \text{Yukawa potential} \quad (3.28)$$

Equation 3.28 is the Green's function (or propagator) for the linear Debye-Hückel theory. Like for the Coulomb interaction, one can calculate  $\Phi$  for any extended object (i.e. a line, a plane, etc.) by superposition of the propagator.

### 3.6 Strong coupling limit

To obtain a solution in the low-temperature limit for our example of the charged wall, a virial expansion via a complicated field theory has to be performed<sup>3</sup>. However, since this is not subject to this course, only the result for the ion distribution near a charged wall is given here:

$$n(z) = 2\pi l_B (n_{2d})^2 e^{(-z/\mu)} \quad \text{Strong coupling limit} \quad (3.29)$$

It has to be noted that although equation 3.29 exhibits an exponential decay, it is not comparable to the derivation of the DHE and its solution for the charged wall. The latter was derived by the linearization of the PBE, whereas the result shown here has been derived independently from PBT. Note that the relevant length scale of equation 3.29 is the Gouy-Chapman length  $\mu$ , and not the Debye-Hückel length  $l_{DH}$ .

### 3.7 Two charged walls

Now we want to investigate the case of two charged walls facing each other by making use of the theories introduced so far, i.e. the PB, the DH and the SC theories. The picture of two charged walls is actually the simplest model for the interaction between two particles. The interaction of charged particle surrounded by counter-ions is not only important in biology, but also e.g. in the earth sciences. In figure 3.6 the formation of river deltas is given as an instructive example.

#### 3.7.1 Poisson-Boltzmann solution

Consider two charged walls which both carry a charge density  $\sigma$  facing each other at a distance  $d$  (compare figure 3.7a). We start with the PBE:

$$\Phi'' = - \frac{e}{\epsilon_0\epsilon} \cdot \underbrace{n_0 \exp\left(-\frac{e\Phi}{k_B T}\right)}_n$$

---

<sup>3</sup>Andre G Moreira and Roland R Netz, *Strong coupling limit for counter-ion distributions*, Europhysics Letters 52, 705-711 (2000).

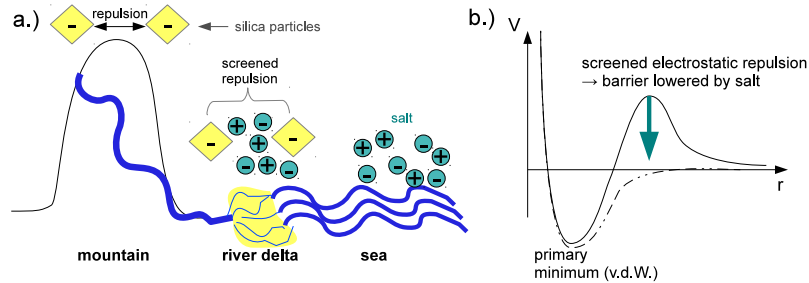


Figure 3.6: The formation of river deltas as a consequence of the interaction of two charged particles in salty solution. (a) A river flows from the mountains into the sea. On its way, negatively charged silica particles dissolve in the water which repel each other due to their charge. As the low-salt water of the river meets the sea water with high salinity, the repulsion between the particles is screened. They aggregate and, hence, form the river delta. (b) Effect of the salt ions on the potential energy. Screening lowers the energy barrier responsible for the repulsion. The corresponding description is known as DLVO-theory in colloidal sciences.

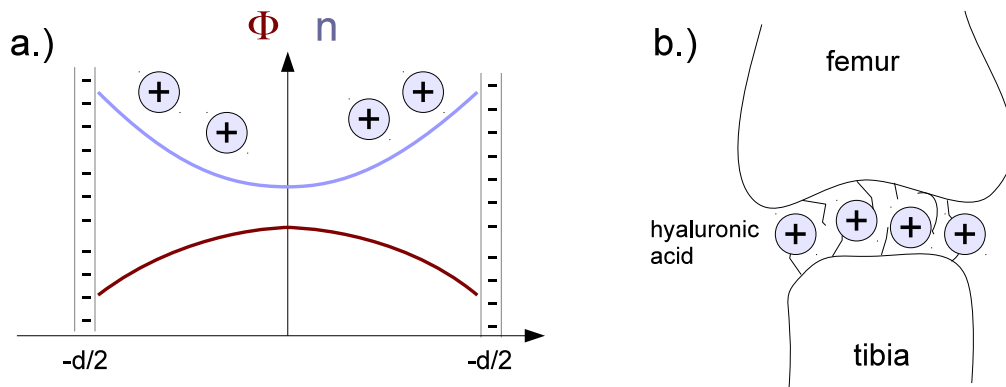


Figure 3.7: (a) PB solution for the potential  $\Phi \sim \ln(\cos^2(K \cdot z))$  (red) and the counterion density  $n \sim 1/\cos^2(K \cdot z)$  (blue) between two charged walls with charge densities  $\sigma_1 = \sigma_2 = \sigma$ . (b) The human knee is stabilized by cartilage containing hyaluronic acid (HA). Hyaluronic acid is a long, high molecular mass polymer of disaccharids, which is negatively charged and therefore responsible for the disjoining pressure caused by its counter-ions.



The two boundary conditions are:

$$\begin{aligned}
\text{symmetry :} \quad & \Phi'(0) = 0 \\
\text{charge neutrality:} \quad & \sigma = \int_0^{d/2} \rho dz = \epsilon_0 \epsilon \int_0^{d/2} \Phi'' dz = \epsilon_0 \epsilon \Phi' \left( \frac{d}{2} \right) \\
& \Rightarrow \Phi' \left( \frac{d}{2} \right) = \frac{\sigma}{\epsilon_0 \epsilon}
\end{aligned}$$

This results in the exact solution of the PBE:

$$\text{Potential} \quad \Phi(z) = \frac{k_B T}{e} \ln \left[ \cos^2 (K \cdot z) \right] \quad (3.30)$$

$$\text{Counter-ion density} \quad n(z) = \frac{n_0}{\cos^2 (K \cdot z)} \quad (3.31)$$

where  $n_0$  denotes the counter-ion density at the mid plane and  $k$  denotes a constant which follows from the boundary condition:

$$\Phi' \left( \frac{d}{2} \right) = \frac{\sigma}{\epsilon_0 \epsilon} = \frac{2k_B T \cdot K}{e} \tan \left( \frac{K \cdot d}{2} \right) \quad (3.32)$$

Equation 3.32 has to be solved numerically for  $K$ . A graphical representation of the analytic result of potential and charge density is shown in figure 3.7a.

Interestingly, the charges tend to accumulate at the sides, although the electrostatic forces between the two plates cancel each other (in practice also the Coulomb repulsion between the charges drives them to the walls, but in a mean field sense, this effect is not included). This leads to a strong "**disjoining pressure**" (counter-ion pressure) which is due to the counter-ions which repel each other. However, they do not condense onto the plate because of the entropy of this finite- $T$  system.

For two membranes with  $\sigma = e^2/nm^2$  facing each other at a distance  $d = 2nm$  and a mid-plane concentration  $n_0 = 0.7M$ , the counter-ion density at the plates is  $n(d/2) = 12M$ . This implies that the density is increased by a factor of 18.5 over a distance of only  $1nm$ . In this case, the potential difference is  $\Delta\Phi = -74mV$ . One can also compute the disjoining pressure and in the limit of small separation ( $d \ll l_B$ ), it obeys an ideal gas equation (without proof):

$$p = k_B T \cdot n_0 = 17 atm \quad (3.33)$$

where  $1 atm \cong 10^5 Pa$ . It can be seen directly that the disjoining pressure is very large and this has many applications in biological systems. For example, disjoining pressure can be found in joints and is actually the reason why we can go jogging (compare figure 3.7b).

### 3.7.2 Debye-Hückel solution

Let us now assume that there is additional salt in between the charged walls. Since the DH equation is a linear differential equation, the solution for this system is

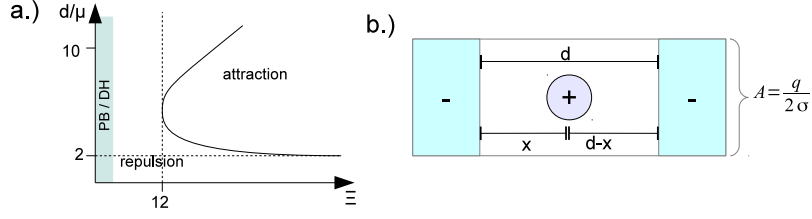


Figure 3.8: (a) Phase diagram showing regions of attraction and repulsion as a function of plate separation  $d/\mu$  and coupling strength  $\Xi$ . Original phase diagram by Moreira & Netz: "Binding of similarly charged plates with counter-ions only." *Phys Rev Lett*, 87(7): 078301, Aug 2001. (b) Small strip of two charged walls with an in-between counter-ion.

simply a superposition of the solution of two single charged walls (equation 3.25). One then gets

$$\Phi'' = \kappa^2 \Phi \Rightarrow \Phi = \Phi_0 \cosh(\kappa z) \quad (3.34)$$

Thus, the DH solution for  $\Phi$  (as well as for  $n$  and  $p$ , respectively) decays exponentially with the distance and, hence, the interaction is short-ranged.

### 3.7.3 Strong coupling limit

The counter-ion density between two charged walls in the strong coupling limit turns out to be relatively flat. In detail it is constant in zero order and parabolic in first order of the virial expansion. Thus superficially it appears to be similar to the PB result. In practise, however, the results are very different, because one finds that the two equally charged walls can in principle attract each other. Whether the interaction between the two planes is attractive or repulsive depends on the distance  $d$  and the coupling strength  $\Xi$ , as shown in the phase diagram in figure 3.8a. The very fact that attraction can occur offers a solution to our DNA riddle.

A simple explanation for this behavior can be given as follows: consider the condensed situation as sketched in figure 3.8b. Because the counter-ions condense with a relatively large lateral distance to each other, we neglect their interaction and only consider the interactions of one counter-ion with the wall in a small strip with area  $A = \frac{q}{2\sigma}$ . There are three contributions to the electrostatic energy now: the two interactions of the counter-ion with the two walls and the interaction of the walls with each other:

$$\begin{aligned} \frac{U_{el}}{k_B T} &= 2\pi(l_B/e^2)q\sigma x + 2\pi(l_B/e^2)q\sigma(d-x) - 2\pi(l_B/e^2)\sigma(\sigma \cdot A)d \\ &= \pi(l_B/e^2)\sigma qd = 2\pi(l_B/e^2)\sigma^2 Ad \end{aligned} \quad (3.35)$$

The energy is minimal for  $d \rightarrow 0$  which leads to attraction of the two charged

walls. For the electrostatic and the entropic pressure we get

$$\begin{aligned}
 \text{electrostatic pressure:} \quad p_{el} &= -\frac{\partial U_{el}}{\partial d} \frac{1}{A} = \frac{-2\pi l_B \sigma^2 k_B T}{e^2} \\
 \text{entropic pressure:} \quad p_{en} &= \frac{k_B T}{A \cdot d} = \frac{2\sigma k_B T}{qd} \\
 \Rightarrow \text{balanced at equilibrium distance} \quad &\boxed{d = \frac{e^2}{\pi l_B q \sigma}} \quad (3.36)
 \end{aligned}$$

The strong coupling limit is biologically relevant, because for  $n_{2d} = 1 \text{ nm}^{-2}$  it can be reached with trivalent counter-ions. In fact, the charged polymer DNA uses many multivalent counter-ions such as speridine and spermine which support DNA condensation in the nucleus. Again the existence of an equilibrium distance also has consequences in other sciences. E.g. it explains why clay particles can be swollen only to a certain distance.

### 3.8 Electrostatics of viruses

In the beginning of this chapter, we asked the question how DNA as a charged polymer can be kept spatially confined such that the distance between the charges is in the range of  $nm$  (which is the case in a nucleus or in a virus). We can answer this now with the help of the previous section: the DNA can be in a condensed state due the effect of counter-ions with high valency. In the nucleus, it is organized in highly complex structure with several levels of organization in order to form chromosomes (compare figure 3.9). Therefore a more accessible model system is DNA-organisation in viruses.

#### 3.8.1 The line charge density of DNA

We already know that DNA is highly charged. Until now we assumed that every base pair carries two negative charges, in other words we assumed that every segment of the DNA was fully dissociated and therefore the linear charge density was  $\lambda = 2e/(0.34 \text{ \AA})$ . We will now see why this assumption can indeed be made. In water, DNA dissociates  $\text{H}^+$  as a counter-ion into the surrounding solution:



The law of mass action gives us the dissociation constant for reaction formula 3.37.

$$K_D = \frac{[\text{H}^+] \cdot [\text{DNA}^-]}{[\text{DNA}]} \quad (3.38)$$

Due to the many orders of magnitude spanned by  $K_D$  values, a logarithmic measure of the dissociation constant is more commonly used in practice.<sup>4</sup>

$$pK := -\log_{10} K_D = \underbrace{-\log_{10} [\text{H}^+]}_{=pH} - \log_{10} [\text{DNA}^-] + \log_{10} [\text{DNA}] \quad (3.39)$$

---

<sup>4</sup>pure water:  $[\text{H}^+] = 10^{-7} \text{ M} \Rightarrow pH = 7$

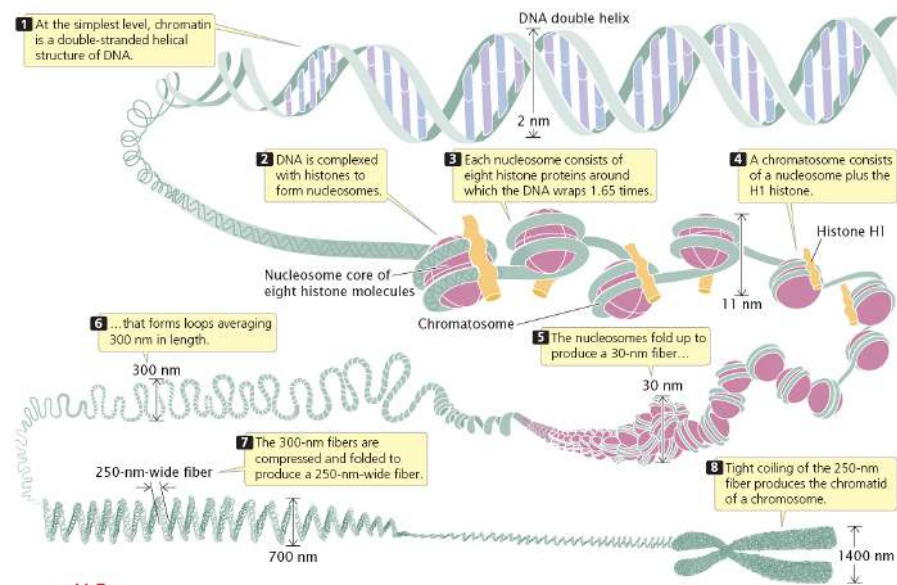


Figure 3.9: Chromatin has a highly complex structure with several levels of organization. Source: Pierce, Benjamin. Genetics: A Conceptual Approach, 2nd ed. (New York: W. H. Freeman and Company 2005).

$$\Rightarrow pK = pH - \log_{10} \frac{[\text{DNA}^-]}{[\text{DNA}]} \quad \text{Henderson-Hasselbalch equation} \quad (3.40)$$

The  $pK$  corresponds to the  $pH$  at which half of the groups have dissociated ( $[\text{DNA}^-] = [\text{DNA}]$ ).

For DNA, we find  $pK = 1$  which implies that DNA is a very strong acid. In cells,  $pH = 7.34$ . With the Henderson-Hasselbalch equation the fraction of dissociated DNA can immediately be calculated.

$$\frac{[\text{DNA}^-]}{[\text{DNA}]} = 10^{6.34}$$

Thus, DNA in the cell is completely dissociated and, therefore, carries a line charge density of

$$\lambda = \frac{2e}{3.4 \text{ \AA}} \quad \text{linear charge density of DNA} \quad (3.41)$$

### 3.8.2 DNA packing in $\phi 29$ bacteriophage

Now we want to focus on DNA packing in viruses. Actually, a virus is not a living object per definition, but rather genetic material, i.e. DNA or RNA, packed into a protein shell, the so-called capsid. Typically, the diameter of a capsid is in the range of 10s to 100s of  $nm$ . Some viruses, e.g. HIV, are in addition wrapped by a lipid bilayer (and are then called "enveloped virus").

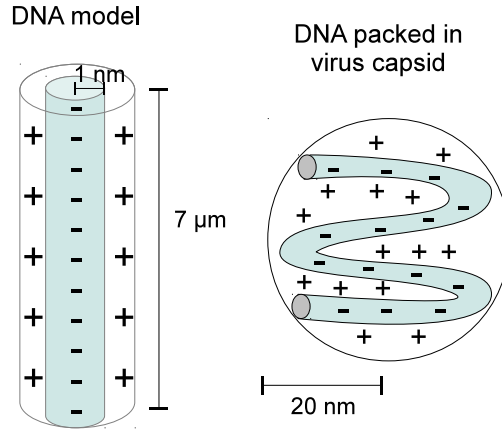


Figure 3.10: Simple model of viral DNA packed in the capsid of the  $\phi 29$  bacteriophage.

As we shall see in the following, the RNA and DNA, respectively, in viruses is very densely packed. Take for instance the  $\phi 29$  bacteriophage (a virus infecting *E. Coli*): Its capsid can be approximated as a sphere of radius  $R_{capsid} = 20 \text{ nm}$  containing  $20 \text{ kbp}$  (corresponding to  $L = 2 \cdot 10^4 \cdot 0.34 \text{ nm} = 7 \mu\text{m}$ ) DNA. We assume  $V_{bp} \approx 1 \text{ nm}^3$  (compare figure 3.10). The **packing ratio** in the capsid can be computed directly:

$$\frac{2 \cdot 10^4 \text{ nm}^3}{\frac{4\pi}{3} (20 \text{ nm})^3} \approx 0.6 \quad (3.42)$$

Comparing this value with the maximal packing density of spherical objects into a crystal ( $\approx 0.71$ ) it can be concluded that DNA packed into a viral capsid must be close to a crystalline structure. Indeed this can be shown by electron microscopy.

If we now pack DNA with the line charge density  $\lambda = 2e/(3.4 \text{ \AA})$  into the virus, how much electrostatic energy do we have to put into the system? Electrostatic energy is the work to bring a charge distribution into its own field and is known to be

$$U_{el} = \frac{1}{2} \int \Phi(\vec{r}) \cdot \rho(\vec{r}) \, dr \quad (3.43)$$

where the factor  $1/2$  is needed to avoid double-counting each interaction. We model the DNA in the virus as a fully charged sphere. At radius  $r$  *within* the sphere, the potential follows from Gauss law as

$$\Phi(r) = \underbrace{\frac{1}{4\pi\epsilon_0\epsilon} \cdot \frac{1}{r}}_{\text{point charge in origin}} \cdot \underbrace{\rho \cdot \frac{4\pi}{3} r^3}_{\text{charge in smaller sphere}} \quad (3.44)$$

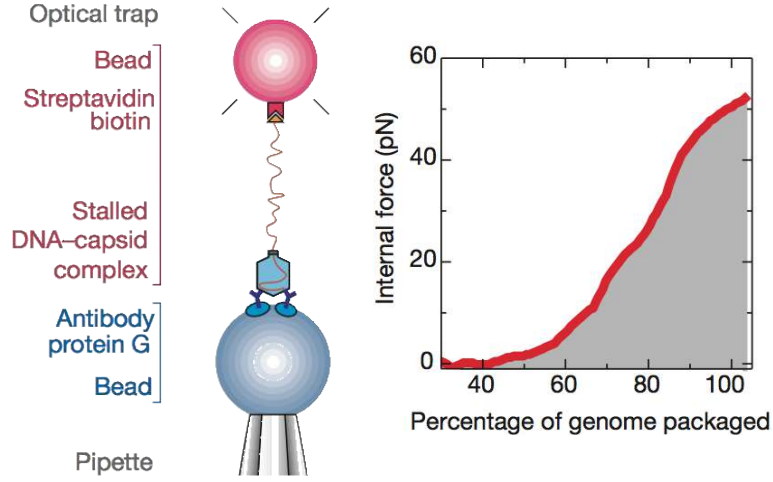


Figure 3.11: Left panel: Experimental set-up of the portal motor force experiment. A single  $\phi 29$  packaging complex is tethered between two microspheres. Optical tweezers are used to trap one microsphere and measure the forces acting on it, while the other microsphere is held by a micropipette. Right panel: Internal force as the function of % genome packed. Note that 100% of the genome corresponds to  $7 \mu\text{m}$  DNA and that the work is obtained by integration of the force (grey area). Images and caption text (partly) taken from reference in footnote 5.

For the total work, we have to add up shell after shell of the sphere:

$$\begin{aligned}
 \Rightarrow U_{el} &= \int_0^R dr \Phi(r) \cdot (\rho \cdot 4\pi r^2) \\
 &= \int_0^R dr \frac{4\pi}{3\epsilon_0\epsilon} \rho^2 r^4 = \frac{4\pi}{15\epsilon_0\epsilon} \rho^2 R^5 \\
 &= \frac{1}{4\pi\epsilon_0\epsilon} \cdot \frac{3Q^2}{5R}
 \end{aligned} \tag{3.45}$$

Here the factor  $1/2$  does not arise because every contact is counted only once as we gradually build up the sphere. For our example of the  $\phi 29$  bacteriophage, we have  $Q = 2e/bp \cdot 20\text{kbp}$  and hence

$$U_{el} = 10^8 \text{pN} \cdot \text{nm} \tag{3.46}$$

The work needed to pack the DNA into the viral capsid has been measured in a single molecule experiment<sup>5</sup> as sketched in figure 3.11. However, in this experiment the work was determined to be much smaller than the one estimated above:

$$W_{exp} \approx \frac{1}{2} 7000 \text{ nm } 60 \text{ pN} = 2.1 \cdot 10^5 \text{ pN} \cdot \text{nm} \tag{3.47}$$

Obviously the above estimate was much too high because we neglected the effect of the counter-ions.

<sup>5</sup>DE Smith et al. "The bacteriophage straight  $\phi 29$  portal motor can package DNA against a large internal force." Nature, 413(6857):748–52, Oct 2001.

There are  $N = 4 \cdot 10^4$  counter-ions packed with the genome (corresponding to 2 counter-ions/bp). We now assume complete neutralization of the charges and consider only the loss of entropy due to the DNA volume:

$$U_{ci} = Nk_B T \cdot \ln \frac{V_{free}}{V_{capsid}} \quad (3.48)$$

The volume  $V_{free}$  is that of the screening cloud (recall that  $L \approx 7 \mu m$ ,  $R_{DNA} \approx 1 nm$ ,  $R_{capsid} \approx 20 nm$  and  $l_{DH} \approx 1 nm$ ).

$$V_{free} = L\pi \left[ (R_{DNA} + l_{DH})^2 - R_{DNA}^2 \right] = 6.6 \cdot 10^4 nm^3 \quad (3.49)$$

$$V_{capsid} = \frac{4\pi}{3} R_{capsid}^3 - L\pi R_{DNA}^2 = 1.2 \cdot 10^4 nm^3 \quad (3.50)$$

$$\Rightarrow U_{ci} = 3 \cdot 10^5 pN \cdot nm \quad (3.51)$$

This result is much closer to the experimental value. A full analysis had to also include the effect of bending the DNA, which requires polymer physics.

Finally the pressure inside the capsid can be calculated:

$$\begin{aligned} p &= \frac{Nk_B T}{V} = \frac{4 \cdot 10^4 \cdot 4.1 pN \cdot nm}{\frac{4\pi}{3} (20 nm)^3} \\ &\approx 5 \frac{pN}{nm^2} = 50 atm \end{aligned} \quad (3.52)$$

This is a huge counter-ion pressure inside the capsid, as was also experimentally confirmed.

### 3.8.3 Electrostatics of viral capsid assembly

Before the DNA can be inserted into the viral capsid by a molecular motor, the capsid itself has to be assembled (for RNA viruses, genome and capsid are often co-assembled, because RNA is more flexible than DNA and therefore more easy to bend during assembly). Viral capsids assemble from so-called capsomers and often form an icosahedral lattice, because this is close to the shape of a sphere which gives the optimal volume to area ratio. For many viruses like Hepatitis B virus (HBV, compare figure 3.12a), assembly is sufficiently robust to also occur in the test tube from the capsomers alone. This proves that it is a spontaneously occurring process that is driven by some gain in Gibbs free energy. We consider two major contributions: a contact energy between the capsomers driving the process and an electrostatic energy opposing it (note that charges are required to stabilize the capsomers and the capsid in solution against aggregation, although this is unfavorable for assembly):

$$\Delta G = \Delta G_{contact} + \Delta G_{electro} \quad (3.53)$$

The equilibrium constant  $K$  then follows as (assuming a dilute solution)

$$\ln K = -\frac{\Delta G}{k_B T} \quad (3.54)$$

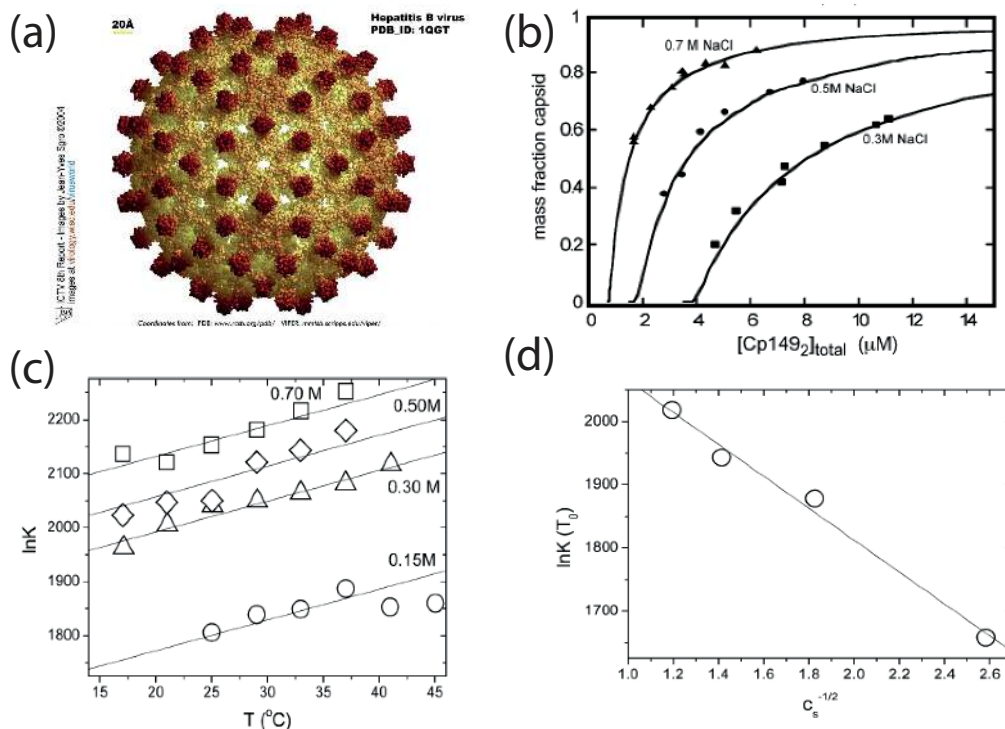


Figure 3.12: (a) Molecular rendering of the structure of the capsid of hepatitis B virus (HBV). (b) Assembly isotherms at different salt concentrations. (c) Fit of equilibrium constant as a function of temperature and salt concentration. (d) Scaling of equilibrium constant with salt concentration. Experimental data from Slotnick group, theory by van der Schoot group.

For HBV,  $K$  has been measured as a function of temperature  $T$  and salt concentration  $c_s$ <sup>6</sup>, compare figure 3.12b-d. Because this virus assembly from 120 capsomers in an all-or-nothing manner, we do not have to consider intermediates and can write a law of mass action:

$$K = \frac{[\textit{capsid}]}{[\textit{capsomer}]^{120}} \quad (3.55)$$

The fraction of complete capsids can be measured by size exclusion chromatography and then be fitted to the corresponding isotherm (with a Hill coefficient of 120). This procedure works very well and gives curves for  $K(T, c_s)$ .

The experimental data gives two main results. First the slope of  $K(T, c_s)$  as a function of  $T$  does not depend on  $c_s$ , suggesting that assembly is driven mainly by contact interactions. The strong temperature dependence points to entropic effects and suggests a hydrophobic interaction, similar to the one driving micelle formation, protein folding or lipid membrane assembly. Second  $K$  increases with  $c_s$ , suggesting that increased salt screens the electrostatic repulsion and thus promotes assembly.

<sup>6</sup>P. Ceres and A. Zlotnick, *Biochemistry* 41: 11525, 2002.



In a theoretical analysis, it has been shown that these experimental results can be fitted nicely using Debye-Hückel theory <sup>7</sup>. We start from the surface potential of a sphere of radius  $R$  in Debye-Hückel theory (equation 3.27):

$$\phi_R = \frac{Q_V}{4\pi\epsilon_0\epsilon \cdot (1 + \kappa R)R} = \frac{Q_V}{4\pi\epsilon_0\epsilon R(R + l_{DH})} \cdot \quad (3.56)$$

The electrostatic energy of the charged spherical shell is now

$$U = \frac{1}{2}Q\phi_R = \frac{1}{2}k_B T \left(\frac{Q}{e}\right)^2 \frac{l_{DH}l_B}{R(R + l_{DH})} \cdot \quad (3.57)$$

With  $l_{DH} = 1nm$  and  $R = 14nm$  we can write  $(R + l_{DH}) \approx R$ . Therefore our final result for the salt-dependent part of the equilibrium constant reads

$$\ln K = -\frac{\Delta G_{electro}}{k_B T} = -\frac{1}{2}k_B T \left(\frac{Q}{e}\right)^2 \frac{l_{DH}l_B}{R^2} \quad (3.58)$$

Thus  $\ln K$  should scale linearly with the screening length  $l_{DH}$  and therefore with  $c_s^{-1/2}$ , exactly as it is observed experimentally, compare figure 3.12d.

---

<sup>7</sup>W.K. Kegel and P. van der Schoot, Biophysical Journal 86: 3905, 2004



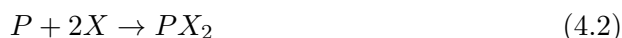
## Chapter 4

# Binding and assembly

Due to Brownian motion, the biomolecules in the cell are in constant motion and continuously bump into each other. Once this happens, their biomolecular interactions decide whether they bind to each other or not. The main functions of binding are information transfer, transport and assembly. We now ask how one can describe the statistics arising from many binding events. We will see that the appropriate formalism is essentially the grandcanonical ensemble and that this will allow us to calculate binding curves as function of monomer concentration, using the concept of the binding polynomial. The most important example for such a binding processes is the cooperative binding of oxygen to hemoglobin, which we will discuss in detail. We finally turn to the assembly of larger supramolecular complexes, like micelles, viruses or cytoskeletal filaments. We will discuss how the Boltzmann statistics naturally leads to threshold phenomena and a narrow size distribution for micelles and viruses.

### 4.1 Binding polynomial

Consider a protein  $P$  that has  $t$  binding sites for a ligand  $X$  with concentration  $[X] = x$ . For each complex we write a reaction equation:



Note that these equations do not describe the actual dynamics, but only the binding equilibria that have to exist in a statistical sense. For each equation we have a law of mass action:

$$\frac{[PX_i]}{[P]x^i} = K_i \quad (4.5)$$

which reaction constants  $K_i$ .

We now ask which fraction is in state  $i$ :

$$\frac{[PX_i]}{[P] + [PX_1] + \dots + [PX_t]} = \frac{K_i x^i}{Q(x)} \quad (4.6)$$

where a factor of  $[P]$  has canceled and we have defined the *binding polynomial*

$$Q(x) = 1 + K_1x + \dots + K_t x^t = \sum_{i=0}^t K_i x^i \quad (4.7)$$

with  $K_0 := 1$ . We next calculate the number of bound ligands:

$$\langle i \rangle = \frac{\sum_i i K_i x^i}{Q} = \frac{x}{Q} \frac{dQ}{dx} = \frac{d \ln Q}{d \ln x} . \quad (4.8)$$

So we see that the binding polynomial generates this result simply by a derivative, using a trick which is well known from statistical mechanics:  $x d_x$  generates the number  $i$  when applied to  $x^i$ . The function of  $Q(x)$  is exactly the one of the grandcanonical partition sum  $Z_G$  in statistical physics or of a generating function  $G$  in probability theory.

For the second moment we have

$$\langle i^2 \rangle = \frac{\sum_i i^2 K_i x^i}{Q} = \frac{x}{Q} \frac{d}{dx} \left( x \frac{dQ}{dx} \right) . \quad (4.9)$$

The mean squared deviation (MSD) then follows from

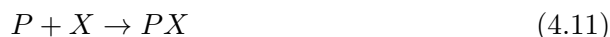
$$\langle (\Delta i)^2 \rangle = \langle (i - \langle i \rangle)^2 \rangle = \langle i^2 \rangle - \langle i \rangle^2 \quad (4.10)$$

and is a measure for the size of the fluctuations.

In the following we will discuss this formalism for three different cases:  $t = 1, 2$  and 4, with the last one being the case of hemoglobin.

## One binding site

We now have only one reaction



and one reaction equilibrium

$$\frac{[PX]}{[P]x} = K \quad (4.12)$$

We then find

$$Q(x) = 1 + Kx \quad (4.13)$$

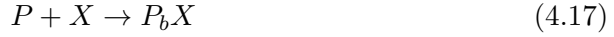
$$\langle i \rangle = \frac{Kx}{1 + Kx} \quad (4.14)$$

$$\langle i^2 \rangle = \frac{Kx}{1 + Kx} = \langle i \rangle \quad (4.15)$$

thus the first two moments are identical. The result for the first moment is known as the *Langmuir isotherm* because it also arises from the grandcanonical ensemble of a two-state system. It has a hyperbolic shape on a linear scale and a sigmoidal shape on a logarithmic scale. The MSD has a maximum at intermediate values of  $x$ , similar to the specific heat of a two-state system (*Schottky hump*).

## Two binding sites

We start with the site-based approach and distinguish between binding sites *a* and *b*. We now have three equilibrium reaction



and three corresponding laws of mass action. We consider the average number of bound ligands:

$$\langle i \rangle = \frac{[P_aX] + [P_bX] + 2[PX_2]}{[P] + [P_aX] + [P_bX] + [PX_2]} = \frac{d \ln Q}{d \ln x} \quad (4.19)$$

with

$$Q(x) = 1 + K_a x + K_b x + K_c x^2 . \quad (4.20)$$

For two independent binding sites (no cooperativity) we have  $K_c = K_a K_b$  and thus

$$Q(x) = 1 + K_a x + K_b x + K_a K_b x^2 = (1 + K_a x)(1 + K_b x) . \quad (4.21)$$

For the binding curve we get the sum of two Langmuir isotherms:

$$\langle i \rangle = \frac{K_a x}{1 + K_a x} + \frac{K_b x}{1 + K_b x} . \quad (4.22)$$

Positive cooperativity would imply  $c = K_c/(K_a K_b) > 1$  and the binding polynomial would not factorize.

In the stoichiometric approach, we do not distinguish between sites *a* and *b* and only consider two reaction:



with reaction constants  $K_1$  and  $K_2$ . The binding polynomial  $Q$  now reads

$$Q(x) = 1 + K_1 x + K_2 x^2 . \quad (4.25)$$

Comparing with the site-based approach gives  $K_1 = K_a + K_b$  and  $K_1 K_2 = K_c$ .

## Four binding sites

This is the case of hemoglobin, which can bind four oxygen atoms with high cooperativity. Without cooperativity, we would have

$$Q(x) = (1 + Kx)^4 = 1 + 4Kx + 6(Kx)^2 + 4(Kx)^3 + (Kx)^4 \quad (4.26)$$

where the binomial coefficients reflect the different ways to distribute the zero to four ligands over the four binding sites. For the first moment we would simply have

$$\langle i \rangle = \frac{4Kx}{1 + Kx}. \quad (4.27)$$

that is a Langmuir isotherm with four ligands in saturation. Experimentally, however, it was realized early on that the binding curve is much steeper, more closely to a Hill binding curve

$$\langle i \rangle = \frac{4Kx^n}{1 + Kx^n} \quad (4.28)$$

with an effective Hill coefficient of  $n \approx 3$ . In the literature, different suggestions have been made to explain such binding curves. While Adair 1925 simply used four different reaction constants, Pauling 1935 came up with a model that has only one more parameter, namely the energy gain for a pairwise interaction between two neighboring ligands on a tetrahedron. Although this model fits the experiments nicely, it does not reflect the additional experimental fact that hemoglobin is allosteric, which means that it can exist in two states called T (tense) and R (relaxed). In 1965, Monod, Wyman and Changeux introduced a model based on this observation. Today the MWC-model is the standard model for cooperativity in binding curves.

We assume that the T-state is more stable than the R-state in the absence of oxygen,  $[T]/[R] = L > 1$ . On the other hand, however, oxygen X binds better to R than to T:



with  $K_R > K_T$ . Thus once X is present, the whole system shifts towards R, which in turn binds even more X, thus having positive cooperativity. The binding polynomial for this model is

$$Q(x) = \frac{(1 + K_Rx)^4 + L(1 + K_Tx)^4}{1 + L} \quad (4.31)$$

leading to

$$\langle i \rangle = \frac{d \ln Q}{d \ln x} = \frac{4K_Rx(1 + K_Rx)^3 + 4LK_Tx(1 + K_Tx)^3}{Q(1 + L)} \quad (4.32)$$

which indeed is similar to a Hill curve with  $n \approx 3$ .

## 4.2 Micelle assembly

As a first example of the assembly of a supramolecular aggregate, we now discuss the formation of micelles, which are spherical assemblies of surfactants (*surface active molecules*), e.g. tensides or lipids, which shield their hydrophobic tails

from the contact with water by forming a droplet. Typically a micelle contains 60 surfactant molecules with cone shapes, that means with bulky head groups of molecular surface area above  $60 \text{ \AA}^2$ . Below this value cylindrical micelles will form, and planar bilayers below  $40 \text{ \AA}^2$ . Here however we only discuss the spherical case.

In principle, the surfactants could assemble into aggregates  $A_n$  of arbitrary size  $n = 1, 2, 3, \dots$ . For each size we have an reaction equilibrium as above. The monomer concentration is  $x = [A_1]$  and the fraction of molecules in aggregates is

$$\nu(x) = \frac{x + 2K_2x^2 + 3K_3x^3 + \dots}{x + K_2x^2 + K_3x^3 + \dots} = \frac{1 + 2K_2x + 3K_3x^2 + \dots}{1 + K_2x + K_3x^2 + \dots} \quad (4.33)$$

and as before  $K_n = e^{-\beta\Delta\mu_n^0}$ . A famous model by Tanford and Israelachvili suggests that the chemical potential should single out an optimal micelle size through surface effects. The larger the micelle, the larger the surface energy described by the surface tension  $\gamma$  between the oily and aqueous parts. A too small surface area however is also unfavorable because then the polar headgroups would start to repel each other too much. They suggested the following equation

$$\Delta\mu^0(a) = \gamma a + \frac{c}{a} \quad (4.34)$$

which leads to an optimal micelle surface area  $a = a^* = (c/\gamma)^{1/2}$ . Then we can rewrite the chemical potential as

$$\Delta\mu^0(a) = \frac{\gamma}{a}(a - a^*)^2 + 2\gamma a^* \approx \frac{\gamma}{a^*}(a - a^*)^2 + 2\gamma a^* \quad (4.35)$$

where the approximation would be a Taylor expansion around  $a = a^*$ . If we now insert this result into the Boltzmann factor, we can conclude that the micelle size will have a Gaussian distribution around  $a = a^*$ . This suggests that micelle formation is essentially a two-state process, with monomers coexisting with fully assembled micelles of size  $a = a^*$ . Indeed this is observed experimentally: at the critical micelle concentration (CMC), fully developed micelles start to develop and monomer concentration plateaus. The CMC can be deduced from a two-state equilibrium between  $A_1$  and  $A_n$  with  $K = [A_n]/x^n$ . Then

$$\nu(x) = \frac{x + nKx^n}{x + Kx^n} = \frac{1 + nKx^{n-1}}{1 + Kx^{n-1}} \quad (4.36)$$

and the CMC is  $x_c = K^{-1/(n-1)}$ .

### 4.3 Virus capsid assembly

Viruses come in many different sizes and shapes, but a typical virus is spherical and has a diameter of 20-100 nm. As a rule of thumb, animal RNA-viruses like Influenza A, Ebola, HIV 1 or SARS-CoV-2 tend to be enveloped by a membrane and therefore assemble at some membrane of the host cell. They also tend to have structural proteins that form a capsid, but this capsid often assembles at

the membrane. Here SARS-CoV-2 is a bit special because its structural proteins do not form a completely connected capsid, in contrast to Influenza A, Ebola or HIV-1. RNA-viruses also tend to assemble their capsid together with the genome, because RNA is relatively easy to bend (see the chapter on biopolymers). In contrast, DNA is relatively hard to bend and therefore DNA-viruses tend to first assemble a capsid and then to fill it with the genome (e.g. bacteriophages, Papilloma, Herpes or smallpox), often with the help of a portal motor. Non-enveloped viruses tend to have a very stable protein capsid that often can assemble in the testtube without any other proteins than the ones needed for the coat. Note however that these are only rules of thumb and that the real situation is much more complex, with many exceptions to these rules. For example, hepatitis B is a DNA-virus and has a very regular capsid that can be assembled in the testtube, but in addition it is enveloped. Many plant viruses such as cowpea mosaic virus (CPMV) or cowpea chlorotic mottle virus capsid (CCMV) form beautiful capsids and are not enveloped, but they are RNA-viruses. Disregarding this diversity, in the following we discuss the assembly of protein capsids from few proteins as a paradigm for the assembly of supramolecular complexes with clearcut structure. Virus capsid assembly is similar to micelle assembly, in the sense that it also turns out to be essentially a two-state system between monomers and the assembled capsid (see below), but the target structure is even more defined because it is a solid protein lattice and not a fluid droplet. It has been noted by Francis Crick and Jim Watson (who also discovered the structure of DNA) that most viruses are spherical or cylindrical because they are made essentially from one protein, so each point on the surface must be equivalent. In addition, however, they must form a lattice. Closed shells with a lattice in which each point is equivalent are the five Platonic solids. Donald Kaspar and Aaron Klug therefore concluded that spherical viruses must have icosahedral symmetry, because the icosahedron is the Platonic solid that comes closest to the sphere (largest number of subunits, namely 20 triangles). As a simple model for a virus capsid, we now discuss a dodecahedron (12 pentagons)<sup>1</sup>. As the dual to the icosahedron, it has the same symmetry properties, but it is easier to treat because it has fewer subunits. Examples for real world viruses which have similar structures would be Polio, Hepatitis B or CCMV. If the capsomeres (monomers for the capsid) are pentagons, this implies that they already have preassembled (typically from five identical viral proteins) before the real capsid assembly starts.

We first argue that there is a linear pathway to assembly, from the monomer  $A_1$  through the intermediates  $A_n$  to the final capsid  $A_{12}$ . The reason is that each addition of an additional monomer takes the route of maximal energy gain, which corresponds to the maximal number of new edges in the lattice. For example,  $A_3$  should be a rosette rather than a chain of three pentagons, because then the gain is  $f_3 = 2$  and not only  $f_3 = 1$  new edges. In the table, we list the number of new edges which one gets over the whole sequence. Note that energy goes always downhill and that the last addition (filling in one missing pentagon in the dodecahedron) leads to the largest gain in energy. Each edge comes with an

---

<sup>1</sup>This model has been published as Adam Zlotnick, To build a virus capsid - an equilibrium model for the self-assembly of polyhedral protein complexes, J. Mol. Biol. 241: 59-67, 1994.



$n$	2	3	4	5	6	7	8	9	10	11	12
$f_n$	1	2	2	2	3	2	3	3	3	4	5
$S_n$	5/2	2/3	3/2	4/2	1/5	5/1	2/4	2/3	3/2	2/5	1/12

Table 4.1: Two important numbers characterizing the step  $A_{n-1} \rightarrow A_n$  in the assembly of a dodecahedral virus capsid: the number  $f_n$  of newly established edges characterizing the energy gain, and the entropic degeneracy  $S_n$ , which is the ratio of number of ways to build up  $A_n$  to the number of ways to dissociate  $A_n$ .

energy gain around  $\Delta\epsilon \approx -5k_B T$  and typically results from hydrophobic patches at the sides of the capsomers (compare the chapter on electrostatics).

Taking the stoichiometric approach, we can write the reaction equilibrium for each step as ( $x = [A_1]$  as before)

$$\frac{[A_n]}{[A_{n-1}]x} = K_n = S_{in} S_n e^{-\beta f_n \Delta\epsilon} \quad (4.37)$$

which includes two statistical factor.  $S_{in} = 5$  is the number of ways an incoming pentagon can dock.  $S_n$  is the ratio of the number of ways to form the new intermediate to the number of ways to dissociate it. For example, we can add a third pentagon to  $A_2$  in two ways, and there are three ways to remove one of the pentagons from  $A_3$ . Thus we would have

$$K_3 = 5 \frac{2}{3} e^{-\beta 2 \Delta\epsilon} . \quad (4.38)$$

Note that because  $\Delta\epsilon$  is negative, this gives a relatively large Boltzmann weight. As before, we now can obtain an equation of the concentration of all aggregates by iteration:

$$[A_n] = S_{in}^{n-1} \left( \prod_{i=2}^n S_i \right) e^{-\beta \Delta\epsilon \sum_{i=2}^n f_i} x^n \quad (4.39)$$

If one plots this distribution, one sees that all values are very low, except the ones for  $A_1$  (monomers are always present due to entropy) and  $A_{12}$  (the full capsid is the end point and has the highest energy gain). Like for micelles, we can look at this as a two-state system. We write the concentration of the capsid using all the numbers given above

$$[A_{12}] = 5^{11} \frac{1}{12} e^{-30\beta \Delta\epsilon} x^{12} . \quad (4.40)$$

Note that the number of edges should be  $12 * 5/2 = 60$ , as seen here, but also follows from the factor  $f_n$  given in the table. The statistical factors present the entropy of building the capsid. In particular, the factor  $1/12$  is the product of all  $S_n$  given in the table. We now define an effective reaction constant and an effective free energy difference by

$$K_{eff} = \frac{[A_{12}]}{x^{12}} , \Delta G_{eff} = -k_B T \ln K_{eff} , \quad (4.41)$$

leading to

$$\Delta G_{eff} = 30\Delta\epsilon - k_B T \ln\left(\frac{1}{5}^{12} 12\right). \quad (4.42)$$

Obviously the first term is the overall energy gain, and the second defines the entropy of building a capsid.

## 4.4 Growth of cytoskeletal filaments

As the last example of assembly of a supramolecular complex, we consider the growth of a cytoskeletal filament, e.g. actin filaments or microtubules. We denote the aggregates by  $P_n$  (because they are polymers) and we only consider growth by monomer addition (alternatively, all sizes could interact with each other, leading to the coagulation-fragmentation equation going back to Smoluchowski and Kolmogorov; the monomer addition scheme treated here is a special case known as the Becker-Döring equations). Again choosing the stoichiometric approach, we have

$$\frac{[P_n]x}{[P_{n-1}]} = K_d \quad (4.43)$$

where now we do not use the reaction constant  $K$ , but its inverse  $K_d = 1/K$ , the dissociation constant. Note that  $K_d$  has the dimension of concentration and in fact it is the concentration at half-occupancy (when  $[P_n] = [P_{n-1}]$ ). The smaller  $K_d$ , the stronger the reaction (the larger the reaction constant  $K$ ) and the fewer monomers are required to reach half-occupancy. We also assume that the reaction constant does not depend on the aggregate size  $n$ , because to first approximation, only the local interface should matter. In marked contrast to micelle and virus assembly, now the aggregate can grow to infinite size, which means that  $n$  can run to infinity.

Like before, by iteration we can write the concentration of the intermediates:

$$[P_n] = k_d \left(\frac{x}{K_d}\right)^n = K_d e^{-\alpha n} \quad (4.44)$$

where we have defined  $\alpha = -\ln(x/K_d)$ , which is possible for  $x < K_d$ . Thus for a fixed concentration  $x$  below the dissociation constant  $K_d$ , there will be an exponential distribution of polymer sizes. However, if concentration approaches  $K_d$  from below, polymer size will diverge. Thus  $x_c = K_d$  is the analogue to the critical micelle concentration where assembly suddenly kicks in, similar to a phase transition, but for a finite-sized system.

For actin, an order of magnitude estimate is  $K_d = k_{off}/k_{on} = (1/s)/(10/\mu Ms) = 0.1\mu M$ . However, the typical actin monomer concentration in cells is  $x = 30\mu M$ . This means that actin in cellular conditions always wants to grow. To regulate this process, cells use capping proteins that locally suppress growth. Addition of one actin monomers corresponds to a increase in length of  $a = 2.75$  nm. The growth velocity follows as  $v = k_{on}ax = \mu m/s$ , which indeed is a typical value observed experimentally.

Growth velocity is reduced by dissociation, leading to

$$\frac{dL}{dt} = ak_{on}x - ak_{off} \quad (4.45)$$

again resulting in the critical concentration  $x_c = k_{off}/k_{on} = K_d$ . Growth would be further reduced if monomer starvation existed, that is if overall actin concentration would be fixed and monomers were used up during growth. Here we assume that we have a unlimited reservoir for monomers which fixes concentration  $x$ .

We now ask the question how biological filaments manage to treadmill, that is one end shrinks while the other end grows such that overall length is constant. In our simple model,  $dL/dt = 0$  is only possible at  $x_c$ , but then both ends are stalled. To break this symmetry, both ends have to have different rates, that is  $k_{off}^+$  and  $k_{on}^+$  at the plus end and  $k_{off}^-$  and  $k_{on}^-$  at the minus end (for actin, these two ends are called the *barbed* and *pointed* ends, respectively). However, the ratio of these rates at each side should be the same, because they have the same binding interface and therefore the same free energy difference  $\Delta G$ , leading to the same reaction constant. This in turn implies that both ends either shrink or grow, thus they have no possibility to have different behaviour at the same monomer concentration  $x$ .

Here nature has invented an ingenious solution, namely a different chemical nature for the two ends using ATP-hydrolysis. The barbed end mainly binds ATP-actin, forming an ATP-cap at the barbed end, which is also the fast growing end. With time ATP is converted into ADP and the pointed end mainly binds ADP-actin. In this way, the two interfaces have different binding energies and therefore two different critical concentrations emerge:  $K_d^+ = 0.5\mu M$  and  $K_d^- = 8\mu M$ . For one unique value in this window, one now can get treading, namely when the growth velocities at the two ends are exactly equal and opposite.

For microtubules, the situation is slightly different, here treading is not required and one end typically is fixed to some nucleation center, e.g. the centrosome. In order to still keep average length constant while allowing for growth, nature has invented another trick, namely occasional catastrophes, when suddenly the whole polymer collapses back to a small size.



## Chapter 5

# Physics of membranes and red blood cells

In a cell, lipid bilayers partition space into functional compartments. This central aspect of lipid bilayers must have been crucial for the development of life. Lipid bilayers are the carriers of many vital processes, including ion separation and transport as well as protein activity. In general, cell membranes regulate the transfer of material and information in and out of cells.

Due to its low bending energy and the thermal environment, the lipid bilayer is in continuous motion. In order to describe the energetics and statistics of membranes, we have to introduce a mathematical description of surfaces and then to identify the corresponding energy (Helfrich bending Hamiltonian). Therefore, we start with a crash course in differential geometry<sup>1</sup>. We then discuss the Helfrich bending Hamiltonian in much detail and its consequences for shapes of minimal energy and thermal fluctuations around these shapes. As a reference point, we always discuss surfaces under tension (e.g. soap bubbles or oil droplets). Finally we discuss the physics of red blood cells, whose shapes and fluctuations can be described well by surface Hamiltonians. However, in contrast to pure membranes, the presence of the actin-spectrin network makes it necessary to add additional terms to the interface Hamiltonian.

---

<sup>1</sup>There are many books on differential geometry, for example the one by Michael Spivak (Comprehensive introduction to differential geometry, vols 1-5, 1979). Here are two books in German that are especially helpful for membrane physics: MP do Carmo, Differentialgeometrie von Kurven und Flächen, 3rd edition Vieweg 1993; JH Eschenburg and J Jost, Differentialgeometrie und Minimalflächen, 2nd edition Springer 2007. The classical review on vesicle shapes is Udo Seifert, Configurations of fluid membranes and vesicles, *Advances in Physics* 46: 13-137, 1997. A great resource is also the script by JL van Hemmen, *Theoretische Membranphysik: vom Formenreichtum der Vesikel*, TU Munich 2001, available at <http://www.t35.physik.tu-muenchen.de/addons/publications/Hemmen-2001.pdf> from the internet.

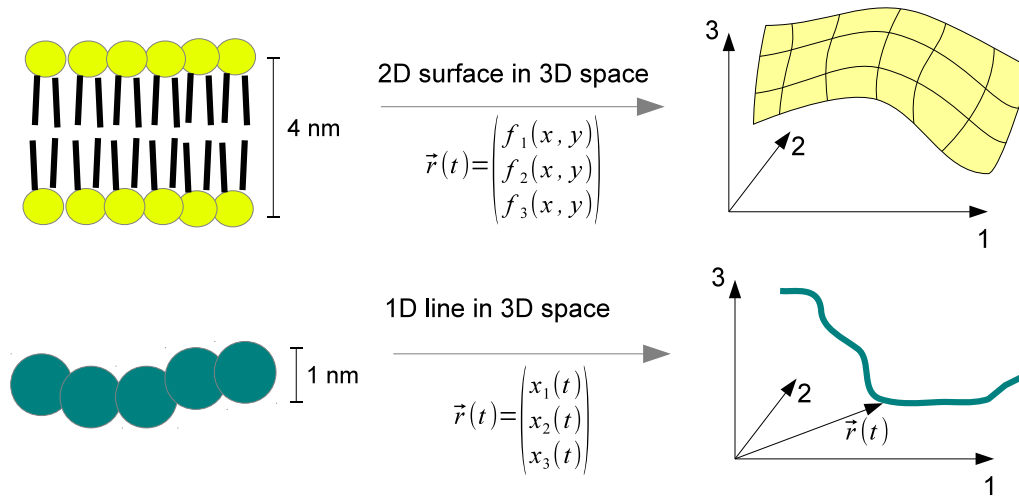


Figure 5.1: Membranes and polymers can be mathematically described as two-dimensional surfaces and one-dimensional curves, respectively, in a three-dimensional space.

## 5.1 A primer of differential geometry

### 5.1.1 Curves in 3D

#### Parametrization and arc length of curves

Consider a curve in 3 dimensions, e.g. a helical curve with radius  $R$  and pitch  $z_0 = b \cdot \frac{2\pi}{\omega}$  (figure 5.2a), parametrized by an internal coordinate  $t$ :

$$\vec{r}(t) = \begin{pmatrix} x_1(t) \\ x_2(t) \\ x_3(t) \end{pmatrix} = \begin{pmatrix} R \cdot \cos(\omega t) \\ R \cdot \sin(\omega t) \\ b \cdot t \end{pmatrix} \quad (5.1)$$

In the limit  $b \rightarrow 0$ , the helix becomes a circle, and in the limit  $b \rightarrow \infty$ , it becomes a straight line. For the velocity of the helix we get:

$$\begin{aligned} \vec{v} = \frac{d\vec{r}}{dt} = \dot{\vec{r}} &= \begin{pmatrix} -R\omega \cdot \sin(\omega t) \\ R\omega \cdot \cos(\omega t) \\ b \end{pmatrix} \\ \Rightarrow v &= \sqrt{R^2\omega^2 + b^2} > R\omega \end{aligned}$$

An important quantity when describing a curve is its arc length  $L$  which is independent of the parametrization that was chosen.

$$\begin{aligned} L &= \int_{t_0}^{t_1} dt \left| \dot{\vec{r}} \right| \stackrel{t=t(u)}{=} \int_{t_0}^{t_1} dt \left| \frac{d\vec{r}}{du} \right| \cdot \left| \frac{du}{dt} \right| \\ &= \int_{u_0}^{u_1} du \left| \frac{d\vec{r}}{du} \right| \end{aligned} \quad (5.2)$$

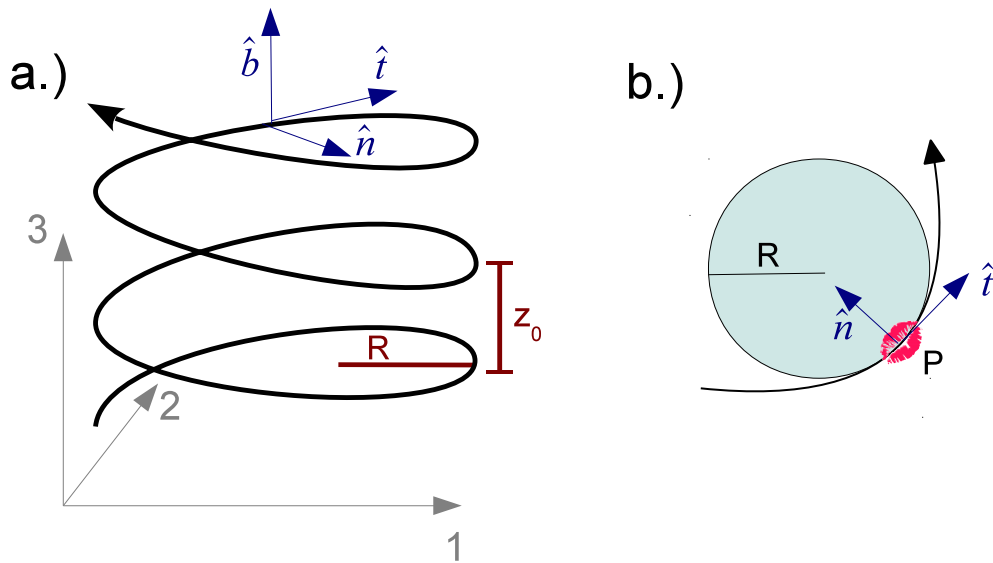


Figure 5.2: a.) Helical curve with radius  $R$  and pitch  $z_0 = b \cdot 2\pi/\omega$ . The tangential vector  $\vec{t}$ , the normal vector  $\vec{n}$  and the binormal vector  $\vec{b}$  are sketched in blue. b.) "Kissing circle" at a point  $P(s)$  with radius  $R(s) = \kappa^{-1}(s)$ .

The **arc length** along a curve

$$s(t) = \int_{t_0}^t dt' |\dot{\vec{r}}(t')| \quad (5.3)$$

can be used to parametrize the curve since it increases strictly with  $t$  ( $\dot{s} = |\dot{\vec{r}}| > 0$ ) and can therefore be inverted to  $t = t(s)$ .

$$\Rightarrow r = r(s) = r(t(s)) \quad \begin{array}{l} \text{parametrization by} \\ \text{arc length (PARC)} \end{array} \quad (5.4)$$

For example, for the helical curve we find

$$v = \sqrt{R^2\omega^2 + b^2} = \frac{ds}{dt} = \text{const}$$

$$\Rightarrow s = v \cdot t \Rightarrow t = \frac{s}{v} \Rightarrow \vec{r} = \begin{pmatrix} R \cdot \cos\left(\frac{\omega s}{v}\right) \\ R \cdot \sin\left(\frac{\omega s}{v}\right) \\ \frac{bs}{v} \end{pmatrix}$$

## The co-moving frame

The co-moving frame (also called "Frenet frame") of a curve consists of three mutually perpendicular unit vectors:

$$\text{tangential vector} \quad \vec{t}(s) := \frac{\dot{\vec{r}}}{|\dot{\vec{r}}|} \stackrel{\text{PARC}}{=} \frac{\frac{d\vec{r}}{ds} \cdot \left| \frac{ds}{dt} \right|}{\left| \frac{ds}{dt} \right|} = \frac{d\vec{r}}{ds} \quad (5.5)$$

$$\text{normal vector} \quad \vec{n}(s) := \frac{d\vec{t}}{ds} \cdot \left| \frac{d\vec{t}}{ds} \right|^{-1} = \frac{1}{\kappa} \frac{d\vec{t}}{ds} \quad (5.6)$$

$$\text{binormal vector} \quad \vec{b}(s) := \vec{t}(s) \times \vec{n}(s) \quad (5.7)$$

The normalization in equation 5.5 is not required for PARC. Therefore, PARC is also called the "natural parametrization". In equation 5.6 we defined the **curvature**  $\kappa$  of the curve at a given point

$$\kappa := \left| \frac{d\vec{t}}{ds} \right| \quad (5.8)$$

which defines the radius of curvature  $R(s) = \kappa^{-1}$ . This is the radius of the so-called "kissing circle" at that specific point (figure 5.2b).

E.g. for the helical path we get:

$$\begin{aligned} \vec{t} = \frac{d\vec{r}(s)}{ds} &= \begin{pmatrix} -\frac{R\omega}{v} \cdot \sin\left(\frac{\omega s}{v}\right) \\ \frac{R\omega}{v} \cdot \cos\left(\frac{\omega s}{v}\right) \\ \frac{b}{v} \end{pmatrix} \Rightarrow |\vec{t}| = \frac{R^2\omega^2}{v^2} + \frac{b^2}{v^2} = 1 \quad \checkmark \\ \frac{d\vec{t}}{ds} &= \begin{pmatrix} -\frac{R\omega^2}{v^2} \cdot \cos\left(\frac{\omega s}{v}\right) \\ -\frac{R\omega^2}{v^2} \cdot \sin\left(\frac{\omega s}{v}\right) \\ 0 \end{pmatrix} \Rightarrow \kappa = \frac{R\omega^2}{v^2} = \frac{R\omega^2}{R^2\omega^2 + b^2} \\ &= \frac{1}{\left(R + \frac{b^2}{R\omega^2}\right)} < \frac{1}{R} \end{aligned}$$

The curvature of the helical path is smaller than for a circle. In the limit  $b \rightarrow 0$ , we have  $\kappa = 1/R$ , denoting a perfect circle. In the limit  $b \rightarrow \infty$ ,  $\kappa$  vanishes, denoting a straight line.

The derivatives of the vectors of the co-moving frame are described in the same basis through the **Frenet formulae**:

$$\begin{aligned} \frac{d\vec{t}}{ds} &= \kappa \vec{n} \\ \frac{d\vec{n}}{ds} &= -\kappa \vec{t} + \tau \vec{b} \\ \frac{d\vec{b}}{ds} &= -\tau \vec{n} \end{aligned} \quad (5.9)$$

where we introduced the **torsion**  $\tau$ :

$$\tau = -\frac{d\vec{b}}{ds} \cdot \vec{n} = \frac{d\vec{n}}{ds} \cdot \vec{b} \quad (5.10)$$



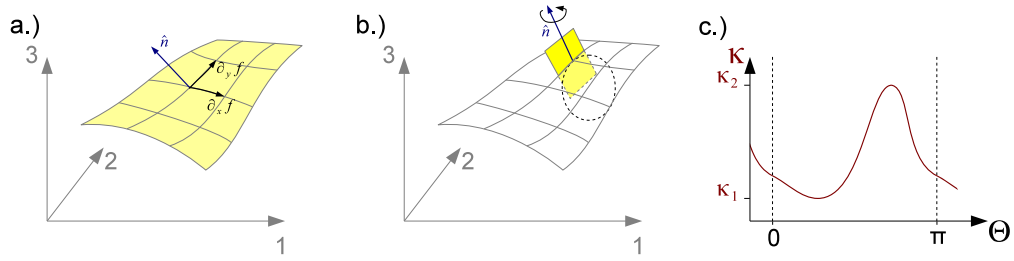


Figure 5.3: a.) Surface in a 3D space with tangential vectors  $\partial_x \vec{f}$  and  $\partial_y \vec{f}$  and unit normal vector  $\vec{n}$  perpendicular to the tangential vectors. b.) Plane (yellow) containing  $\vec{n}$  and rotating. c.) For each position  $\Theta$  of the rotating plane a curvature can be determined.

$\tau$  measures how strongly the curve is twisted out of the plane. E.g. for the helical path

$$\tau = -\vec{n} \cdot \frac{d\vec{b}}{ds} = \frac{b\omega}{v^2} = \frac{b\omega}{R^2\omega^2 + b^2} \xrightarrow[b \rightarrow 0]{b \rightarrow \infty} 0$$

## 5.1.2 Surfaces in 3D

### Tangential vectors, normal and curvatures

We next consider a surface in 3 dimensions. For the parametrization, we need two internal parameters  $x$  and  $y$ :

$$\vec{f}(x, y) = \begin{pmatrix} f_1(x, y) \\ f_2(x, y) \\ f_3(x, y) \end{pmatrix} \quad (5.11)$$

The tangential vectors  $\partial_x \vec{f}$  and  $\partial_y \vec{f}$  span the tangential plane (compare figure 5.3a). The unit normal vector then is defined as

$$\vec{n} = \frac{\partial_x \vec{f} \times \partial_y \vec{f}}{|\partial_x \vec{f} \times \partial_y \vec{f}|} \quad (5.12)$$

Note that in contrast to the case of space curves, we do not normalize the tangential vectors.

In order to introduce definitions for the curvature, we can construct a plane containing  $\vec{n}$  which we then rotate by 180 degrees through a given point  $(x, y)$  on the surface, as sketched in figure 5.3b. The kissing circle for each span curve defined by a rotation angle  $\Theta$  of the plane gives us a curvature in this certain direction (figure 5.3c).

The curvature will have a minimum  $\kappa_1$  and a maximum  $\kappa_2$ , the so-called "**principal curvatures**". With these two curvatures and the radii of the corresponding kiss-

ing circles  $R_1$  and  $R_2$ , respectively, we can define two important concepts:

$$\text{Mean curvature: } H := \frac{\kappa_1 + \kappa_2}{2} = \frac{1}{2} \left( \frac{1}{R_1} + \frac{1}{R_2} \right) \quad (5.13)$$

$$\text{Gaussian curvature: } K := \kappa_1 \cdot \kappa_2 = \frac{1}{R_1 \cdot R_2} \quad (5.14)$$

$H$  and  $K$  can be used to classify a point  $(x, y, z)$  on a surface: If  $K(x, y, z) > 0$ , it is called elliptic point or sphere-like, if  $K(x, y, z) < 0$ , it is called hyperbolic or saddle-like, and if  $K(x, y, z) = 0$ , it is called parabolic or cylinder-like. Three examples with constant  $K$  are shown in table 5.1.

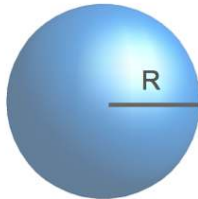

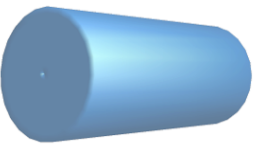
	Sphere (elliptic)	Saddle (hyperbolic)	Cylinder (parabolic)
Example			
Radii of kissing circles	$R_1 = R_2 = R$	$R_1 = -R_2$	$R_1 = R, R_2 = \infty$ (straight line)
Mean curvature	$H = \frac{1}{R}$	$H = 0$	$H = \frac{1}{2R}$
Gaussian curvature	$K = \frac{1}{R^2} > 0$ (cannot be mapped onto plane)	$K = -\frac{1}{R_1^2} < 0$	$K = 0$ (can be mapped onto plane)

Table 5.1:  $H$  and  $K$  can be used to classify surfaces. For the examples shown here,  $K$  is constant, and hence each point on the surface is elliptic, hyperbolic or parabolic, respectively.

For the Gaussian curvature  $K$ , Gauss formulated two important theorems:

1. **Theorema egregium** (Latin: "remarkable theorem"):  $K$  depends only on the inner geometry of the surface. The normal  $\vec{n}$  is not required to calculate it. In fact there exists an explicit formula to calculate  $K$  from the two tangent vectors and their derivatives, without the need to use the normal.
2. **Gauss-Bonnet theorem**:  $K$  integrated over a *closed* surface is a topological constant.

$$\oint dA K = 2\pi\chi \quad (5.15)$$

where  $\chi$  is the so-called "Euler characteristic". It can be used to calculate the number of handles  $G$  ("genus") of a surface:

$$\chi = 2 - 2 \cdot G \quad (5.16)$$

Because  $\chi$  is a topological quantity, one can calculate it from topologically equivalent polyhedra (for examples, see table 5.2). Then one can use the **Euler theorem**:

$$\chi = F - E + V \quad \begin{array}{l} \text{F: Number of faces} \\ \text{E: Number of edges} \\ \text{V: Number of vertices} \end{array} \quad (5.17)$$

### Recipe from differential geometry

In order to evaluate integrals like  $\int dA K$ , one needs formulae for  $dA = dA(x, y) = f_A(x, y) dx dy$  and  $K = K(x, y)$ . To this end, we calculate the three  $2 \times 2$  matrices  $g$ ,  $h$  and  $a$ . Let us first define the symmetric matrix  $g$ , also called "first fundamental form" or "metric tensor":

$$g_{ij} := \partial_i \vec{f} \cdot \partial_j \vec{f} = \begin{pmatrix} |\partial_x \vec{f}|^2 & \partial_x \vec{f} \cdot \partial_y \vec{f} \\ \partial_x \vec{f} \cdot \partial_y \vec{f} & |\partial_y \vec{f}|^2 \end{pmatrix} \quad \text{metric tensor} \quad (5.18)$$

$$\Rightarrow g_{ij}^{-1} = \frac{1}{\det g} \begin{pmatrix} |\partial_y \vec{f}|^2 & -\partial_x \vec{f} \cdot \partial_y \vec{f} \\ -\partial_x \vec{f} \cdot \partial_y \vec{f} & |\partial_x \vec{f}|^2 \end{pmatrix} \quad (5.19)$$

where  $\det g = |\partial_x \vec{f} \times \partial_y \vec{f}|^2$ .  $g_{ij}$  depends on  $\partial_x \vec{f}$  and  $\partial_y \vec{f}$ , but not on the unit normal  $\vec{n}$ . It describes the metrics in the surface:

$$A(S) = \int_S dx dy |\partial_x \vec{f} \times \partial_y \vec{f}| = \int_S dx dy (\det g)^{1/2} \quad (5.20)$$

The "second fundamental form" is defined as

$$h_{ij} := -\partial_i \vec{n} \cdot \partial_j \vec{f} \stackrel{\vec{n} \cdot \partial_i \vec{f} = 0}{=} \vec{n} \cdot \partial_i \partial_j \vec{f} \Rightarrow \boxed{h_{ij} = \vec{n} \cdot \partial_i \partial_j \vec{f}} \quad \text{second fundamental form} \quad (5.21)$$

which, in contrast to the metric tensor, depends on the unit normal  $\vec{n}$ .

With the matrices  $g$  and  $h$ , the matrix  $a$  can be defined:

$$\boxed{a := h \cdot g^{-1}} \quad \text{Weingarten matrix} \quad (5.22)$$

Like curvature  $\kappa$  and torsion  $\tau$  tell us how the normal changes along a space curve, the Weingarten matrix tells us how the normal changes along a surface:

$$\partial_i \vec{n} = -\sum_j a_{ij} \partial_j \vec{f} \quad (5.23)$$

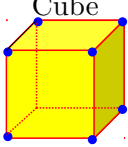
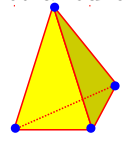
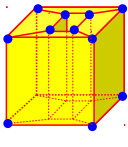
Object	Topological equivalence	Euler characteristic $\chi = F - E + V$	Genus $G = \frac{2 - \chi}{2}$
a.) Sphere	Cube 	$\chi = 6 - 12 + 8$ $= 2$	$G = 0$
	Tetrahedron 	$\chi = 4 - 6 + 4$ $= 2$	$G = 0$
b.) $n$ spheres	$n$ cubes	$\chi = 2 \cdot n$	$G = 1 - n$
c.) Torus	punctured cube 	$\chi = 16 - 32 + 16$ $= 0$	$G = 1$
d.) Double torus		$\chi = -2$	$G = 2$

Table 5.2: a.) The sphere is topologically equivalent to a cube and a tetrahedron, respectively.  $\chi$  can also be calculated from the Gauss-Bonnet theorem (equation 5.15):  $\oint dA K = 4\pi R^2 \cdot \frac{1}{R^2} = 2\pi \cdot 2$ . b.) The Euler characteristic is additive over multiple bodies. The more bodies, the larger  $\chi$  and the more negative  $G$ . c.) The torus is topologically equivalent to toroidal polyhedra, e.g. a punctured cube. Note that  $G = 1$ , denoting that the object has one handle. d.) For topologically more complex structures, like the double or triple torus, it is more reasonable to determine the number of handles  $G$  and then calculate  $\chi$  from equation 5.16 than to find a topologically equivalent polyhedron. Generally we find: The more handles, the larger  $G$  and the more negative  $\chi$ .

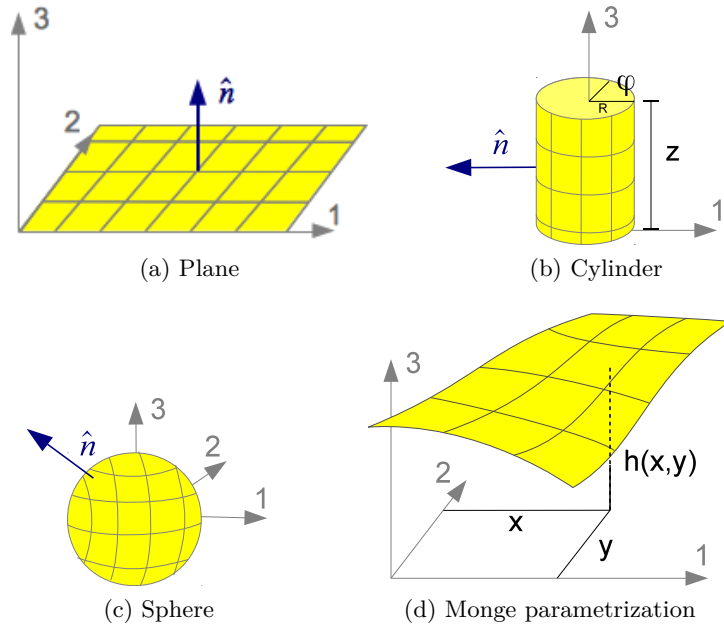


Figure 5.4

From the Weingarten matrix we now can compute the mean curvature  $H$  and the Gaussian curvature  $K$  for any given surface  $\vec{f}$  (without proof):

$$K = \det a = \frac{\det h}{\det g} \quad (5.24)$$

$$H = \frac{1}{2} \operatorname{tr} a \quad (5.25)$$

In the following, we will use this recipe for some important examples.

1. **Plane** (figure 5.4a)

$$\begin{aligned} \vec{f} &= \begin{pmatrix} x \\ y \\ 0 \end{pmatrix} \Rightarrow \partial_x \vec{f} = \begin{pmatrix} 1 \\ 0 \\ 0 \end{pmatrix}, \partial_y \vec{f} = \begin{pmatrix} 0 \\ 1 \\ 0 \end{pmatrix}, \vec{n} = \begin{pmatrix} 0 \\ 0 \\ 1 \end{pmatrix} \\ \Rightarrow g &= \begin{pmatrix} 1 & 0 \\ 0 & 1 \end{pmatrix} \Rightarrow \det g = 1, dA = \sqrt{\det g} dx dy = dx dy \\ h &= a = \begin{pmatrix} 0 & 0 \\ 0 & 0 \end{pmatrix} \Rightarrow H = K = 0 \end{aligned}$$

2. **Cylinder** (figure 5.4b, internal coordinates  $\phi$  and  $z$ )

$$\begin{aligned}\vec{f} &= \begin{pmatrix} R \cdot \cos \phi \\ R \cdot \sin \phi \\ z \end{pmatrix} \Rightarrow \partial_\phi \vec{f} = \begin{pmatrix} -R \cdot \sin \phi \\ R \cdot \cos \phi \\ 0 \end{pmatrix}, \partial_z \vec{f} = \begin{pmatrix} 0 \\ 0 \\ 1 \end{pmatrix}, \vec{n} = \begin{pmatrix} \cos \phi \\ \sin \phi \\ 0 \end{pmatrix} \\ \Rightarrow g &= \begin{pmatrix} R^2 & 0 \\ 0 & 1 \end{pmatrix} \Rightarrow \det g = R^2, dA = R d\phi dz \\ h &= \begin{pmatrix} -R & 0 \\ 0 & 0 \end{pmatrix} \quad a = \begin{pmatrix} -\frac{1}{R} & 0 \\ 0 & 0 \end{pmatrix} \\ &\Rightarrow H = -\frac{1}{2R}, K = 0\end{aligned}$$

3. **Sphere** (figure 5.4c, internal coordinates  $\varphi$  and  $\theta$ )

$$\begin{aligned}\vec{f} &= R \cdot \begin{pmatrix} \cos \theta \cdot \cos \varphi \\ \cos \theta \cdot \sin \varphi \\ \sin \theta \end{pmatrix} \Rightarrow \partial_\varphi \vec{f} = R \cdot \begin{pmatrix} -\cos \theta \cdot \sin \varphi \\ \cos \theta \cdot \cos \varphi \\ 0 \end{pmatrix}, \\ &\partial_\theta \vec{f} = R \cdot \begin{pmatrix} -\sin \theta \cdot \cos \varphi \\ -\sin \theta \cdot \sin \varphi \\ \cos \theta \end{pmatrix}, \\ &\vec{n} = \frac{1}{R} \cdot \vec{f} \\ \Rightarrow g &= \begin{pmatrix} R^2 \cdot \cos^2 \theta & 0 \\ 0 & R^2 \end{pmatrix} \Rightarrow \det g = R^4 \cdot \cos^2 \theta, dA = R^2 \cdot \cos \theta d\varphi d\theta \\ h &= -\frac{1}{R} \cdot g \quad a = -\frac{1}{R} \hat{\mathbb{1}} \\ &\Rightarrow H = -\frac{1}{R}, K = \frac{1}{R^2}\end{aligned}$$

4. **Monge parametrization** (figure 5.4d). This parametrization is valid for surfaces without overhangs (such a surface is also called a *graph*). The surface is described by a height function  $h(x, y)$ . In the following we will assume the surface to be nearly flat, i.e.  $|\vec{\nabla} h(x, y)| \ll 1$ .

$$\begin{aligned}\vec{f} &= \begin{pmatrix} x \\ y \\ h(x, y) \end{pmatrix} \Rightarrow \partial_x \vec{f} = \begin{pmatrix} 1 \\ 0 \\ \partial_x h \end{pmatrix}, \partial_y \vec{f} = \begin{pmatrix} 0 \\ 1 \\ \partial_y h \end{pmatrix}, \\ &\vec{n} = \frac{1}{\sqrt{1 + (\partial_x h)^2 + (\partial_y h)^2}} \begin{pmatrix} \partial_x h \\ \partial_y h \\ 1 \end{pmatrix} \\ \Rightarrow g &= \begin{pmatrix} 1 + (\partial_x h)^2 & \partial_x h \cdot \partial_y h \\ \partial_x h \cdot \partial_y h & 1 + (\partial_y h)^2 \end{pmatrix} \Rightarrow \det g \approx 1 + (\partial_x h)^2 + (\partial_y h)^2 = 1 + (\vec{\nabla} h)^2\end{aligned}$$

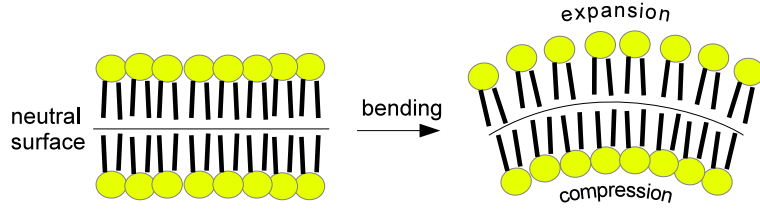


Figure 5.5: Sketch of a bent lipid double layer.

$$dA \approx \sqrt{1 + (\vec{\nabla}h)^2} dx dy \approx \left[ \underbrace{1}_{\text{reference plane}} + \underbrace{\frac{1}{2}(\vec{\nabla}h)^2}_{\text{excess area, } >0} \right] dx dy \quad (5.26)$$

$$h = \frac{1}{\sqrt{\det g}} \begin{pmatrix} \partial_{xx}h & \partial_{xy}h \\ \partial_{xy}h & \partial_{yy}h \end{pmatrix} \approx a$$

For calculating the Weingarten matrix, in lowest order we have  $g \approx 1$  and thus  $a \approx h$ . Therefore the mean and Gaussian curvatures are

$$H \approx \frac{1}{2}(\partial_{xx}h + \partial_{yy}h) = \frac{1}{2}\Delta h \quad (5.27)$$

$$K \approx \partial_{xx}h \cdot \partial_{yy}h - (\partial_{xy}h)^2 \quad (5.28)$$

## 5.2 Curvature energy and minimal energy shapes

### 5.2.1 Bending Hamiltonian

What is the energy of a biomembrane? Because the membrane is fluid, it has no in-plane elastic energy (the shear modulus vanishes). As a fluid, it has in-plane compression, but the corresponding energy cost is so high due to the dense packing of the hydrocarbon chains, so that we can neglect this mode compared to others. Assuming mechanical equilibrium, the viscosity of the fluid membrane also does not count. As a fluid, the membrane has no physical coordinate system and thus its energy cannot depend on its parametrization. Thus the only relevant energy contribution we are left with is out-of-plane bending of the membrane. Hence, the Hamiltonian must be a function of the curvatures  $H$  and  $K$

$$\mathcal{H} = \int dA f(H, K)$$

One can expand the Hamiltonian in small curvatures (or, in other words, in small  $1/R$ ) up to order  $1/R^2$  to obtain<sup>2</sup>

$$\boxed{\mathcal{H} = \int dA \{ \sigma + 2\kappa(H - c_0)^2 + \bar{\kappa}K \}} \quad \textbf{Helfrich-Canham Hamiltonian}$$

Recall that  $H \sim \mathcal{O}(1/R)$  and  $K \sim \mathcal{O}(1/R^2)$ . Higher order terms have also been investigated but lead to very complex structures.

The Helfrich-Canham Hamiltonian contains four material parameters:

1.  $\sigma$  denotes the surface tension.  $\mathcal{H} = \sigma \int dA$  governs the physics of liquid droplets and soap bubbles. It can be interpreted as a chemical potential for the area. For liquid droplets and soap bubbles, surface area can be generated by simply changing film thickness. This is not possible for lipid bilayers, but there too reservoirs for surface area exist: first there is excess area stored in membrane fluctuations, and second lipids can flow into the area of interest. In cells, there are more biological reservoirs for area, like protein-mediated membrane invaginations called *caveolae* and vesicles close to the membrane that fuse on demand. The value of the surface tension of the water-air interface is very high ( $73 \text{ mN/m} = 73 \text{ dyn/cm}$ ) because water is such a cohesive fluid. In our body, such a high surface tension can harm biomolecules and cells avoid to have direct contact to air; a notable exception are our lungs, where this cannot be avoided and special precautions have to be taken to prevent collapse. Usually cells are surrounded by aqueous medium and the surface tensions in the plasma membrane are much smaller (of the order of  $300 \text{ pN}/\mu\text{m} = 0.3 \text{ mN/m}$  as measured by tether pulling, see below). The cortical tension of human cells is around  $2 \text{ mN/m}$ , but this should not be confused with the membrane tension, the lipid bilayer would rupture at that value, so it has to be protected from such high values (cortex and plasma membrane are connected by linkers which decouple the both).
2.  $\kappa$  denotes the bending rigidity.  $\mathcal{H} = 2\kappa \int dA H^2$  is the bending Hamiltonian which governs the physics of vesicles. As a typical value one finds  $\kappa = 20 k_B T$ , both for vesicles and cells.  $\kappa$  is a classical elastic modulus that also emerges in elasticity theory of thin plates.
3.  $c_0$  reflects any asymmetry of the bilayer, hence denoting the spontaneous (mean) curvature of the membrane. Asymmetries can be caused for instance by embedded or adsorbed proteins or different lipid composition of the two opposing layers of the bilayer, to name but a few.

---

<sup>2</sup>The two classical papers on this Hamiltonian are: PB Canham: "The minimum energy of bending as a possible explanation of the biconcave shape of the human red blood cell", J Theor Biol. 1970, 26:61-81, and W Helfrich: "Elastic properties of lipid bilayers: theory and possible experiments." Z Naturforschung C 1973, 28:693-703. There are also two very good books on membrane biophysics as developed from this Hamiltonian: Reinhard Lipowsky and Erich Sackmann, editors, Structure and dynamics of membranes, two volumes, North Holland 1995, and Patricia Bassereau and Pierre Sens, editors, Physics of biological membranes, Springer 2018.



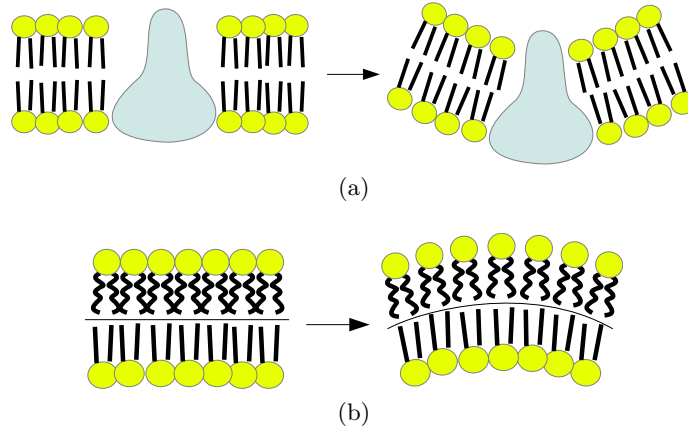


Figure 5.6: Spontaneous curvature of the membrane due to asymmetries caused by a.) embedded proteins (adsorbed proteins would have similar effect) and by b.) different lipid compositions in outer versus inner leaflet.

4.  $\bar{\kappa}$  is called the saddle-splay modulus and is related to the topology by the Gauss-Bonnet theorem (equation 5.15).  $\bar{\kappa}$  denotes a chemical potential for the number of objects and hence describes the membrane's tendency to merge or split.

If we consider  $\sigma = 0$  and  $c_0 = 0$ , then :

$$\begin{aligned}
 \mathcal{H} &= \int dA \{2\kappa H^2 + \bar{\kappa} K\} \\
 &= \int dA \left\{ 2\kappa \left( \frac{\kappa_1 + \kappa_2}{2} \right)^2 + \bar{\kappa} \cdot \kappa_1 \kappa_2 \right\} \\
 &= \int dA \left\{ \frac{\kappa_+}{2} (\kappa_1 + \kappa_2)^2 + \frac{\kappa_-}{2} (\kappa_1 - \kappa_2)^2 \right\}
 \end{aligned}$$

with  $\kappa_+ = \kappa + \frac{\bar{\kappa}}{2}$  and  $\kappa_- = -\frac{\bar{\kappa}}{2}$ . This indicates two topological instabilities:

- $\kappa_+ < 0 \implies \kappa_1 = \kappa_2 \longrightarrow \infty$ , describes a system of many small droplets.
- $\kappa_- < 0 \implies \kappa_1 = -\kappa_2 \longrightarrow \infty$ , describes a saddle-like surface with very small lattice constant (e.g sponge or egg-carton).

This is why stability requires  $\kappa_+$  and  $\kappa_-$  both to be larger than zero. This implies  $-2\kappa < \bar{\kappa} < 0$ , so  $\bar{\kappa}$  is expected to be small and negative.

One can use the elasticity theory for linear isotropic material to derive the two elastic moduli of the thin membrane as a function of the two elastic moduli of the bulk material:

$$\kappa = \frac{Ed^3}{12(1-\nu)^2}, \quad \bar{\kappa} = \frac{-Ed^3}{6(1+\nu)} \quad (5.29)$$

where  $E$  is the Young's modulus of the material and  $\nu$  its Poisson's ratio. The bulk material relevant here is the hydrocarbon fraction of the bilayer.  $d = 4nm$  is its thickness. With the value  $\nu = 0.5$  for incompressible material, a bending

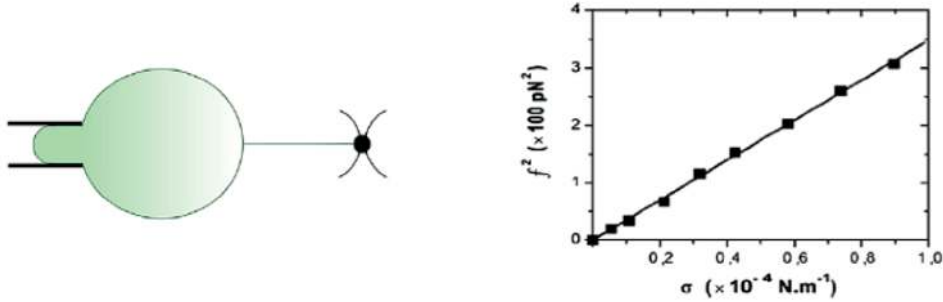


Figure 5.7: The force to pull a tether out of a vesicle scales with the square root of the tension. P. Basserau et al. *Advances in Colloid and Interface Science* 208 (2014) 47-57.

rigidity  $\kappa$  of  $20 k_B T$  is achieved for a Young's modulus around  $E = 10 \text{ MPa}$ , which is a very reasonable value. For the saddle splay modulus we have  $\bar{\kappa}/\kappa = -1/3$ , which lies in the range between  $-2$  and  $0$  discussed above.

The bending Hamiltonian is an *energy functional* — it is a scalar that depends on a function, e.g. in Monge representation  $\mathcal{H} = \mathcal{H}[h(x, y)]$ . We now have to deal with two important issues that complement each other:

- **Energetics** deals with the question what is the surface with minimal energy. These surfaces have to solve the Euler-Lagrange equations, also called shape equations  $\frac{\delta \mathcal{H}}{\delta h} = 0$ . Here  $\frac{\delta}{\delta h}$  is a *functional derivative*.
- **Statistics** answers the question what is the effect of thermal fluctuations on membranes. Here the starting point is the partition sum  $Z = \int \mathcal{D}h \exp(-\beta \mathcal{H}[h])$ , which is a *path integral* or *functional integral* (integral over all possible functions).

Together the minimal energy state and the fluctuations around it describe the main features of interest.

## 5.2.2 Tether pulling

We briefly discuss a first case of minimal energy shapes, namely if a tether is pulled out of a vesicle or cell, which is a standard setup to measure membrane tension. Experimentally one grabs an adhesive bead with an optical tweezer and moves it onto the membrane. If adhesion is successful, a cylindrical tether is pulled out of the membrane upon retraction. Experimentally it was found that after overcoming an initial barrier, the force will be constant; in contrast to an elastic situation, when force should rise with distance, this indicates that membrane is flowing into the tether.

We write the Helfrich-Hamiltonian for a cylinder with tension and bending rigidity and add a term for the pulling:

$$E = 2\pi RL \left[ \frac{\kappa}{2R^2} + \sigma \right] - FL \quad (5.30)$$

where  $L$  is the length of the cylinder and  $F$  the pulling force. We minimize for  $R$  to get:

$$R = \sqrt{\frac{\kappa}{2\sigma}} \quad (5.31)$$

At equilibrium, membrane energy and pulling energy should balance and thus

$$F = 2\pi\sqrt{2\kappa\sigma} \quad (5.32)$$

Therefore the force  $F$  scales as the square root of  $\sigma$ , as has been shown experimentally, compare figure 5.7. In reverse, the force can be used to measure  $\sigma$ .

### 5.2.3 Particle uptake

As a very important example for which one needs to solve the shape equations for minimal energy shapes, we now consider particle uptake. Cells continuously take up small particles or viruses with sizes of the order of 10 – 300 nm. In first order, these particles are wrapped by the membrane. In addition, rigid coats are assembling on the membrane, which is the main mechanism that drives vesicle budding and that enables material transport within cells. Different coat proteins (clathrin, COPI, COPII) can polymerise onto the membrane, forming a rigid coat or shell with the shape of a spherical cap. These coats assemble on the membrane of different organelles (plasma membrane, endosome, Golgi apparatus, endoplasmatic reticulum) and grow until the formation of a nearly complete sphere. Both, particle uptake and vesicle budding require that the energetic gain of particle adhesion and coat polymerisation overcomes the energetic cost of membrane deformations.

The shape of the membrane will assume a minimal energy configuration during uptake, i.e. the membrane shape will be such that the energy, given by the Helfrich Hamiltonian, becomes minimal. Hence, we are dealing with a *variational problem*. The Hamiltonian reads

$$\mathcal{H} = \int dA \left\{ \sigma + 2\kappa (H - c_0)^2 + \bar{\kappa}K \right\} + wA_{\text{ad}}, \quad (5.33)$$

where  $w$  is the adhesion energy of the particle or polymerisation energy of the coat times the area  $A_{\text{ad}}$  where the particle adheres to the membrane or where the coat is polymerised. As this term does not influence the shape of the membrane we first neglect this term in the following. For simplicity we consider a spherical particle (cf. Fig. 5.8) that obeys axial symmetry with radius  $R$  and a symmetric membrane ( $c_0 = 0$ ). As the integral over the Gaussian curvature is only a constant (Gauss-Bonnet) it will drop out during minimisation. Therefore, we formally set  $\bar{\kappa} = 0$ . Then the membrane is parametrised by the cylindrical coordinates  $r(s)$  and  $z(s)$ , where  $s$  is the arc length along the shape contour of the membrane and  $\phi$  is the polar angle

$$\vec{r} = \begin{pmatrix} r(s) \cos \phi \\ r(s) \sin \phi \\ z(s) \end{pmatrix}. \quad (5.34)$$

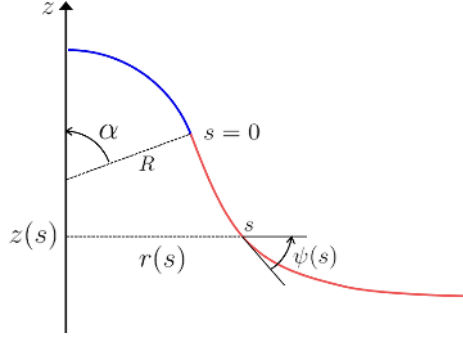


Figure 5.8: Parametrisation. The blue curve represents the part of the membrane that adheres to the particle or is covered by the coat; the red line is the free part of the membrane. Figure taken from Foret, Lionel. "Shape and energy of a membrane bud induced by protein coats or viral protein assembly." *The European Physical Journal E* 37.5 (2014): 42.

Importantly, we can express  $r(s)$  and  $z(s)$  by means of the the tangential angle  $\psi(s)$  as

$$\dot{r} = \cos \psi(s) \quad \dot{z} = -\sin \psi(s) \quad (5.35)$$

Our aim is to calculate the principal curvatures  $C_1$  and  $C_2$ . Hence, we calculate the metric  $g$ , the normal vector  $\vec{n}$ , the second fundamental form  $h$  and the Weingarten matrix  $a$ . We find

$$g = \begin{pmatrix} 1 & 0 \\ 0 & r^2 \end{pmatrix} \quad (5.36)$$

$$\vec{n} = \begin{pmatrix} \cos \phi \sin \psi \\ \sin \phi \sin \psi \\ \cos \psi \end{pmatrix} \quad (5.37)$$

$$h = \begin{pmatrix} -\dot{\psi} & 0 \\ 0 & -r \sin \psi \end{pmatrix} \quad (5.38)$$

$$a = \begin{pmatrix} -\dot{\psi} & 0 \\ 0 & -\sin \psi / r \end{pmatrix} \quad (5.39)$$

Thus, the principal curvatures are given by the eigenvalues of  $a$ ,  $C_1 = -\dot{\psi}$  and  $C_2 = -\sin \psi / r$ . Then the Helfrich Hamiltonian reads with the mean curvature  $2H = C_1 + C_2$

$$\mathcal{H} = \int ds d\phi \left\{ \sigma + \frac{\kappa}{2} \left( \dot{\psi} + \sin \frac{\psi}{r} \right)^2 \right\} r. \quad (5.40)$$

In order to minimise  $\mathcal{H}$  with respect to  $r(s)$  and  $\psi(s)$  we have to include an additional Lagrange multiplier  $\gamma(s)$  to incorporate Eq. (5.35). We note that

because of the spherical geometry we do not need a second Lagrange multiplier, as variations of the contour endpoints are independent. We define an action

$$\mathcal{S}[r(s), \psi(s)] = \frac{\mathcal{H}}{2\pi\kappa} + \int ds \gamma(s)(\dot{r} - \cos \psi) = \int ds \mathcal{L}(\psi, \dot{\psi}, r, \dot{r}), \quad (5.41)$$

with a Lagrange function  $\mathcal{L}$

$$\mathcal{L}(\psi, \dot{\psi}, r, \dot{r}) = \frac{1}{2} \left( \dot{\psi} + \frac{\sin \psi}{r} \right)^2 r + \frac{r}{\lambda^2} + \gamma(\dot{r} - \cos \psi), \quad (5.42)$$

where  $\lambda = \sqrt{\kappa/\sigma}$  defines the characteristic lengthscale of the membrane. The Euler-Lagrange equations are the solutions to the variational problem

$$\delta \mathcal{S} = 0 \leftrightarrow \frac{d}{dt} \frac{\partial \mathcal{L}}{\partial \dot{q}_k} - \frac{\partial \mathcal{L}}{\partial q_k}, \quad (5.43)$$

where  $q_k = \{r, \psi\}$ . Thus,

$$\begin{aligned} \ddot{\psi} &= -\frac{\dot{\psi} \cos \psi}{r} + \frac{\cos \psi \sin \psi}{r^2} + \frac{\gamma \sin \psi}{r} \\ \dot{\gamma} &= \frac{1}{2} \dot{\psi}^2 - \frac{\sin^2 \psi}{2r^2} + \frac{1}{\lambda^2}. \end{aligned} \quad (5.44)$$

In the usual case, the contour length is variable. Because  $\mathcal{L}$  does not explicitly depend on  $s$ ,  $F = \dot{r} \partial_{\dot{r}} \mathcal{L} + \dot{\psi} \partial_{\dot{\psi}} \mathcal{L} - \mathcal{L}$  is conserved. Since a variation of  $\mathcal{S}$  with respect to the contour lengths at the two end points has to vanish, one obtains that  $F$  has to vanish at the end points. Hence

$$F = \frac{r \dot{\psi}^2}{2} - \frac{r}{2} \left( \frac{\sin \psi}{r} \right)^2 - \frac{r}{\lambda^2} + \gamma \cos \psi = 0. \quad (5.45)$$

Using Eq. (5.45) we can eliminate  $\gamma$  from Eq. (5.44) to get the shape equation for axial symmetry

$$\ddot{\psi} \cos \psi + \frac{\dot{\psi} \cos^2 \psi}{r} + \frac{\dot{\psi}^2 \sin \psi}{2} - \frac{\sin \psi}{2r^2} (2 \cos^2 \psi + \sin^2 \psi) - \frac{1}{\lambda^2} \sin \psi = 0. \quad (5.46)$$

Eq. (5.46) together with Eq. (5.35) and the boundary conditions

$$r(0) = R \sin \alpha, \psi(0) = \alpha, \psi(\infty) = 0, \dot{\psi}(\infty) = 0, z(\infty) = 0, \quad (5.47)$$

then fully describe the membrane's shape.

In general the shape equations, as a set of ODEs, can be solved numerically, for example by means of the shooting method. The membrane parameter  $\lambda$  sets the typical extension of the membrane deformation (cf. Fig. 5.9). Note that for typical parameter values of  $\kappa$  and  $\sigma$  we get  $\lambda = 10 - 100$  nm. Depending on the  $\lambda$  and the particle or coat radius  $R$  one can define three membrane regimes.

- For a tense membrane ( $\lambda/R \gg 1$ ) the deformation is concentrated in a very narrow and highly curved region near the particle or coat.

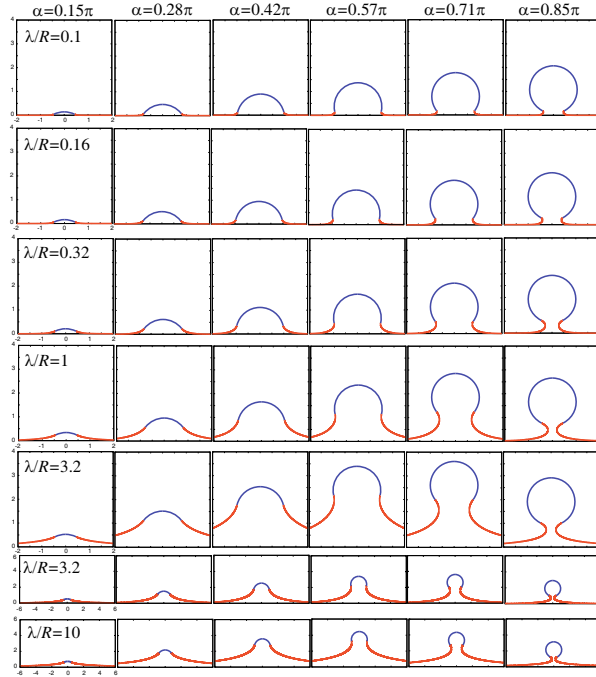


Figure 5.9: Membrane shapes for different opening angles  $\alpha$  and different values of  $\lambda/R$ . In blue: the membrane that adheres to the particle or which is covered by the coat. In red: the free part of the membrane. Figure taken from Foret, Lionel. "Shape and energy of a membrane bud induced by protein coats or viral protein assembly." *The European Physical Journal E* 37.5 (2014): 42.

- For an intermediate membrane ( $\lambda/R \approx 1$ ) the deformation propagates some intermediate distance into the membrane
- For a loose membrane ( $\lambda/R \ll 1$ ) the deformation propagates far from the particle or coat into the membrane.

We now aim for a phase diagram of particle uptake<sup>3</sup>. For simplicity, now we neglect the contribution from the free membrane. In general, for a particle to be taken up, it has to be adhesive and the adhesion energy has to balance the bending energy. The Helfrich Hamiltonian reads

$$\mathcal{H} = \int dA(2\kappa H^2 + \sigma) - wA_{ad} \quad (5.48)$$

<sup>3</sup>The two classical papers on this subject are: R Lipowsky and HG Doebereiner, Vesicles in contact with nanoparticles and colloids, *Europhysics Letters* 43:219-225, 1998; and M Deserno, Elastic deformation of a fluid membrane upon colloidal binding, *Phys Rev E* 69:031903, 2004.

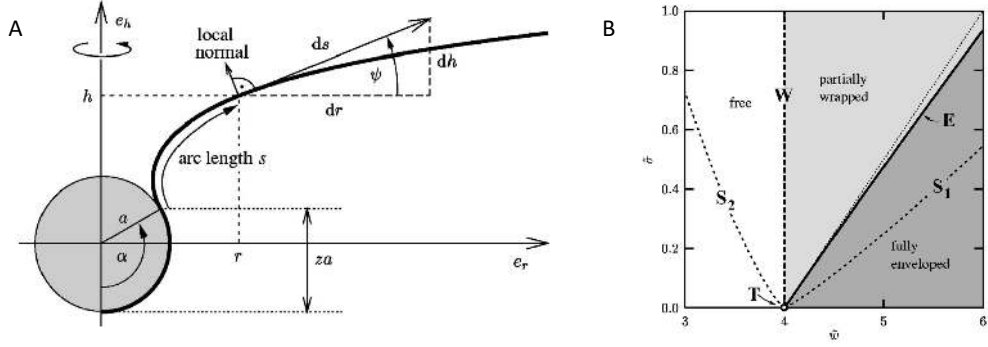


Figure 5.10: (A) Particle uptake by membrane wrapping. (B) Phase diagram of particle wrapping by membranes as function of surface tension  $\sigma$  and adhesion energy  $w$ . Taken from M Deserno, PRE 2004.

where  $A_{ad}$  is the adherent membrane area and  $w$  the adhesion energy area density. A typical value would be  $w = 0.1 \text{ mJ/m}^2$ .

We next consider a sphere of radius  $R$ . If we denote the angle  $\alpha$  to describe where the contact line between membrane and sphere is located (compare figure 5.10A), then the wrapping variable  $z = 1 - \cos \alpha$  will run from 0 to 2 as the membrane wraps the particle. If we neglect the contributions from the bending of the free membrane, we get

$$E = 4\pi z\kappa + \pi R^2 z^2 \sigma - 2\pi R^2 z w \quad (5.49)$$

The first term is the bending energy, which is independent of radius. The second and last term are the surface tension and adhesion energy terms, respectively. While both have the same  $R^2$ -scaling, they have different scaling with  $z$ . The last term has the trivial  $z$ -scaling. The second term however scales as  $z^2$ , because here the excess area  $A_{excess} = A_{ad} - A_{projected}$  matters:

$$A_{excess} = 2\pi R^2(1 - \cos \alpha) - \pi R^2 \sin^2 \alpha = \pi R^2(1 - 2 \cos \alpha + \cos^2 \alpha) = \pi R^2 z^2 \quad (5.50)$$

We now non-dimensionalize the energy and get

$$\bar{E} = \frac{E}{\pi\kappa} = 4z + \bar{\sigma}z^2 - \bar{w}z = -(\bar{w} - 4)z + \bar{\sigma}z^2 \quad (5.51)$$

where  $\bar{\sigma} = \sigma R^2/\kappa$  and  $\bar{w} = 2wR^2/\kappa$ . This energy function gives rise to a phase diagram as shown in figure 5.10B. For  $\bar{w} < 4$ , the energy is always positive and no wrapping can occur. This corresponds to the free state. Note that  $\bar{w} = 4$  translates into a minimal radius  $R = \sqrt{2\kappa/w} \approx 50 \text{ nm}$ , below which uptake is not possible. For  $\bar{w} > 4 + 4\bar{\sigma}$ , the minimal energy is found for  $z = 2$ , the fully wrapped state. Inbetween there is a parameter region where the minimum lies at a finite value of  $z$ , here the partially wrapped state is stable.

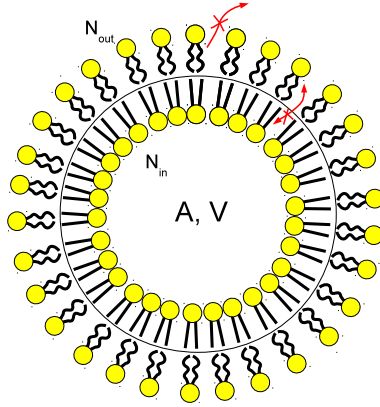


Figure 5.11: Schematics of a lipid vesicle with constant surface  $A$  and volume  $V$ . Although lipid bilayers are permeable to water, there are always some ions caged in the vesicle, fixing an osmotic pressure, which keeps the volume constant. Also the number of lipids on the outside  $N_{out}$  and inside  $N_{in}$  is constant, because of the energy barrier that does not allow for the lipids to jump from one side of the membrane to the other or to escape.

#### 5.2.4 Minimal energy shapes for vesicles

In this section we are looking at closed surfaces; therefore  $\bar{\kappa}$  is irrelevant due to the Gauss-Bonnet theorem. Also  $c_0 = 0$  because we assume symmetric membranes. We add a term  $-pV$  to control the volume. In practice, one prepares a suspension of vesicles, e.g. by ultrasound or electroporation acting on a lipid-water mixture, and then selects vesicles of interest, e.g. with optical tweezers or a micropipette. Each vesicle then has fixed values for area and volume which can be measured with e.g. video or fluorescence microscopy. Using  $A = 4\pi R_0^2$ , one can define the radius of the equivalent sphere. Then the only relevant parameter of the system is the reduced volume  $v$ :

$$v = \frac{V}{\frac{4\pi}{3}R_0^3}$$

Each vesicle class has an individual value for  $v$ , and  $v \leq 1$  should be always fulfilled;  $v < 1$  describes a deflated vesicle with excess area for non-trivial shapes. Shape with  $v = 1$  is a sphere and has the optimal  $\frac{A}{V}$  ratio. Note that

$$\mathcal{H} = 2\kappa \int dA H^2 \underset{\text{for sphere}}{=} 2\kappa 4\pi R^2 \cdot \frac{1}{R^2} = 8\pi\kappa = \text{const.}$$

which indicates that the solutions are independent of rescaling (this is part of a more general property called *conformal invariance*).

In order to obtain a phase diagram as a function of  $v$ , we have to solve the corresponding Euler-Lagrange equations (*shape equations*). These are derived by varying the surface in normal direction

$$\vec{f}(x, y) = \vec{f}_0(x, y) + \epsilon\phi(x, y)\vec{n}(x, y) \quad (5.52)$$



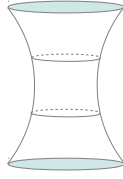


Figure 5.12: Catenoid as an example of a minimal surface, which is not compact and has  $H = 0$ .

and then asking for the first  $\epsilon$ -derivative of the energy functional to vanish for arbitrary  $\phi(x, y)$  (one can show that a tangential variation does not matter in this order). The result can be written as<sup>4</sup>:

$$\boxed{p + 2\sigma H - 2\kappa(2H(H^2 - K) - \Delta H) = 0} \quad \text{Euler-Lagrange equation} \quad (5.53)$$

where  $\Delta$  is the Laplace-Beltrami operator (only for the almost flat membrane we get the Laplace operator  $\Delta = \partial_x^2 + \partial_y^2$ ). The Euler-Lagrange equation is a partial differential equation (PDE) of the 4<sup>th</sup> order with a famous limit for  $\kappa = 0$ , namely the Laplace law for soap bubbles

$$\boxed{H = -\frac{p}{2\sigma}} \quad \text{Laplace law for soap bubbles} \quad (5.54)$$

Here a simple derivation of the Laplace law

$$\begin{aligned} \sigma dA &= -p dV \\ \sigma d(4\pi R^2) &= -p d\left(\frac{4\pi}{3}R^3\right) \\ \sigma 4\pi 2R dR &= -p \frac{4\pi}{3} 3R^2 dR \\ \Rightarrow \frac{1}{R} &= -\frac{p}{2\sigma} \end{aligned} \quad (5.55)$$

As the only compact surface with constant mean curvature (CMC-surface) is the sphere, a soap bubble is spherical. CMC-surfaces are critical points of the area functional under the constraint of a constant volume.

For  $p = 0$  the shape equation is simply  $\boxed{H = 0}$ , which describes a minimal surface, i.e. a surface under tension with minimal energy given a particular boundary curve. Those surfaces are always saddle-like, because  $H = 0$  means  $R_1 = -R_2 \Rightarrow K = -\frac{1}{R_1^2}$ , which is always negative. The implication is that those surfaces cannot be compact, because a surface that is saddle-shaped cannot be enclosed by a boundary. A well-known example for a minimal surface is the catenoid connecting two wireframes, compare figure 5.12.

The solutions to the Euler-Lagrange equation for  $\sigma = 0$  and finite  $\kappa$  are called *Willmore surfaces*. Because they are solutions to  $\mathcal{H} = 2\kappa \int dA H^2$ , minimal surfaces with  $H = 0$  are included. But due to their saddle-like shape, minimal

<sup>4</sup>ZC Ou-Yang and W Helfrich, Bending energy of vesicle membranes: General expressions for the first, second, and third variation of the shape energy and applications to spheres and cylinders, Phys. Rev. A 39: 5280-5288, 1989.

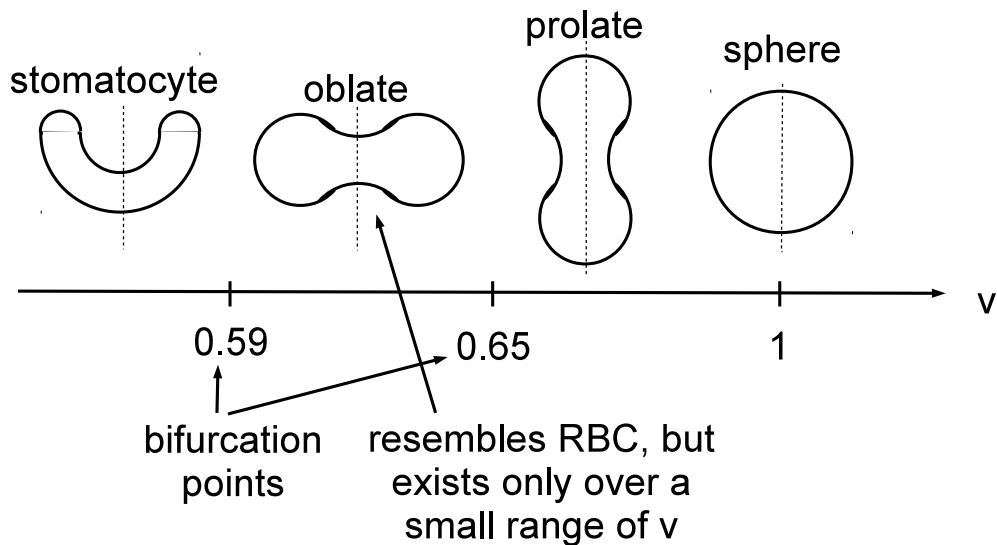


Figure 5.13: The shape diagram represents the minimal energy shapes for given points in the phase space.

surfaces without edges cannot be compact, so we are interested in Willmore surfaces with  $H \neq 0$  as solutions for the vesicle shape problem. Note that these solutions will not be CMC-surfaces, which arise from another energy function.

The main methods to solve the shape equations for the vesicles are solution of the shape equations for axisymmetric shapes (4th order ODE), solutions for the shape equations with FEM-methods for arbitrary shapes (4th order PDE) or minimization for triangulated surfaces (e.g. with the software *Surface Evolver* from Ken Brakke). Each of these methods gives the one-dimensional shape diagram shown in figure 5.13<sup>5</sup>. One clearly sees a sequence of symmetry breaks as the reduced volume goes down (in terms of the differential equations, we are dealing with bifurcations; this is in analogy to phase transitions in thermodynamics). The obtained shapes describe many of the observed vesicle and cell shapes, e.g. the biconcave vesicle looks like a red blood cell (discocyte). The problem of this theory is that it does not describe all the shapes seen in nature, e.g. budding vesicles. This means that we are close to the right solution, but the model has to be expanded and more features of the real system have to be added.

A more complete theory is given by the Area Difference Elasticity model (ADE model)<sup>6</sup>, which has two parameters. In addition to the reduced volume, we now also consider the possibility that the number of lipids may be different in the outside and the inside monolayers of the lipid bilayer. Until now we assumed an infinitely thin membrane, but now we no longer disregard its thickness. We define an area difference  $\Delta A_0 = a(N_{in} - N_{out})$ , where  $N_{in}$  is the number of lipids

<sup>5</sup>U Seifert, K Berndl and R Lipowsky, Shape transformations of vesicles: Phase diagram for spontaneous-curvature and bilayer-coupling models, *Physical Review A* 44.2: 1182, 1991

<sup>6</sup>Ling Miao, Udo Seifert, Michael Wortis, and Hans-Günther Döbereiner, Budding transitions of fluid-bilayer vesicles: The effect of area-difference elasticity, *Physical Review E* 49, 1994

on the inner side of the vesicle,  $N_{out}$  is the number on the outside, and  $a$ , which is the typical area per lipid, has the dimensions of  $nm^2$ . Since  $A_{in}$  and  $A_{out}$  do not change, for energy reasons,  $\Delta A_0$  stays constant for a vesicle. The bending Hamiltonian for the ADE model is

$$\mathcal{H} = 2\kappa \int dA H^2 + \frac{\alpha}{2} (\Delta A - \Delta A_0)^2$$

The differential geometry result for the integrated mean curvature is  $\Delta A = 2d \int dA H$ , with  $d = 4$  nm. The resulting shape diagram is now two-dimensional as shown in figure 5.13. It now contains the budded shape as well as non-axisymmetric shapes like the starfish vesicle. In the literature, many similar models have been discussed, including the spontaneous curvature and the bilayer-couple models, to explain the zoo of vesicle shapes, but the ADE-model seems to be the most appropriate one. Therefore it is also used as the standard starting point to explain the shape of red blood cells, which are known to have very asymmetric membrane leaflets.

### 5.3 Shape of red blood cells

We have seen above that the Helfrich Hamiltonian predicts shapes that resemble the biconcave disc of a red blood cell (RBC, also known as erythrocyte). However, this discocyte is stable only over a very small range of reduced volume  $v$ . The ADE-model predicts a variety of additional shapes, including stomatocytes (shaped like a cup or mouth). However, it does not predict echinocytes (shaped like a hedgehog), which are also often observed for RBCs. In general, there is whole zoo of RBC-shapes seen under different conditions (pH, ATP-concentration, temperature, lipid composition, etc). A comprehensive understanding of these RBC-shapes is very important because it is often used to detect pathological situations by simply checking for shapes under the microscope. In Fig. 5.15 we show the main shapes that are seen experimentally and how they can be predicted computationally. The upper left part shows electron microscopy images arranged in the so-called stomatocyte-discocyte-echinocyte (SDE) sequence, a sequence of shape transitions that can be caused by different agents that all seem to have the same physical consequences. The lower right half shows shapes predicted by an expanded ADE Hamiltonian as explained below. It also shows the sequence of free energy surfaces which leads to the transitions. We conclude that the shape of RBCs can be understood very well from physical shape models<sup>7</sup>. We start our discussion with some general remarks on RBCs. First observed by Anton van Leeuwenhoek in 1674, they are the carriers of hemoglobin and

<sup>7</sup>A comprehensive review is given by Gerald Lim H. W., Michael Wortis and Ranjan Mukhopadhyay, Red Blood Cell Shapes and Shape Transformations: Newtonian Mechanics of a Composite Membrane, in the book *Soft Matter, Vol. 4: Lipid Bilayers and Red Blood Cells*, edited by G. Gompper and M. Schick, Wiley-VCH Weinheim 2008. The original paper was HW Gerald Lim, Michael Wortis and Ranjan Mukhopadhyay, Stomatocyte-discocyte-echinocyte sequence of the human red blood cell, *PNAS* 99: 16766, 2002. A more recent treatment along these lines is Geekiyanage et al., A coarse-grained red blood cell membrane model to study stomatocyte-discocyte-echinocyte morphologies, *PLoS One* 14: e0215447, 2019.

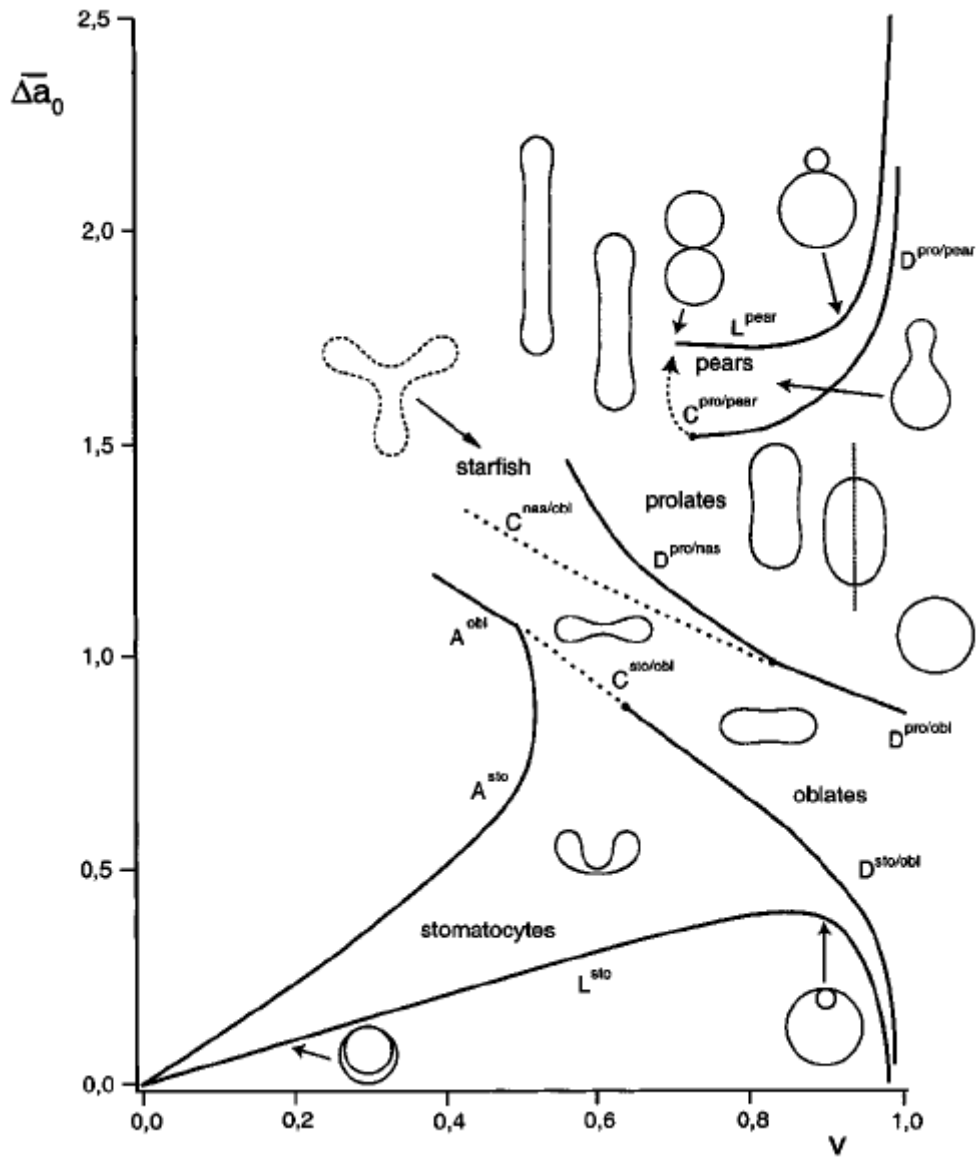


Figure 5.14: Two dimensional shape diagram from ADE model. For each region, minimal energy shapes are indicated. The horizontal axis is the reduced volume  $v$ ; spheres again correspond to  $v = 1$ . The vertical axis shows the effective differential area between inside and outside monolayers.

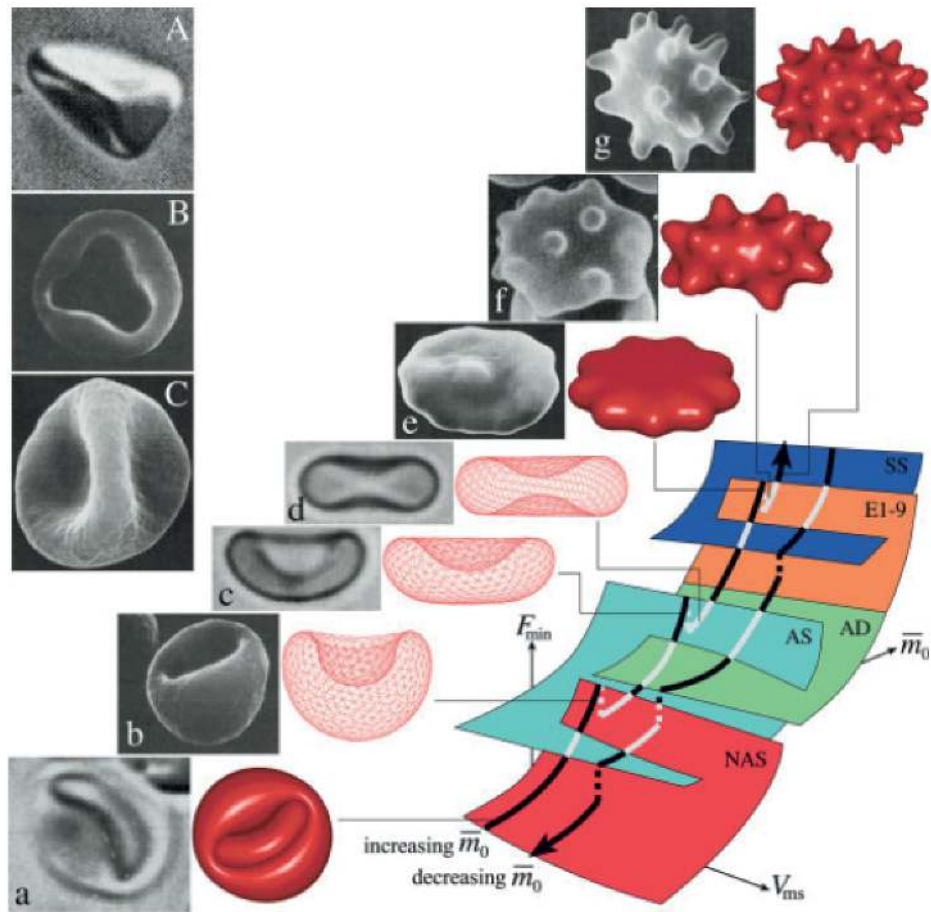


Figure 5.15: Shape of red blood cells: comparison of experimentally observed and computationally predicted shapes and their transitions. From the review by Gerald Lim and colleagues.

therefore of oxygen in our body. During their 120 days lifetime, they travel  $10^5$  times through our circulation (each round trip takes 100 s) before they are sorted out because they become stiffer. There are around  $2.6 \cdot 10^{13}$  RBCs in our body (out of  $3.1 \cdot 10^{13}$  all together), making them the most abundant cell type<sup>8</sup>. An amazing number of  $2 \cdot 10^6$  new ones are produced in every second in our bone marrow. A RBC has a diameter of  $8 \mu m$ , a thickness of  $2 \mu m$  at the rim and of  $1 \mu m$  at the middle of the biconcave disc. Its volume is  $100 \mu m^3$  and its area  $140 \mu m^2$ . This corresponds to a reduced volume of  $v = 0.642$ , in agreement with the range from the vesicle theory in which we expect discocytes.

Under physiological conditions, area and volume do not change much and therefore can be taken as constant for our mathematical treatment. For area, this results from the large area expansion modulus of  $K_A = 0.5 J/m^2$ . The corresponding energy is  $(K_A/2)\Delta A^2/A_0$  and if we equate this with the bending energy  $\kappa = 50 k_B T$  of RBCs, we get  $\Delta A/A_0 = 10^{-5}$ , thus area does not change significantly. In fact the membrane would rupture at one percent relative area dilation and the large area expansion modulus protects it from this.

Volume control is more complicated. It mainly arises from osmotic pressure arising from  $c_0 = 290 mM$  of osmotically active molecules inside the cell. This leads to an osmotic modulus  $K_V = RTc_0 = 7 \cdot 10^5 J/m^3$ . Equating the energy  $(K_V/2)\Delta V^2/V_0$  with the bending energy  $\kappa$ , we now get  $\Delta V/V_0 = 10^{-5}$ , thus volume is also constant for practical purposes.

The standard model for RBC-shape was established in the beautiful paper by Lim, Wortis and Mukhopadhyay in PNAS 2002. As shown in Fig. 5.16, the plasma membrane of the RBC is reinforced by a polymer network (made mainly from the intermediate filament spectrin) underlying it, thus forming a composite or sandwich structure. The overall thickness however is so small that the system can still be considered to be two-dimensional on the scale of the cell. Therefore the authors expanded the ADE-model for the membrane by an elastic energy for the polymer network. This elastic component is modeled as an isotropic hyperelastic material. Isotropy is justified by the hexagonal network structure, but linearity is not because the RBC is known to strain harden under the conditions in the blood flow. Similar to the derivation of the Helfrich Hamiltonian, we write the elastic Hamiltonian as a Taylor expansion, but this time not as a function of curvature, but as a function of the two in-plane strain invariants  $\alpha$  and  $\beta$ :

$$\mathcal{H} = \frac{K_\alpha}{2} \int dA \left( \alpha^2 + \alpha_3 \alpha^3 + \alpha_4 \alpha^4 \right) + \mu \int dA \left( \beta + b_1 \alpha \beta + b_2 \beta^2 \right) \quad (5.56)$$

where  $K_\alpha$  is the stretch modulus and  $\mu$  the shear modulus. The two strain invariants follow from the principal extension ratios  $\lambda_1$  and  $\lambda_2$  of a deformed ellipse as

$$\alpha = \lambda_1 \lambda_2 - 1, \quad \beta = \frac{1}{2} \left( \frac{\lambda_1}{\lambda_2} + \frac{\lambda_2}{\lambda_1} - 2 \right) \quad (5.57)$$

In contrast to the Hamiltonian for the lipid bilayer, one now also needs a reference shape to calculate the elastic energy. A computational procedure has been

---

<sup>8</sup>Compare the book by Ron Milo and Rob Phillips, Cell biology by the numbers, Garland Science 2016

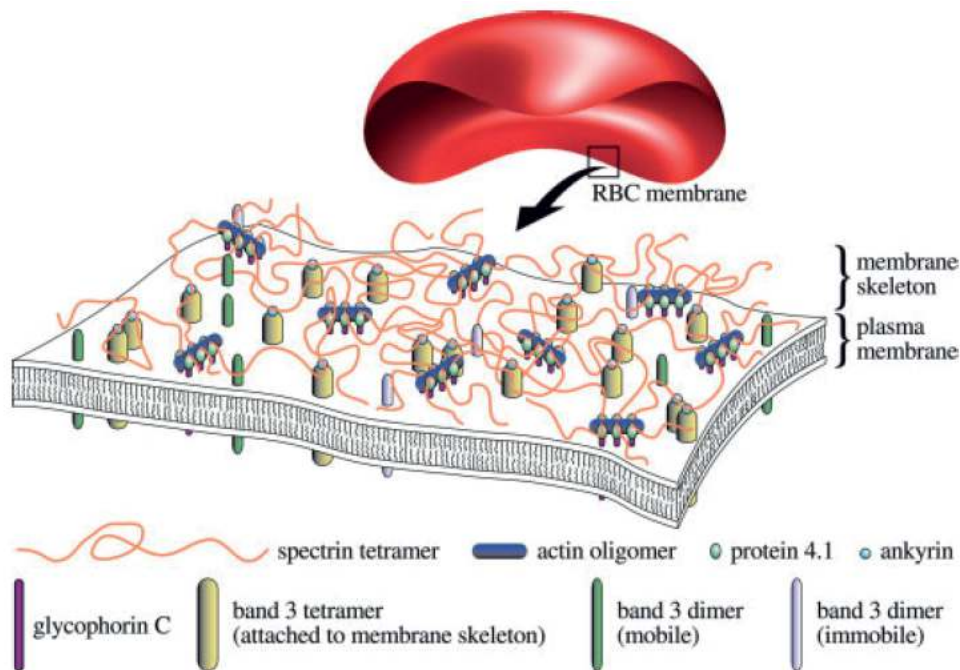


Figure 5.16: The shape of RBCs is determined by the nature of its composite membrane. While the outside layer is a lipid membrane with differential lipid composition in the two leaflets, the inside layer is a polymer network (made mainly from the polymer spectrin) that is attached to the membrane at discrete points (band 3 tetramer, band 4.1 protein). These anchor points form a hexagonal lattice and have a typical distance of 76 nm.

developed to estimate this shape (which is determined by microscopic defects and cannot be measured directly) and it has been found to be an oblate (not a sphere as used by earlier models). The final shape as shown in Fig. 5.15 is then calculated by minimization of triangulated shapes under the combined action of the ADE- and the elastic Hamiltonians. The excellent agreement with the experiments validate the theory. It is also in agreement with the famous 1974 bi-layer couple hypothesis by Sheetz and Singer who suggested that different agents lead to the same SDE-sequence because the main control parameter is membrane curvature. Finally the theory explains the origin of the echinocyte, which was missing from the Helfrich-type models: it corresponds to a membrane that wants to bud, but the budding is prevented by strong stretch in the spectrin network.

We finally can ask how RBC-shape changes as the cell is moving in shear flow, both at low and high density (in the blood of healthy persons, RBCs make up 45 percent of the volume, the so-called *hematocrit*). This requires hydrodynamic theories and has been studied recently with many different methods<sup>9</sup>. One finds that single RBCs assume parachute and slipper shapes, and that multiple RBCs

<sup>9</sup>An excellent review is given by Fedosov, Dmitry A., Hiroshi Noguchi, and Gerhard Gompper, Multiscale modeling of blood flow: from single cells to blood rheology, *Biomechanics and modeling in mechanobiology* 13.2 (2014): 239-258.

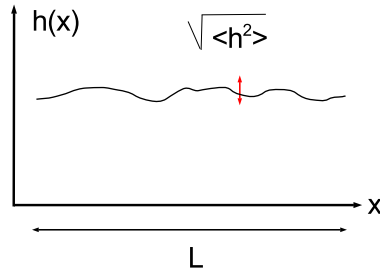


Figure 5.17: Fluctuating membrane of lateral length  $L$  and typical deviation from a flat membrane  $\sqrt{\langle h^2 \rangle}$

arrange in zig-zack-configurations, as observed experimentally. Interestingly, single RBCs at the wall are lifted up due to high Reynolds-number effects and due to their deformability. At physiological hematocrit, they all move as a plug in the middle of the capillary, leaving a cell-free-layer at the side that effectively lubricates the flow and thus makes it faster than expected for a Newtonian fluid (*Fahraeus effect*). Other cells like white blood cells, platelets, tumour or stem cells also circulating with the blood are expelled from the plug and tend to contact the wall (*margination*).

## 5.4 Membrane fluctuations

### 5.4.1 Thermal roughening of a flat membrane

In this section we will investigate the mean square deviation  $\langle h^2 \rangle$  of a flat lipid membrane fluctuating at temperature  $T$ , see figure 5.17. Its square root is a measure for the size of typical excursions. In lowest order, the energy functional for the almost flat membrane is (compare equations 5.26 and 5.27)

$$\mathcal{H}[h(x, y)] = 2\kappa \int dA H^2 = \frac{\kappa}{2} \int dx dy (\Delta h(x, y))^2$$

Calculating this correlation function is a standard problem in statistical field theory and we solve it using Fourier transforms. Because we have  $d = 2$  for membranes, we now use vector notation:

$$h(\vec{x}) = \frac{1}{(2\pi)^{d/2}} \int d\vec{k} h(\vec{k}) \exp(i\vec{k} \cdot \vec{x}) \quad (5.58)$$

$$h(\vec{k}) = \frac{1}{(2\pi)^{d/2}} \int d\vec{x} h(\vec{x}) \exp(-i\vec{k} \cdot \vec{x}) \quad (5.59)$$

$$\delta(k) = \frac{1}{(2\pi)^d} \int_{-\infty}^{\infty} d\vec{x} \exp(i\vec{k} \cdot \vec{x}) \quad (5.60)$$



$h(\vec{x})$  has to be real

$$\begin{aligned}
h(\vec{x}) &= \frac{1}{(2\pi)^{d/2}} \int d\vec{k} h(\vec{k}) \exp(i\vec{k} \cdot \vec{x}) \\
&= h(\vec{x})^* = \frac{1}{(2\pi)^{d/2}} \int d\vec{k} h(\vec{k})^* \exp(-i\vec{k} \cdot \vec{x}) \\
\Rightarrow h(\vec{k}) &= h(-\vec{k})^*
\end{aligned}$$

Now we write  $h(\vec{k})$  in real and imaginary part

$$\begin{aligned}
h(\vec{k}) &= a(\vec{k}) + i b(\vec{k}) \\
\Rightarrow a(\vec{k}) &= a(-\vec{k}) \\
b(\vec{k}) &= -b(-\vec{k})
\end{aligned}$$

The Hamiltonian can be calculated as

$$\begin{aligned}
\mathcal{H} &= \frac{\kappa}{2(2\pi)^d} \int d\vec{x} \left( \int d\vec{k} (ik)^2 h(\vec{k}) \exp(i\vec{k} \cdot \vec{x}) \right) \left( \int d\vec{k}' (ik')^2 h(\vec{k}') \exp(i\vec{k}' \cdot \vec{x}) \right) \\
&= \frac{\kappa}{2} \int d\vec{k} \int d\vec{k}' k^2 k'^2 \delta(\vec{k} + \vec{k}') h(\vec{k}) h(\vec{k}') \\
&= \frac{\kappa}{2} \int d\vec{k} k^4 h(\vec{k}) h(-\vec{k}) \\
&= \frac{\kappa}{2} \int d\vec{k} k^4 h(\vec{k}) h(\vec{k})^*
\end{aligned}$$

$$\boxed{\mathcal{H}[h(\vec{k})] = \kappa \int_{k>0} d\vec{k} k^4 [a^2(\vec{k}) + b^2(\vec{k})]} \quad (5.61)$$

The result is the same for  $k > 0$  and for  $k < 0$  and the case  $k = 0$  is irrelevant, because  $a(\vec{k}) = a(-\vec{k})$  and  $b(\vec{k}) = b(-\vec{k})$ . Therefore we restrict the integration to positive  $k$ , which gives a factor of 2. The bending energy is the sum of the squares of the decoupled amplitudes. The  $k^4$ -dependency is typical for bending.

The partition sum is a functional integral over all possible membrane conformations

$$\begin{aligned}
Z &= \int \mathcal{D}h \exp(-\beta \mathcal{H}[h(x)]) \\
&= \prod_{k>0} \int_{-\infty}^{\infty} da(\vec{k}) \int_{-\infty}^{\infty} db(\vec{k}) \exp(-\beta \kappa k^4 [a(\vec{k})^2 + b(\vec{k})^2]) \\
&= \prod_{k>0} \frac{k_B T}{\kappa k^4}
\end{aligned}$$

because this is simply a product of many Gauss integrals. For the free energy, we therefore get

$$F = -k_B T \ln Z = k_B T \int_{k>0} dk \ln \frac{\kappa k^4}{k_B T} \quad (5.62)$$

However, here we are interested in the correlation functions, not in  $Z$  or  $F$  directly. For each  $\vec{k}$ , there are two independent and harmonic degrees of freedom. We therefore have

$$\begin{aligned} \langle a^2(\vec{k}) \rangle &= \frac{k_B T}{2\kappa k^4} \\ \langle b^2(\vec{k}) \rangle &= \frac{k_B T}{2\kappa k^4} \\ \langle a(\vec{k})a(\vec{k}') \rangle & \underset{\vec{k} \neq \vec{k}', \vec{k} \neq -\vec{k}'}{=} \langle a(\vec{k}) \rangle \langle a(\vec{k}') \rangle = 0 \quad \text{etc.} \end{aligned}$$

which is an example of the equipartition theorem for harmonic systems. For  $h$  this means

$$\begin{aligned} \langle h(\vec{k})h(\vec{k}') \rangle &= \langle (a(\vec{k}) + ib(\vec{k})) (a(\vec{k}') + ib(\vec{k}')) \rangle \\ &= \langle a(\vec{k})a(\vec{k}') \rangle + i \langle a(\vec{k})b(\vec{k}') \rangle + i \langle b(\vec{k})a(\vec{k}') \rangle - \langle b(\vec{k})b(\vec{k}') \rangle \\ &= \langle a(\vec{k})a(\vec{k}') \rangle - \langle b(\vec{k})b(\vec{k}') \rangle \\ &= \begin{cases} 0 - 0 = 0 & \vec{k}' \neq \vec{k}, \vec{k}' \neq -\vec{k} \\ \langle a^2(\vec{k}) \rangle - \langle b^2(\vec{k}) \rangle = 0 & \vec{k}' = \vec{k} \\ \langle a^2(\vec{k}) \rangle + \langle b^2(\vec{k}) \rangle = \frac{k_B T}{\kappa k^4} & \vec{k}' = -\vec{k} \end{cases} \end{aligned} \quad (5.63)$$

where in the last line we have used  $b(-\vec{k}) = -b(\vec{k})$ . We now get in Fourier space:

$$\boxed{\langle h(\vec{k})h(\vec{k}') \rangle = \frac{k_B T}{\kappa k^4} \delta(\vec{k} + \vec{k}')} \quad (5.64)$$

For the backtransform to real space, we get

$$\begin{aligned} \langle h^2(\vec{x}) \rangle &= \left\langle \left( \frac{1}{(2\pi)^{d/2}} \int d\vec{k} h(\vec{k}) \exp(i\vec{k}\vec{x}) \right) \left( \frac{1}{(2\pi)^{d/2}} \int d\vec{k}' h(\vec{k}') \exp(i\vec{k}'\vec{x}) \right) \right\rangle \\ &= \frac{1}{(2\pi)^d} \int d\vec{k} \int d\vec{k}' \exp(i(\vec{k} + \vec{k}')\vec{x}) \frac{k_B T}{\kappa k^4} \delta(\vec{k} + \vec{k}') \end{aligned}$$

Now the space-dependance drops out due to the delta function (the underlying reason is translational invariance) and we are left with one integral only. If we define  $a$  as the microscopic cutoff (molecular size) and  $L$  as macroscopic cutoff (system size) and use  $d = 2$ , we get in polar coordinates:

$$\begin{aligned} \langle h^2(x, y) \rangle &= \frac{2\pi}{(2\pi)^2} \int_{\frac{2\pi}{L}}^{\frac{2\pi}{a}} k dk \frac{k_B T}{\kappa k^4} \\ &= \frac{2\pi}{(2\pi)^2} \frac{1}{2} \frac{k_B T}{\kappa} \left[ \left( \frac{L}{2\pi} \right)^2 - \left( \frac{a}{2\pi} \right)^2 \right] \\ &= \boxed{\frac{k_B T}{16\pi^3 \kappa} L^2} = \langle h^2 \rangle \end{aligned} \quad (5.65)$$

Equation 5.65 shows that the mean square deviation is proportional to temperature  $T$ , inversely proportional to bending rigidity  $\kappa$ , and increases quadratically with the system size  $L$ . Note that the limit  $a \rightarrow 0$  is unproblematic.

In order to better understand the fluctuations of membranes we can put in numbers:

$$\begin{aligned}\kappa &= 20k_B T \\ L &= 10 \text{ nm} \Rightarrow \sqrt{\langle h^2 \rangle} = 1 \text{ \AA} \\ L &= 1 \text{ cm} \Rightarrow \sqrt{\langle h^2 \rangle} = 100 \mu\text{m}\end{aligned}$$

Thus the effect is relatively weak on the scale of vesicles, but relatively strong on macroscopic scales. For a biomembrane fluctuations are relevant, but not on small scales.

It is instructive to compare this result to the one for interfaces under tension (e.g. oil droplets or soap bubbles). The we start from the Hamiltonian

$$\mathcal{H}[h(x, y)] = \frac{\sigma}{2} \int dx dy (\nabla h(x, y))^2$$

and therefore arrive at

$$\langle h(\vec{k})h(\vec{k}') \rangle = \frac{k_B T}{\sigma k^2} \delta(\vec{k} + \vec{k}') \quad (5.66)$$

The backtransform then gives

$$\langle h^2 \rangle = \frac{k_B T}{2\pi\sigma} \ln\left(\frac{L}{a}\right) \quad (5.67)$$

which is a much weaker dependance on  $L$  than for membranes. For  $\sigma = 100 \text{ erg/cm}^2$  and  $a = 3 \text{ \AA}$ , a system size of  $L = 10 \text{ nm}$  gives a mean deviation of  $1.5 \text{ \AA}$ . For  $L = 1 \text{ cm}$ , this goes up only to  $7.5 \text{ \AA}$ .

Another way to quantify membrane fluctuations is to investigate how much the membrane loses its orientation due to fluctuations. A measure for this is the persistence length  $L_p$ . Systems with characteristic length shorter than  $L_p$  can be considered as elastic planes or rods (for polymers). The properties of systems with characteristic length larger than  $L_p$  solutions can be described with statistical methods for random walks. Formally, the persistence length is defined as the length over which correlations in the direction of the normal are lost.

Let us again work in the Monge representation, see figure 5.18. The normal vector is

$$\begin{aligned}\vec{n} &= \frac{1}{\sqrt{\det g}} \begin{pmatrix} h_x \\ h_y \\ 1 \end{pmatrix}, \text{ with } \det g = 1 + (\nabla h)^2 \\ &= \frac{1}{\sqrt{1 + \partial_x h^2 + \partial_y h^2}} \begin{pmatrix} h_x \\ h_y \\ 1 \end{pmatrix}\end{aligned}$$

Let us define the angle between normal vectors at different points on the membrane as  $\theta$  and

$$\cos \theta \simeq 1 - \frac{\theta^2}{2} = n_z = \frac{1}{\sqrt{1 + \partial_x h^2 + \partial_y h^2}} \simeq 1 + \frac{1}{2} \underbrace{(\partial_x h^2 + \partial_y h^2)}_{=(\nabla h)^2}$$

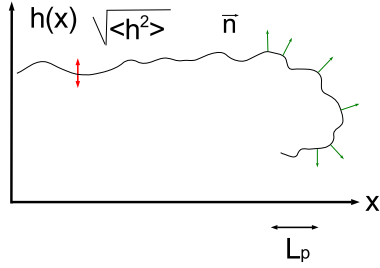


Figure 5.18: Persistent length  $L_p$  for fluctuating membrane, Monge representation.  $\vec{n}$  is the normal to the membrane vector.

This means that

$$\begin{aligned}
 \langle \theta^2 \rangle &= \underbrace{\langle (\vec{\nabla} h)^2 \rangle}_{\text{average over all possible h}} \\
 &= \frac{2\pi k_B T}{(2\pi)^2 \kappa} \int_{\frac{2\pi}{L_p}}^{\frac{2\pi}{a}} k dk \frac{k^2}{k^4} \\
 &= \frac{k_B T}{(2\pi) \kappa} \ln \left( \frac{L_p}{a} \right)
 \end{aligned}$$

If we now set  $\langle \theta^2 \rangle = \pi^2$  for the extreme case that orientation has turned around, we can define a length scale at which the membrane is not flat anymore:

$$\boxed{L_p = a \exp\left(2\pi^3 \frac{\kappa}{k_B T}\right)} \quad \text{Persistence length for membranes} \quad (5.68)$$

The persistence length for membranes was calculated by de Gennes and Taupin in 1982<sup>10</sup>.

For better illustration we look again at typical numbers. As already mentioned in this section, for biomembranes  $\kappa \simeq 20k_B T$ , which makes  $L_p \simeq a \cdot \exp(400)$ . Although membranes are only 4 nm thick, this thickness is sufficient to conserve their rigidity and flatness. Another example is the water-oil interface stabilized by tensides (substances, that reduce surface tension and allow easier dispersion), see figure 5.19. In this case  $\kappa \simeq 1 \cdot k_B T$ ,  $L_p$  is small and the interface is thermally roughened.

#### 5.4.2 Steric (Helfrich) interactions

In the chapter on interactions we have learned that entropic effects might lead to effective interactions, e.g. the attractive depletion interaction between large particles in a sea of small particles or the crystallization of hard spheres at high

<sup>10</sup>de Gennes P.-G. and Taupin C., J. Phys. Chem., 86 (1982) 2294.

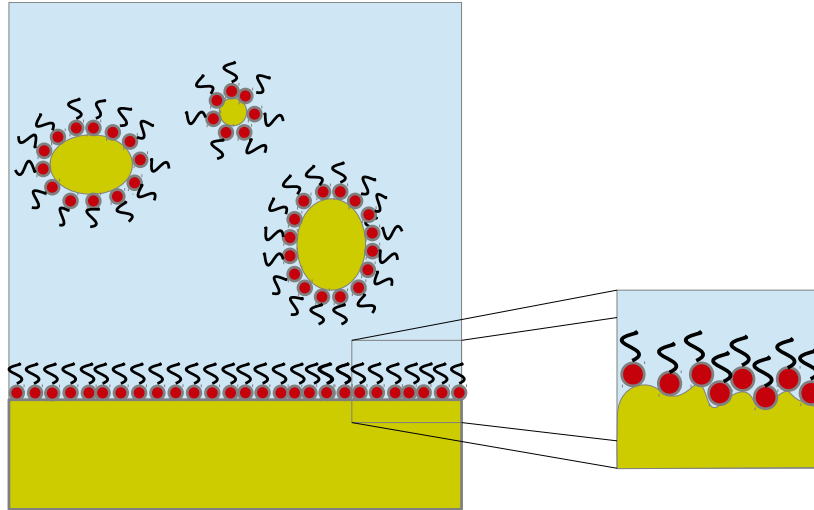


Figure 5.19: Surface interaction between oil and water mediated by surfactants. The surfactants, represented by red circles with black tails, are responsible for the dispersion of oil droplets into water. They reduce the surface tension, that is why the interface is rough.

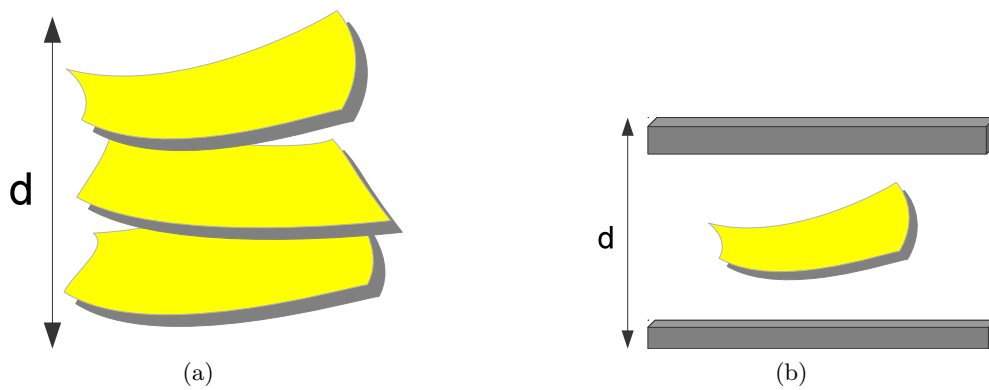


Figure 5.20: Steric interactions for a) stack of membranes and b) membrane trapped between two walls. Characteristic dimension is the distance  $d$  for both cases. The principal idea for the description of both cases is the same, but there are more degrees of freedom for the stack of membranes.

density. We now will see that entropic effects lead to an effective repulsion between membranes. Consider a stack of membranes or a single membrane trapped between two walls, see figure 5.20. We are interested in the free energy of the system, which in this case is a function of the distance  $d$  between the membranes or the membrane and the wall. We already can sense that this free energy increase with increasing  $d$  because the membrane will gain entropy if the confinement decreases.

### Scaling argument

The membrane has “humps” of size  $h^2 \sim \frac{k_B T}{\kappa} \cdot L_p^2$  as calculated above. For each hump, the membrane loses entropy per area  $\frac{k_B}{L_p^2}$  and the bending energy per area for a hump is  $\kappa \left(\frac{h}{L_p}\right)^2$ . From this argument we can conclude, that the free energy per area is

$$\frac{\Delta F}{A} \sim \kappa \left(\frac{h}{L_p}\right)^2 - T \left(\frac{-k_B}{L_p^2}\right) \sim \frac{(k_B T)^2}{\kappa} \cdot \frac{1}{h^2}$$

For a membrane in a stack or between two walls,  $h$  scales like  $d$  and therefore we get the fluctuation or Helfrich interaction<sup>11</sup>:

$$\boxed{\frac{\Delta F}{A} \sim \frac{(k_B T)^2}{\kappa} \cdot \frac{1}{h^2}} \quad \text{Helfrich 1978}$$

Although this argument involves bending energy, this too arises from thermal fluctuations. Therefore the whole effect is a thermal one and vanishes with  $T \rightarrow 0$ .

### More rigorous treatment

An exact solution is not known, but a reasonable calculation starts with the confinement effect modeled by a harmonic potential<sup>12</sup>. Thus we consider the mean squared deviation in the Monge representation for an almost flat membrane that fluctuates under a harmonic potential:

$$\mathcal{H} = \frac{\kappa}{2} \int dx dy \left\{ (\Delta h)^2 + \frac{1}{\xi^4} h^2 \right\} = \frac{1}{2} \int dx dy \left\{ \kappa (\Delta h)^2 + \gamma h^2 \right\}$$

where  $\xi$  is called the confinement length and  $\gamma$  the confinement parameter. We transform the problem into Fourier space:

$$\begin{aligned} \langle h^2 \rangle &= \frac{1}{(2\pi)^2} 2\pi \int dk k \frac{k_B T}{\kappa(k^4 + \xi^{-4})} \\ &= \frac{k_B T}{8\kappa} \cdot \xi^2 = \frac{k_B T}{8\sqrt{\kappa\gamma}} \end{aligned}$$

<sup>11</sup>Helfrich, W. Steric interaction of fluid membranes in multilayer systems. Z. Naturforsch 33 (1978): 305-315.

<sup>12</sup>Janke, W., and H. Kleinert. Fluctuation pressure of membrane between walls. Physics Letters A 117.7 (1986): 353-357.

We now assume a simple geometrical scaling of the excursion with the confinement,  $\langle h^2 \rangle = \mu d^2$ . Here  $\mu$  is a constant prefactor, that has been found in Monte-Carlo computer simulations to be  $\mu = \frac{1}{6}$ . Combining the two expressions for  $\langle h^2 \rangle$ , we can solve for  $\xi$  as a function of  $d$ . Because we have a harmonic (Gaussian) system, for the free energy difference between the confined and the free membrane we get (compare the introduction, free energy of a harmonic system)

$$\begin{aligned} \frac{\Delta F}{A} &= -k_B T \cdot \ln Z \\ &= \frac{k_B T}{(2\pi)^2} 2\pi \int k dk \ln \left( \frac{k^4 + \xi^{-4}}{k^4} \right) \\ &= \frac{k_B T}{8} \cdot \xi^{-2} \end{aligned}$$

From this follows:

$$\boxed{\frac{\Delta F}{A} = \frac{(k_B T)^2}{64\kappa\mu d^2}} \quad \text{Steric interaction between membranes}$$

This is the same result as from the scaling analysis, but now with exact prefactors. This result has been confirmed both with computer simulations and in experiments.

If we repeat the same analysis for the case of surface tension, we have for the squared mean displacement

$$\langle h^2 \rangle = \frac{1}{(2\pi)^2} 2\pi \int dk k \frac{k_B T}{\sigma k^2 + \gamma} \quad (5.69)$$

Now the integral is not  $(1/2) \arctan(k^2)$ , but  $(1/2) \ln(1 + k^2)$ , thus it diverges for large  $k$  and we have to use a microscopic cutoff. If we combine both surface tension and bending rigidity, however, we get a well-defined result again.

### 5.4.3 Flickering spectroscopy for red blood cells

RBCs are continuously fluctuating (*flickering*), as can be observed and measured with an optical microscope. There are two ways to analyze such data. First one can assume that one observes the fluctuations of the membrane as it is constrained by the spectrin network. Then the relevant Hamiltonian would be<sup>13</sup>

$$\mathcal{H}[h(x, y)] = \int dx dy \left\{ \frac{\sigma}{2} (\nabla h(x, y))^2 + \frac{\kappa}{2} (\Delta h(x, y))^2 + \frac{\gamma}{2} h(x, y)^2 \right\}$$

where  $\gamma$  is a confinement parameter. In Fourier space we then have

$$\langle h(\vec{k}) h(\vec{k}') \rangle = \frac{k_B T}{\sigma k^2 + \kappa k^4 + \gamma} \delta(\vec{k} + \vec{k}') \quad (5.70)$$

<sup>13</sup>Nir S Gov and Sam A Safran, Red blood cell membrane fluctuations and shape controlled by ATP-induced cytoskeletal defects, Biophysical journal 88.3 (2005): 1859-1874.

This procedure has been applied successfully to RBCs under various conditions and it has been found that shape is the main determinant of the fluctuations<sup>14</sup>. We note that assuming an almost flat membrane is a strong assumption and that a more rigorous analysis had to consider also the role of curvature.

Alternatively, one can assume that the whole shell is one composite and fluctuates as such, as we have assumed above to derive the minimal energy shape. Then one has to work with thin shell elasticity and the results are much more complicated. In this way, it has been shown that at low and high frequencies, the fluctuations are dominated by active and passive fluctuations<sup>15</sup>. Active fluctuations depend on ATP and arise e.g. from the actin-spectrin network or ion pumps and channels.

---

<sup>14</sup>Yoon, Young-Zoon, et al., Flickering analysis of erythrocyte mechanical properties: dependence on oxygenation level, cell shape, and hydration level, *Biophysical journal* 97.6 (2009): 1606-1615.

<sup>15</sup>Turlier, Herve, et al., Equilibrium physics breakdown reveals the active nature of red blood cell membrane fluctuations, *Nat. Phys.* (2016). There are two excellent reviews on this subject: Turlier, Herve, and Timo Betz, *Fluctuations in active membranes*, *Physics of Biological Membranes*, Springer 2018. 581-619, and Turlier, Herve, and Timo Betz, *Unveiling the Active Nature of Living-Membrane Fluctuations and Mechanics*, *Annual Review of Condensed Matter Physics* 10 (2019): 213-232.



## Chapter 6

# Physics of polymers

Polymers are chain molecules that can be described as space curves in three dimensions  $\vec{r}(s)$  using the language and tools of differential geometry as introduced in the membrane chapter. Motivated by the phenomenological approach to membranes, we could start in a continuum framework with a bending Hamiltonian:

$$\mathcal{H}[\vec{r}(s)] = \frac{\kappa_p}{2} \int_0^L ds \left( \frac{d^2 \vec{r}(s)}{ds^2} \right)^2 \quad (6.1)$$

where  $\kappa_p = k_B T l_p$  is a bending rigidity for polymers and  $l_p$  is the persistence length. This Hamiltonian describes a *semi-flexible polymer* (also called *worm-like chain* (WLC) or *Kratky-Porod model*). Below we will derive it as a limit of the freely rotating chain (FRC) model. In biophysics, this is the most relevant polymer model as many biofilaments (actin, collagen, cellulose, etc) are semi-flexible.

In contrast to membranes, however, this bending Hamiltonian is just one out of several important models. Due to the variety of different types of polymers, their microscopic physics is richer. Note that biomembranes assemble due to the hydrophobic effect and form large structure whose mechanics does not depend on the molecular details of the lipids, while polymers are formed by covalent bonds between monomers who are strongly exposed to the environment. As we will see below, there is actually a simpler phenomenological model for polymers than the WLC:

$$\mathcal{H}[\vec{r}(s)] = \frac{3k_B T}{2b} \int_0^L ds \left( \frac{d\vec{r}(s)}{ds} \right)^2 \quad (6.2)$$

where  $b$  is the Kuhn length (effective monomer length) of the polymer. This *Gaussian chain* (GC) model is the continuum limit of the freely jointed chain (FJC) model which is purely entropic in nature. This polymer model is appropriate for many synthetic polymers like for example polyethylene. In this chapter we will discuss both cases (WLC versus GC) as the two most important classes of polymer models<sup>1</sup>.

---

<sup>1</sup>The two standard textbooks on polymer physics are M Doi and SF Edwards, *The theory of*

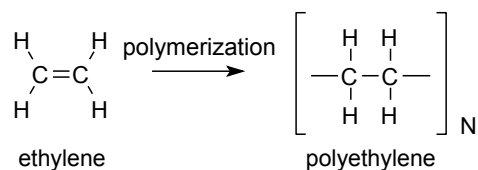


Figure 6.1: Polymerization of ethylene. Polyethylene (PE) is made by opening the double bond between the carbon atoms in ethylene, flipping it over and thus connecting to the next ethylene monomer. The subscript  $N$  is the degree of polymerization.

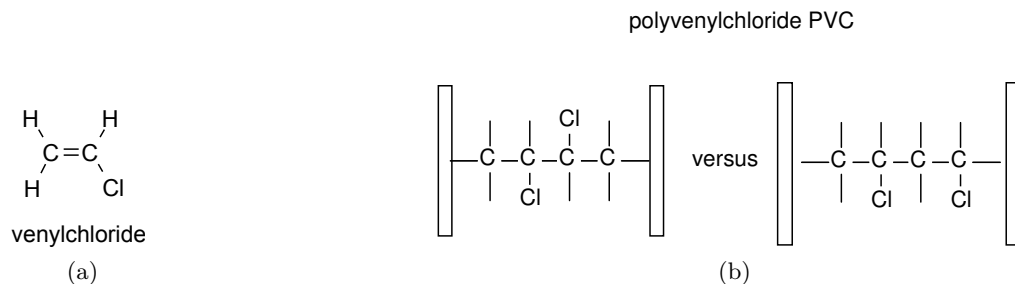


Figure 6.2: Isomers of polyvinylchloride (PVC)

## 6.1 General introduction to polymers

Polymers are made by binding monomers together in a process called polymerization, see figure 6.1. The number of monomers  $N$ , is called degree of polymerization. A typical value for synthetic polymers is  $N = 10^5$ , but it can go up to  $N = 10^{10}$  monomers.

Often monomers can be bonded together in different ways (“isomerism”). Isomers are molecules with the same chemical composition, but different space configuration, see figure 6.2, and hence have different physical properties. Therefore, microscopic interactions are vital for the configurations of polymers. This is true both for the conformation of single chains and for the interactions of different chains.

The study of polymer physics started in the 1920s (mainly through the work of Hermann Staudinger at Freiburg, who was awarded the Nobel prize for chemistry in 1953), when people realized that polymers are chain molecules that can be build up of only one type of monomers (homopolymers) or of different monomers (heteropolymers), see table 6.1.

Polymers can have different architectures, see table 6.2. This affects many of the physical properties of the polymers, including their size and their interaction, e.g. their ability to slide on top of one another.

If the polymers in a melt are connected by crosslinks one gets a “polymer network”. These polymer networks are elastic solids with shape memory, see figure 6.3. Therefore, we can define an elasticity modulus for this polymer gel. To first

---

*polymer dynamics*, Oxford University Press 1986 and Michael Rubinstein and Ralph H. Colby, *Polymer physics*, Oxford University Press 2003.

Type of polymer	Sketch	Example
homopolymer	-A-A-...-A-	Homopolymers are mostly synthetic polymers, e.g. PE
heteropolymer	-A-B-A-C-...-	DNA, which has 4 different monomers Proteins, which have 20 different monomers
diblock-copolymer	-A-...-A-B-...-B-	Those are heteropolymers with two blocks, each build up of a different monomer. This structure is similar to lipids.

Table 6.1: Different types polymers, separation on type of building blocks.


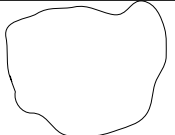
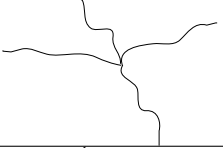

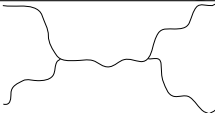

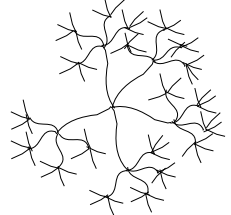
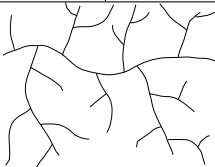
Type of polymer	Sketch	Remarks
linear polymer		
ring polymer		1D analog to vesicles
star polymer		For the description of star polymers one needs to know the number of arms and the length of each one of them In the case of $N \rightarrow 0$ , it becomes a soft sphere.
comb polymer		Can be compared with polymer brushes, which have immobile backbones.
H-polymer		
ladder polymer		
dendrimer		To form a dendrimer you start with a given number of branches, then after a certain length from the end point of each branch evolve the same number of branches and so on. This is a self controlling shape, because after a certain number of branches the system becomes too dense, and the growth stops.
branched polymer		This structure is typical for sugars.

Table 6.2: Polymer architectures.

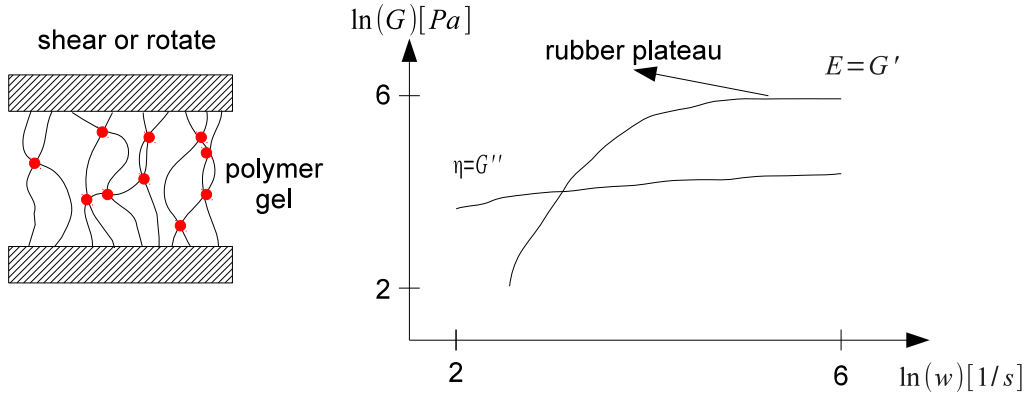


Figure 6.3: The elastic properties of polymer gels can be studied by putting them between two walls and then rotating or shearing those walls against each other. The typical mechanical behaviour of the polymer network is depicted on the right side. The logarithm of the elastic moduli is shown as a function of the logarithm of the frequency  $w$ . At low frequencies the material is viscous, but it becomes elastic at high frequencies.

approximation the Young's modulus is

$$E = \frac{k_B T}{\xi^3} \quad (6.3)$$

where  $\xi$  is the meshsize of the network. The most common examples of permanently cross-linked polymer networks are rubber (e.g. vulcanized natural rubber, polyisoprene) and silicone elastomers (e.g. polydimethylsiloxane, PDMS).

If the crosslinks are not permanent, which is usually the case in biological polymer networks, they will flow like a fluid on a long time scale. The theory of flowing systems is called rheology. A hydrogel is a polymer network in water. In order to investigate the elastic properties of a hydrogel, we have to put the gel between two plates and then rotate or shear them (in conical or parallel plate rheometers, respectively), see figure 6.3. The prime examples for biological hydrogels are cytoskeleton and extracellular matrix, giving structural stability to cells and tissues, respectively.

## 6.2 Basic models for polymers

### 6.2.1 Freely jointed chain (FJC)

This is the simplest microscopic model for a polymer. It considers  $N$  segments or links,  $\vec{r}_i$ , each representing a monomer with a constant length  $a$ :

$$\begin{aligned} \vec{r}_i &= \vec{R}_i - \vec{R}_{i-1} \\ |\vec{r}_i| &= a \end{aligned}$$

The  $\vec{R}_i$  are the position vectors for the nodes of the chain.  $\vec{R}$  is the end-to-end vector, giving a characteristic dimension of the polymer, see figure 6.4. As each

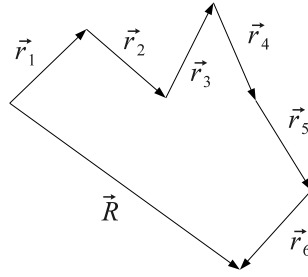


Figure 6.4: Freely jointed chain FJC model for polymers. A short polymer is schematically depicted, as a chain consisting of segments  $\vec{r}_i$ , represented as vectors. All segments have the same length  $a$ .  $\vec{R}$  is the end-to-end vector.

link points in a random direction, we have

$$\langle R \rangle = \sum_{i=1}^N \langle \vec{r}_i \rangle = 0 .$$

In analogy to the mean squared deviation  $\langle h^2 \rangle$  for membranes, we look at the mean squared end-to-end distance

$$\begin{aligned} \langle R^2 \rangle &= \left\langle \left( \sum_i \vec{r}_i \right) \cdot \left( \sum_j \vec{r}_j \right) \right\rangle \\ &= \sum_{i=1}^N \underbrace{\langle \vec{r}_i^2 \rangle}_{=a^2} + \sum_{i \neq j} \underbrace{\langle \vec{r}_i \cdot \vec{r}_j \rangle}_{=0} = Na^2 \end{aligned} \quad (6.4)$$

$$\boxed{R = \sqrt{Na}} \quad \text{typical extension of polymer chain} \quad (6.5)$$

The square root relation is typical for a random walk. We introduce time  $t = N\tau$  (with stepping time  $\tau$ ) and get

$$\langle R^2 \rangle = 2dDt$$

with  $D = a^2/2\tau$  the diffusion constant and  $d$  spatial dimension. In fact our polymer model is exactly the prescription of how to implement a random walk.

In a real polymer there are correlations between the different bond vectors,  $\langle \vec{r}_i \cdot \vec{r}_j \rangle \neq 0$  even for  $i \neq j$ . However, in most cases, the polymer becomes “ideal” in the sense that there are no correlations between monomers at large distance along the chain,  $\langle \vec{r}_i \cdot \vec{r}_j \rangle = 0$  for  $|i - j| \rightarrow \infty$ . Therefore the sum over these

Ideal polymer	$C_\infty$	$b[\text{\AA}]$
polyethylen $-CH_2CH_2-$	7.4	14
polybutadiene $-CH_2CH=CHCH_2-$	5.3	9.6
polyisoprene (rubber) $-CH_2CH=CHCHCH_3-$	4.6	8.2
polydimethylsiloxane (elastomere) $-OSi(CH_3)_2-$	6.8	13

Table 6.3: Flory's characteristic ratio and Kuhn lengths for different polymers

correlations converges to a finite value:

$$\begin{aligned}
\langle R^2 \rangle &= a^2 \sum_{i=1}^N \sum_{j=1}^N \langle \cos \theta_{ij} \rangle \\
&= a^2 \sum_{i=1}^N C_i \\
&= a^2 N \underbrace{\frac{1}{N} \sum_{i=1}^N C_i}_{=: C_N} \\
&= C_N N a^2 \xrightarrow{N \rightarrow \infty} C_\infty N a^2
\end{aligned} \tag{6.6}$$

with  $C_\infty = C_i \forall i$  with  $1 \leq C_\infty < \infty$ .  $C_\infty$  is called "Flory's characteristic ratio", see table 6.3.

Ideal polymers correspond to a FJC with redefined monomer length  $b$  and degree of polymerization  $N$ :

$$L = N \cdot b, \quad \langle R^2 \rangle = N \cdot b^2 = b \cdot L$$

$$\boxed{
\begin{aligned}
b &= \frac{\langle R^2 \rangle}{L} \\
N &= \frac{\langle R^2 \rangle}{b^2} = \frac{L^2}{\langle R^2 \rangle}
\end{aligned}
} \quad \text{Kuhn length} \tag{6.7}$$

The Kuhn length is a measure for the statistical segment length and tabulated in table 6.3.

### 6.2.2 Freely rotating chain (FRC)

We now fix not only the monomer size  $a$ , but also the bond angle  $\theta$ , see figure 6.5. The degree of freedom that is left is the torsion angle  $\phi$ , which keeps our polymer flexible. For polyethylene,  $a = 1.54 \text{\AA}$  and  $\theta = 68^\circ$ . Only the component along the bond vectors is transmitted down the chain. For each bond only a component  $\cos \theta$  remains:

$$\langle \vec{r}_i \cdot \vec{r}_j \rangle = a^2 (\cos \theta)^{|j-i|}$$

Because  $\cos \theta < 1$ , the series decays exponentially:

$$(\cos \theta)^{|j-i|} = e^{|j-i| \ln(\cos \theta)} = e^{-\frac{|j-i|a}{l_p}} \tag{6.8}$$

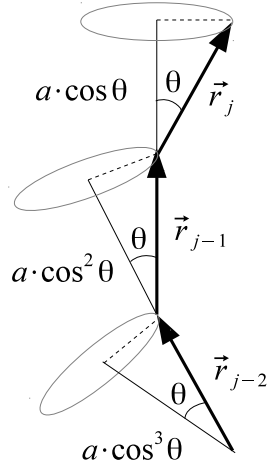


Figure 6.5: Schema of the freely rotating chain model (FRC). Here the length  $a$  and the bond angle  $\theta$ , between the segments, are kept constant. The torsion angle  $\phi$  is still free and makes the FRC flexible.

Here  $l_p$  is the persistence length:

$$l_p = -\frac{a}{\ln(\cos \theta)} \quad (6.9)$$

The persistence length has the same meaning as in membrane physics, it denotes the length scale over which the correlations decay.

We now can use this exponential decay to calculate the mean squared end-to-end distance:

$$\langle R^2 \rangle = \sum_{i=1}^N \sum_{j=1}^N \langle \vec{r}_i \cdot \vec{r}_j \rangle \quad (6.10)$$

$$= \sum_{i=1}^N \left( \sum_{j=1}^{i-1} \langle \vec{r}_i \cdot \vec{r}_j \rangle + \langle \vec{r}_i \rangle^2 + \sum_{j=i+1}^N \langle \vec{r}_i \cdot \vec{r}_j \rangle \right) \quad (6.11)$$

$$= a^2 N + a^2 \sum_{i=1}^N \left( \sum_{j=1}^{i-1} (\cos \theta)^{i-j} + \sum_{j=i+1}^N (\cos \theta)^{j-i} \right) \quad (6.12)$$

$$= a^2 N + a^2 \sum_{i=1}^N \left( \sum_{k=1}^{i-1} (\cos \theta)^k + \sum_{k=1}^{N-i} (\cos \theta)^k \right) \quad (6.13)$$

The two sums can be extended to infinity because at large distances, the correlation has decayed. We then simply have a geometrical series:

$$\sum_{k=1}^{\infty} (\cos \theta)^k = \frac{\cos \theta}{1 - \cos \theta}$$

Therefore

$$\langle R^2 \rangle = a^2 N + 2a^2 N \frac{\cos \theta}{1 - \cos \theta} \quad (6.14)$$

such that the final result reads

$$\boxed{\langle R^2 \rangle = Na^2 \frac{1+\cos\theta}{1-\cos\theta}} \quad \begin{array}{l} \text{mean square} \\ \text{end-to-end distance} \\ \text{for freely rotating chain} \end{array} \quad (6.15)$$

If we compare this result with equation 6.6, we see that  $C_\infty = \frac{1+\cos\theta}{1-\cos\theta}$ . The values for  $C_\infty$  are typically between 5 and 8, see table 6.3.

### 6.2.3 Worm-like chain (WLC)

In the limit of  $\theta \rightarrow 0$ , the chain becomes very stiff and rod-like:

$$\begin{aligned} \cos\theta &\approx 1 - \frac{\theta^2}{2} \\ \ln \cos\theta &\approx -\frac{\theta^2}{2} \end{aligned}$$

That means, that the persistence length  $l_p$  and Flory's characteristic ratio  $C_\infty$  both diverge:

$$l_p = \frac{2a}{\theta^2}, C_\infty = \frac{2 - \frac{\theta^2}{2}}{\frac{\theta^2}{2}} \approx \frac{4}{\theta^2} \quad (6.16)$$

The WLC model as shown in figure 6.6 is defined in the limit  $\theta \rightarrow 0$  and  $a \rightarrow 0$  such that  $l_p = \frac{2a}{\theta^2} = \text{const}$ . Then also the Kuhn length will be finite and simply twice as large as the persistence length:

$$b = \frac{\langle R^2 \rangle}{L} = \frac{C_\infty Na^2}{Na} = \frac{4a}{\theta^2} = 2l_p \quad (6.17)$$

For example a double stranded DNA (dsDNA) has persistence length  $l_p = 50$  nm and Kuhn length  $b = 100$  nm.

The mean-square end-to-end distance of the WLC can be evaluated using the exponential decay of correlations between tangent vector along the chain:

$$\begin{aligned} \langle R^2 \rangle &= a^2 \sum_{i=1}^N \sum_{j=1}^N (\cos\theta)^{|j-i|} \\ &= a^2 \sum_j \sum_i e^{-|j-i|a/l_p} \end{aligned}$$

In the continuum limit we get

$$\begin{aligned} \langle R^2 \rangle &= \int_0^L du \int_0^L dv e^{-|u-v|/l_p} \\ &= \int_0^L du \int_0^u dv e^{-(u-v)/l_p} + \int_0^L du \int_u^L dv e^{-(v-u)/l_p} \\ &= 2l_p L - 2l_p^2 (1 - e^{-L/l_p}) \end{aligned} \quad (6.18)$$

$$\boxed{\langle R^2 \rangle = 2l_p L - 2l_p^2 (1 - e^{-L/l_p})} \quad (6.19)$$

Looking at equation 6.19 we can distinguish two limiting cases:



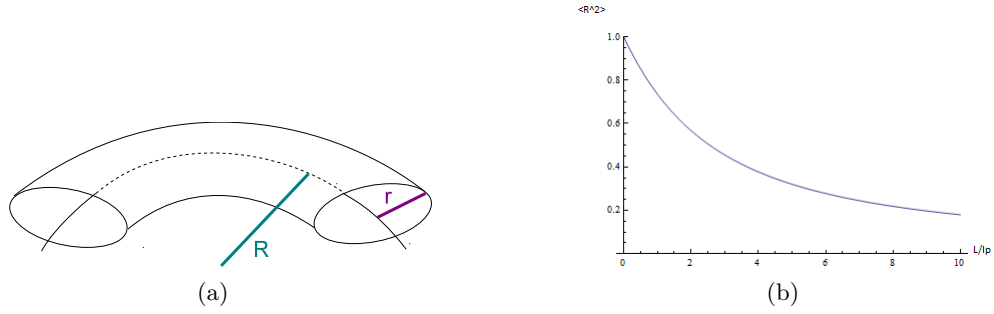


Figure 6.6: a.) The worm-like chain model describes an elastic rod. This polymer model is similar to the Helfrich Hamiltonian for membranes. b.) The dependency of the mean squared end-to-end distance on the ratio of the contour and persistence lengths of a polymer in the WLC model.

1.  $L \gg l_p$  so we can neglect the exponential term and get a flexible polymer with

$$\langle R^2 \rangle = 2l_p L = bL = b^2 N \ll L^2 \quad (6.20)$$

2.  $L \ll l_p$  now the exponential term becomes important and we make a Taylor expansion. Then we get a rigid chain with

$$\langle R^2 \rangle = 2l_p L - 2l_p^2 \left( 1 - 1 + \frac{L}{l_p} - \frac{1}{2} \left( \frac{L}{l_p} \right)^2 \right) = L^2 \quad (6.21)$$

The general expression is a smooth crossover between the two, see figure 6.6b:

$$\frac{\langle R^2 \rangle}{L^2} = \frac{2}{x} - \frac{2}{x^2} (1 - e^{-x})$$

with  $x = L/l_p$ . This defines three different regimes: the flexible chain at  $x \gg 1$ , the semiflexible chain with  $x \approx 1$ , and the rigid polymer with  $x \ll 1$ . Biological examples are DNA, actin and microtubules.

#### 6.2.4 Radius of gyration

The mean squared end-to-end distance  $\langle R^2 \rangle$  gives a measure for the extension of the polymer, but it is very hard to measure it directly and what one usually measures in experiments is the *radius of gyration* (e.g. with light scattering or size-exclusion chromatography). We now clarify the relation between the two. Assumed the monomer mass is constant, for the center of mass we have:

$$\vec{R}_{cm} = \frac{1}{N} \sum_{i=1}^N \vec{R}_i$$

Now we will calculate the mean squared radius of gyration  $\langle R_g^2 \rangle$ :

$$\begin{aligned}
R_g^2 &= \frac{1}{N} \sum_{i=1}^N (\vec{R}_i - \vec{R}_{cm})^2 \\
&= \frac{1}{N} \sum_{i=1}^N (\vec{R}_i^2 - 2\vec{R}_i \vec{R}_{cm} + \vec{R}_{cm}^2) \\
&= \frac{1}{N} \sum_{i=1}^N \vec{R}_i^2 \underbrace{\left( \frac{1}{N} \sum_{j=1}^N \right)}_{=1} - \frac{1}{N} \sum_{i=1}^N 2\vec{R}_i \frac{1}{N} \sum_{j=1}^N \vec{R}_j \\
&\quad + \left( \frac{1}{N} \sum_{i=1}^N \vec{R}_i \right) \left( \frac{1}{N} \sum_{j=1}^N \vec{R}_j \right) \\
&= \frac{1}{N^2} \sum_i \sum_j (\vec{R}_i^2 - \underbrace{2\vec{R}_i \vec{R}_j}_{=-\vec{R}_i \vec{R}_j} + \vec{R}_i \vec{R}_j) \tag{6.22}
\end{aligned}$$

This expression does not depend on the choice of summation indices and we rewrite it in a symmetric form:

$$\begin{aligned}
R_g^2 &= \frac{1}{N^2} \frac{1}{2} \left[ \sum_i \sum_j (\vec{R}_i^2 - \vec{R}_i \vec{R}_j) + \sum_j \sum_i (\vec{R}_j^2 - \vec{R}_j \vec{R}_i) \right] \\
&= \frac{1}{2N^2} \sum_i \sum_j (\vec{R}_i^2 - 2\vec{R}_i \vec{R}_j + \vec{R}_j^2) \\
&= \frac{1}{2N^2} \sum_i \sum_j (\vec{R}_i - \vec{R}_j)^2 \\
&= \frac{1}{N^2} \sum_{i=1}^N \sum_{j=i}^N (\vec{R}_i - \vec{R}_j)^2 \\
\boxed{\langle R_g^2 \rangle} &= \frac{1}{N^2} \sum_{i=1}^N \sum_{j=i}^N \langle (\vec{R}_i - \vec{R}_j)^2 \rangle \tag{6.23}
\end{aligned}$$

The radius of gyration can be expressed in terms of the average square distance between all pairs of monomers.

For an ideal polymer chain, the sums can be changed into contour integrals:

$$\langle R_g^2 \rangle = \frac{1}{N^2} \int_0^N du \int_u^N dv \langle (\vec{R}(u) - \vec{R}(v))^2 \rangle$$

We now use the fact that the contour between  $u$  and  $v$  should behave also like a (shorter) ideal chain, see figure 6.7:

$$\langle (\vec{R}(u) - \vec{R}(v))^2 \rangle = (v - u)b^2$$

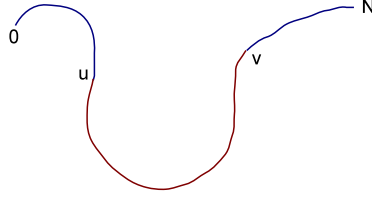


Figure 6.7: Integration along the ideal polymer. Assumption that the contour between  $u$  and  $v$  also behave like an ideal chain.

with  $v \geq u$ , Kuhn length  $b$  and independent of the outer segments:

$$\begin{aligned}
\langle R_g^2 \rangle &= \frac{b^2}{N^2} \int_0^N du \int_u^N dv (v - u) \\
&\stackrel{v-u=v'}{=} \frac{b^2}{N^2} \int_0^N du \int_0^{N-u} dv' v' \\
&= \frac{b^2}{N^2} \int_0^N du \frac{1}{2} (N - u)^2 \\
&\stackrel{N-u=u'}{=} \frac{b^2}{2N^2} \int_0^N du' u'^2 = \frac{Nb^2}{6} \tag{6.24}
\end{aligned}$$

$$\boxed{\langle R_g^2 \rangle = \frac{\langle R^2 \rangle}{6}} \quad \text{Debye result} \tag{6.25}$$

This is a very important result. It means that for an ideal chain we can work both with  $\langle R^2 \rangle$  or  $\langle R_g^2 \rangle$ , they are essentially the same, except for a constant factor of 6.

### 6.2.5 Gaussian Chain model (GCM)

Until now we have calculated  $\langle R^2 \rangle$  and  $\langle R_g^2 \rangle$  as measures for the **average** spatial extension of a polymer. We now calculate the full distribution  $p(\vec{R})$  for the end-to-end distance of the FJC. We start from the probability distribution for the segments:

$$p(\vec{r}_1, \dots, \vec{r}_N) = \prod_{i=1}^N \frac{1}{4\pi a^2} \delta(|\vec{r}_i| - a) \tag{6.26}$$

In the FJC, the segments have fixed length  $a$ , but free orientation. We then have:

$$\begin{aligned}
1 &= \prod_{i=1}^N \int d\vec{r}_i p(\vec{r}_1, \dots, \vec{r}_N) \\
p(\vec{R}) &= \prod_{i=1}^N \int d\vec{r}_i p(\vec{r}_1, \dots, \vec{r}_N) \delta(\vec{R} - \sum_{i=1}^N \vec{r}_i) \tag{6.27}
\end{aligned}$$

with

$$\delta(\vec{R} - \sum_{i=1}^N \vec{r}_i) = \frac{1}{(2\pi)^3} \int d\vec{k} e^{i\vec{k}(\vec{R} - \sum \vec{r}_i)}$$

We therefore obtain

$$p(\vec{R}) = \frac{1}{(2\pi)^3} \int d\vec{k} e^{i\vec{k}\vec{R}} \left[ \int d\vec{r} e^{-i\vec{k}\vec{r}} \frac{1}{4\pi a^2} \delta(|\vec{r}| - a) \right]^N$$

Evaluating the integral in the brackets

$$\begin{aligned} \int d\vec{r} e^{-i\vec{k}\vec{r}} \frac{1}{4\pi a^2} \delta(|\vec{r}| - a) &= \frac{1}{4\pi a^2} \int_0^\infty r^2 dr \int_0^{2\pi} d\phi \int_0^1 d(\cos\theta) e^{-ikr \cos\theta} \delta(r - a) \\ &= \frac{2\pi}{4\pi a^2} \int dr r^2 \delta(r - a) 2 \frac{\sin kr}{kr} \\ &= \frac{\sin(ka)}{ka} \end{aligned}$$

because

$$\int_{-1}^1 e^{-ikrx} dx = \frac{1}{-ikr} (e^{-ikr} - e^{ikr}) = \frac{\sin(kr)}{kr}$$

For  $N \gg 1$  we can assume  $N \rightarrow \infty$ , so only  $ka \ll 1$  is relevant. We now make a Taylor expansion around 0:

$$\left( \frac{\sin(ka)}{ka} \right)^N \approx \left( 1 - \frac{k^2 a^2}{6} \right)^N \approx e^{-\frac{Nk^2 a^2}{6}}$$

So we get

$$\begin{aligned} p(\vec{R}) &= \frac{1}{(2\pi)^3} \underbrace{\int d\vec{k} e^{i\vec{k}\vec{R}} e^{-\frac{Nk^2 a^2}{6}}}_{\text{Gauss integral}} \\ &= \frac{1}{(2\pi)^3} \prod_{\alpha=x,y,z} \int dk_\alpha e^{-ik_\alpha R_\alpha - Nk_\alpha^2 \frac{a^2}{6}} \\ &= \frac{1}{(2\pi)^3} \left( \frac{6\pi}{Na^2} \right)^{\frac{3}{2}} e^{-\frac{3}{2} \frac{\vec{R}^2}{a^2 N}} \end{aligned} \quad (6.28)$$

Our final result thus is

$$p(\vec{R}) = \left( \frac{3}{2\pi Na^2} \right)^{\frac{3}{2}} e^{-\frac{3\vec{R}^2}{2Na^2}} \quad (6.29)$$

The distribution function of the end-to-end vector is Gaussian. The feature that  $R > Na$  is an artifact of our expansion, but that does not matter, because the respective weights are negligible.

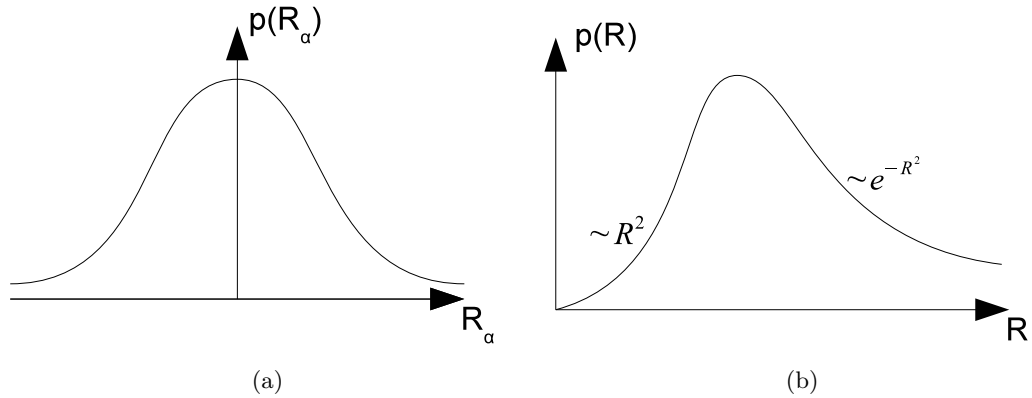


Figure 6.8: (a) Gaussian distribution of one component  $R_\alpha$  of the end-to-end distance vector  $\vec{R}$ . (b) Probability distribution of the radial component of  $\vec{R}$  (in spherical coordinates). Note the similarity to the Maxwell-Boltzmann distribution.

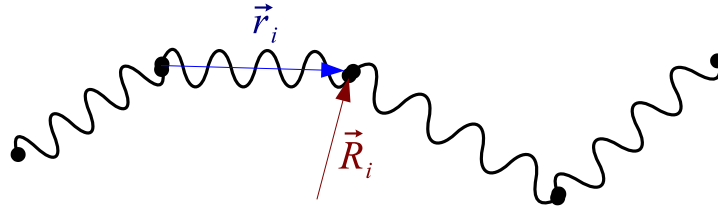


Figure 6.9: The Gaussian Chain Model. The Gaussian length distribution of the bond lengths are depicted as springs with the entropic spring constant  $k$ .

In Cartesian coordinates, equation 6.29 reads for the single components (compare also figure 6.8a):

$$\begin{aligned}
 p(\vec{R}) &= \prod_{\alpha=x,y,z} \left( \frac{3}{2\pi Na^2} \right)^{\frac{1}{2}} \exp \left( -\frac{3R_\alpha^2}{2Na^2} \right) & (6.30) \\
 \Rightarrow & \int dR_\alpha p(R_\alpha) = 1 \\
 \Rightarrow & \langle R_\alpha^2 \rangle = \int dR_\alpha p(R_\alpha) R_\alpha^2 = \frac{Na^2}{3}
 \end{aligned}$$

In spherical coordinates, one finds for the modulus of the radius:

$$p(R) = \left( \frac{3}{2\pi na^2} \right)^{\frac{3}{2}} \exp \left( -\frac{3R^2}{2Na^2} \right) \cdot 4\pi R^2 \quad (6.31)$$

This result for  $p(R)$  (figure 6.8b) is equivalent to the Maxwell-Boltzmann distribution for the distribution of the modulus of the velocity for an ideal gas. The same Gaussian distribution is obtained by starting from a symmetric random walk on a lattice, i.e. from the binomial distribution.

These results from the FJC motivate us to define a new polymer model that assumes the Gaussian property to be valid for every segment. In the Gaussian chain

model (GCM) one assumes that every bond has a Gaussian length distribution (instead of a fixed length  $a$  as in the FJC):

$$p(\vec{r}) = \left(\frac{3}{2\pi a^2}\right)^{\frac{3}{2}} \exp\left(-\frac{3\vec{r}^2}{2a^2}\right) \quad (6.32)$$

That implies that  $\langle \vec{r}^2 \rangle = a^2$ . With  $\vec{r}_i = \vec{R}_i - \vec{R}_{i-1}$  it follows that

$$p(\vec{r}_1, \dots, \vec{r}_N) = \left(\frac{3}{2\pi a^2}\right)^{\frac{3N}{2}} \exp\left(-\sum_{i=1}^N \frac{3(\vec{R}_i - \vec{R}_{i-1})^2}{2a^2}\right) \quad (6.33)$$

This corresponds to a Boltzmann distribution for  $N + 1$  bonds connected by harmonic springs (compare figure 6.9). The Hamiltonian now reads:

$$\mathcal{H} = \frac{3}{2a^2} k_B T \sum_{i=1}^N (\vec{R}_i - \vec{R}_{i-1})^2 \quad (6.34)$$

with

$$\boxed{k = \frac{3k_B T}{a^2}} \quad \text{entropic spring constant of a single bond} \quad (6.35)$$

In the continuum limit:

$$\mathcal{H} = \frac{3k_B T}{2a^2} \int_0^N dn \left(\frac{\partial \vec{R}}{\partial n}\right)^2 = \frac{3k_B T}{2a} \int_0^L ds \left(\frac{\partial \vec{R}}{\partial s}\right)^2$$

where we have used the substitution  $ds = adn$ . Note that this Hamiltonian is fundamentally different from the WLC Hamiltonian from equation 6.1 because it describes stretching and not bending.

We now consider the free energy of the Gaussian chain:

$$\begin{aligned} F &= \underbrace{U}_{=0} - TS \\ &= -T \cdot k_B \ln \Omega(\vec{R}) \\ &= -k_B T \cdot \ln \left( p(\vec{R}) \cdot \int d\vec{R} \Omega(\vec{R}) \right) \end{aligned}$$

Since  $\int d\vec{R} \Omega(\vec{R})$  is independent of  $\vec{R}$ , the free energy  $F$  can be written as:

$$\boxed{F = \frac{3}{2} k_B T \frac{\vec{R}^2}{Na^2} + F_0} \quad (6.36)$$

where  $F_0$  does not depend on  $\vec{R}$ . The free energy of a Gaussian chain increases quadratically with  $R$ , because the number of possible configurations and hence the entropy decreases. This leads to Hooke's law:

$$\vec{F} = -\frac{3k_B T}{Na^2} \cdot \vec{R} \quad (6.37)$$

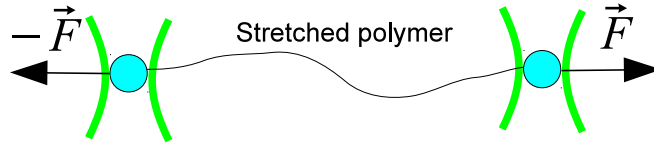


Figure 6.10: A force applied to two beads attached to the polymer, e.g. by optical tweezers. The polymer is stretched and the force needed to stretch it to a certain length is measured.

where  $3k_B T / (Na^2)$  is the entropic spring constant of the whole chain.

Note that for higher temperatures, the entropic spring constant increases or, in other words, the bonds become harder to stretch. In the limit  $T \rightarrow \infty$ , the chain contracts into a single point. The reason for this surprising behaviour is that the effective energy that is needed to stretch the polymer is entirely related to the loss of entropy. It is therefore easier to stretch polymers with a larger number of monomers  $N$ , larger monomer size  $a$  and *lower* temperature  $T$ . This is different for energy-dominated materials such as metals, which become softer at *higher* temperature.

## 6.3 Stretching polymers

### 6.3.1 Stretching the FJC

The entropic spring constant energy of the Gaussian Chain suggests to study the behavior of a FJC under stretch. Imagine placing beads at the ends and pulling them apart along the  $z$ -axis with optical tweezers (figure 6.10). Today, the pulling of biopolymers with AFM, optical or magnetic tweezers, electric fields or hydrodynamic flow, to name but a few, is a standard experiment in biophysics. Obviously, the Gaussian result (equation 6.29) cannot be true for large extensions, i.e. close to the contour length. In the following we will approach the problem of calculating the force-extension curve for finite contour length first by a scaling argument and then by an analytical calculation.

#### Scaling analysis

We now introduce a powerful scaling approach for polymers, namely "blobology". Stretching the polymer changes the symmetry to an oriented random walk. On large scales, the polymer is oriented in  $z$ -direction. On small scales  $\zeta$ , however, it is an unperturbed random walk, represented by a "blob" with ideal chain statistics (figure 6.11):

$$\zeta^2 = gb^2 \tag{6.38}$$

where  $\zeta$  denotes the blob size and  $g$  denotes the number of monomers per blob. Hence, the total number of blobs is simply  $N/g$ . From here on we use the symbol  $b$  for the Kuhn length as the segment length.

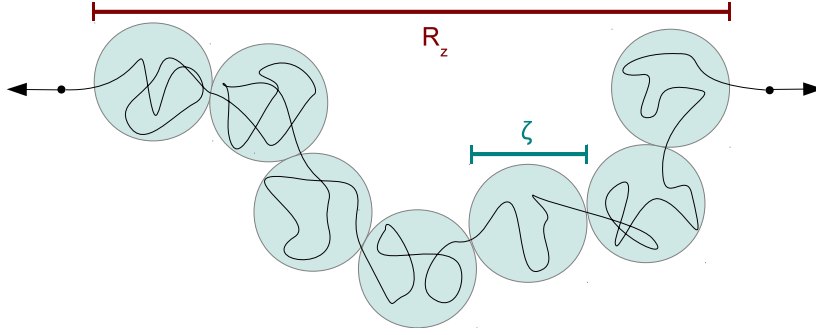


Figure 6.11: Polymer depicted as a chain of "blobs" which on the blob scale  $\zeta$  behaves as an unperturbed random walk. On the large scale  $R_z$ , the blobs are oriented in z-direction.

The blobs are arranged sequentially:

$$R_z \approx \zeta \cdot \frac{N}{g} = \frac{Nb^2}{\zeta} \quad (6.39)$$

$$\Rightarrow \zeta = \frac{Nb^2}{R_z}, \quad g = \frac{N^2b^2}{R_z^2} \quad (6.40)$$

Being extended on the large scale  $R_z$ , but not on the small scale  $\zeta$ , allows the chain to maximize its conformational entropy. On the other hand, due to stretching on the length scale  $\zeta$  a blob becomes oriented and therefore the free energy increases with  $k_B T$ :

$$F \approx k_B T \cdot \frac{N}{g} \approx k_B T \cdot \frac{R_z^2}{Nb^2} \quad (6.41)$$

As we have now seen, the scaling argument also results in Hooke's law with an entropic spring constant  $k = k_B T / (Nb^2)$ . Except for a numerical prefactor 3 which does not affect the overall scaling, it is the same as already obtained for the Gaussian chain (equation 6.35).

From the free energy  $F$  the force needed to stretch the chain  $F_z$  can immediately be calculated:

$$F_z = \frac{\partial F}{\partial R_z} \approx k_B T \cdot \frac{R_z}{Nb^2} = \frac{k_B T}{\zeta} \quad (6.42)$$

### Full analytical calculation

We parametrize each bond vector  $\vec{r}_i$  as:

$$\vec{r}_i = b \begin{pmatrix} \sin \Theta_i \cdot \cos \phi_i \\ \sin \Theta_i \cdot \sin \phi_i \\ \cos \Theta_i \end{pmatrix} \quad (6.43)$$

The FJC is purely entropic, but stretching it introduces some energy represented by the following Hamiltonian (compare figure 6.12):

$$\mathcal{H} = -F_z \cdot z_N = -F_z \sum_{i=1}^N b \cdot \cos \Theta_i \quad (6.44)$$



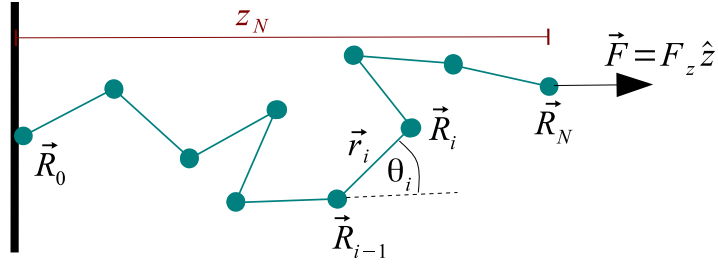


Figure 6.12: A force  $F_z$  applied to a freely jointed chain. The chain consists of  $N$  bond vectors  $\vec{r}_i$  with a fixed length  $b$ .

$$\begin{aligned}
\Rightarrow \mathcal{Z} &= \prod_{i=1}^N \int_0^{2\pi} d\phi_i \int_{-1}^1 d(\underbrace{\cos \Theta_i}_{:=x_i}) e^{-\frac{\mathcal{H}}{k_B T}} \\
&= \prod_{i=1}^N \int_0^{2\pi} d\phi_i \int_{-1}^1 d(x_i) \exp \left( \underbrace{\frac{F_z b}{k_B T}}_{:=f} \cdot \sum_{i=1}^N x_i \right) \\
&= (2\pi \int_{-1}^1 dx e^{fx})^N \\
&= \left[ \frac{2\pi}{f} (e^f - e^{-f}) \right]^N = \left( \frac{4\pi}{f} \sinh(f) \right)^N \tag{6.45}
\end{aligned}$$

For the free energy  $F$  we find:

$$F = -k_B T \ln \mathcal{Z} = -k_B T N [\ln(4\pi \sinh f) - \ln f] \tag{6.46}$$

With the free energy, the expectation value of the spatial extension in  $z$ -direction can be computed:

$$\begin{aligned}
\langle R_z \rangle &= -\frac{\partial F}{\partial F_z} = -\frac{\partial F}{\partial f} \cdot \frac{\partial f}{\partial F_z} \\
\Rightarrow \langle R_z \rangle &= bN \cdot \left[ \coth f - \frac{1}{f} \right] = bN \cdot \mathcal{L}(f) \tag{6.47}
\end{aligned}$$

where we introduced the Langevin function  $\mathcal{L}(f)$ . Equation 6.47 has two interesting limits (compare also figure 6.13):

1. **The limit of small force:  $f \ll 1$ .**

In this regime  $\mathcal{L}(f)$  can be approximated by a linear function:

$$\begin{aligned}
\coth f &= \frac{e^f + e^{-f}}{e^f - e^{-f}} \\
&\approx \frac{(1 + f + \frac{1}{2}f^2) + (1 - f + \frac{1}{2}f^2)}{(1 + f + \frac{1}{2}f^2 + \frac{1}{6}f^3) - (1 - f + \frac{1}{2}f^2 - \frac{1}{6}f^3)} = \frac{\frac{1}{f} + \frac{f}{2}}{1 + \frac{1}{6}f^2} \\
&\approx \left(\frac{1}{f} + \frac{f}{2}\right)\left(1 - \frac{1}{6}f^2\right) \\
&\approx \frac{1}{f} + \frac{1}{3}f \\
\Rightarrow \mathcal{L}(f) &\approx \frac{f}{3} \\
&\Rightarrow \boxed{\langle R_z \rangle = bN \frac{F_z b}{3k_B T}} \tag{6.48}
\end{aligned}$$

## 2. The limit of large force: $f \gg 1$ .

In this regime we find

$$\begin{aligned}
\coth f &\approx \frac{e^f}{e^f} = 1 \\
\Rightarrow \mathcal{L}(f) &= 1 - \frac{1}{f} \\
&\Rightarrow \boxed{\langle R_z \rangle = bN \left(1 - \frac{k_B T}{F_z b}\right)} \tag{6.49}
\end{aligned}$$

The force  $F_z$  diverges at the contour length  $L = bN$ :

$$F_z = \frac{k_B T}{b} \left( \frac{L}{L - \langle R_z \rangle} \right) \tag{6.50}$$

with an exponent  $-1$ .

### 6.3.2 Stretching the WLC

#### Bending Hamiltonian

In the beginning of this chapter we already encountered the bending Hamiltonian of the WLC in arc-length parametrization, compare equation 6.1:

$$\mathcal{H} = \frac{\kappa_p}{2} \int_0^L ds \left( \frac{d^2 \vec{r}}{ds^2} \right)^2 = \frac{\kappa_p}{2} \int_0^L ds \left( \frac{d\vec{t}}{ds} \right)^2 \tag{6.51}$$

where  $\vec{t}$  is the tangential vector ( $|\vec{t}| = 1$ ). There are three ways to derive this Hamiltonian:

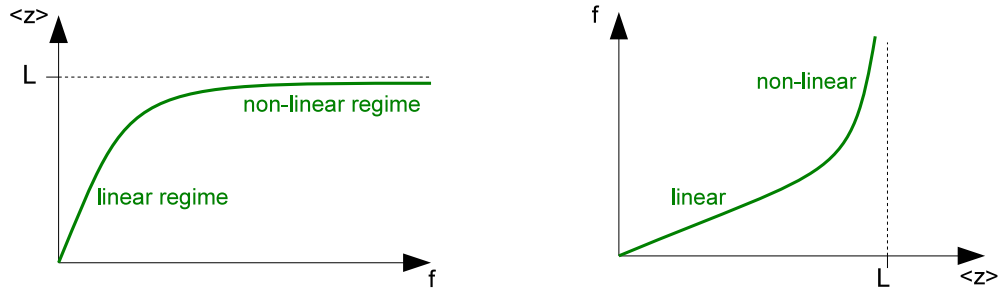


Figure 6.13: The expectation value of the extension in  $z$ -direction as a function of the (dimensionless) force parameter  $f = F_z b / (k_B T)$  (left) and vice versa. For small force and small extension, respectively, the relation is approximately linear. For large forces the extension approaches the contour length  $L$  and the force diverges.

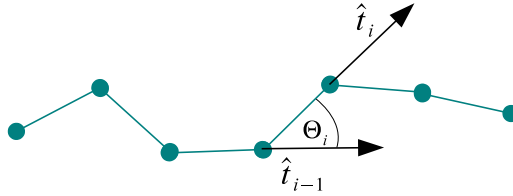


Figure 6.14: The WLC, discretized into small segments.

1. **Phenomenologically**, similar to the Helfrich-Canham Hamiltonian for membranes.
2. From **beam theory**: With the Young's modulus  $E$  of the elastic rod one finds

$$\kappa_p = E \cdot I \quad (6.52)$$

where

$$I = \int dA \frac{r^2}{2} = 2\pi \int_0^R r dr \frac{r^2}{2} = \frac{\pi R^4}{4} \quad (6.53)$$

denotes its area moment of inertia (compare figure 6.6).

3. From **microscopic models** such as the FRC, see above.

The bending energy can be calculated by discretizing the WLC into small segments as shown in figure 6.14. This model is similar to the FRC. However, the main difference is that for the FRC the angle  $\Theta$  was held constant whereas now the second moment  $\langle \Theta^2 \rangle \sim k_B T b / \kappa_p$  is a constant. The bending Hamiltonian

in equation 6.51 then gives

$$\begin{aligned}
E_b &= \sum_{i=1}^N \frac{\kappa_p}{2b} \cdot (\vec{t}_i - \vec{t}_{i-1})^2 \\
&= \sum_{i=1}^N \frac{\kappa_p}{b} \cdot (1 - \cos \Theta_i) \\
\text{small curvature} \Rightarrow E_b &\approx \sum_{i=1}^N \frac{\kappa_p}{2b} \Theta_i^2
\end{aligned} \tag{6.54}$$

### Persistence length

In the continuum model the tangential vector diffuses on a sphere (theory of rotational random walks). With Greens function formalism it can be shown that this leads to

$$\langle \vec{t}(s) \cdot \vec{t}(0) \rangle = e^{-\frac{k_B T}{\kappa_p} \cdot s} = e^{-\frac{s}{l_p}} \tag{6.55}$$

where

$$\boxed{l_p = \frac{\kappa_p}{k_B T}} \quad \text{persistence length} \tag{6.56}$$

Equation 6.56 can be made plausible by a simple scaling argument (similar to the Bjerrum length in electrostatistics):

$$\begin{aligned}
\underbrace{k_B T}_{\text{thermal energy}} &= \underbrace{\frac{\kappa_p}{2} L \cdot \frac{1}{R_{bend}^2}}_{\text{bending energy}} \\
\text{on scale } l_p \Rightarrow \text{ } L \approx R_{bend} & \quad k_B T = \frac{\kappa_p}{2l_p} \\
\Rightarrow l_p &\sim \frac{\kappa_p}{k_B T}
\end{aligned}$$

Values of the persistence length can vary from several *nm* ( $l_p = 50 \text{ nm}$  for ds-DNA) to several  $\mu\text{m}$  ( $l_p = 17 \mu\text{m}$  for actin) or even several *mm* ( $l_p = 6 \text{ mm}$  for microtubules).

With the persistence length we can calculate the mean-square end to end distance as before (compare eq. 6.19):

$$\begin{aligned}
\langle \vec{R}^2 \rangle &= \int_0^L du \int_0^L dv \exp\left(-\frac{|u-v|}{l_p}\right) \\
&= 2l_p L - 2l_p^2 (1 - e^{-\frac{L}{l_p}}) = L^2 f(x)
\end{aligned} \tag{6.57}$$

with  $f(x) = 2x - 2x^2(1 - e^{-1/x})$  and  $x = l_p/L$ . Below we will make use of the scaling function  $f(x)$ .

## Extension in z-direction

We now stretch the WLC into  $z$ -direction:

$$\frac{\mathcal{H}}{k_B T} = \frac{l_p}{2} \int_0^L ds \left( \frac{d\vec{t}}{ds} \right)^2 - \underbrace{\frac{F_z}{k_B T} \int_0^L ds t_z}_{:=f \quad R_z} \quad (6.58)$$

$$\Rightarrow \text{extension } \langle R_z \rangle = \frac{1}{\mathcal{Z}} \int \mathcal{D}\vec{t} R_z e^{-\frac{\mathcal{H}}{k_B T}} = \frac{d \ln \mathcal{Z}}{df} \quad (6.59)$$

In contrast to the FJC an exact solution to equation 6.59 is not known. However, the two asymptotic limits can be treated analytically:

### 1. small stretch, $fR_z \ll 1$ :

We can expand the partition sum  $\mathcal{Z}$  in small values of  $f$ :

$$\begin{aligned} \mathcal{Z} &= \int \mathcal{D}\vec{t} e^{-\frac{l_p}{2} \int_0^L ds \left( \frac{d\vec{t}}{ds} \right)^2} \cdot \left[ 1 + f \int_0^L ds t_z + \frac{f^2}{2} \int_0^L du \int_0^L dv t_z(u) t_z(v) + \mathcal{O}(f^3) \right] \\ &= \mathcal{Z}_0 \left[ 1 + f \int_0^L ds \underbrace{\langle t_z \rangle_0}_{=0} + \frac{f^2}{2} \int_0^L du \int_0^L dv \langle t_z(u) t_z(v) \rangle_0 \right] \end{aligned}$$

Since

$$\int_0^L du \int_0^L dv \langle t_z(u) t_z(v) \rangle_0 = \frac{1}{3} \langle \vec{R}^2 \rangle \stackrel{L \gg l_p}{\approx} \frac{1}{3} \cdot 2Ll_p$$

we finally find for the partition sum:

$$\mathcal{Z} = \mathcal{Z}_0 \left[ 1 + \frac{f^2 l_p L}{3} \right] \quad (6.60)$$

And hence with equation 6.59

$$\langle R_z \rangle = \frac{\frac{2fl_pL}{3}}{1 + \frac{f^2 l_p L}{3}} \approx \frac{2fl_pL}{3}$$

$$\Rightarrow \boxed{\langle R_z \rangle = \frac{2l_p L}{3k_B T} \cdot F_z} \quad \text{extension of WLC for small forces} \quad (6.61)$$

Therefore the extension of the WLC in response to a small stretch exhibits, similar to the FJC, a linear force-extension dependency with an entropic spring constant  $k_{WLC} = 3k_B T / (2l_p L)$ . Recall, that for the entropic spring constant for the FJC we found  $k_{FJC} = 3k_B T / (bL)$  (compare equation 6.48).

### 2. large stretch, $fR_z \gg 1$

In this regime we are dealing with an almost straight chain and can therefore use a Monge parametrization for  $\vec{t}$  (compare figure 6.15a):

$$\vec{t} = \begin{pmatrix} t_x \\ t_y \\ 1 - \frac{1}{2}(t_x^2 + t_y^2) \end{pmatrix} \quad (6.62)$$

where for the  $z$ -component we have used the fact that  $\vec{t}$  is normalized and a Taylor expansion. Our Hamiltonian now reads

$$\begin{aligned} \frac{\mathcal{H}}{k_B T} &= \frac{l_p}{2} \int ds \left[ \left( \frac{dt_x}{ds} \right)^2 + \left( \frac{dt_y}{ds} \right)^2 + \underbrace{\left( \frac{dt_z}{ds} \right)^2}_{\approx 0} \right] - f \int ds t_z \\ &= \frac{l_p}{2} \int ds \left[ \left( \frac{dt_x}{ds} \right)^2 + \left( \frac{dt_y}{ds} \right)^2 \right] + \frac{f}{2} \int ds [t_x^2 + t_y^2] - f \cdot L \end{aligned} \quad (6.63)$$

This Hamiltonian is quadratic and therefore the partition sum is a Gaussian path integral (the constant term does not matter). In Fourier space we thus have

$$\stackrel{\text{Fourier}}{\Rightarrow} |t_\alpha(k)|^2 = \frac{k_B T}{k_B T (l_p k^2 + f)} \quad (6.64)$$

$$\begin{aligned} \Rightarrow \langle R_z \rangle &= \int_0^L ds \langle t_z \rangle = \int_0^L ds \langle (1 - \frac{1}{2}(t_x^2 + t_y^2)) \rangle \\ &= L - \frac{1}{2} \int_0^L ds (\langle t_x^2 \rangle + \langle t_y^2 \rangle) = L - \frac{1}{2} L \cdot 2 \langle t_x^2 \rangle \\ &= L \cdot (1 - \frac{1}{2\pi} \int_{-\infty}^{\infty} dk \frac{1}{l_p k^2 + f}) = L \cdot (1 - \frac{1}{2\pi f} \int_{-\infty}^{\infty} dk \frac{1}{(\sqrt{\frac{l_p}{f}} k)^2 + 1}) \\ &= L \cdot (1 - \frac{1}{2\pi f} \underbrace{\int_{-\infty}^{\infty} \frac{dk}{\sqrt{\frac{l_p}{f}}} \frac{1}{k^2 + 1}}_{\pi}) \\ &= L (1 - \frac{1}{2\sqrt{f l_p}}) \end{aligned} \quad (6.65)$$

$$\Rightarrow \boxed{\frac{L - \langle R_z \rangle}{L} = \frac{1}{2\sqrt{f l_p}}} \quad (6.66)$$

This is a square-root divergence  $\sim 1/\sqrt{F_z}$  (figure 6.15b). Recall that the FJC in the large extension regime diverges with  $1/F_z$  (compare equation 6.50) which is crucially different. In experiments, stretching semiflexible biopolymers like dsDNA has shown that they can *not* be described by the FJC<sup>2</sup>.

<sup>2</sup>Smith, Steven B., Laura Finzi, and Carlos Bustamante. Direct mechanical measurements of the elasticity of single DNA molecules by using magnetic beads. *Science* 258.5085 (1992): 1122-1126; Bustamante, C., Marko, J. F., Siggia, E. D., and Smith, S. Entropic elasticity of lambda-phage DNA. *Science* (1994): 1599-1599; Bustamante, Carlos, Zev Bryant, and Steven B. Smith. Ten years of tension: single-molecule DNA mechanics. *Nature* 421.6921 (2003): 423-427.

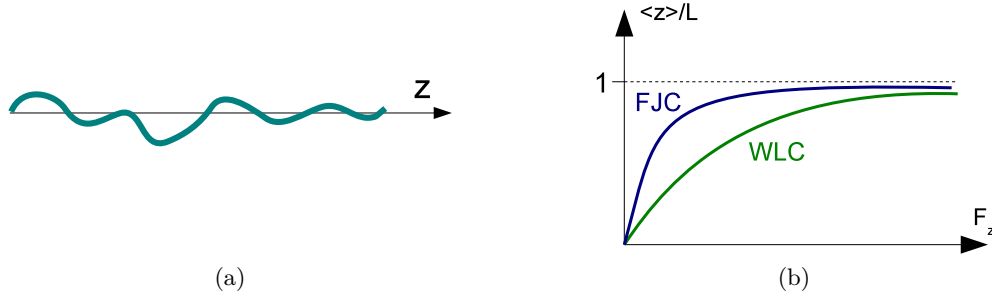


Figure 6.15: a.) A WLC under large stretch. The polymer is now almost straight and can be assumed to have no overhangs. Hence, in analogy to membrane physics, we can choose a parametrization that is similar to the Monge parametrization. b.) Force-extension dependence for the FJC and the WLC. For the FJC the scaling is  $(L - \langle R_z \rangle) / L \sim F_z^{-1}$ , whereas for the WLC we find  $(L - \langle R_z \rangle) / L \sim F_z^{-1/2}$ .

Although an exact formula for the WLC is still lacking, the two limits shown here can be combined in an interpolation formula with an error smaller than 10%<sup>3</sup>:

$$\begin{aligned}
 1. \text{ small stretch} \quad & f \cdot l_p = \frac{3 \langle R_z \rangle}{2L} \\
 2. \text{ large stretch} \quad & f \cdot l_p = \frac{1}{4 \cdot \left(1 - \frac{\langle R_z \rangle}{L}\right)^2}
 \end{aligned}$$

$$\Rightarrow \boxed{f \cdot l_p = \frac{F_z l_p}{k_B T} = \frac{\langle R_z \rangle}{L} + \frac{1}{4 \cdot \left(1 - \frac{\langle R_z \rangle}{L}\right)^2} - \frac{1}{4}} \quad \text{interpolation formula} \quad (6.67)$$

### Scaling analysis of stretched WLC

The two limiting cases of the stretched WLC can be obtained also from a blob scaling analysis, which helps to better understand the underlying physics. We consider a chain segment of length  $l$  which is bent to an angle  $\theta$ . As discussed above, this costs the bending energy

$$E_b \sim \frac{\kappa_p (1 - \cos \theta)}{l} \approx \frac{\kappa_p \theta^2}{l} \quad (6.68)$$

which diverges with  $l \rightarrow 0$ , because we would get infinite curvature. In order to work against the external force  $F_z$ , we need the stretching energy

$$E_s \sim F_z l (1 - \cos \theta) \approx F_z l \theta^2 \quad (6.69)$$

that increases with  $l$ . Therefore a crossover length  $\xi$  exists at which the two energies balance:

$$\xi := \sqrt{\frac{\kappa_p}{F_z}} = \sqrt{\frac{k_B T l_p}{F_z}} \quad (6.70)$$

<sup>3</sup>JF Marko and ED Siggia: "Stretching DNA", *Macromolecules* 1995, 28:8759–8770

We interpret  $\xi$  as the contour length per blob. Below it, the chain does not feel the effect of force and is dominated by bending. Above it, the chain becomes elongated in z-direction and is dominated by stretching. In the blob picture, we assume that we have an unperturbed WLC below  $\xi$  and a stretched FJC of blobs above  $\xi$ .

We next recall the two scaling functions that we have calculated above. For the unperturbed WLC, we have defined a scaling function  $f(x)$  for the mean squared end-to-end distance in eq. 6.57. We now use it to define the size of a blob as

$$b_b^2 := \xi^2 f\left(\frac{l_p}{\xi}\right). \quad (6.71)$$

For the FJC of blobs, we can use the Langevin function  $\mathcal{L}(x)$  defined in eq 6.47. We note that we have  $L/\xi$  blobs, each of size  $b_b$ , and therefore the overall relative extension will be

$$\frac{\langle R_z \rangle}{L} \sim \frac{1}{L} \frac{L}{\xi} b_b \mathcal{L}\left(\frac{F_z b_b}{k_B T}\right) \quad (6.72)$$

where  $b_b$  depends on the regime in which the scaling function  $f(x)$  is evaluated. A closer look shows that the overall result is controlled only by one scaling parameter, namely  $f := F_z l_b / (k_B T)$ .

We now can look at the two limiting cases. For strong stretching,  $f \gg 1$ , we have  $\mathcal{L}(x) = 1 - 1/x$  and  $f(x) = 1$ . Thus  $b_b = \xi$  (the blob is rigid with linear scaling) and therefore

$$\frac{\langle R_z \rangle}{L} \sim 1 - \frac{k_B T}{F_z \xi}. \quad (6.73)$$

We rearrange to find

$$\frac{L - \langle R_z \rangle}{L} \sim \frac{k_B T}{F_z \xi} \sqrt{\frac{k_B T}{F_z l_p}} \quad (6.74)$$

exactly as found above, except that the scaling analysis misses a factor of 2.

For weak stretching,  $f \ll 1$ , we have  $\mathcal{L}(x) = x/3$  and  $f(x) = 2x$ . Thus  $b_b^2 = 2\xi l_p$  (the blob is flexible with square root scaling) and we get

$$\frac{\langle R_z \rangle}{L} \sim \frac{\sqrt{\xi l_p}}{\xi} \frac{F_z \sqrt{\xi l_p}}{k_B T} = \frac{F_z l_p}{k_B T} \quad (6.75)$$

because  $\xi$  cancels out. This is the linear response regime that we also found above. Here we miss a numerical factor of 2/3 compared with the exact result. Overall we conclude that the blob analysis gives the right scaling results in both limits, in particular the inverse square root for the divergence at strong stretching, which sets the WLC apart from the FJC, and the linear response regime at weak stretching.

### Final remarks on stretching the WLC

Experimentally, biopolymers have been shown to correspond to the WLC-model in many different cases, most prominently in the case of dsDNA<sup>4</sup>. For dsDNA,

<sup>4</sup>Smith, Steven B., Laura Finzi, and Carlos Bustamante. Direct mechanical measurements of the elasticity of single DNA molecules by using magnetic beads. *Science* 258.5085 (1992): 1122-



but also for other biopolymers like actin, it is known that after the thermal fluctuations in the contour length have been pulled out, the backbone can give out additional length due to internal changes (overstretching in the case of dsDNA, twist in the case of actin). This situation is described by the stretchable WLC-model, which can be solved with the same methods as described above for the WLC-model, and which is a combination of the GC and the WLC.

The following references are recommended for further reading:

- R Phillips et al., Physical biology of the cell, chapter 10; especially appendix 10.8 on the math of the WLC on page 401
- P Nelson, Biological Physics, very detailed discussion of different models
- Kroy, Klaus, and Erwin Frey. Force-extension relation and plateau modulus for wormlike chains. Physical Review Letters 77.2 (1996): 306.
- J Kierfeld et al. Stretching of semiflexible polymers with elastic bonds, Eur. Phys. J. E 2004, 14:17-34
- Koester, S., J. Kierfeld, and T. Pfohl. Characterization of single semiflexible filaments under geometric constraints. The European Physical Journal E 25.4 (2008): 439-449.

## 6.4 Interacting polymers

### 6.4.1 Self-avoidance and Flory theory

Until now we have neglected the fact that the chain can encounter itself and then becomes repelled as is the case for a real polymer. Due to this excluded volume effect real chains are more extended than ideal ones. The **Edwards-Hamiltonian** takes account of the excluded volume:

$$\beta\mathcal{H} = \frac{k}{2} \int_0^N ds \left( \frac{\partial \vec{r}}{\partial s} \right)^2 + w \int_0^N ds \int_0^N ds' \delta(\vec{r}(s) - \vec{r}(s')) \quad (6.76)$$

where  $w$  denotes the excluded volume parameter. Unfortunately, further calculation with the Edwards Hamiltonian are rather complicated.

The *Flory theory* offers a very simple and powerful approach to the problem. Here we take a look at the scaling of the involved contributions to the free energy  $F$ , namely energy and entropy:

1. **Interaction energy:** we assume infinitely hard potentials that repel monomers. Each collision of the polymer with itself costs  $k_B T$  in energy. With a monomer density of  $\rho = N/R^3$  and an excluded volume  $v$  we end up with an internal free energy:

$$F_{int} \approx k_B T v \rho N = k_B T v \frac{N^2}{R^3} \quad (6.77)$$

---

1126; Bustamante, C., Marko, J. F., Siggia, E. D. and Smith, S. (1994). Entropic elasticity of lambda-phage DNA. Science 1599-1599.

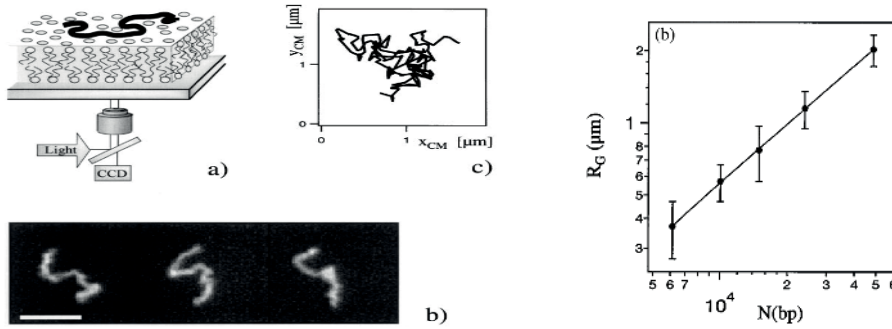


Figure 6.16: The extension of DNA has been measured on supported bilayers and resulted in an exponent 0.79 very close to 2D Flory theory. From B. Maier and J.O. Rädler, Phys. Rev. Lett. 82, 1911, 1999.

2. **Stretching:** what is the counterforce avoiding that the polymers spreads out due to excluded volume effects ? Of course this costs entropy as the polymer would be less able to fluctuate. Assuming we stretch a Gaussian chain (compare equation 6.36):

$$F_{stretch} \approx k_B T \frac{R^2}{N b^2} \quad (6.78)$$

This results in a total free energy:

$$F = F_{int} + F_{stretch} = k_B T \left( v \frac{N^2}{R^3} + \frac{R^2}{N b^2} \right) \quad (6.79)$$

The optimal size  $R_F$  follows from the minimizing the free energy  $F$  with respect to  $R$ :

$$\begin{aligned} \frac{\partial F}{\partial R} &= 0 = k_B T \left( -3v \frac{N^2}{R_F^4} + 2 \frac{R_F}{N b^2} \right) \\ \Rightarrow R_F &= v^{\frac{1}{5}} b^{\frac{2}{5}} N^{\frac{3}{5}} \end{aligned} \quad (6.80)$$

$$\Rightarrow \boxed{R_F \sim N^\nu} \quad \text{with } \nu = \frac{3}{5} = 0.6 \quad (6.81)$$

Computer simulations and experiments yield  $\nu = 0.588$ . Thus Flory theory seems to be close to reality. In  $d$  dimensions one finds  $\nu = 3/(d+2)$ , which agrees with the exact results in  $d = 2$  ( $\nu = 3/4$ ) and  $d = 4$  ( $\nu = 1/2$ ). In two dimensions, this exponent has been measured for negatively charged DNA of various lengths absorbed to positively charged lipid bilayers, compare figure 6.16.

However, it is very difficult to improve on Flory theory. The reason is that its success is due to a fortuitous cancellation of errors since both the repulsion energy and the entropic stretching are overestimated. Nevertheless it is very useful for many situations of interest, such as polyelectrolytes, ring polymers or adsorption.

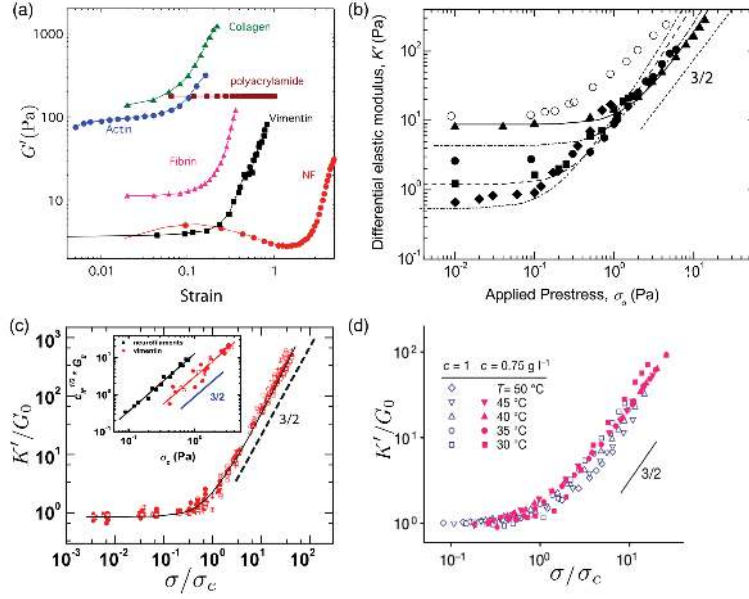


Figure 6.17: Experimental results and scaling laws for the modulus of different polymer networks. (a) Note that the synthetic polyacrylamide gel is the only one that does not strain-stiffen. (b) Actin network crosslinked by scruin. (c) Neurofilament network. (d) Polyisocyanopeptide hydrogel. The power  $3/2$  is the prediction of the affine thermal model. Taken from Broedersz and MacKintosh review, figure 15.

### 6.4.2 Semiflexible polymer networks

The mechanical stability of cells and tissues results mainly from networks of semiflexible polymers (e.g. actin inside the cells and collagen between the cells). These kinds of networks are stabilized both by topological entanglement and by crosslinkers (e.g. alpha-actinin, fascin, filamin, fimbrin, scruin etc for actin). Despite the fact that molecular details and network architecture can vary widely in these systems, they all share one outstanding property, namely that they stiffen under strain, as shown in the experimental plots shown in figure 6.17. We have seen this already for the single WLC, but it is non-trivial to find this result also for the network. A nice review on this subject is by Chase P. Broedersz and Fred C. MacKintosh, *Reviews of Modern Physics* 2014, volume 86, pages 995-1036.

We cannot go into the details here, but would like to mention one difficulty: if one couples different polymers into a bulk material, most deformation modes will include both stretch and compression of polymers. However, these two modes are very asymmetric on the level of the molecules. Under compression, the polymer does buckle at the Euler threshold. This can be seen easily by noting that the thermal fluctuation of a beam is

$$\mathcal{H} \sim (\sigma + \kappa k^2)k^2 \quad (6.82)$$

which can become negative for  $\sigma < -\kappa k^2$ . Because the critical wavelength is

related to beam length  $L$  by  $k^* = \pi/L$ , we get for the critical tension at buckling

$$\sigma_c = \kappa \left(\frac{\pi}{L}\right)^2 = \pi^2 E \left(\frac{R}{L}\right)^2 \quad (6.83)$$

with bending stiffness  $\kappa = ER^2$ , Young's modulus  $E$  and radius  $R$ . Thus the longer a polymer, the more easily it buckles. A complete theory of a polymer gel has to incorporate this asymmetry, the scale on which the polymers are crosslinked, and the nature of the crosslinks.

## Chapter 7

# Molecular motors

Molecular motors are molecules that generate motion and force. They do this by converting electrochemical energy into mechanical work, for example by hydrolysing ATP or by letting ions flow down a gradient. Thus they work like heat engines, but they cannot be Carnot engines, because molecular diffusion is too fast as to allow for any temperature gradients. Thus they have to achieve the conversion without the intermediate form of heat and to operate at constant temperature (isothermally). Molecular motors are extremely fascinating molecular machines and it is still not completely clear how they have been optimized by evolution to perform their tasks. An important aspect of understanding them is to build new ones, for example by reengineering their different parts or by using different material (e.g. small molecules or DNA rather than proteins). In 2016, the Nobel prize for chemistry has been awarded *for the design and synthesis of molecular machines* and a Nobel prize for medicine for the investigation of biological molecular motors might come in the future.

Why did nature evolve motors ? Obviously this is a very direct way to generate force, e.g. in the muscle for moving body parts or in the beating flagella of sperm cells. In regard to transport, for examples of vesicles and organelles, but also of viruses, motors are needed not only to provide specificity and direction, but also to beat the physical limits of diffusion. With a typical molecular diffusion constant of  $(10 \mu m)^2/s$ , diffusion starts to become slow in regard to the required response times of  $s$  on the length scale of cells ( $10 \mu m$ ). With a typical velocity of  $\mu m/s$ , molecular motors outcompete diffusion on cellular and tissue length scales. However, we also note that for body length scales, we need other transport modes. For example, small molecules such as hormones and many cell types (red blood cells, platelets, white blood cells, stem cells and cancer cells) are transported with the blood (average velocity 0.4 m/s in the aorta and 0.3 mm/s in the capillaries) and nerve impulses are transmitted as action potentials (velocities 10-100 m/s).

In this chapter, we will discuss the theoretical basis of understanding molecular motors. As we will see, the appropriate framework is the one of stochastic equations (master equation, Fokker-Planck equation) and the theory of molecular motors has advanced considerably over the last two decades and still is a very

active research area <sup>1</sup>.

## 7.1 Classification

Molecular motors can be classified in the following way:

**Translational motors** These motors move along tracks, e.g. myosin motors along actin filaments (e.g. in the muscle), kinesin and dynein along microtubules (e.g. kinesin in axons for transport towards the synaptic cleft, and dynein in cilia and flagella to bend them), and polymerases and helicases along DNA.

**Rotary motors** These motors typically have a stator embedded into the membrane and containing a rotor. The most important example is the  $F_0 F_1$  ATP Synthase, which in cells of all species generates ATP from ADP and  $P_i$  (1 ATP per 120 degree rotation, at 100 Hz this gives 300 ATP per second). It is driven by a proton gradient and needs six protons for each turn. An adult burns 120 W and needs 2.400 kcal / day and thus  $1.7 \times 10^{26}$  ATP molecules, amounting to 140 kg that are essentially produced in our mitochondria. The required energy comes from our metabolism (aerobic respiration of glucose, which essentially was produced before by plants using photosynthesis). If there is plenty of ATP, the motor reverses and builds up the proton gradient. Another famous example is the bacterial flagellar motor, which is basically constructed like a ion turbine using 1.000 protons to drive one turn. This motor has to create more torque than the ATP Synthase because it has to turn the bulky flagellum.

**Polymerization motors** By (de)polymerization, biopolymers like actin or MT can create force. The most important example is the lamellipodium of migration cells, when a complete network is polymerized against the leading membrane to push the cell forward. Another example are pilli of bacteria that pull against their environment by depolymerization of the base in order to move the cell forward.

**Translocation motors** These are used to push biomolecules through a hole, e.g. when an empty virus capsid is loaded with DNA, when proteins are targeted into a proteasome for degradation, or when a folding protein is treaded from a ribosome directly into another compartment.

Although these motors are very different on the molecular level, they share the basic principle, namely stochastic operation at constant temperature to create biased movement along cyclic phase space trajectories.

---

<sup>1</sup>In the introduction and the discussion of the force-velocity relation, we follow the book Physical biology of the cell by Rob Phillips and coworkers. For the more mathematical discussion, we follow two excellent review papers on this subject: Frank Jülicher, Armand Ajdari and Jacques Prost, Modeling molecular motors, Reviews of Modern Physics 69, 1269-1281, 1997; Tom Duke, Modelling motor protein systems, course 3 in Physics of bio-molecules and cells, volume 75 of the Les Houches series, pages 95-143, 2002.

In order to foster model building, we start with the simplest example, namely a translational motor walking along a track. We consider a processive motor like kinesin or myosin V, that can make many steps without falling off the track (this is different for non-processive motors like myosin II, that stay on track only for a short time and thus can work productively only in groups). Such motors are typically two-headed and move in a hand-over-hand fashion. Moreover each step is related to exactly one ATP being consumed. We label the track position by the spatial coordinate  $x$  and assume that each motor has only a finite number of discrete states, which we label with the index  $m$ . Thus our central quantity is the probability  $p_m(x, t)$  to be in state  $m$  and at position  $x$  at time  $t$ .

## 7.2 One-state model

We start with a one-state model, thus we can drop the label  $m$ . We assume that the motor jumps to the right and to the left with rates  $k_+$  and  $k_-$ , respectively. Note that in a model for passive physical particles, these two rates should be equal; here we already assume some kind of symmetry break that for molecular motors should be related to track polarity and ATP consumption. We allow only for discrete binding sites at  $x = na$ . We now deal with a discrete one-dimensional random walk with bias and can write the following flux balance:

$$p(n, t + \Delta t) = k_+ \Delta t p(n-1, t) + k_- \Delta t p(n+1, t) + (1 - k_- \Delta t - k_+ \Delta t) p(n, t) \quad (7.1)$$

The two gain terms come from motors hopping in from left and right, respectively, and the two loss terms come from motors hopping away to the left and right, respectively. We rearrange and take the continuum limit  $\Delta t \rightarrow 0$  to get

$$\dot{p}(n, t) = k_+(p(n-1, t) - p(n, t)) + k_-(p(n+1, t) - p(n, t)) \quad (7.2)$$

We next take the continuum limit in regard to space and use the Taylor expansion

$$p(x \pm a, t) \approx p(x, t) \pm p'(x, t)a + \frac{1}{2}p''(x, t)a^2 \quad (7.3)$$

We then end up with the famous Fokker-Planck or Smoluchowski equation

$$\dot{p}(x, t) = -vp'(x, t) + Dp''(x, t) \quad (7.4)$$

with drift velocity and diffusion constant defined by

$$v = (k_+ - k_-)a, \quad D = (k_+ + k_-)\frac{a^2}{2} \quad (7.5)$$

For a Delta function as initial condition, this equation is solved by

$$p(x, t) = \frac{1}{\sqrt{4\pi Dt}} e^{-(x-vt)^2/4Dt} \quad (7.6)$$

Thus the motor moves with a drift velocity  $v$  to the right, but it also disperses with a diffusion constant  $D$ .

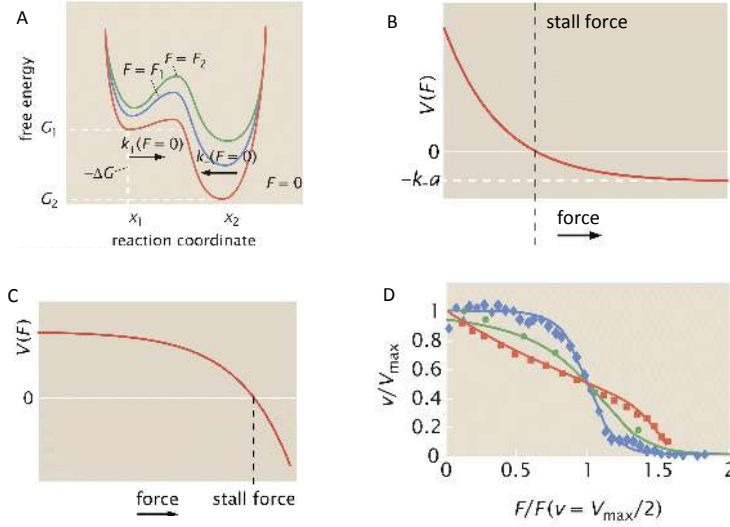


Figure 7.1: Force dependence. (A) Scheme how force will change the free energy landscape of a motor hopping to the right. (B) Force-velocity relation when force dependence is in  $k_+$ . (C) Force-velocity relation when force dependence is in  $k_-$ . (D) Some experimentally measured force-velocity relations: kinesin (green), RNA polymerase (blue), phage packaging motor (red). All four graphs taken from the book *Physical Biology of the Cell*, chapter 16 on molecular motors.

We also note that one can derive a dispersion relation from here. We use the Fourier ansatz  $p(x, t) = C \exp(i(kx - \omega t))$  and get

$$(-i\omega + vik + Dk^2)C = 0 \quad (7.7)$$

which in turn leads to

$$\omega = vk - iDk^2 \quad (7.8)$$

The first term is well-known from e.g. electromagnetic waves (photons) or mechanical waves in crystals (phonons), which have linear dispersion relations (for phonons only for small  $k$ ). The second term is special for diffusion.

### 7.3 Force dependence

Next we discuss the force dependence of the motor drift velocity  $v = (k_+ - k_-)a$ . We go back to the discrete picture and consider steady state, so the time dependence drops out. The principle of detailed balance says that at equilibrium, the currents between two states should cancel each other:

$$k_+p(n) = k_-p(n+1) \quad (7.9)$$

The state probabilities themselves should obey Boltzmann statistics in equilibrium:

$$p(n) = \frac{1}{Z} e^{-\beta(G_n + Fna)} \quad (7.10)$$



where  $G_n$  is the Gibbs free energy at position  $n$  and  $F$  is the external force against which the motor has to work. Thus equilibrium dictates

$$\frac{k_+}{k_-} = e^{-\beta(\Delta G + Fa)} \quad (7.11)$$

where  $\Delta G = G_{n+1} - G_n$ . Obviously  $\Delta G$  has to be negative for the motor to gain free energy as it moves to the right hand side (compare Fig. 7.1A). We immediately see that the motor gets stalled ( $v = 0$ ) if the force reaches the stall force value  $F_s = -\Delta G/a$  (we define a positive force to pull to the left).

We now turn to non-equilibrium. As we have seen, the equilibrium considerations only determine how the ratio of the two rates should depend on  $F$ . In the absence of more information, we now consider two extreme cases. We first consider the possibility that the force dependence resides completely in  $k_+$ . Then we get for the force-velocity relation

$$v(F) = a(k_+(F) - k_-) = ak_- \left( e^{-\beta(\Delta G + Fa)} - 1 \right) \quad (7.12)$$

using the equilibrium condition from equation 7.11. Thus we get a finite free velocity at  $F = 0$ , then a convex up decay to the stall force  $F_s$  and finally a plateau at negative values (compare 7.1B). Indeed such a force-velocity relation is known from many motors, e.g. for myosin II (although this is a non-processive motor, so this is the average result when working in a group) and to some extent for kinesin.

An alternative scenario would be that the force dependence resides completely in  $k_-$ . We then get

$$v(F) = a(k_+ - k_-(F)) = ak_+ \left( 1 - e^{\beta(\Delta G + Fa)} \right) \quad (7.13)$$

This force-velocity relation is convex down (compare Fig. 7.1C) and is similar to the one measured for myosin V, although the divergence to negative values at large  $F$  is of course unrealistic. Fig. 7.1D shows some examples for measured force-velocity curves and demonstrates that we were able to capture their general features well with our simple one-state model.

## 7.4 ATP dependence

Like for the force dependence, we start with a statement how the free energy landscape is changed by ATP-concentration. We use the well-known formula for dilute solutions (derivation with chemical potential for ideal gas):

$$\Delta G_h = \Delta G_0 - k_B T \ln \frac{[ATP]}{[ADP][P_i]} \quad (7.14)$$

The first term represents the energetic part of breaking the high-energy bond in ATP and gives a value around  $-12.5k_B T$  (to avoid entropic effects, here we consider very high concentrations, namely  $M$ ). The second term represents the

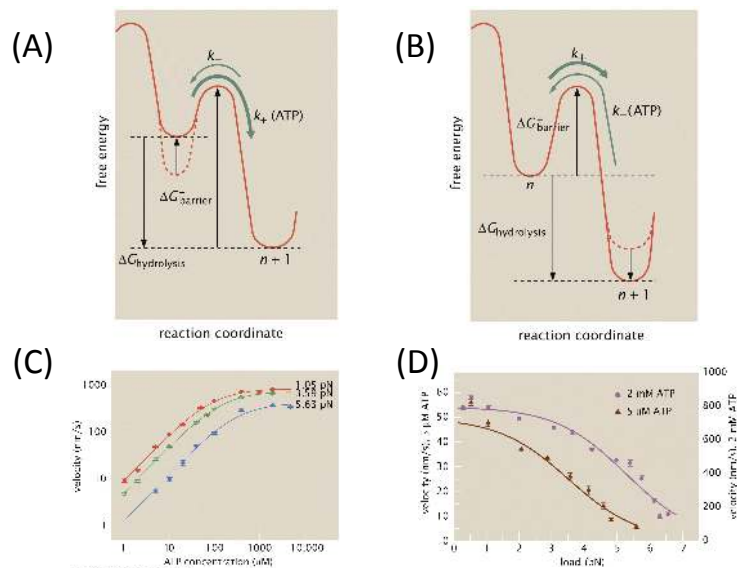


Figure 7.2: ATP dependence. (A) When the ATP-dependence is only in the forward rate, then only the free energy barrier height  $\Delta G_+$  changes when ATP concentration is changed. (B) When the ATP-dependence is only in the backward rate, then only the free energy barrier height  $\Delta G_-$  changes when ATP concentration is changed. (C) The experimental results for kinesin show the linear dependence at low ATP and the plateau at high ATP predicted by the theory. (D) Force dependence of kinesin for different ATP concentrations. All four graphs taken from the book *Physical Biology of the Cell*, chapter 16 on molecular motors.

entropic part and corresponds to the law of mass action. For physiological conditions ( $[ATP] = mM$ ,  $[ADP] = 10\mu M$ ,  $[P_i] = mM$ ) and the reference concentration of  $M$  to make the argument dimensionless, we get  $-11.5k_B T$ . Thus together we have  $\Delta G_h = -24k_B T$ . Note that an ATP-molecule is an energy currency that is valid twice as much inside the cell than with the reference concentrations, because the cell keeps ATP at a much higher concentration than ADP. In general, the free energy gain from ATP-hydrolysis depends on environmental conditions but usually is between  $20k_B T$  and  $30k_B T$ . This is usually more than enough for a molecular motor to perform its powerstroke. With a powerstroke distance of around  $8nm$  and a stall force of around  $5pN$  (typical values for kinesin), we have an energy of  $40nmpN \approx 10k_B T$ , which correspond to an efficiency of around 0.5, if one ATP-molecule gives around  $20k_B T$ .

Like for the force dependence, the equilibrium considerations do not completely determine the ATP-dependence of the jump rates. We again consider the two extreme cases that the external factor affects only one of the two rates. We first consider that ATP only affects the forward rate. We now use Kramers reaction rate theory that states that the transition rate  $k$  depends on attempt frequency  $\Gamma$  and barrier height  $\Delta G$  as

$$k = \Gamma e^{-\beta \Delta G} \quad (7.15)$$

The exponential dependence between barrier height and transition rate is also known as Arrhenius factor in physical chemistry and should not be understood to be a Boltzmann factor. This law means that the transition rate goes down dramatically (exponentially) if the barrier height increases.

For our problem we can write

$$-\Delta G_h = \Delta G_- - \Delta G_+ \quad (7.16)$$

to relate the two barrier heights to each other (we count the two barrier heights as positive, while the free energy difference is negative, therefore the minus sign on the left). If we assume that only the forward rate is changed by ATP, then this means that only  $\Delta G_+$  is changed when changing ATP (compare Fig. 7.2(A)). We now can write the two rates as

$$k_+ = \Gamma_+ e^{-\beta \Delta G_+} = \Gamma_+ e^{-\beta(\Delta G_- + \Delta G_h)} \quad (7.17)$$

$$k_- = \Gamma_- e^{-\beta \Delta G_-} \quad (7.18)$$

and therefore the velocity follows as

$$v = a(k_+[ATP] - k_-) = a(\Gamma_+ e^{-\beta(\Delta G_- + \Delta G_0)} \frac{[ATP]}{[ADP][P_i]} - \Gamma_- e^{-\beta \Delta G_-}) \quad (7.19)$$

where except for  $[ATP]$ , all other quantities are constant. Thus it increases linearly with ATP-concentration. However, this relation cannot be valid at high  $[ATP]$ , because then the barrier disappears (the left well is pushed up over the barrier) and Kramers theory is not valid anymore. Thus this must be a result for low  $[ATP]$ .

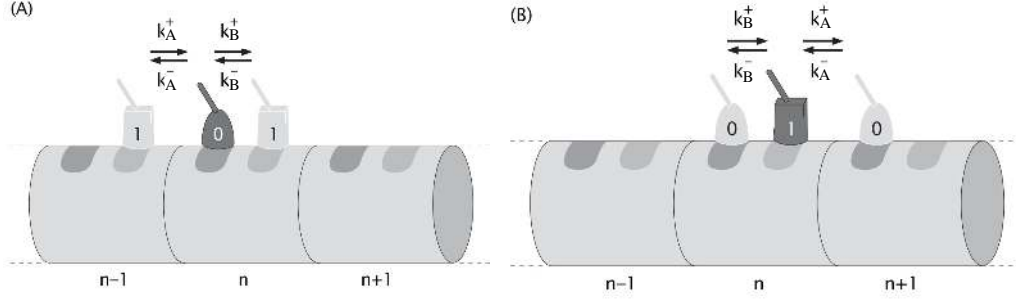


Figure 7.3: (A) In the two-state model, the motor in state 0 has to convert to state 1. During this process, it can remain stationary or take a step to the left. (B) The motor in state 1 has to convert to state 0. During this process, it can remain stationary or take a step to the right.

As the second case, we assume that only the backward rate is ATP-dependent. Now only the barrier height  $\Delta G_-$  is assumed to be ATP-dependent (compare Fig. 7.2(B)) and we get

$$k_+ = \Gamma_+ e^{-\beta \Delta G_+} \quad (7.20)$$

$$k_- = \Gamma_- e^{-\beta \Delta G_-} = \Gamma_- e^{-\beta(\Delta G_+ - \Delta G_h)} \quad (7.21)$$

and therefore

$$v = a(k_+ - k_-([ATP])) = a(\Gamma_+ e^{-\beta \Delta G_+} - \Gamma_- e^{-\beta(\Delta G_+ - \Delta G_h)} \frac{[ADP][P_i]}{[ATP]}) \quad (7.22)$$

Thus now the dependence is inverse in  $[ATP]$ . The divergence at low  $[ATP]$  cannot be valid because then the barrier vanishes (the right well is pushed up over the barrier). Thus this result says that the dependence should plateau at high  $[ATP]$ .

Together, we now have found that the velocity should increase linearly at low  $[ATP]$  and the plateau at a constant value at high  $[ATP]$ . This is exactly the experimentally measured dependence for all motors. Fig. 7.2(C) shows this for kinesin. The plateau velocity is typically around  $\mu m/s$  and the crossover concentration at sub- $mM$ . Fig. 7.2(D) shows the force-velocity relation for kinesin for different ATP concentrations.

## 7.5 Two-state model

Molecular motors are often modeled as  $N$ -state systems. The different states of the system are difficult to determine, this requires careful experimentation or molecular dynamics simulations. As a first step towards the complexity of molecular motors, we consider  $N = 2$ . Thus each motor has two internal states, 0 and 1, with probabilities  $p_0(n, t)$  and  $p_1(n, t)$ , respectively. The system can

move to the left and right only through the state 0 and 1, respectively, with the rates given in Fig. 7.3. The corresponding master equations are

$$\frac{dp_0(n, t)}{dt} = k_A^+ p_1(n-1, t) + k_B^- p_1(n, t) - k_A^- p_0(n, t) - k_B^+ p_0(n, t), \quad (7.23)$$

$$\frac{dp_1(n, t)}{dt} = k_A^- p_1(n+1, t) + k_B^+ p_0(n, t) - k_A^+ p_1(n, t) - k_B^- p_1(n, t). \quad (7.24)$$

These dynamical equations can be solved by using a continuum limit and a Fourier ansatz. To obtain the drift velocity, however, it is sufficient to use steady state arguments. We introduce the total probabilities to be in state 0 or 1:  $P_i(t) = \sum_n p_i(n, t)$ . The different positions in the master equation now do not matter anymore because we sum over them. The dynamic equations for the total probabilities follow from above as

$$\frac{dP_0(t)}{dt} = (k_A^+ + k_B^-)P_1(t) - (k_A^- + k_B^+)P_0(t), \quad (7.25)$$

$$\frac{dP_1(t)}{dt} = (k_A^- + k_B^+)P_0(t) - (k_A^+ + k_B^-)P_1(t). \quad (7.26)$$

These linear equations can be solved easily. For the steady state, however, we do not even have to do this, but we simply set the time derivatives to zero and get

$$(k_A^+ + k_B^-)P_1(t) = (k_A^- + k_B^+)P_0(t) \quad (7.27)$$

With the normalization  $P_0 + P_1$ , we finally get

$$P_0(t) = \frac{(k_A^+ + k_B^-)}{(k_A^- + k_B^- + k_A^+ + k_B^+)}, \quad (7.28)$$

$$P_1(t) = \frac{(k_A^- + k_B^+)}{(k_A^- + k_B^- + k_A^+ + k_B^+)}. \quad (7.29)$$

We now can calculate the drift velocity:

$$v = a(k_A^+ P_1 - k_A^- P_0) = \frac{(k_A^+ k_B^+ - k_A^- k_B^-)}{(k_A^- + k_B^- + k_A^+ + k_B^+)} \quad (7.30)$$

from which we can also read of the effective rates defined by  $v = a(k_+ - k_-)$ :

$$k_+ = \frac{(k_A^+ k_B^+)}{(k_A^- + k_B^- + k_A^+ + k_B^+)}, \quad (7.31)$$

$$k_- = \frac{(k_A^- k_B^-)}{(k_A^- + k_B^- + k_A^+ + k_B^+)}. \quad (7.32)$$

We note that this form of the overall rate is rather generic and also follow e.g. for the steady state approximation of Michaelis-Menten kinetics for enzymatic processes. The enumerator is a product of rates because it describes a sequence of steps, and the denominator is a sum of all rates, which is the speed limit for the process.

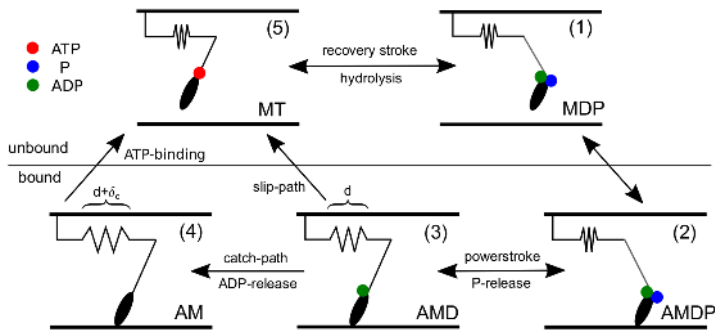


Figure 7.4: Schematics of the myosin II motor cycle with five steps. The two states above the line are unbound and the three below are bound. Binding and unbinding corresponds to establishing and removing a crossbridge between motor and actin filament, respectively. Myosin II makes two powerstrokes with the second one being a catch bond (slower under force), such that muscle can work also under high load. It also has a safety exit (the slip path) to unbind if force is too large. It finally unbinds from the rigor state by binding ATP. If no ATP is present, the system crosslinks and becomes rigid (this happens in dead bodies).

## 7.6 Ratchet model for single motors

In principle, we now could go on with a two-state model and try to solve the corresponding master equation in time. We also could start to include more relevant states, compare Fig. 7.4 for myosin II, which generates force in our muscles. As one can see from the scheme, the different states can be grouped into bound and unbound. Thus we have arrived at the model class of *crossbridge models*, where a motor cycles between bound and unbound by forming a crossbridge to the filament. In a three-state model, we would in addition add the powerstroke on the filament. We also could add the recovery stroke and distinguish between release of  $ADP$  and  $P_i$ , arriving at more states. For single motor heads like the myosin II heads in a minifilament or muscle, one rarely goes beyond five-state crossbridge-models. However, if one analyses a two-headed motor like kinesin, one can easily get more states. The same holds of course for assemblies of motor heads. In general, one ends up with high-dimensional and complex master equations that have to be treated with computer simulations. Most importantly, in crossbridge models one does not model the movement of the motor explicitly, but it is associated implicitly with one of the transitions. This agrees with experimental observations and results from molecular dynamics simulations that show that movement of motor parts is always much faster than the dwelling times in the different states.

Here we want to follow another route and turn to a two-state model that uses the concept of continuous diffusion to explain how directed motion can emerge out of random switching. This class of models is called *isothermal ratchet models* and they are more general, but also less specific than crossbridge models. In contrast to the Feynman ratchet or a Carnot machine, the system does not operate at different temperatures, but isothermally. Here we present the mathematical analysis that identifies the two essential prerequisites to obtain directed motion.

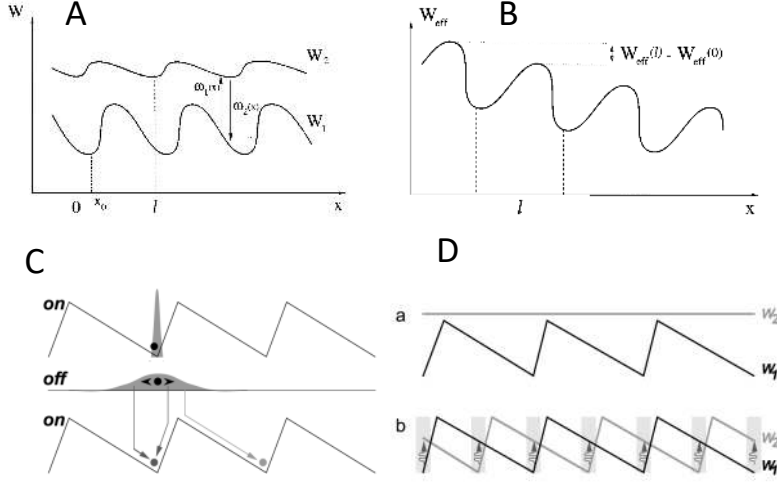


Figure 7.5: (A) Typical potentials for the two-state isothermal ratchet model. Both the potentials  $W_i$  and the transition rates  $\omega_i$  have to be periodic. Motion ensues if detailed balance for the rates is broken. (B) Motion corresponds to a tilt in the effective potential  $W_{eff}$ . (C) The simplest example would be the switch between a flat potential and an asymmetric sawtooth potential. (D) Two sawtooth potentials with a shift between them as well as with localized transition rates are more effective. This scheme seems to correspond to the hand-over-hand motion of kinesin. (A) and (B) from Julicher review, (C) and (D) from Duke review.

We start with the Fokker-Planck equation from eq. 7.4 and rewrite it as continuity equation

$$\dot{p}(x, t) + J'(x, t) = 0 \quad (7.33)$$

with the flux

$$J = vp - Dp' \quad (7.34)$$

We next assume overdamped dynamics (no mass) and write the velocity as

$$v = \mu F = \mu [-W' - F_{ext}] \quad (7.35)$$

where the mobility  $\mu$  is the inverse of the friction coefficient and the force  $F$  is divided into force from a potential  $W(x)$  and an external force  $F_{ext}$  (the minus for  $F_{ext}$  means that the force is positive if it acts to the left, against the movement of the motor, like above for the one-state motor). We also make use of the Stokes-Einstein relation  $D = k_B T \mu$ , which is an example of the fluctuation-dissipation theorem ( $D$  is fluctuation,  $\mu$  is dissipation, and the two are not independent of each other, but related by temperature). Thus we now have for the flux

$$J = -\mu [(W' + F_{ext})p + k_B T p'] \quad (7.36)$$

Together Eqs. 7.33 and 7.36 define the FPE as we use it here.

We now write the Fokker-Planck equations for two states with switching between them:

$$\dot{p}_1 + J'_1 = -\omega_1(x)p_1(x) + \omega_2(x)p_2(x) \quad (7.37)$$

$$\dot{p}_2 + J'_2 = \omega_1(x)p_1(x) - \omega_2(x)p_2(x) \quad (7.38)$$

$$J_i = -\mu_i [(W'_i + F_{ext})p_i + k_B T p'_i] \quad (7.39)$$

Note that the switching terms with the rates  $\omega_1$  and  $\omega_2$  differ only by a minus sign between the two states. For simplicity, in the following we assume  $\mu_1 = \mu_2 = \mu$ . The two potentials  $W_i$  define the two states. An extreme case would be a sawtooth potential and a flat potential, for example because one state is charged and the other is not. At any rates, the potentials  $W_i(x)$  and the switching rates  $\omega_i(x)$  should have the same periodicity with unit cell size  $l$ , because this is imposed by the track with repeat distance  $l$ . We also note that the two potentials are of purely physical (passive) origin and therefore should not be tilted, what means that

$$\Delta W_i = W_i(x=l) - W_i(x=0) = 0 \quad (7.40)$$

Otherwise the motor would exhibit motion to the right simply because it moves down a gradient. What we want to model here is the opposite, namely the fact that molecular motors spontaneous generate motion in a non-tilted energy landscape by locally burning energy, without a global gradient.

The beauty of this model is that we do not have to specify potentials and rates to get the general results we are after. We define total probability and total flux as

$$P(x) = \sum_i p_i(x), \quad J(x) = \sum_i J_i(x) \quad (7.41)$$

If we sum up the first two equations from Eq. 7.39, the switching terms drop out and we get a FPE without source terms:

$$\dot{P}(x, t) + J'(x, t) = 0 \quad (7.42)$$

We next define local fractions of occupation

$$\lambda_i(x) = \frac{p_i(x)}{P(x)} \Rightarrow \sum_i \lambda_i = 1 \quad (7.43)$$

We now calculate the total flux. Using  $p_i = \lambda_i P$  and the product rule we get

$$J = -\mu \sum_i [\lambda_i W'_i + k_B T \lambda'_i + \lambda_i F_{ext}] P + k_B T \lambda_i P' \quad (7.44)$$

$$= -\mu \left[ \left( \sum_i \lambda_i W'_i + 0 + F_{ext} \right) P + k_B T P' \right] \quad (7.45)$$

Thus we have exactly the general form for the flux, compare eq. 7.36, if we define an effective potential by

$$W_{eff}(x) = \int_0^x dx' \left( \sum_i \lambda_i(x') W'_i(x') \right) \quad (7.46)$$



Note that the switching rates  $\omega_i$  enter indirectly through the occupancies  $\lambda_i$ .

We now consider the case without external force  $F_{ext}$  and ask under which conditions the system can generate directed motion by itself. Such motion appears if the effective potential is tilted over one period. We therefore define

$$\Delta W_{eff} = \int_0^l dx' \left( \sum_i \lambda_i(x') W_i'(x') \right) \quad (7.47)$$

and ask under which conditions this quantity becomes finite. We then immediately see that two conditions have to be satisfied:

- The potentials  $W_i(x)$  and/or the transition rates  $\omega_i(x)$  have to be asymmetric under  $x \rightarrow -x$ . Otherwise the integrand was symmetric and the integral vanished. A simple example for this would be an asymmetric sawtooth potential. Then the transition rates in principle could be symmetric, but one can show that this is not very efficient, so one expects both potentials and transition rates to be asymmetric.
- The switching rates have to break detailed balance, which means that the system has to be out of equilibrium. Otherwise the steady state distribution would be the Boltzmann distribution

$$\lambda_i(x) = \frac{e^{-W_i/k_B T}}{\sum_i e^{-W_i/k_B T}} \quad (7.48)$$

We then would have

$$\sum_i \lambda_i(x) W_i'(x) = \partial_x \left[ (-k_B T) \ln \left( \sum_i e^{-W_i(x)/k_B T} \right) \right] \quad (7.49)$$

Thus the integrand in Eq. 7.47 would be a total derivative and the integral would vanish.

These two conclusions are non-trivial and must be valid for any specific motor model. One also can show that they are true for the case  $\mu_1 \neq \mu_2$ .

For many purposes, it is useful to define the deviation from equilibrium. This can be done by writing

$$\omega_1 = \omega_2 e^{\beta(W_1 - W_2)} + \Omega(x) \quad (7.50)$$

thus detailed balance corresponds to  $\Omega(x) = 0$ . If one further defines  $\Omega(x) = \Omega \theta(x)$ , then the scalar amplitude  $\Omega$  is a measure for deviation from equilibrium. The excitation distribution  $\theta(x)$  usually is localized around the minimum of the potential  $W_1$  (active site). Note that switching from the minimum is exactly the opposite of what would happen in equilibrium, where switching would occur at the maximum due to detailed balance.

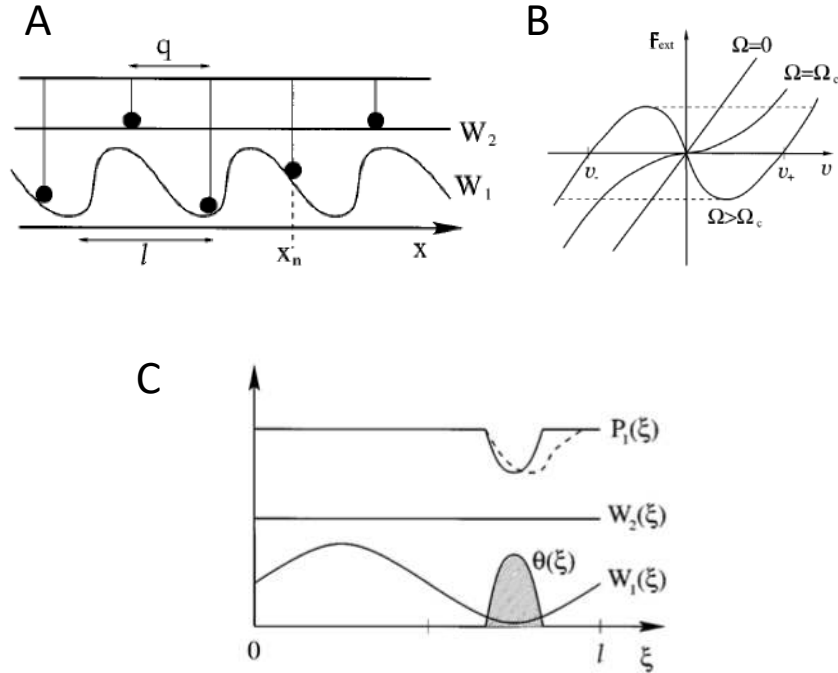


Figure 7.6: (A) We consider an ensemble of motors that is coupled through a rigid backbone. Each motor can bind to the filament and slide down the potential corresponding to the current state. (B) For sufficient deviation  $\Omega > \Omega_c$  from equilibrium, the force-velocity relation becomes negative and spontaneous symmetry breaking with finite velocities  $v_+$  and  $v_-$  occurs at zero forcing. As the external force is varied, a hysteresis loop emerges. (C) Spontaneous motion occurs because excitation causes a dip in  $p_1(x)$  that then moves to the right with velocity  $v$ . This effectively increases the numbers of motors pulling further to the right. Like during a phase transition, this is an instability.

## 7.7 Ratchet model for motor ensembles

As we have seen, the isothermal two-state ratchet model is ideal to identify the conditions for movement of a single motor. We now carry this approach further to address collective effects in ensembles of molecular motors (alternatively, we could look at collective effects in master equations for groups of motors). In the cell, motors rarely work alone, but usually are coupled together in a group, e.g. when transporting cargo along filaments or generating force in the cytoskeleton, in flagella and cilia, or in the muscle. We consider the case that the motors are coupled to a rigid backbone, thus at each time  $t$ , they have the same velocity  $v$ . As we will see, this coupling is sufficient to result in collective effects which resemble phase transitions. Each of the motors can bind to the filament at position  $x$  and then generates a force  $F = -\partial_x W_i(x)$ , depending on which state  $i$  it is in.

We consider a mean field theory, that is many motors that are homogeneously distributed along the backbone, in a manner that is incommensurate with the

potentials with periodicity  $l$ , compare Fig. 7.6(A). We consider the variable  $x$  to be cyclic, thus we only have to deal with a unit cell with  $0 \leq x \leq l$ . We again consider the Fokker-Planck equation for two states, but now for a common velocity  $v$ :

$$\dot{p}_1 + v\partial_x p_1 = -\omega_1(x)p_1 + \omega_2(x)p_2 \quad (7.51)$$

$$\dot{p}_2 + v\partial_x p_2 = \omega_1(x)p_1 - \omega_2(x)p_2 \quad (7.52)$$

The force balance reads

$$v = \mu(F_{ext} + F_{int}) \quad (7.53)$$

where  $\mu$  is mobility and  $F_{ext}$  is the given external force (provided e.g. by an optical tweezer). The internal force is

$$F_{int} = - \int_0^l dx (p_1 \partial_x W_1 + p_2 \partial_x W_2) \quad (7.54)$$

Normalization reads

$$p_1(x, t) + p_2(x, t) = \frac{1}{l} \Rightarrow p_2 = \frac{1}{l} - p_1 \quad (7.55)$$

and  $\int dx (p_1 + p_2) = 1$ .

We now consider steady state,  $\dot{p}_i = 0$ . Together with the normalization, the first of the two Fokker-Planck equations now gives

$$v\partial_x p_1 = -(\omega_1 + \omega_2)p_1 + \frac{\omega_2}{l} . \quad (7.56)$$

The force balance (or momentum conservation) gives

$$F_{ext} = \frac{v}{\mu} - F_{int} = \frac{v}{\mu} + \int_0^l dx p_1 \partial_x (W_1 - W_2) \quad (7.57)$$

where the constant term drops out because we integrate over  $\partial_x W_2$  and  $W_2$  is periodic.

For specific choices of the potentials  $W_i$  and the rates  $\omega_i$ , these equations for the steady state  $p_1(x)$  can now be solved. This will then lead to a force-velocity relation  $F_{ext}(v)$ . Here we want to proceed with generic properties of this theory and therefore make a Taylor expansion in small velocity  $v$ :

$$p_1(x) = \sum_{n=0}^{\infty} p_1^{(n)}(x) v^n . \quad (7.58)$$

The Fokker-Planck equation leads to a recursion relation for the coefficients:

$$p_1^{(0)}(x) = \frac{\omega_2}{(\omega_1 + \omega_2)l}, \quad p_1^{(n)}(x) = \frac{-1}{(\omega_1 + \omega_2)} \partial_x p_1^{(n-1)}(x) \quad (7.59)$$

For the force-velocity relation we get

$$F_{ext} = F^{(0)} + \left(\frac{1}{\mu} + F^{(1)}\right)v + \sum_{n=2}^{\infty} F^{(n)}v^n \quad (7.60)$$

with

$$F^{(n)} = \int dx p_1^{(n)} \partial_x (W_1 - W_2). \quad (7.61)$$

For simplicity we next specify for symmetric potentials ( $W_i(x) = W_i(-x)$ ), so all even coefficients vanish ( $F^{(0)} = F^{(2)} = \dots = 0$ ) and the force-velocity relation  $F_{ext}(v)$  becomes anti-symmetric:

$$F_{ext} = \left(\frac{1}{\mu} + F^{(1)}\right)v + F^{(3)}v^3 + O(v^5) \quad (7.62)$$

For detailed balance ( $\Omega = 0$  in Eq. 7.50), we can calculate

$$F^{(1)} = \int dx \frac{\beta}{l} \frac{e^{\beta(W_1 - W_2)}}{(1 + e^{\beta(W_1 - W_2)})^2} \frac{(\partial_x(W_1 - W_2))^2}{(\omega_1 + \omega_2)} \quad (7.63)$$

thus this quantity is positive and the only solution to the force-velocity relation at zero forcing ( $F_{ext} = 0$ ) is  $v = 0$ . Thus with detailed balance, no spontaneous motion can occur. However, at  $\Omega_c > 0$  the coefficient  $F^{(1)}$  can be negative with  $F^{(1)} = -1/\mu$ . Then finite values for  $v$  become possible for  $\Omega > \Omega_c$ , compare Fig. 7.6(B), and the velocity rises as  $\pm(\Omega - \Omega_c)^{1/2}$ . Thus for sufficiently large deviation from equilibrium, the system spontaneously starts to move. The scaling exponent 1/2 is typical for the mean field theory and the system has to spontaneously break symmetry to move either right or left with velocities  $v_+$  and  $v_-$ , respectively. Note that in contrast to the single motor case, spontaneous motion ensues even for symmetric potentials; for single motors, the asymmetric potential is required to give it its direction, but for multiple motors, the system is persistent and a spontaneous symmetry break occurs. If one now switches on the external force, one can move the velocity away from its value at the transition point, compare Fig. 7.6(B). For example, if the ensemble moves to the right with velocity  $v_+$ , one can pull it to smaller velocities with a negative external force  $F_{ext}$ . However, at a critical value of  $F_{ext}$ , this branch loses stability and jumps to a negative velocity. The same works in the other direction and there is a hysteresis loop. In general, the mathematical structure of this theory is exactly the same as for the second order phase transition of the Ising model for ferromagnetism. Velocity  $v$  corresponds to the magnetization  $M$ , external force  $F_{ext}$  to the magnetic field  $H$ , and the deviation from equilibrium  $\Omega$  to the inverse temperature  $\beta$ . If the system works against an external spring, oscillations occur, as observed often in experiments with molecular motors. A famous example are spontaneous oscillations of hair bundles in the inner ear, which lead to otoacoustic emissions.

Fig. 7.6(C) shows the main mechanism generating the instability leading to spontaneous motion. As the motors are excited at the minimum of  $W_1(x)$ , one gets a dip in  $p_1(x)$ . This dip moves to the right, effectively repopulating the motor population pulling to the right. Thus any fluctuation will be increased and the system is unstable. The same mechanism is at work in phase transition, when the system does not counteract a fluctuation.

## 7.8 Master equation approach for motor ensembles

The main advantage of the ratchet models is that they allow us to analyze the fundamental requirements for motion. In order to describe the function of motor ensembles in close comparison to experiments, however, one usually turns to master equations. Here we discuss a simple version that describe cooperative cargo transport by an ensemble of motors<sup>2</sup>. Rather than focusing on the spatial position of the motor ensemble, we rather will later enforce movement in one direction, but focus on the physical limits of this movement, that is on the possibility that the walk stops because the ensemble loses contact with its track. Therefore we now will consider the relevant internal state of the ensemble, namely the number of bound motors. Similar approaches have been used before to describe the internal dynamics of adhesion clusters<sup>3</sup>.

We consider  $N$  motors, of which  $0 \leq n \leq N$  are bound at any time  $t$ . The variable  $n(t)$  is described by a one-step master equation:

$$\dot{p}_n = \epsilon_{n+1}p_{n+1} + \pi_{n-1}p_{n-1} - (\epsilon_n + \pi_n)p_n \quad (7.64)$$

where  $\epsilon_n$  and  $\pi_n$  are dissociation and association rates, respectively. The stationary state leads to the detailed balance condition

$$\epsilon_{n+1}p_{n+1} = \pi_n p_n \quad (7.65)$$

and this allows us to calculate the steady state probabilities in a recursive manner:

$$p_n = p_0 \prod_{i=0}^{n-1} \frac{\pi_i}{\epsilon_{i+1}} \quad (7.66)$$

where normalization  $\sum_{n=0}^N p_n = 1$  gives us the starting condition

$$p_0 = \left( 1 + \sum_{n=1}^N \prod_{i=0}^{n-1} \frac{\pi_i}{\epsilon_{i+1}} \right)^{-1} = \left( 1 + \sum_{n=0}^{N-1} \prod_{i=0}^n \frac{\pi_i}{\epsilon_{i+1}} \right)^{-1}. \quad (7.67)$$

From here we define a few quantities of interest. The average number of bound motors is

$$N_b = \sum_{n=1}^N n \frac{p_n}{1 - p_0} \quad (7.68)$$

where we have excluded the state  $n = 0$  from the sum and have normalized in respect to the bound states only. The average velocity is

$$v_{eff} = \sum_{n=1}^N v_n \frac{p_n}{1 - p_0} \quad (7.69)$$

---

<sup>2</sup>Our treatment is taken from Stefan Klumpp and Reinhard Lipowsky, Cooperative cargo transport by several molecular motors, PNAS 201: 17284-17289, 2005. Compare also the related paper by Melanie Müller, Stefan Klumpp and Reinhard Lipowsky, Tug-of-war as a cooperative mechanism for bidirectional cargo transport by molecular motors, PNAS 105: 4609-4614, 2008, which generalizes this ansatz to two competing motor ensembles pulling in opposite directions.

<sup>3</sup>Compare Thorsten Erdmann and Ulrich S. Schwarz, Stability of adhesion clusters under constant force, Phys. Rev. Lett., 92:108102, 2004.

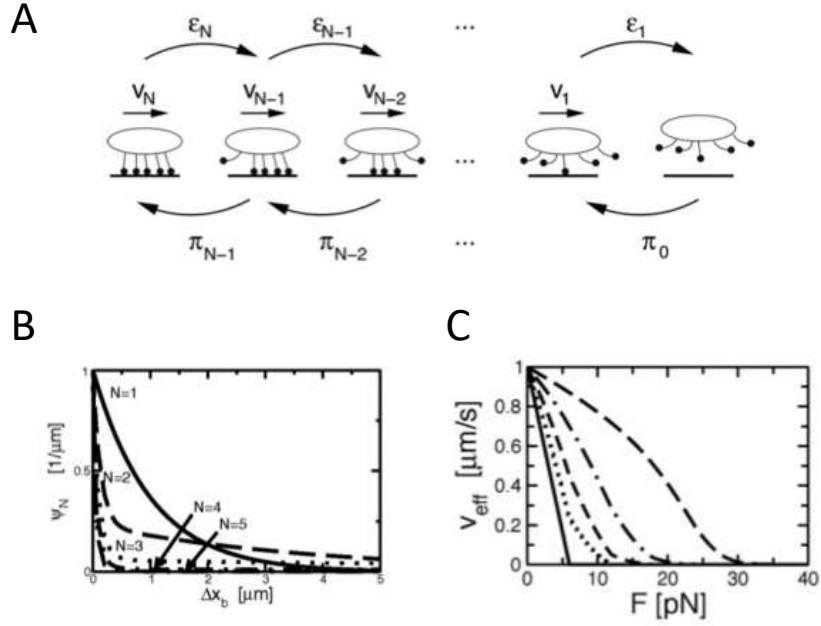


Figure 7.7: (A) Definition of the one-step master equation for cooperative transport by motor ensembles. (B) Distribution of walking distances for group size  $N = 1, 2, 3, 4, 5$  kinesin motors without load. For large  $N$ , these distributions become very flat and their averages grow. (C) Force-velocity relation for  $N = 1, 2, 3, 5, 10$  kinesin motors. The effective stall force increases and the curve changes from linear to concave-down. From Klumpp and Lipowsky PNAS 2005.

and the effective unbinding rate  $\epsilon_{eff}$  is defined by

$$\epsilon_{eff}(1 - p_0) = \pi_0 p_0 . \quad (7.70)$$

The inverse of this would be the average time  $\langle \Delta t_b \rangle$  it takes for the ensemble to unbind. We can calculate

$$\epsilon_{eff} = \pi_0 \frac{p_0}{1 - p_0} = \frac{\pi_0}{\left( \sum_{n=0}^{N-1} \prod_{i=0}^n \frac{\pi_i}{\epsilon_{i+1}} \right)} = \frac{\epsilon_0}{\left( 1 + \sum_{n=1}^{N-1} \prod_{i=1}^n \frac{\pi_i}{\epsilon_{i+1}} \right)} \quad (7.71)$$

Finally we define the average walking distance  $\langle \Delta x_b \rangle$ . This can be simply achieved by replacing  $\epsilon_n$  by  $\epsilon_n/v_n$  and  $\pi_n$  by  $\pi_n/v_n$  in the formula for  $\langle \Delta t_b \rangle$  (thus replacing inverse time steps by inverse step sizes):

$$\langle \Delta x_b \rangle = \frac{v_1}{\epsilon_1} \left( 1 + \sum_{n=1}^{N-1} \prod_{i=1}^n \frac{\pi_i v_{i+1}}{\epsilon_{i+1} v_i} \right) \quad (7.72)$$

### 7.8.1 Without load

Our model definition is now concluded and to continue, we have to specify rates and velocity for the different states  $n$ . We first consider the case of vanishing external load. We set

$$\epsilon_n = n\epsilon, \pi_n = (N - n)\pi, v_n = v \quad (7.73)$$

assuming that each bond dissociates and associates with constant rates  $\epsilon$  and  $\pi$ , respectively, independent of the others, thus leading to the combinatorial factors, and that velocity  $v$  is independent of state. We define  $\gamma = \pi/\epsilon$ , the dimensionless (re)binding rate. The probability distribution now is simply a binomial distribution, because each bond is open and closed with the probabilities  $1/(1 + \gamma)$  and  $\gamma/(1 + \gamma)$ , respectively:

$$p_n = \binom{N}{n} \left(\frac{1}{1 + \gamma}\right)^n \left(\frac{\gamma}{1 + \gamma}\right)^{N-n} = \binom{N}{n} \frac{\gamma^n}{(1 + \gamma)^N} \quad (7.74)$$

With some work, one can check that this agrees with the general formulae given above. In particular, we have  $p_0 = 1/(1 + \gamma)^N$ .

The average number of bound motors follows from the average of the binomial distribution (with the normalization to the bound states):

$$N_b = \frac{1}{1 - p_0} \langle n \rangle = \frac{1}{1 - p_0} \frac{\gamma}{1 + \gamma} N = \frac{\gamma(1 + \gamma)^{N-1}}{(1 + \gamma)^N - 1} N \approx \frac{\gamma}{1 + \gamma} N \quad (7.75)$$

with the last expression being valid in the limit of very large  $N$ . In the limit of large  $\gamma$  we get  $N_b \approx N$ . The effective unbinding rate follows as

$$\epsilon_{eff} = \pi_0 \frac{p_0}{1 - p_0} = \frac{N\gamma\epsilon}{(1 + \gamma)^N - 1} \quad (7.76)$$

and therefore the average bound time is

$$\langle \Delta t_b \rangle = \frac{1}{\epsilon_{eff}} = \frac{(1 + \gamma)^N - 1}{N\gamma\epsilon} \quad (7.77)$$

From here we get the average run length

$$\langle \Delta x_b \rangle = v \langle \Delta t_b \rangle = \frac{v}{N\gamma\epsilon} [(1 + \gamma)^N - 1] \quad (7.78)$$

Thus we see that it increases exponentially with  $N$ , thus larger clusters can walk for much longer distances as long as  $\gamma > 1$ . In the limit of very weak binding, we make a Taylor expansion in  $\gamma$  and find

$$\langle \Delta x_b \rangle \approx \frac{v}{\epsilon} \left[1 + \frac{(N - 1)}{2} \gamma\right] \quad (7.79)$$

The first term corresponds to the single motor. In this case, the additional increase due to cooperativity is only linear in  $N$ .

In the case of kinesin, we have  $v = \mu\text{m/s}$ ,  $\epsilon = 1 \text{ Hz}$  and  $\pi = 5 \text{ Hz}$ , thus  $\gamma = 5$  and run length increases exponentially with motor number. For  $N = 5$ , we are already up from 1 to 311  $\mu\text{m}$ , and 100 motors give one meter. However, this is only a statement on the average. One can also calculate the full distribution and finds that it becomes very broad for large collectives.

### 7.8.2 With load

In order to deal with the case of mechanical load  $F$ , we use the linearized force-velocity relation:

$$v_n(F) = v \left(1 - \frac{F}{nF_s}\right) \quad (7.80)$$

Very importantly, here we account for the fact that force  $F$  is distributed over the bound motors (*load sharing*), thus dissipating its effect over the cluster. While the association is usually assumed to be force-independent, for the dissociation we have to take force into account:

$$\pi_n = (N - n)\pi, \epsilon_n(F) = n\epsilon e^{F/(nF_d)} \quad (7.81)$$

The second equation (*Bell-relation*) takes into account that dissociation is exponentially increased by force, as explained by Kramers theory. Here again we also take load sharing into account. For kinesin, the stall force  $F_s$  and the detachment force  $F_d$  are 6 and 3 pN, respectively. If one now evaluates the formulae given above for these rates, one finds that increasing  $N$  leads to a much slower decay in the force-velocity relation, and changes its character from linear to concave-down.



## Chapter 8

# Diffusion

Life is motion. In the preceding chapter on molecular motors we have learned how biological systems actively generate directed motion. However, there is an even simpler mode of motion that cells can always rely on, and this is passive diffusion due to the relatively high temperature of biological systems. Diffusive motion can be modeled by symmetric random walks, as used before for polymers, and indeed we get the same scaling laws. The diffusion constant is closely related to the viscosity of the surrounding fluid as described by the Stokes-Einstein relation. In order to derive this relation, we have to start with some remarks on hydrodynamics. The laws of viscous hydrodynamics (low Reynolds number) determine how molecules ( $nm$ ) and cells ( $\mu m$ ) move, and these laws are very different from hydrodynamics on macroscopic scales ( $m$ , large Reynolds number). Because the low Reynolds number world is beyond our everyday experience, we have to build some intuition how life is like on the small scale of molecules and cells. Once we have established the theoretical values for the diffusion constant, we can ask how to measure it experimentally. Today this is usually being done using fluorescence microscopy and we introduce the corresponding theory<sup>1</sup>.

### 8.1 Life at low Reynolds-number

We consider many particles moving with a smooth flow field  $\vec{v}(\vec{r}, t)$ , see figure 8.1. We first note that in the absence of sources and sinks, what flows in has to flow out. This is described by the continuity equation:

$$\begin{aligned} \frac{\partial}{\partial t} \int \rho dV &= \int \dot{\rho} dV = - \int (\rho \vec{v}) d\vec{A} = - \int \vec{\nabla} \cdot (\rho \vec{v}) dV \\ \Rightarrow \dot{\rho} + \vec{\nabla} \cdot (\rho \vec{v}) &= 0 \stackrel{\rho = const}{\Rightarrow} \vec{\nabla} \cdot \vec{v} = 0 \end{aligned} \quad (8.1)$$

where the last equation follows for an incompressible fluid.

---

<sup>1</sup>The physics of low Reynolds number and diffusion to capture are discussed in the classical book by Howard Berg, *Random walks in Biology*, Princeton University Press 1993. The calculations for FRAP and FCS follow the original literature. FRAP (but not FCS) is also explained in the book by Rob Phillips.

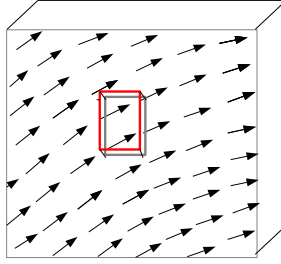


Figure 8.1: For many molecules moving together, we can assume a smooth flow field  $\vec{v}(\vec{r}, t)$ .

The exact movement of fluids is described by the Navier-Stokes equation, which follows from momentum conservation. We first write Newton's second law:

$$\underbrace{\rho \frac{d\vec{v}(\vec{r}, t)}{dt}}_{\text{force density}} = \underbrace{\vec{f}(\vec{v})}_{\text{all forces}} = \vec{f}_e + \vec{f}_i$$

where  $\vec{f}_e$  is the external force (e.g. gravity) and  $\vec{f}_i$  is the internal force (viscous force and pressure). For our further discussion we neglect  $\vec{f}_e$  and focus on the internal forces, that follow from the stress tensor  $\sigma_{ij} = \eta(\partial_i v_j + \partial_j v_i) - p\delta_{ij}$  with shear viscosity  $\eta$  as

$$\vec{f}_i = \vec{\nabla} \cdot \sigma = \eta \Delta \vec{v} - \vec{\nabla} p$$

if we assume incompressibility  $\partial_i v_i = 0$  (otherwise also bulk viscosity becomes relevant). It is important to remember that molecules move both in space and time, so we have to Taylor expand the flow field vector  $\vec{v}(\vec{r}, t)$  as

$$d\vec{v}(\vec{r}, t) = \vec{v}(\vec{r} + \vec{v}dt, t + dt) - \vec{v}(\vec{r}, t) = \frac{\partial \vec{v}}{\partial t} \Delta t + \vec{v} \cdot \vec{\nabla} \cdot \vec{v} \Delta t + \dots$$

Under the assumption that the fluid is incompressible, we thus get a non-linear partial differential equation of motion, the Navier-Stokes equation:

$$\boxed{\rho \underbrace{\left[ \frac{\partial \vec{v}}{\partial t} + (\vec{v} \cdot \vec{\nabla}) \vec{v} \right]}_{\text{inertial forces}} = \eta \Delta \vec{v} - \vec{\nabla} p} \quad \text{Navier-Stokes equation} \quad (8.2)$$

Together with the continuity equation, we have four equations for the four variables  $\vec{v}(\vec{r}, t)$  and  $p(\vec{r}, t)$ .

In the Navier-Stokes equation inertial and viscous forces compete with a relative magnitude called *Reynolds number*:

$$\frac{\frac{\rho v^2}{L}}{\frac{\eta v}{L^2}} = \frac{\rho v L}{\eta} =: Re \quad \text{Reynolds number} \quad (8.3)$$

Here  $L$  is the typical length scale.  $Re \gg 1$  implies predominance of inertia, and  $Re \ll 1$  means predominance of viscosity. To illustrate this we look at two examples of movement in water ( $\rho = 1 \frac{\text{kg}}{\text{l}} = 1 \frac{\text{g}}{\text{cm}^3}$  and  $\eta = 10^{-3} \text{ Pa} \cdot \text{s}$ ).

- For humans (swimming)  $Re = \frac{\frac{\text{g}}{\text{cm}^3} \frac{\text{m}}{\text{s}} m}{10^{-3} \text{ Pa} \cdot \text{s}} = 10^6$
- for molecules/cells  $Re = \frac{\frac{\text{g}}{\text{cm}^3} \frac{\mu\text{m}}{\text{s}} \mu\text{m}}{10^{-3} \text{ Pa} \cdot \text{s}} = 10^{-6}$

The difference in the Reynolds numbers is twelve orders of magnitude, which emphasizes the different character of the motion. For humans swimming in water the predominant forces are of inertial origin, but for the molecules the hydrodynamic forces have viscous character.

We can say that molecules live in an Aristotelian world, while our intuition comes from a Newtonian one. Being a molecule or cell means living in syrup — everything is very viscous. Contrary to our every day intuition, the movement of molecules in water stops if there is no force to sustain it. In this limit ( $Re \ll 1$ ) the Navier-Stokes equation becomes the Stokes equation

$$\boxed{\eta \Delta \vec{v} = -\vec{\nabla} p} \quad (8.4)$$

For example, from the Stokes equation one can calculate the *Stokes force* required to drag a sphere of radius  $R$  with velocity  $v$  through a viscous fluid ( $\eta$ ), see figure 8.2:

$$\boxed{F_S = 6\pi\eta R v} \quad (8.5)$$

We call the constant term  $6\pi\eta R$  the friction coefficient  $\xi$ .

The most drastic difference between the Navier-Stokes and the Stokes equations is that the time-dependence has dropped out. This implies that if we stop and reverse a motion, we get back exactly to the initial state. Therefore a microscopic swimmer cannot move by reversing a one-dimensional process, like the up and down movement of a rigid appendix (*scallop theorem*, because the macroscopic scallop moves by opening and closing its shells). Microswimmers have evolved two main strategies to beat the scallop theorem: either a flexible appendix (like the eukaryotic flagellum of e.g. sperm cells or green algae, making the forward and backward strokes very different) or a helical appendix that can turn without reversing its motion (like the bacterial flagellum).

Despite the viscous nature of its environment, there is one type of forces, which always keeps molecules on the move, namely thermal forces. The resulting motion

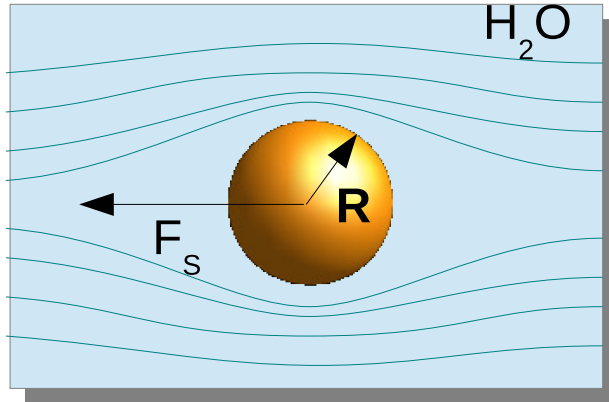


Figure 8.2: A sphere with radius  $R$  moving through water under the action of force  $F_S$ .

is diffusive (random walk, compare chapter 6)

$$\begin{aligned}
 \langle \bar{r}^2 \rangle &= \left\langle \left( \sum_i \vec{r}_i \right) \left( \sum_j \vec{r}_j \right) \right\rangle = \sum_{i=1}^N \langle \vec{r}_i^2 \rangle \\
 &= dN\Delta x^2 = 2d \frac{t}{\Delta t} \frac{1}{2} \Delta x^2 \\
 &= \boxed{2dDt} \tag{8.6}
 \end{aligned}$$

with

$$\boxed{D = \frac{\Delta x^2}{2\Delta t}} \quad \text{diffusions coefficient}$$

Note that the mean squared displacement grows only linearly with time, like the mean squared end-to-end distance of polymers grows only linearly with their contour length.

We next want to relate the diffusion constant to the viscosity. We start with some simple arguments and later present a rigorous derivation. We now consider a small biomolecule of mass  $100kDa$ :

$$\begin{aligned}
 \frac{1}{2}mv^2 &= \frac{k_B T}{2} \quad \text{equipartition} \\
 \Rightarrow v &= \left( \frac{k_B T}{m} \right)^{\frac{1}{2}} = \left( \frac{4.1 \text{ pN} \cdot \text{nm}}{100 \text{ kDa}} \right)^{\frac{1}{2}} = 10 \frac{\text{m}}{\text{s}}
 \end{aligned}$$

This is the typical velocity between collisions. Dynamically molecular velocity can be thought to be generated by some thermal force  $F$ , acting between the collisions:

$$\begin{aligned}
 m\ddot{x} &= F \\
 \Rightarrow \Delta x &= \frac{F}{2m} (\Delta t)^2 \\
 \Rightarrow v &= \frac{\Delta x}{\Delta t} = \frac{F\Delta t}{2m} = \frac{F}{\xi}
 \end{aligned}$$

Here  $\xi$  is the friction coefficient.

$$\begin{aligned}
 \xi &= \frac{2m}{\Delta t} \\
 \Rightarrow D\xi &= m \frac{\Delta x^2}{\Delta t^2} = mv^2 = k_B T \\
 \Rightarrow \boxed{D = \frac{k_B T}{\xi}} & \quad \text{Einstein relation} \\
 & \quad \text{connecting diffusion and friction} \quad (8.7)
 \end{aligned}$$

This is an example of a fluctuation ( $D$ ) - dissipation ( $\xi$ ) relation. We can substitute the Stokes result for the friction coefficient:

$$\boxed{D = \frac{k_B T}{6\pi\eta R}} \quad \text{Stokes-Einstein relation} \quad (8.8)$$

Thus the more viscous the environment, the smaller the diffusion constant.

A numerical example for a biomolecule is

$$D = \frac{4.1 \text{ pN nm}}{6\pi \cdot 10^{-3} \text{ Pa} \cdot \text{s} \cdot 1 \text{ nm}} = 10^{-6} \frac{\text{cm}^2}{\text{s}} = \frac{(10 \mu\text{m})^2}{\text{s}} \quad (8.9)$$

Thus it takes a typical molecule 1 s to diffuse across the cell ( $\frac{10 \mu\text{m}}{10 \frac{\text{m}}{\text{s}}} = \mu\text{s}$  without collisions). Note that this value is relatively universal because temperature and viscosity are essentially fixed for a biological systems. It has been argued that cells are typically of micrometer size because intracellular transport and signal transduction becomes too slow on larger scales. We also estimate

$$\Delta x = \frac{2D}{v} = \frac{2 \cdot 10^{-6} \frac{\text{cm}^2}{\text{s}}}{10 \frac{\text{m}}{\text{s}}} = 0.2 \text{ \AA}$$

and

$$\Delta t = \frac{\Delta x}{v} = \frac{0.2 \text{ \AA}}{10 \frac{\text{m}}{\text{s}}} = 2 \text{ ps}$$

One can conclude that mean free path length and collision time are extremely small.

We now present a more rigorous derivation of the Einstein relation starting from the Fokker-Planck (or Smoluchowski) equation:

$$\begin{aligned}
 \dot{p} &= -\vec{\nabla} \cdot \vec{J}(\vec{r}) \\
 \vec{J}(\vec{r}) &= \underbrace{-D\vec{\nabla}p}_{\text{diffusion}} + \underbrace{p \cdot \vec{v}}_{\text{drift}} \quad (8.10)
 \end{aligned}$$

We introduce a viscous force:

$$\vec{F} = -\vec{\nabla}U = \xi\vec{v}$$

and look how the system reacts. In equilibrium  $\dot{p} = 0$ , which means that  $\vec{\nabla} \cdot \vec{J}(\vec{r}) = 0$ . If the system is confined, the flux has to vanish. That means

$$\begin{aligned}
 D\vec{\nabla}p &= p \cdot \vec{v} = -p \frac{\vec{\nabla}U}{\xi} \\
 \Rightarrow p(\vec{x}) &= p_0 \exp\left(-\frac{U}{D\xi}\right) = p_0 \underbrace{\exp\left(-\frac{U}{k_B T}\right)}_{\text{Boltzmann factor}} \\
 \Rightarrow \boxed{D = \frac{k_B T}{\xi} = \frac{k_B T}{6\pi\eta R}} &\quad \text{Stokes-Einstein relation}
 \end{aligned}$$

We again get the Stokes-Einstein relation for the diffusion coefficient. In contrast to the scaling argument above, this derivation is rigorous.

## 8.2 Measuring the diffusion constant

How can we measure the diffusion coefficient of a biomolecule? Usually the molecules of interest have to be marked, e.g. with a fluorophore like the Green Fluorescent Protein (GFP). Then several different techniques are possible, including single molecule tracking, Fluorescence Recovery After Photo-bleaching (FRAP) and Fluorescence Correlation Spectroscopy (FCS).

### 8.2.1 Single particle tracking

Following the trajectory of a single particle in a medium is a challenging task. The best way to track a molecule is to observe the fluorescence it emits. But since the mean distance between the particles is on the order of 10 nm and the focused laser beam has a typical diameter on the order of a few 100 nm, one excites a few  $10^3$  molecules at the same time. One solution to this problem is to use gold particles as markers, instead of fluorophores, because they can be attached to a sub-population. Another way is to use super-resolution microscopy (STED, PALM, STORM, etc). In general, single particle tracking works best if the molecule is diffusing in a membrane, like a surface receptor.

### 8.2.2 Fluorescence Recovery After Photo-bleaching (FRAP)

By this method intense laser light is used to bleach (destroy) the fluorophores in a well-defined region, e.g. a stripe with diameter  $2a$  on a plate with length  $2L$ , see figure 8.3.

For example one can monitor the concentration of fluorophores over time at a given point in space, e.g.  $c(x=0, t)$ . Then the recovery kinetics allows one to fit the diffusion constant  $D$ .

For the full calculation we have to know the initial conditions:

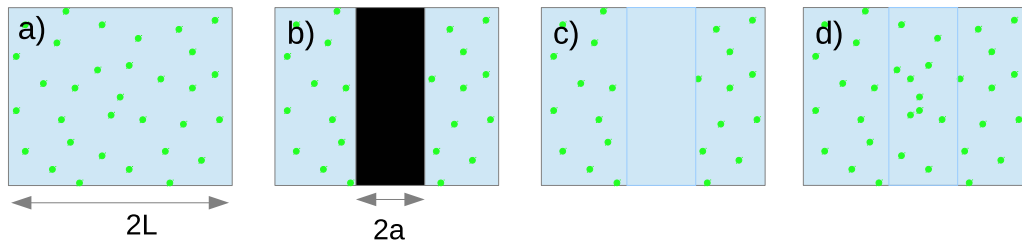


Figure 8.3: FRAP. Concentration of fluoreophores on a plate of length  $2L$ . a) System before bleaching. b) System at time  $t = 0$ , when the laser light bleaches a stripe of width  $2a$ . c) Bleached spot d) Recovery of the system after some time  $\Delta t$ .

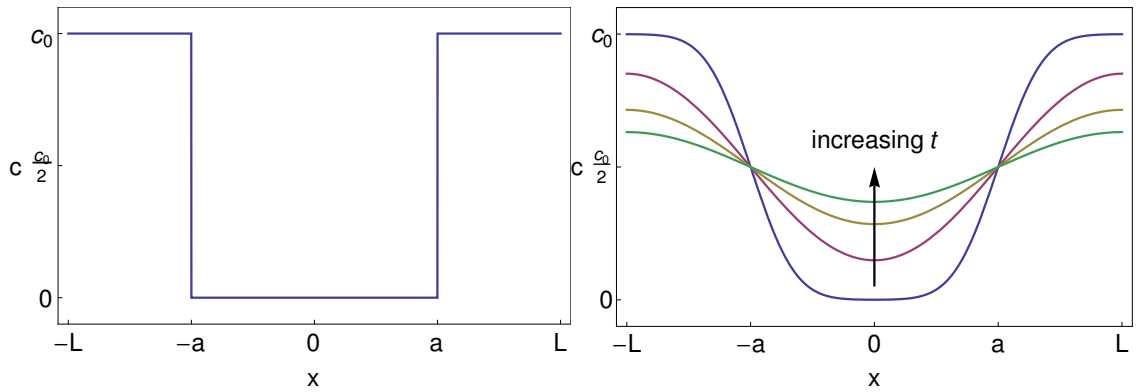


Figure 8.4: Fluorescence intensity as a function of the space coordinate after bleaching. On the left side you can see the bleached spot at the initial moment. On the right-hand side you can follow the recovery of the intensity with time.

$$c(x, 0) = \begin{cases} c_0 & -L < x < -a \\ 0 & -a < x < a \\ c_0 & a < x < L \end{cases}$$

We also need to define some boundary conditions, e.g. no flux at the boundaries:

$$c'(x, t)|_{x=\pm L} = 0$$

We separate the variables using Fourier expansion:

$$c(x, t) = A_0(t) + \sum_{n=1}^{\infty} A_n(t) \cos\left(\frac{xn\pi}{L}\right)$$

Now we have an even function with the right boundary conditions, and we still have to find the coefficients  $A_0$  and  $A_n$ .

The cosine functions form an orthogonal system:

$$\int_{-L}^L \cos\left(\frac{xn\pi}{L}\right) \cos\left(\frac{xm\pi}{L}\right) dx = L\delta_{nm}$$

$$\begin{aligned} \Rightarrow \frac{\partial A_0}{\partial t} + \sum_{n=1}^{\infty} \frac{\partial A_n}{\partial t} \cos\left(\frac{xn\pi}{L}\right) &= D \sum_{n=1}^{\infty} \left(-A_n \frac{n^2\pi^2}{L^2}\right) \cos\left(\frac{xn\pi}{L}\right) \\ \Rightarrow \frac{\partial A_0}{\partial t} &= 0 \\ \frac{\partial A_n}{\partial t} &= -\frac{Dn^2\pi^2}{L^2} A_n \\ A_n(t) &= A_n(0) \exp\left(-\left(D \frac{n^2\pi^2}{L^2}\right)t\right) \end{aligned}$$

We still need the initial values (Fourier transform of the step function):

$$A_0(0) = \frac{1}{2L} \int_{-L}^L dx c(x, 0) = c_0 \frac{L-a}{L} = c_{\infty}$$

$$A_n(0) = \frac{1}{L} \int_{-L}^L dx c(x, 0) \cos\left(\frac{xn\pi}{L}\right)$$

Here we can use the symmetry of the system and calculate the integral just for  $x$  between  $a$  and  $L$  and multiply the result by 2.



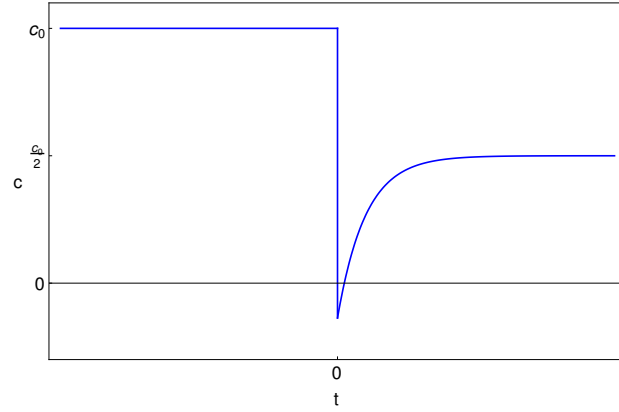


Figure 8.5: Behaviour of the concentration of fluorophores in time by a FRAP experiment, with  $a = \frac{L}{2}$ ,  $x = 0$ ,  $n = 1$ . The negative value  $c(0,0)$  is an artefact of using  $n = 1$ . The relaxation time is  $t_1 = \frac{L^2}{D\pi^2}$ . In reality, one has to sum over many modes, thus including all time scales  $t_n$ .

$$\begin{aligned}
 &= \frac{2c_0}{L} \int_a^L dx \cos\left(\frac{xn\pi}{L}\right) \\
 &= \frac{2c_0}{L} \frac{L}{n\pi} \sin\left(\frac{xn\pi}{L}\right) \Big|_a^L \\
 &= -\frac{2c_0}{n\pi} \sin\left(\frac{an\pi}{L}\right)
 \end{aligned}$$

Thus we get

$$c(x, t) = c_0 \left[ \left(1 - \frac{a}{L}\right) - \frac{2}{\pi} \sum_{n=1}^{\infty} \frac{1}{n} \sin\left(\frac{an\pi}{L}\right) \exp\left(-D \frac{n^2 \pi^2}{L^2} t\right) \cos\left(\frac{xn\pi}{L}\right) \right]$$

This sum converges slowly, which means that if one wants a precise result, one has to take many modes into account. Each mode has its own time scale  $t_n = \frac{L^2}{D\pi^2 n^2}$ . This makes the calculations very difficult. A convenient choice for simplification of the equation is  $a = \frac{L}{2}$ . And to qualitatively understand the result we look just at the first mode, see figure 8.5, e.g.

$$\begin{aligned}
 x &= 0 \\
 n &= 1 \\
 c(x=0, t) &= c_0 \left[ \frac{1}{2} - \frac{2}{\pi} \exp\left(-\frac{t}{t_1}\right) \right]
 \end{aligned}$$

Here  $c(x=0, t=0)$  becomes negative, which is an artefact of using only  $n = 1$ . For a circular bleach spot a closed form solution exists involving modified Bessel

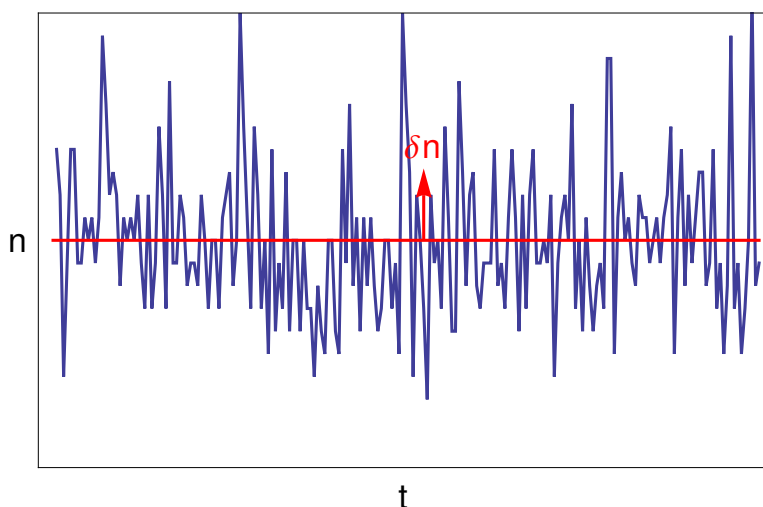


Figure 8.6: Photon count over time  $n(t)$  for molecules freely diffusing in and out of the focal volume.

function <sup>2</sup>:

$$F(t) = \exp\left(-\frac{\tau_D}{2t}\right) \left[ J_0\left(\frac{\tau_D}{2t}\right) + J_1\left(\frac{\tau_D}{2t}\right) \right] \quad (8.11)$$

Here  $F(t)$  is normalized average over the bleached spot;  $\tau_D = \frac{w^2}{D}$ , with  $w$  the radius of the focused beam and  $J_0$  and  $J_1$  are the Bessel functions of zeroth and first order.

### 8.2.3 Fluorescence Correlation Spectroscopy (FCS)

The FCS method was developed and published in the 1970s<sup>3</sup>.  $N$  fluorescent molecules pass through the sub-femtoliter detection volume  $V$  of a confocal microscope (the standard instrument for FCS). One can measure the number of photons  $n(t)$  in the photomultiplier as a function of time, see figure 8.6.

Then one calculates the auto-correlation function

$$G(\tau) = \frac{\langle \delta n(t) \delta n(t + \tau) \rangle}{\langle n \rangle^2}$$

where  $\delta n(t) = n(t) - \langle n \rangle$  are the variations of  $n$ . The auto-correlation function is the convolution of the signal at time  $t$  with the signal at the same place after

<sup>2</sup>Axelrod, D., Koppel, D. E., Schlessinger, J., Elson, E. & Webb, W. W. Mobility measurement by analysis of fluorescence photobleaching recovery kinetics. *Biophys. J.* 16, 1055-1069 (1976); Soumpasis, D. M. 1983. Theoretical analysis of fluorescence photobleaching recovery experiments. *Biophys. J.* 41:95-97; Sprague, B.L. et al., Analysis of binding reactions by fluorescence recovery after photobleaching, *Biophys. J.* 86: 3473-3495 (2004).

<sup>3</sup>D. Magde, E. Elson, and W. W. Webb, *Phys. Rev. Lett.*, 29,705 (1972); D. Magde, E. L. Elson, and W. W. Webb, *Biopolymers*, 13,29 (1974); S. R. Aragon and R. Pecora, *J. Chem. Phys.* 64, 179 (1976)

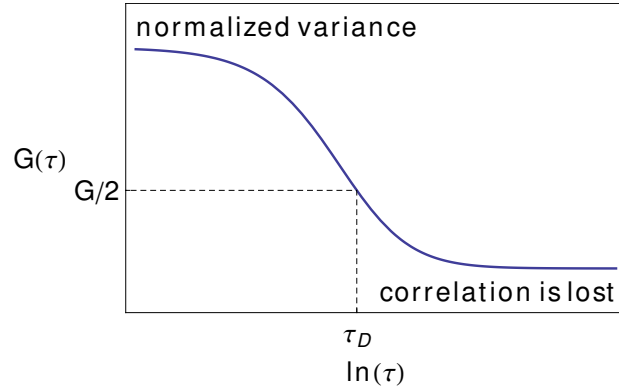


Figure 8.7: Auto-correlation function. This fit measures the self-similarities of the signal after a lag time  $\tau$ .

a lag time  $\tau$  normalized by the squared mean intensity. An equivalent form is

$$\begin{aligned}
 G(\tau) &= \frac{\langle (n(t) - \langle n \rangle)(n(t + \tau) - \langle n \rangle) \rangle}{\langle n \rangle^2} \\
 &= \frac{\langle n(t)n(t + \tau) \rangle}{\langle n \rangle^2} - 1
 \end{aligned} \tag{8.12}$$

Note that the mean number of photons  $\langle n \rangle = \frac{1}{M} \sum_{i=0}^M n_i$  is time independent. Now we calculate the auto-correlation function from a reasonable model. We assume free diffusion. A Gaussian beam is focused to a volume  $V$ , which has some elongation  $K$  in the z-axis:

$$\rho(x, y, z) = \rho_0 \exp\left(-\frac{2(x^2 + y^2 + \frac{z^2}{K^2})}{w^2}\right)$$

$w$  is the  $e^{-2}$  size of the detection volume. For the laser power we get

$$P = \int d\vec{r} \rho(\vec{r}) = \rho_0 \underbrace{\left(\frac{\pi}{2}\right)^{3/2} w^3 K}_{\text{effective detection volume } V}$$

Assuming perfect emission efficiency, the photon count is

$$n(t) = \int d\vec{r} \rho(\vec{r}) c(\vec{r}, t)$$

which means that  $\langle n \rangle = \langle c \rangle V = N$  is the number of molecules in the focus.

$$\Rightarrow \delta n(t) = \int d\vec{r} \rho(\vec{r}) \delta c(\vec{r}, t)$$

The concentration fluctuations relax according to the diffusion equation

$$\frac{\partial(\delta c(\vec{r}, t))}{\partial t} = D \nabla^2 \delta c(\vec{r}, t)$$

with the boundary condition  $\delta c(\vec{r} = \infty, t) = 0$ .

Now, we transform to Fourier space:

$$\begin{aligned}\frac{\partial(\delta c(\vec{k}, t))}{\partial t} &= -Dk^2 \delta c(\vec{k}, t) \\ \Rightarrow \delta c(\vec{k}, t) &= \delta c(\vec{k}, 0) \exp(-Dk^2 t),\end{aligned}$$

because the back transformation is  $f(x) \rightarrow f(k) = \int dx f(x) \exp(-ikx)/(2\pi)$  and the second derivative gives a factor of  $-k^2$ .

$$\begin{aligned}G(\tau) &= \frac{\langle \delta n(0) \delta n(\tau) \rangle}{\langle n \rangle^2} \\ &= \frac{1}{N^2} \int d\vec{r} \int d\vec{r}' \rho(\vec{r}) \rho(\vec{r}') \langle \delta c(\vec{r}, 0) \delta c(\vec{r}', \tau) \rangle\end{aligned}\quad (8.13)$$

We first evaluate

$$\langle \delta c(\vec{r}, 0) \delta c(\vec{r}', \tau) \rangle = \int d\vec{k} \exp(i\vec{k}\vec{r}') \langle \delta c(\vec{r}, 0) \underbrace{\delta c(\vec{k}, \tau)}_{=\delta c(\vec{k}, 0) \exp(-Dk^2 \tau)} \rangle$$

We transform back to get the correlation at equal times:

$$\langle \delta c(\vec{r}, 0) \delta c(\vec{r}', \tau) \rangle = \frac{1}{(2\pi)^3} \int d\vec{k} \exp(i\vec{k}\vec{r}') \exp(-Dk^2 \tau) \int d\vec{r}'' \exp(-i\vec{k}\vec{r}'') \underbrace{\langle \delta c(\vec{r}, 0) \delta c(\vec{r}'', 0) \rangle}_{=\langle c \rangle \delta(\vec{r}-\vec{r}'')}$$

Thus we assume that spatial correlation only exists at the same position and that the second moment is proportional to the average (typical for a Poisson process). Therefore

$$\langle \delta c(\vec{r}, 0) \delta c(\vec{r}', \tau) \rangle = \frac{\langle c \rangle}{(2\pi)^3} \int d\vec{k} \exp(-i\vec{k}(\vec{r} - \vec{r}')) \exp(-Dk^2 \tau)$$

At this point we want to remind briefly that for Gaussian integrals

$$\begin{aligned}\int \exp(-ax^2 \pm ibx) &= \sqrt{\frac{\pi}{a}} \exp\left(-\frac{b^2}{4a}\right) \\ \int \exp(-ax^2 + bx) &= \sqrt{\frac{\pi}{a}} \exp\left(\frac{b^2}{4a}\right)\end{aligned}$$

Therefore

$$\langle \delta c(\vec{r}, 0) \delta c(\vec{r}', \tau) \rangle = \frac{\langle c \rangle}{(2\pi)^3} \left(\frac{\pi}{D\tau}\right)^{\frac{3}{2}} \exp\left(-\frac{(\vec{r} - \vec{r}')^2}{4D\tau}\right)$$

The integral separates in the three spatial dimensions. We calculate it for the

x-direction:

$$\begin{aligned}
& \int dx \int dx' \exp\left(-\frac{2x^2}{w^2}\right) \exp\left(-\frac{2x'^2}{w^2}\right) \exp\left(-\frac{(x-x')^2}{4D\tau}\right) \\
\stackrel{u=x-x'}{=} & \int du \int dx' \exp\left(-2\frac{(u^2 + 2ux' + x'^2)}{w^2}\right) \exp\left(-2\frac{x'^2}{w^2}\right) \exp\left(\frac{-u^2}{4D\tau}\right) \\
= & \int du \exp\left(-\left(\frac{2}{w^2} + \frac{1}{4D\tau}\right)u^2\right) \underbrace{\int dx' \exp\left(-\frac{4x'^2}{w^2}\right) \exp\left(-\frac{4ux'}{w^2}\right)}_{=\left(\frac{\pi w^2}{4}\right)^{\frac{1}{2}} \exp\left(\frac{u^2}{w^2}\right)} \\
= & \left(\frac{\pi w^2}{4}\right)^{\frac{1}{2}} \int du \exp\left(-\left(\frac{1}{w^2} + \frac{1}{4D\tau}\right)u^2\right) \\
= & \left(\frac{\pi w^2}{4}\right)^{\frac{1}{2}} \left(\frac{\pi}{\frac{1}{w^2} + \frac{1}{4D\tau}}\right)^{\frac{1}{2}} \\
= & \frac{\pi w}{2} \left(\frac{1}{1 + \frac{\tau}{\tau_D}}\right)^{\frac{1}{2}} (4D\tau)^{\frac{1}{2}} \quad \text{with } \tau_D = \frac{w^2}{4D} \\
\Rightarrow G(\tau) = & \frac{\langle c \rangle \rho_0}{(2\pi)^{\frac{3}{2}} N^2} \left(\frac{\pi}{D\tau}\right)^{\frac{3}{2}} \left(\frac{\pi w}{2}\right)^2 \frac{1}{\left(1 + \frac{\tau}{\tau_D}\right)} (4D\tau)^{\frac{3}{2}} \left(\frac{\pi K w}{2}\right) \left(\frac{1}{1 + \frac{\tau}{K^2 \tau_D}}\right)^{\frac{1}{2}} \\
\stackrel{\langle c \rangle = V=N}{=} & \frac{\rho_0^2}{N} \left(\frac{1}{1 + \frac{\tau}{\tau_D}}\right) \left(\frac{1}{1 + \frac{\tau}{K\tau_D}}\right)^{\frac{1}{2}}
\end{aligned}$$

If we assume symmetrical focal volume  $V$  ( $K = 1$ ) and initial intensity  $\rho_0 = 1$ , then for the auto-correlation function we get the simple result

$$G(\tau) = \frac{1}{N} \frac{1}{\left(1 + \frac{\tau}{\tau_D}\right)^{\frac{3}{2}}} \quad \text{with } \tau_D = \frac{w^2}{4D} \quad (8.14)$$

Thus a fit to the experimental data would allow us not only to extract  $D$ , but also  $N$  ( $w$  is known). This calculation has been extended in many ways, e.g. reactions, 2D rotational diffusion, 2D diffusion (membranes), anomalous diffusion of polymers, protein complexes, etc.

### 8.3 Diffusion to capture

Some examples of diffusion to capture processes are the growth of actin filaments and the binding process of transcription factors on the DNA double-helix shown in figure 8.8.

In this chapter we are going to concentrate on another diffusion to capture example - the binding of ligands to receptors. Consider ligand molecules  $L$  binding to receptors  $R$  on the cell surface, see figure 8.9. A typical number of surface

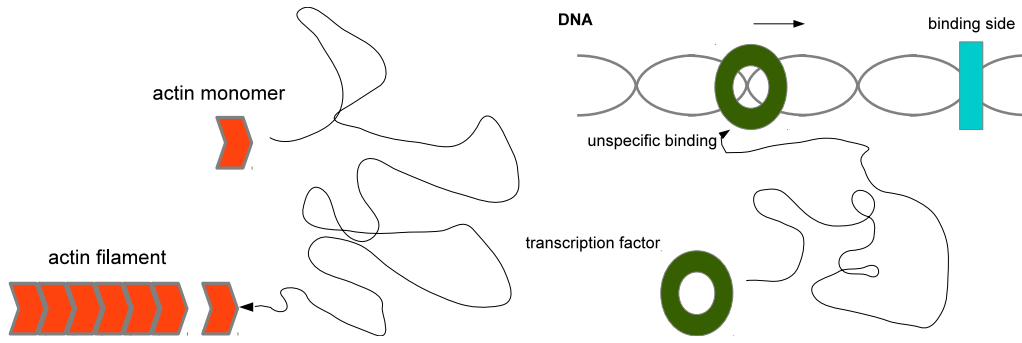
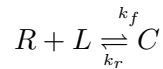


Figure 8.8: Two examples of diffusion to capture processes. On the left-hand side is a scheme of actin filament growth. The actin monomers diffuse in the cytosol and when they meet the growing filament, they attach to it. On the right hand side the binding of a transcription factor to the DNA double helix is depicted. At first the transcription factor binds unspecifically and slides along the DNA molecule, until it finds the specific binding side.

receptors is  $10^4$ . The ligands undergo Brownian diffusion and obey the diffusion equation

$$\dot{c} = D\Delta c \quad (8.15)$$

For a well-mixed situation we would have standard reaction kinetics



where  $k_f$  is the forward reaction constant and  $k_r$  the reverse reaction constant.

$$\begin{aligned} \dot{c} &= k_f RL - k_r C \\ \xrightarrow{\dot{c} \approx 0} \frac{RL}{C} &= \frac{k_r}{k_f} = K_D \end{aligned}$$

Here  $K_D$  is the dissociation constant as specified by the law of mass action. For low affinity receptors a typical value for  $K_D$  is  $10^{-6}M$ , and for high affinity ones  $K_D = 10^{-12}M$ .

Note that  $R, C$  are not concentrations, but absolute numbers in this case. To understand the  $K_D$  we look at the half-occupancy

$$\begin{aligned} L &= K_D \\ \Rightarrow R &= C \end{aligned}$$

Reaction rates from non-equilibrium measurements for association, without initial bound receptor-ligand complexes ( $c_0 = 0$ ) provide the concentration relaxation time dependency  $c(t) = k_f R_T L_0 t$ . For dissociation, when the initial number of free ligands is zero ( $L_0 = 0$ ),  $c(t) = c_0 \exp(-k_r t)$ . We are interested in the decay of the complex concentration in time. If we look at the concentration fluctuations

$$\frac{\delta c}{c} = \left( \frac{K_D}{LR_T} \right)^{\frac{1}{2}}$$

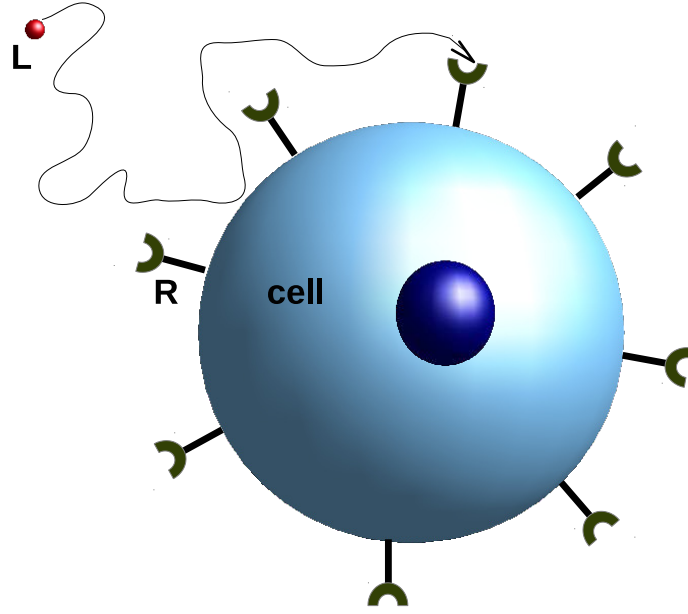


Figure 8.9: Cell with receptors  $R$  on its surface. The cell explores its immediate environment, by responding to the signal from those receptors, when ligands  $L$  are binding or unbinding. Before binding to the receptors the signal molecules first have to diffuse to the surface of the cell.

where  $R_T$  is the total number of receptors, we see that this is again a Poisson process. If  $R = 10^4$  and  $L = K_D$ , then the concentration fluctuations  $\frac{\delta c}{c} = 1\%$ , which is a relatively large number. One percent deviation of  $c$  can lead to cellular response and change in the cell behaviour (e.g. chemotaxis by *E. coli*). The cell has to integrate the signal in order to react adequately to the changes in the environment. To understand this we have to investigate the role of the diffusion.

In order to understand the effect of diffusion, we consider the cell to be a perfect spherical adsorber of radius  $R$ . The diffusion equation in spherical coordinates reads

$$\dot{c} = D \frac{1}{r^2} \partial_r (r^2 \partial_r c)$$

In steady state ( $\dot{c} = 0$ ),  $r^2 \partial_r c$  must be constant. For the perfect spherical adsorber  $c(R) = 0$

$$c(r) = c_0 \left( 1 - \frac{R}{r} \right)$$

For  $r = R$  the concentration is zero and for  $r \rightarrow \infty$  it acquires some constant value  $c_0$ , see figure 8.10.

The local concentration flux is  $j = -D \partial_r c$ . Then the total current on the sphere is

$$J = 4\pi R^2 j(R) = -4\pi R^2 D \left( c_0 \frac{R}{R^2} \right) = -4\pi R D c_0$$

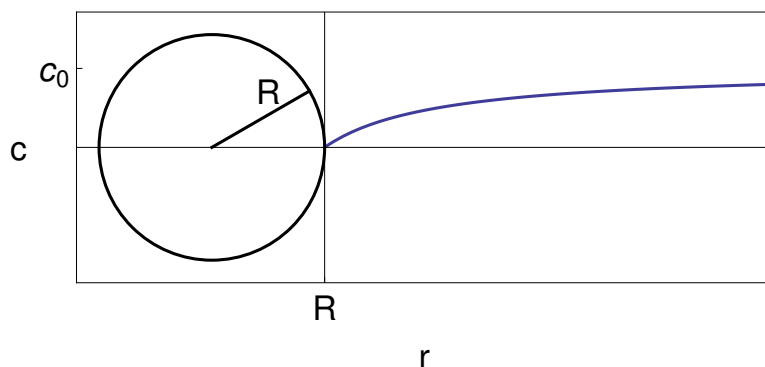


Figure 8.10: Relaxation of the ligand concentration  $c(r)$  over time for a perfect adsorbing sphere. At the surface of the sphere the concentration is zero, and far away it reaches a constant value  $c_0$ .

Thus  $J$  depends linearly on  $R$  because the gradient and the surface area give counteracting trends.  $c_0$  is the driving force here, because adding more ligands results in stronger current.

The diffusion determines the rate at which the ligands hit the surface of the cell. The association rate for pure diffusion is

$$k_+ = \frac{|J|}{c_0} = 4\pi DR$$

This famous result is called the *Smoluchowski rate*. Using typical values for proteins ( $R = 4nm$ ,  $D = 2(10\mu m)^2/s$ ), one gets a rate of  $k_+ = 6 \times 10^9 1/(Ms)$ , which is 3-4 order of magnitude larger than experimentally measured diffusion-limited association rates<sup>4</sup>. The reason is the assumption of isotropic reactivity. Solc and Stockmayer have shown that one gets the experimentally measured values if one takes anisotropic reaction patches and rotational diffusion into account. We conclude that the localization of binding to surface patches effectively decreases association by 3-4 orders of magnitude. Association can be increased in the range of the Smoluchowski rate by attractive interactions (*steering*) between the reaction partners, with the highest known rates around  $10^{10} 1/(Ms)$ . In figure 8.11 we give an overview over the resulting scenario.

In order to calculate the dissociation rate, we consider a sphere with concentration  $c_0$  on its surface and a perfect sink at infinity:

$$\begin{aligned} c(r) &= \frac{c_0 R}{r} \\ \Rightarrow J &= 4\pi DR^2 D c_0 \frac{R}{R^2} = 4\pi DR c_0 \end{aligned}$$

which is basically the same current as for association, but in the reverse direction,

<sup>4</sup>For an excellent review on this subject, compare Gideon Schreiber, Gilad Haran, and Huan-Xiang Zhou, Fundamental aspects of protein-protein association kinetics, Chemical Reviews 109:839-860, 2009



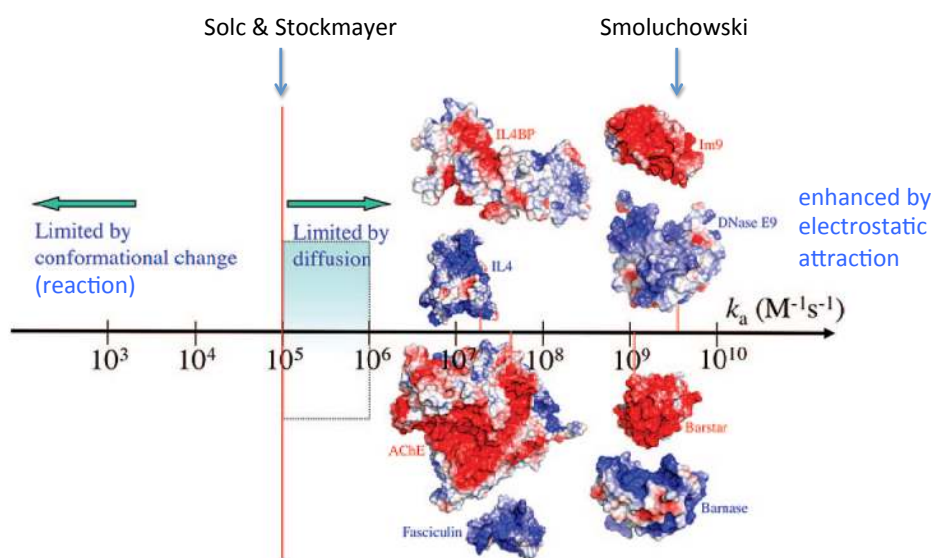


Figure 8.11: Experimentally measured association rates and identification of three regimes: reaction-limited, diffusion-limited and attraction-enhanced. We also indicate the values resulting from the calculations of Smoluchowski (isotropic reactive spheres) and Solc and Stockmayer (reaction patches). Adapted from the review of Gideon Schreiber, Gilad Haran, and Huan-Xiang Zhou, Fundamental aspects of protein-protein association kinetics, Chemical Reviews 109:839-860, 2009.

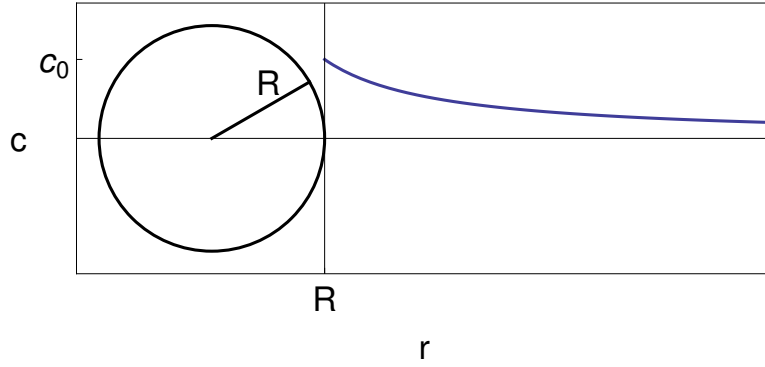


Figure 8.12: Sphere with concentration  $c_0$  on the surface. Now the concentration of ligands decays from its initial value to zero away from the sphere.

see figure 8.12. But note, that  $c_0$  here is different

$$\begin{aligned}
 c_0 &= \frac{1}{\frac{4\pi R^3}{3}} \\
 \Rightarrow k_- &= \frac{|J|}{c_0} = \frac{3D}{R^2} \\
 K_D &= \frac{k_-}{k_+} = \frac{3}{4\pi R^3}
 \end{aligned}$$

Although  $k_+$  and  $k_-$  both depend on the diffusion constant,  $K_D$  does not because it is an equilibrium quantity.

Until now we have assumed that diffusion dominates the binding process. In order to account also for the reaction part we now consider a partially adsorbing sphere. We employ the radiation boundary condition

$$\begin{aligned}
 J &= 4\pi R^2 D c'(R) = k c(R) \\
 c(r) &= c_0 \left(1 - \frac{\alpha}{r}\right) \\
 \Rightarrow \alpha &= \frac{kR}{4\pi DR + k} \\
 \Rightarrow k_f &= \frac{|J|}{c_0} = \frac{4\pi DRk}{4\pi DR + k} = \left(\frac{1}{k_+} + \frac{1}{k}\right)^{-1}
 \end{aligned}$$

where  $k_+ = 4\pi DR$  is the result for the perfect adsorber. The factor  $\alpha$  expresses the combination of the two rates — diffusion and reaction. Now we can determine what kind of process is dominating by looking at the relation between  $k$  and  $k_+$ . If  $k \gg k_+$ , then  $k_f = k_+$  and we have a diffusion limited case. If  $k \ll k_+$  then  $k_f = k$  and the process is reaction-limited.

We can also translate this relation in a relation for the characteristic times  $\tau_f = \tau_+ + \tau_r$ . The time for association is a sum of the time the ligand needs to diffuse to the sphere and the time needed for the reaction to take place.

In order to calculate  $J$  for other geometries one can make use of the analogy to electrostatics, see table 8.1.

Diffusion	Electrostatics
concentration $\Delta c = 0$	potential $\Delta \phi = 0$
flux $\vec{j} = -D\nabla c$	electrical field $\vec{E} = -\nabla \phi$
total current $J = \int \vec{j} d\vec{A}$	charge $Q = \frac{1}{4\pi} \int \vec{E} d\vec{A}$

Table 8.1: Analogy of diffusion and electrostatics

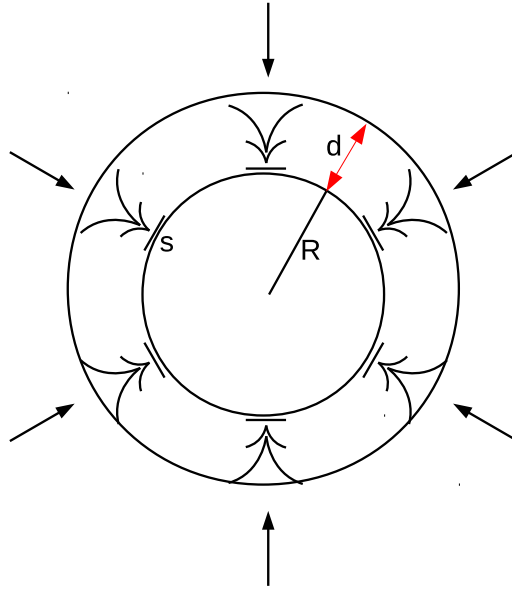


Figure 8.13: Model receptors as small patches with radius  $s$  on the sphere with radial dimension  $R$ . Now the flux is not rotationally symmetric, because the current flows only towards the patches. That is why there is no exact solution in this case. But if we look at a slightly bigger radius,  $R + d$ , then the flux is again uniform.

From the relations given in table 8.1 one finds that  $J = 4\pi DRc_0$  as calculated above. Using the same analogies, one can find e.g. that the flux from a halfspace onto a disc of radius  $R$  is  $J = 4DRc_0$  (same scaling, but no factor  $\pi$ ).

Until now we have treated the cell as uniformly reactive. In practice, it is covered only by  $N$  receptors, which can be modeled as  $N$  disc-like adsorbers of capture radius  $s \ll R$ . The rest of the sphere is considered to be reflecting. For simplicity we consider the diffusion-limited case. We use the electrostatic analogy, where the total current  $J$  is equal to the ratio of driving force (voltage) over the Ohm's resistance  $R_0$ :

$$J = \frac{c_0}{R_0}$$

Because in this case there is no radial symmetry, see figure 8.13, there is no longer an exact solution. For a good approximation (5% compared to computer simulations) we introduce a slightly larger radius  $R + d$  and look at  $r > R + d$ , where the flux is uniform again. Since  $d \ll R$  by definition, we put  $d \rightarrow 0$  in the calculations. For better illustration we introduce the equivalent electric current diagram, see figure 8.14, where  $R_{0R}$  is the Ohm's resistance of the sphere and

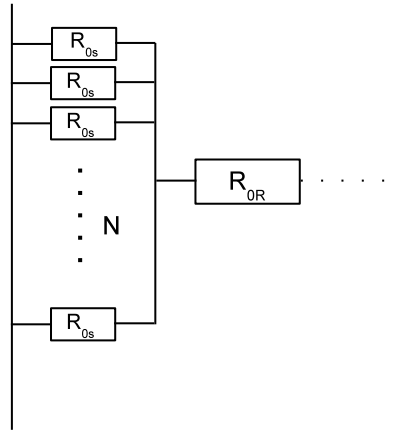


Figure 8.14: Electrical current schema equivalent to the model of receptor patches on the cell surface. It represents a combination of  $N$  receptors with resistance  $R_{0s}$  connected in parallel.

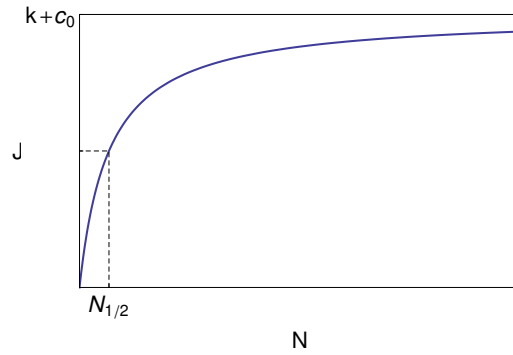


Figure 8.15: Current flow as a function of the number of receptors  $N$ . For small  $N$  the dependency is linear, and with higher  $N$  the current  $J$  gets to saturation.

$R_{0s}$  is the resistance of the individual receptor patches.

$$\begin{aligned}
 R_{0R} &= \frac{1}{4\pi DR} \\
 R_{0s} &= \frac{1}{4Ds} \\
 \text{and } R_0 &= R_{0R} + \frac{R_{0s}}{N}
 \end{aligned}$$

$$\begin{aligned}
 \Rightarrow J &= c_0 \frac{1}{\frac{1}{4\pi DR} + \frac{1}{4DsN}} \\
 &= \frac{4\pi DRc_0}{1 + \frac{\pi R}{sN}} = \begin{cases} 4\pi DRc_0 & \text{for } N \rightarrow \infty \\ 4DsNc_0 & \text{for } N \rightarrow 0 \end{cases} \quad (8.16)
 \end{aligned}$$

Half of the maximal current is achieved for  $N_{\frac{1}{2}} = \frac{\pi R}{s}$ . Inserting some typical numbers ( $R = 5 \mu\text{m}$ ,  $s = 1 \text{ nm}$ ) gives us  $N_{\frac{1}{2}} = 15.700$ , which is a typi-

cal number for surface receptors. The adsorbing fraction of the sphere is then only  $\frac{N\pi s^2}{4\pi R^2} = 1.6 \cdot 10^{-4}$  and the distance between neighbouring receptors is only  $\left(\frac{4\pi R^2}{N}\right)^{\frac{1}{2}} = 140 \text{ nm} = 140 \cdot s$ . This shows that diffusion is not efficient for traveling long distances, but is very efficient for exploring space on short distances. Because random walks are locally exhaustive, few receptors are sufficient. This explains why the cell can accommodate so many different systems in parallel: they do not need to be space filling and leave sufficient space for other systems.



## Chapter 9

# Reaction kinetics

The aim of this chapter is to give a quantitative description of biochemical reactions, mainly using ordinary differential equations (ODE) for the concentrations of reactants. Such reactions are vital for cells, which can be compared to biochemical factories. After an introduction to the relevance of biochemical reaction networks, we first discuss some central control motifs in networks. We then analyze one case in great detail, namely Michaelis-Menten kinetics. Finally we introduce a general framework to analyze reaction kinetics, namely non-linear dynamics, in particular bifurcations, phase plane analysis, linear stability analysis and limit cycle oscillations. We then use these tools to discuss some important models, including the famous Hodgkin-Huxley model for action potentials, which is an example of an excitable system. We finally add space to our description and discuss how diffusion can destabilize a reaction system (the famous Turing instability) <sup>1</sup>.

### 9.1 Biochemical reaction networks

Cells have evolved highly complicated networks of biochemical reactions. Different networks have different functions and therefore also different design principles. The main types of cellular networks are:

- **Metabolic networks:** one purpose of metabolism is the conversion of nutrients (e.g. glucose) through many intermediates to produce ATP, the energy currency of the cell (the other one is the production of new biomolecules). ATP stands for adenosine triphosphate. There are two main solutions to this: organisms use either oxidation (with  $O_2$ ) or fermentation (without  $O_2$ ). Oxidation is carried out by the electron transport chain in the inner

---

<sup>1</sup>For the classical parts of this chapter, we follow the book by JD Murray, *Mathematical biology*, 3rd edition (now in volumes I and II), Springer 2002. The material on non-linear dynamics is also contained in our script on this subject, which in turn follows the book by Steven Strogatz, *Nonlinear dynamics and chaos*, Westview 1994. For the network modules, we follow the great review by Tyson, John J., Katherine C. Chen, and Bela Novak, *Sniffers, buzzers, toggles and blinkers: dynamics of regulatory and signaling pathways in the cell*, *Current opinion in cell biology* 15.2 (2003): 221-231.

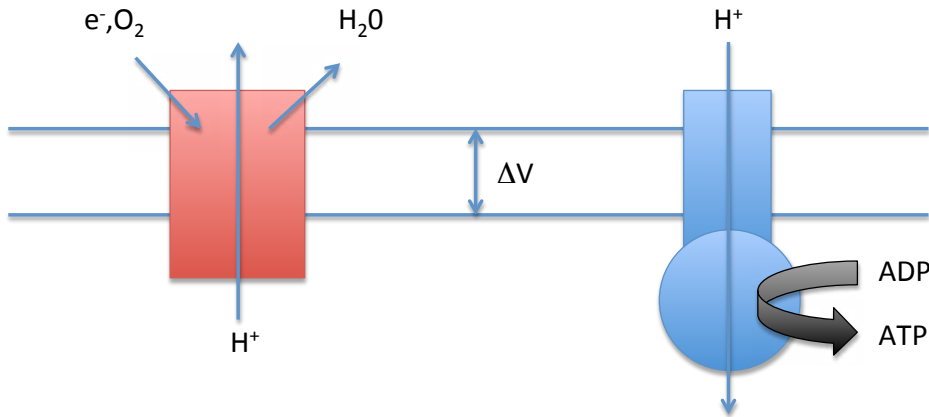
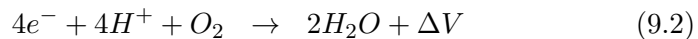
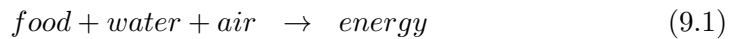


Figure 9.1: The electron transport chain in the inner membrane of mitochondria ends with cytochrome C oxidase (left), that builds up a proton gradient ( $\Delta V = 200 \text{ mV}$ ). This gradient is then used by the ATP synthase (right) to convert ADP into ATP, the energy currency of the cell. Typical concentrations for ATP and ADP in the cell are mM and  $10 \mu\text{M}$ , respectively.

membrane of mitochondria and is closely coupled to the citric acid cycle. Together these processes can generate 30-38 ATP molecules out of one glucose molecule. In humans about 80 mols ( $\approx 40 \text{ kg}$ ) ATP are produced per day, which corresponds to  $10^7$  ATP molecules per cell per second. In a vague way, this process can be summarized by the following formula:



where  $\Delta V$  is the membrane potential around 200 meV storing the energy (compare figure 9.1). This gradient is then used by ATP synthase to produce ATP molecules. The network motifs of metabolic networks are strongly shaped by optimality in regard to the use of chemical and energy resources.

- **Genetic networks:** due to the genome sequencing projects, today we know the genomes of most organisms. Databases store the sequence for each gene and annotate them with a description of the function of their products (mainly RNA and proteins). Genes interact with each other in the following way. First genes are expressed. Gene expression takes place in two main stages. The first one is called transcription. In this phase a copy of the gene is rewritten in the RNA alphabet. After the RNA sequence is made, it leaves the nucleus and goes to the ribosomes, where it is converted to an amino acid chain, in a process called translation. If this protein or a downstream target of it is a transcription factor, then it influences the expression of other genes (it either up- or down-regulates them). In this way a gene expression network is generated. Important control motifs in



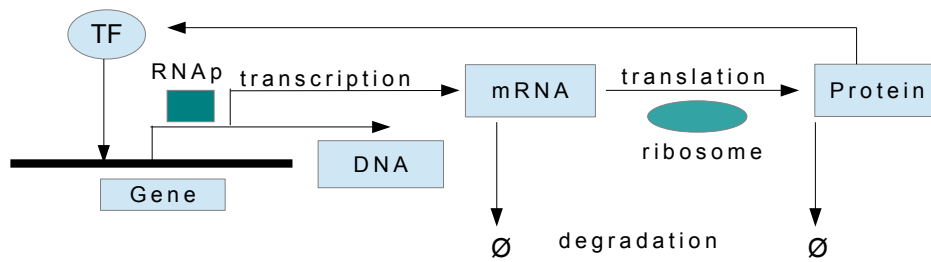


Figure 9.2: A gene on the DNA is expressed by the sequential processes of transcription and translation. The resulting protein can feedback on this or another gene through transcription factors. Feedback onto itself can be either positive (gene is turned on) or negative (homeostasis). Feedback onto other genes can be either upregulating or inhibiting. In this way, a complex gene expression network emerges. Humans have around 24.000 genes resulting in more than 60.000 proteins (through alternative splicing).

gene expression are positive feedback (leading to the switching on of genes) and negative feedback (leading to constant protein levels or oscillations). Compare figure 9.3.

- **Signal transduction networks:** extracellular signals are taken up by membrane receptors and processed (filtering, integration, etc) and transmitted towards the nucleus. A well-known example is the MAPK (mitogen activated protein kinase) pathway leading to cell division as a response to growth factors. This pathway consists of three levels of phosphorylation. Mathematical analysis shows that this surprising design leads to strong sensitivity of the pathway. Signal transduction networks are designed for reliable propagation of signals and therefore have a more dynamic nature than the other two types of networks mentioned above (they often experience wave-like excitations).
- **Neuronal networks:** the brain of higher organisms relies on the propagation of action potentials along neurons and across synapses. It is believed that in this case, most information is encoded in the temporal sequence of excitations (spikes) rather than in their exact shape. The most important aspect here is the plasticity of the network, which leads to the ability to memorize and learn. Neuronal networks are highly dynamic and special mathematical tools have been developed to describe their function (for example the adaptive exponential integrate-and-fire model implemented on different network architectures like the one of the cerebral cortex). Apart from this higher level function of the brain, however, it is also essential to understand the biophysics of the underlying processes, namely the action potential, and the standard models to explain it (Hodgkin-Huxley, FitzHugh-Nagumo).

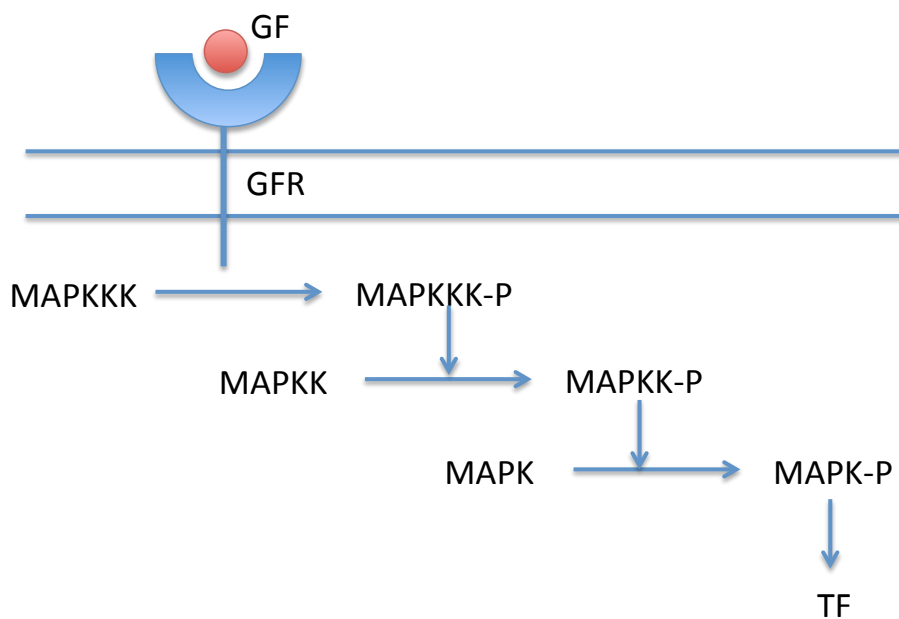
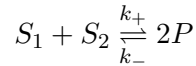


Figure 9.3: One of the most important signal transduction pathways is the MAPK-pathway (mitogen activated protein kinases, leads to cell division). A growth factor activates a GF-receptor, e.g. epidermal growth factor (EGF). Then a cascade of three levels of kinases is used to amplify the signal, eventually leading to activation of a transcription factor (TF). The hierarchical structure of the pathway leads to ultrasensitivity. In general, many signaling pathways are branched and interact with other signaling pathways. In this way, a signal transduction network emerges. Again such networks based on protein-protein interactions are stored in databases. The interaction strengths can be measured e.g. with the yeast-two-hybrid method.

## 9.2 Law of mass action

The mathematics to describe biochemical networks starts with the law of mass action. To understand this law we consider a container filled with reactive species of molecules with homogenous concentration (well-mixed assumption, good for small reaction volumes such as an E. Coli cell). We want to know how fast the reactions take place and how fast the concentrations of the reacting molecules change. The answer is given by the law of mass action. This law states that the reaction speed is proportional to the number of combinations of reacting molecules. The number of combinations is in turn proportional to the concentrations of the reactants. The proportionality constant is called reaction rate constant  $k$ , which summarizes all effects going in the effective reaction (movement in space, encounter, final complexation).

Consider for example two species of substrates ( $S_1, S_2$ ), which react with each other to produce two identical product molecules ( $P$ ). Schematically the reaction looks like this



Here  $k_-$  and  $k_+$  are the rate constants for the backward and forward reactions, they are called dissociation and association rates. The forward reaction depends on two processes. First the molecule have to diffuse through the medium and get close to each other and then they can react. These two situations are described by the rate constants  $k_d$  (diffusion) and  $k_a$  (association). These we can combine, to get the rate constant for the forward reaction:

$$\frac{1}{k_+} = \frac{1}{k_d} + \frac{1}{k_a} \quad (9.3)$$

For the forward reaction the number of combinations of  $S_1$  and  $S_2$  is  $N_{S_1, S_2} = S_1 S_2 \sim s_1 s_2$ , where  $s_1, s_2$  are the concentrations of the two substrates. The speed of the forward reaction is

$$v_+ = k_+ s_1 s_2$$

The number of combinations of  $P$  for the reverse reaction is

$$N_P = P(P-1) \stackrel{\text{for } P \gg 1}{\approx} P^2 \sim p^2$$

where  $p$  is the concentration of the product molecules. The speed of the reverse reaction is

$$v_- = k_- p^2$$

The net speed of the reaction can be calculated as the sum of the speeds of the forward and the reverse reactions, taken with the appropriate sign:

$$v = v_+ - v_- = k_+ s_1 s_2 - k_- p^2 \quad (9.4)$$

Often  $v$  is called the rate constant of the reaction.

For biochemical reaction the concentrations of all the participating molecules are important. With a set of ODE, derived from the law of mass action, we can

describe the rates at which those concentrations change. The rate at which the concentration of substrate  $S_1$  changes with time is given by

$$\frac{ds_1}{dt} = -v_+ + v_- = -v = -k_-s_1s_2 + k_-p^2 = \frac{ds_2}{dt}$$

The rate, at which the concentration of  $S_2$  changes in time, is the same as the rate for  $S_1$ . For the change of the concentration of the product over time we get

$$\frac{dp}{dt} = 2v_+ - 2v_- = 2v = 2(k_+s_1s_2 - k_-p^2)$$

We should keep in mind that the total number of molecules is conserved

$$s_1 + s_2 + p = \text{const}$$

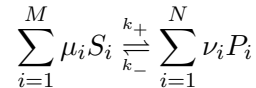
This means that we can get rid of one variable and work with one ODE less. Note that  $v$  has the dimension  $\frac{M}{s}$  and  $k_+$  and  $k_-$  have the dimension  $\frac{1}{M \cdot s}$ .

Now we want to look at the set of ODE for the concentrations for stationary states. We assume a system that does not change in time, so that  $\frac{ds_1}{dt} = \frac{ds_2}{dt} = 0$  and  $\frac{dp}{dt} = 0$ . For the speed this means  $v = 0$ , so the forward and the reverse reactions occur with the same rate  $v_+ = v_-$ .  $K_{eq}$  is the rate constant that describes the equilibrium state between forward and backward reactions and is called the equilibrium constant:

$$K_{eq} := \frac{k_+}{k_-} = \frac{(p^{eq})^2}{s_1^{eq} s_2^{eq}} \quad (9.5)$$

This is the law of mass action for this special case.

For a generalized description we have to look at  $M$  substrate species with multiplicity  $\mu_i$ , and  $N$  product species with multiplicity  $\nu_i$ . The reaction can be written as



For the reaction speed we get a generalized expression

$$\begin{aligned} v_+ &= k_+ \prod_{i=1}^M S_i^{\mu_i} \\ v_- &= k_- \prod_{i=1}^N P_i^{\nu_i} \\ \Rightarrow K_{eq} &= \frac{k_+}{k_-} = \frac{\prod_{i=1}^N P_i^{\nu_i}}{\prod_{i=1}^M S_i^{\mu_i}} \end{aligned} \quad (9.6)$$

The ODE for the generalized system are

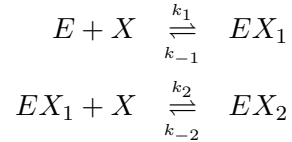
$$\begin{aligned} \frac{ds_i}{dt} &= -\mu_i(v_+ - v_-) \\ \frac{dp_i}{dt} &= \nu_i(v_+ - v_-) \end{aligned} \quad (9.7)$$

In this section we used a classical reaction kinetics approach, which assumes deterministic macroscopic systems with large number of molecules, spatial homogeneity and fast diffusion. This approach cannot describe systems with small number of molecules, with slow movements (e.g. in a crowded environment) or with spatial heterogeneities. For these situations, more sophisticated approaches exist, in particular particle-based computer simulations.

### 9.3 Cooperative binding

Many molecules (e.g. enzymes, receptors, DNA) can bind to more than one ligand. The binding is cooperative if the first binding changes the affinity of the further binding sites. Cooperative binding requires that the macromolecules have more than one binding site.

Let us look at the following example. If an enzyme  $E$  binds up to two molecules  $X$ , then we can write the reaction equation as:



We define  $x$  to be the concentration of molecules  $X$ ,  $e$  to be the concentration of molecules  $E$ , and  $c_i$  to be the concentration of complexes of the type  $EX_i$ . Now we look at the kinetics of the equilibrium state, where  $k_1^{eq}$  and  $k_2^{eq}$  are the rate constants of the equilibrium state of the reactions as defined above:

$$\begin{aligned} k_1^{eq} &= \frac{c_1}{ex} \\ k_2^{eq} &= \frac{c_2}{c_1x} = \frac{c_2}{k_1^{eq}ex^2} \end{aligned}$$

From these we can derive the expressions for the concentrations:

$$\begin{aligned} c_1 &= k_1^{eq}ex \\ c_2 &= k_1^{eq}k_2^{eq}ex^2 \end{aligned}$$

The total number of molecules  $E$  is then given by

$$e_0 = e + c_1 + c_2 = e \underbrace{(1 + k_1^{eq}x + k_1^{eq}k_2^{eq}x^2)}_{:=Q} \quad (9.8)$$

$Q$  is called binding polynomial, it is the sum over all possible ligation states.  $Q$  can be interpreted as a partition sum.

We are interested in the fraction of all  $E$  molecules in the solution, which have  $i$  bonded ligands. We look at the cases for  $i = 0, 1, 2$ :

$$\begin{aligned} p_0 &= \frac{1}{Q} \\ p_1 &= \frac{k_1^{eq}x}{Q} \\ p_2 &= \frac{k_1^{eq}k_2^{eq}x^2}{Q} \end{aligned}$$

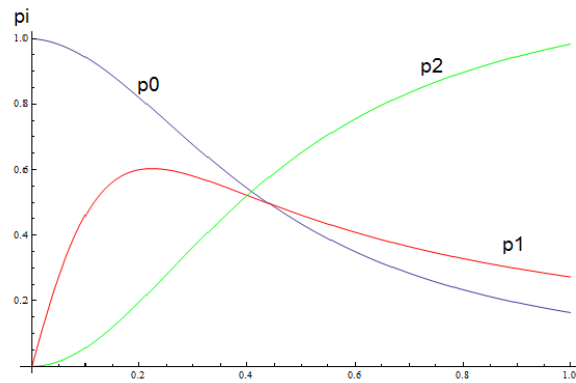


Figure 9.4: Many enzymes can bind to more than one substrate. If the binding is cooperative, than the affinity of the remaining binding sites changes. The fraction of molecules with no bonded substrates is depicted in blue, the fraction with one bonded molecule is represented by the red line and the fraction with two bonded molecules is the green line, all represented as functions of the substrate concentration  $x$ .

We can see in figure 9.4 how the different states are populated in respect to the ligand concentration  $x$ .

We can also estimate the number of bound molecules of type  $X$

$$\langle i \rangle = \frac{k_1 x + k_1 k_2 x^2}{Q}$$

To illustrate the effect of cooperativity we put in some typical values and look at the distribution, assuming  $p_0 = p_2$ :

- For neutral binding

$$\begin{aligned} k_1 &= k_2 = 100 \\ \Rightarrow x_{mid} &= 0.01 \text{ and } Q = 3 \\ \Rightarrow p_0 &= p_1 = p_2 = \frac{1}{Q} \end{aligned}$$

- For inhibitory binding

$$\begin{aligned} k_1 &= 10^3 \gg k_2 = 10 \\ \Rightarrow x_{mid} &= 0.01 \text{ and } Q = 12 \\ \Rightarrow p_0 &= p_2 = \frac{1}{Q} \text{ and } p_1 = \frac{10}{Q} \end{aligned}$$

In such cases the intermediate states are more probable.

- For activating binding

$$\begin{aligned} k_1 &= 1 \ll k_2 = 10^4 \\ \Rightarrow x_{mid} &= 0.01 \text{ and } Q = 2.01 \\ \Rightarrow p_0 &= p_2 = \frac{1}{Q} \text{ and } p_1 = \frac{0.01}{Q} \end{aligned}$$

This indicates that strong reinforcement of binding depopulates the intermediate state.

For  $\frac{k_1}{k_2} \rightarrow 0$

$$p_2 = \frac{\langle i \rangle}{2} \approx \frac{k_1 k_2 x^2}{1 + k_1 k_2 x^2} = \frac{K x^2}{1 + K x^2} \quad \text{Hill-function for } n=2 \quad (9.9)$$

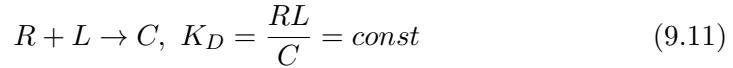
Here  $n$  is the Hill-coefficient, which is a measure of cooperativity in a binding process.  $n = 1$  indicates independent binding,  $n > 1$  shows positive cooperativity. The general formula of the Hill-function is

$$\frac{\langle i \rangle}{n} = p_n = \frac{K x^n}{1 + K x^n} \quad (9.10)$$

which is sigmoidal for  $n > 1$ . The Hill coefficient is usually extracted from data by a Hill plot.

## 9.4 Ligand-receptor binding

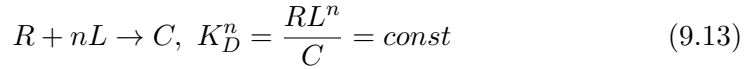
We now consider a simple example of mass action kinetics, namely receptor-ligand binding:



We now write down the probability that the ligand is bound:

$$p_b = \frac{C}{R + C} = \frac{(RL/K_D)}{R + (RL/K_D)} = \frac{L}{K_D + L} \quad (9.12)$$

Thus this probability increases hyperbolically with ligand concentration on the scale  $K_D$  (ligand concentration at half occupancy). This law is also known as *Langmuir isotherm* in surface science: it describes how binding sites on a surface are occupied as ligand concentration is increased in the solution. It is also easy to describe cooperativity in this framework, namely by assuming that  $n$  ligand simultaneously bind the receptor:



where  $K_D$  has been defined somehow differently in order to get the same dimension as  $L$ . We now get

$$p_b = \frac{C}{R + C} = \frac{L^n}{K_D^n + L^n} \quad (9.14)$$

thus  $n$  is the Hill coefficient of this system and  $K_D$  the threshold value.

In order to obtain a more mechanistic understanding for  $n = 1$ , we now consider a lattice model and treat it with the canonical formalism. Consider a lattice with  $\Omega$  sites. We have  $L \ll \Omega$  ligands which are distributed over the lattice, each with unbound energy  $\epsilon_u$ . The corresponding partition sum is

$$Z_u = \frac{\Omega!}{L!(\Omega - L)!} e^{-\beta L \epsilon_u} \approx \frac{\Omega^L}{L!} e^{-\beta L \epsilon_u} \quad (9.15)$$

We now add one receptor to the system that can bind a ligand with binding energy  $\epsilon_b$ . This gives a second part to the partition sum:

$$Z_b = \frac{\Omega!}{(L-1)!(\Omega-(L-1))!} e^{-\beta(L-1)\epsilon_u - \beta\epsilon_b} \approx \frac{\Omega^{L-1}}{(L-1)!} e^{-\beta(L-1)\epsilon_u - \beta\epsilon_b} \quad (9.16)$$

We again calculate the probability to be bound:

$$p_b = \frac{Z_b}{Z_u + Z_b} = \frac{(L/\Omega)e^{-\beta\Delta\epsilon}}{1 + (L/\Omega)e^{-\beta\Delta\epsilon}} \quad (9.17)$$

with  $\epsilon = \epsilon_b - \epsilon_u < 0$ . We next change to continuum quantities:  $L/\Omega = c/c_0$  where  $c$  is concentration and  $c_0 = 1/a^3$  with  $a$  being the linear size of a lattice size. Thus we get

$$p_b = \frac{c}{K_D + c} \quad (9.18)$$

like in the Langmuir isotherm but now with a mechanistic definition for the dissociation constant:

$$K_D = c_0 e^{\beta\Delta\epsilon} \quad (9.19)$$

A typical value for  $c_0$  would be  $1M = 6 \times 10^{23}/dm^3 = 0.6/nm^3$ . The more negative  $\beta\Delta\epsilon$ , the smaller  $K_D$ . For binding energies in  $k_B T$  of  $-7.5$ ,  $-10$  and  $-12.5$ , we get  $553$ ,  $45$  and  $4 \mu M$  for  $K_D$ .

Another way to get a mechanistic understanding of  $K_D$  is to consider receptor-ligand binding in the grand canonical ensemble. At equilibrium, the chemical potentials should be equal:

$$\mu_R + \mu_L = \mu_C \quad (9.20)$$

We use the ideal gas expressions for the chemical potential:

$$\left(\mu_{R0} + k_B T \ln \frac{R}{R_0}\right) + \left(\mu_{L0} + k_B T \ln \frac{L}{L_0}\right) = \left(\mu_{C0} + k_B T \ln \frac{C}{C_0}\right) \quad (9.21)$$

This leads to the following result:

$$\frac{RL}{C} = \frac{R_0 L_0}{C_0} = e^{-\beta(\mu_{R0} + (\mu_{L0} - \mu_{C0}))} = K_D \quad (9.22)$$

Thus  $K_D$  can be calculated when one knows the chemical potentials at equilibrium.

## 9.5 Network motifs

As we have seen, different biological networks have different functions. This in turn requires different network motifs being incorporated into them. In fact we might expect that historically small networks with a clear function were the starting point and only later grew into larger networks. We now discuss some paradigmatic small networks that tend to appear as motifs in larger biological networks. We follow the excellent review by John J Tyson, Katherine C Chen



and Bela Novak, *Sniffers, buzzers, toggles and blinkers: dynamics of regulatory and signaling pathways in the cell*, Current Opinion in Cell Biology 15:221-231, 2003. The corresponding plots are taken from this paper, too. Very similar conclusions about the high level functions of network motifs have been reached also in engineering (control theory).

### 9.5.1 Synthesis and degradation (steady state)

We consider a protein  $R$  (for response) that is synthesized and degraded according to the laws of mass action. We control synthesis by some parameter  $S$  (for signal):

$$\frac{dR(t)}{dt} = \dot{R} = k_0 + k_1 S - k_2 R \quad (9.23)$$

The first two terms are the gain (positive) and the last term is the loss (negative). If we plot the two terms, there is an intersection which corresponds to a steady state (gain = loss). In mathematics and non-linear dynamics, this is also called a fixed point. The steady state follows from  $\dot{R}$  through an algebraic relation:

$$R_{ss} = \frac{k_0 + k_1 S}{k_2} \quad (9.24)$$

If we increase  $R$  from  $R_{ss}$ , the loss dominates and we are driven back to the steady state. If we decrease  $R$  from  $R_{ss}$ , the gain dominates and we are also driven back to the steady state. Thus the steady state is stable. The general criterion for a stable fixed point is that the derivate of  $\dot{R}$  as a function of  $R$  should be negative. An unstable fixed point has a positive derivative and for a vanishing derivative, we cannot make a statement on the level of linear stability analysis. We also note that without degradation, such a system would not be stable. Biology has evolved many degradation processes to make sure that its networks are stable.

### 9.5.2 Phosphorylation and dephosphorylation (buzzer)

For a phosphorylation / dephosphorylation cycle we have in addition that the overall concentration of the protein is constant,  $R_T = R + R_p = const.$  For simplicity, we set the basal rate  $k_0 = 0$ . Thus we have

$$\dot{R}_p = k_1 S (R_T - R_p) - k_2 R_p \quad (9.25)$$

Again we find a stable steady state. This time we get

$$R_{p,ss} = \frac{R_T S}{k_2/k_1 + S} \quad (9.26)$$

thus we have a hyperbolic response curve. As long as  $S$  is present at sufficient amounts we have a response, but if we remove it, the response goes away. Thus this is called a buzzer. If the signal enters in a more complex form, e.g. as  $S^n$  due to cooperativity

$$R_{p,ss} = \frac{R_T S^n}{K_D^n + S^n} \quad (9.27)$$

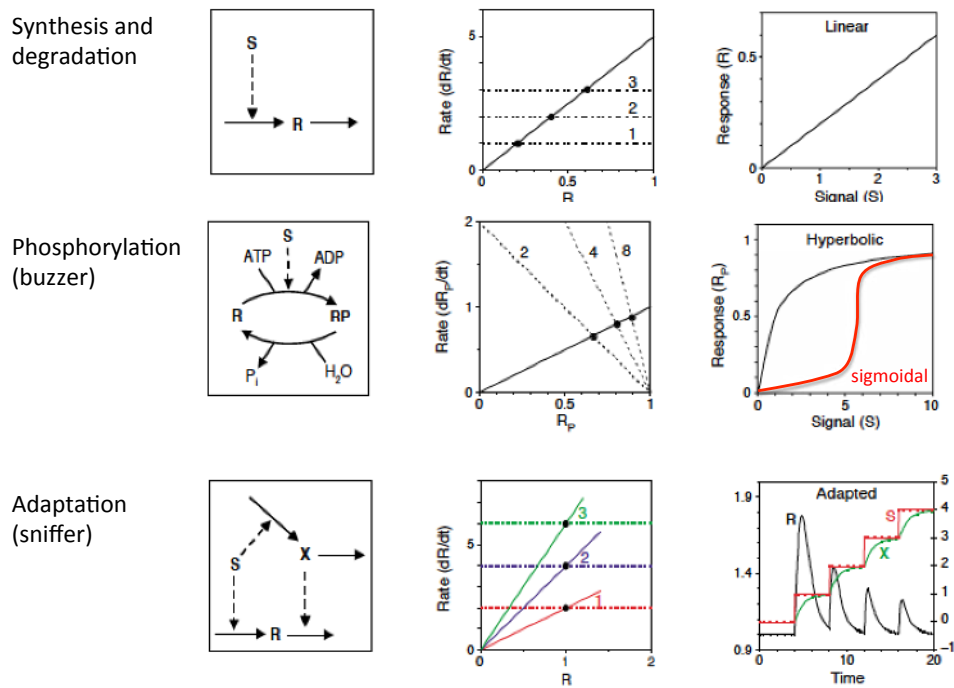


Figure 9.5: Three simple networks motifs that all three lead to stable fixed points. Left: the reaction scheme. Middle: plot of gain and loss terms. The intersection is the fixed point. Because loss / gain dominates at higher / lower values, it is stable. Right: the steady state or bifurcation diagram as a function of input signal  $S$ . The hyperbolic response of the buzzer becomes sigmoidal if cooperativity or enzyme kinetics are involved. For the sniffer, we show the time course, because only in this way the adaptation response becomes clear (the steady state for  $R$  does not change as a function of  $S$ , but it shows a transient each time  $S$  is changed).

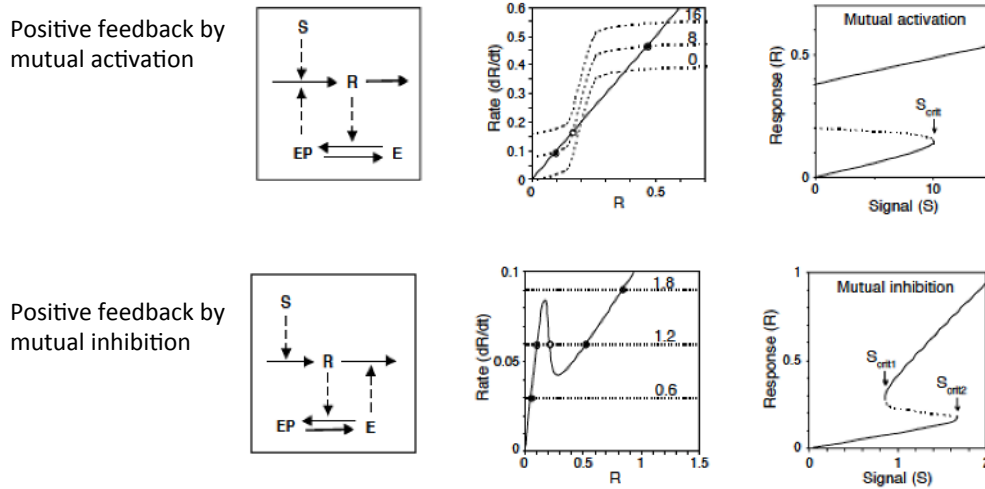


Figure 9.6: Two examples of positive feedback both leading to bistability and toggle switches. An essential element is the non-linearity of the system leading to the S-curves.

or through a Goldbeter-Koshland function due to Michaelis-Menten enzyme kinetics, then the response curve becomes sigmoidal and we have a clear threshold value for  $R_{p,ss}$  (e.g. at  $K_D$ ) as a function of  $S$ . Below we assume that we have such sharp responses. We still would call this a buzzer, though.

### 9.5.3 Adaptation (sniffer)

To get more complex responses, we can now add a second species. We discuss first a feed forward motif that leads to adaptation:

$$\dot{R} = k_1 S - k_2 X R, \quad \dot{X} = k_3 S - k_4 X \quad (9.28)$$

The steady state is

$$R_{ss} = \frac{k_1 k_4}{k_2 k_3}, \quad X_{ss} = \frac{k_3 S}{k_4} \quad (9.29)$$

Due to the special design of this motif,  $R_{ss}$  is independent of  $S$ . Therefore the system adapts to reach always the same value of  $R_{ss}$  in the long run. This behaviour is typical for sensory adaptation, e.g. in the way our eyes, nose or ears work: our senses are usually designed such that they can function over many orders of magnitude of the input stimulus  $S$ . Therefore we call this a sniffer.

### 9.5.4 Positive feedback (toggle switch)

We now come to the first example with feedback. A typical example for positive feedback would be mutual activation, such that the protein  $R$  upregulates a

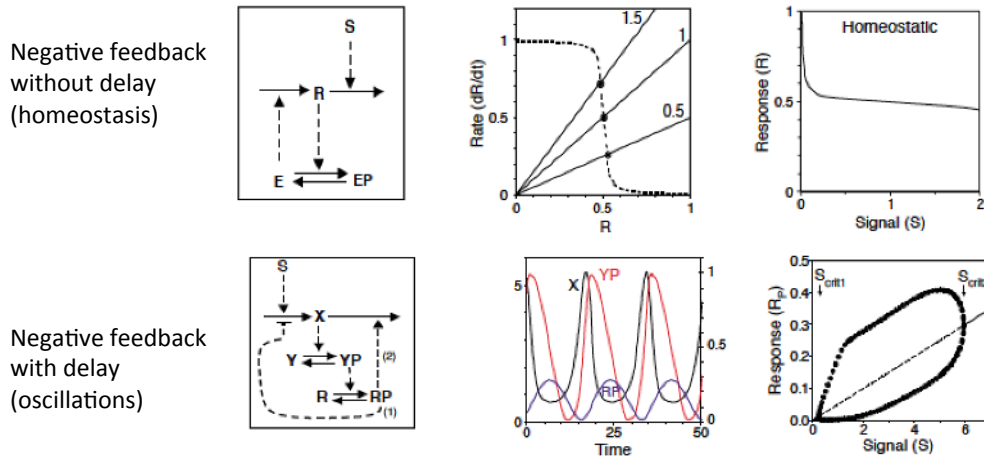


Figure 9.7: Negative feedback can lead either to homeostasis or oscillations, depending on whether the system has sustained delay or not.

species  $E_p$  that in turn leads to increased  $R$ -production. The corresponding equation would be

$$\dot{R} = k_0 E_p(R) + k_1 S - k_2 R \quad (9.30)$$

where  $E_p(R)$  is a sigmoidal function as discussed above. Plotting gain and loss as a function of  $R$  shows that we have either one intersection with a stable fixed point or three intersections with three fixed points, of which only the two outer ones are stable and the intermediate one is unstable. The steady state of bifurcation diagram then shows a window of bistability, in which the two stable fixed points (solid) are separated by an unstable branch (dashed). Outside this window of bistability, at low and high  $S$  we only find the low or high  $R$  fixed points to be stable, respectively. We conclude that positive feedback leads to bistability. Functionally this is a switch-like behaviour. Even if we reduced  $S$ , the response might stay in the high level, thus this is a toggle switch rather than a buzzer. The jumps and hysteresis effects found here are also typical for first order phase transitions.

Positive feedback can also be achieved by mutual inhibition. In this case the governing equation reads

$$\dot{R} = k_0 + k_1 S - k_2 R - k_3 E(R) \quad (9.31)$$

where  $E(R)$  now decreases as a function of  $R$  in a step-wise manner (because it is inhibitory). The resulting bifurcation diagram looks qualitatively the same as for mutual activation, i.e. it also leads to bistability and a toggle switch.

### 9.5.5 Negative feedback without delay (homeostasis)

We now turn to negative feedback, which is a common strategy to keep a quantity of interest at a constant value (e.g. in PID-control). Historically this has been studied in great detail in the 19th century for the steam engine, where one wants

to achieve a constant power output. Here we study this for a biochemical system (chemostat).

We consider a species  $R$  that inhibits a species  $E$ , which however helps to produce  $R$ . Thus if too much / too little of  $R$  exists, less / more is produced (production on demand). The dynamical equation is

$$\dot{R} = k_0 E(R) - k_1 S R \quad (9.32)$$

where again  $E(R)$  is a decreasing function of  $R$  (inhibition) with a threshold. If the parameters are such that  $S$  leads to intersections in the steep part of  $E(R)$ , then we obtain a close to constant value for  $R_{ss}$  as a function of  $S$ . This regulatory function is called homeostasis and is used a lot in physiology, e.g. to keep our insulin or glucose levels in the blood constant.

### 9.5.6 Negative feedback with delay (blinker)

For steam engines, it was found that the delay between the sensor and the actuator can lead to oscillations. For engines, this has to be avoided, but in biology, oscillations are often put to good use, e.g. to anticipate the break of dawn (circadian rhythm). In order to get some delay into the negative feedback cycle, we introduce a new species. We consider  $X$  upregulating  $Y_p$  and  $Y_p$  upregulating  $R_p$ , but  $R_p$  inhibiting  $X$ . Thus we have a negative feedback as before, but it takes more time to propagate the signal. The following system of equations describe such a system:

$$\dot{X} = k_0 + k_1 S - k_2 X - k_7 R_p X \quad (9.33)$$

$$\dot{Y}_p = \frac{k_3 X (Y_T - Y_p)}{K_{m3} + (Y_T - Y_p)} - \frac{k_4 Y_p}{K_{m4} + Y_p} \quad (9.34)$$

$$\dot{R}_p = \frac{k_5 Y_p (R_T - R_p)}{K_{m5} + (R_T - R_p)} - \frac{k_6 R_p}{K_{m6} + R_p} \quad (9.35)$$

$$(9.36)$$

For all three species as a function of  $S$ , there exists a region in which oscillations occur. The amplitude of these oscillations appears and vanishes in a smooth manner (Hopf-bifurcation). Although a steady state does not exist in this region, the system still can be represented in a bifurcation diagram by showing the minimal and maximal values. Biochemical oscillations often use the negative feedback motif (blinker). Often they also involve space (waves resulting from reaction-diffusion systems) and / or mechanics (like the otoacoustic oscillations in our ears). Hopf bifurcations are very common in biological systems which want to regulate the amplitude of the oscillations. If the oscillation would jump to a finite amplitude, this could lead to a catastrophe (this can occur e.g. for bridges suddenly collapsing after a small change in the bifurcation parameter).

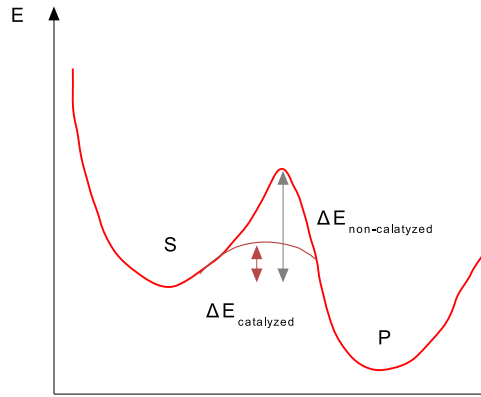


Figure 9.8: Energy landscape of a reaction with (dark red line) and without (light red line) enzymes. Enzymes do not take part of the reaction itself, they rather decrease the energy barrier  $\Delta E$  of the system, thus enabling the substrates to easily convert into product molecules.

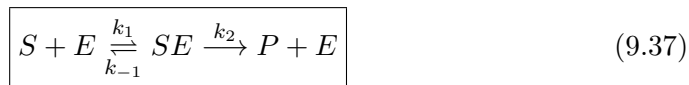
## 9.6 Enzyme kinetics

Enzymes are biomolecules which very efficiently catalyze chemical reactions by binding to the substrates. With their help reaction rates increase  $10^6$  to  $10^{12}$  times. This can be estimated by looking at the ratio of the rate constants for the catalyzed and the spontaneous reactions:

$$\frac{k_{cat}}{k_{spont}} \sim \exp\left(-\frac{\Delta E}{k_B T}\right)$$

For a biological reaction a typical value for  $\Delta E$  is  $\Delta E \approx -14 k_B T$ . Thus we get  $10^6$  fold increase of the reaction speed. Enzymes do not change during the reaction, they just speed it up, by decreasing the energy barrier, see figure 9.8. After the product is made, they can be recycled and used for the next reaction. We note that enzymes are very specific, not only in biochemistry, but in chemistry in general, e.g. the iron catalyst used for ammonia production in the Haber-Bosch process.

A basic enzyme reaction takes place in two stages. First the substrate  $S$  binds reversibly to an enzyme  $E$  to form an  $SE$  complex. Then the  $SE$  is converted to the product  $P$  and the enzyme is released.



Here  $k_1$  is the rate constant of formation of the enzyme-substrate complex,  $k_{-1}$  is the rate constant of dissociation of the enzyme-substrate complex, and  $k_2$  is the catalysis rate constant. In effect the substrates are turned into products. The classical analysis of this central scheme of enzyme kinetics goes back to Leonor Michaelis und Maud Menten in 1913. A more rigorous analysis has been worked out later by different mathematicians, most prominently by Lee Segel. For more details, see chapter 6 of the book by Murray on mathematical biology.

From now on we will use the following abbreviations for the concentrations of the reacting molecules:  $s = [S]$ ,  $e = [E]$ ,  $c = [SE]$ ,  $p = [P]$ . To define the system of the molecules, we need to define the initial conditions for the concentrations

$$s(0) = s_0; \quad e(0) = e_0; \quad c(0) = 0; \quad p(0) = 0$$

We get the ODE describing the concentration changes of the molecules in time by applying the law of mass action on our reaction:

$$\begin{aligned} \frac{ds}{dt} &= -k_1 es + k_{-1} c \\ \frac{de}{dt} &= -k_1 es + (k_{-1} + k_2) c \\ \frac{dc}{dt} &= k_1 es - (k_{-1} + k_2) c \\ \frac{dp}{dt} &= k_2 c \end{aligned} \tag{9.38}$$

Since the ODE for the product rate is decoupled from the other three, we can directly give the concentration dependency on time

$$p(t) = k_2 \int_0^t c(t') dt' \tag{9.39}$$

if we know how  $c(t)$  behaves.

The enzyme concentration is conserved, because the enzyme does not react:  $e + c = \text{const} = e_0$  and we are left with only two ODEs:

$$\boxed{\begin{aligned} \frac{ds}{dt} &= -k_1 e_0 s + (k_1 s + k_{-1}) c && \text{with } s(0) = s_0 \\ \frac{dc}{dt} &= k_1 e_0 s - (k_1 s + k_{-1} + k_2) c && \text{with } c(0) = 0 \end{aligned}} \tag{9.40}$$

Unfortunately this non-linear system cannot be solved analytically. We first explain the standard treatment and then the rigorous mathematical treatment.

### 9.6.1 Standard treatment

We first note that the reaction is irreversible and that all substrate will be used up eventually. The classical Michaelis-Menten analysis assumes that enzyme is present in a small quantity and quickly converted into the complex, which then

is in a steady state until all substrate has been used up; then also the complex has to vanish again. Therefore their main assumption is

$$\frac{dc}{dt} \approx 0 \quad (9.41)$$

The ODE for  $c$  now becomes an algebraic relation

$$c(t) = \frac{e_0 s(t)}{s(t) + K_m} \quad (9.42)$$

and the ODE for  $s$  has the form

$$\frac{ds}{dt} = -\frac{v_{max} s(t)}{s(t) + K_m} = -\frac{dp}{dt} \quad (9.43)$$

where we have defined the Michaelis constant

$$K_m := \frac{k_{-1} + k_2}{k_1} \quad \text{Michaelis-constant}$$

and the maximal velocity

$$v_{max} = k_2 e_0$$

The famous result for the production rate therefore reads

$$\boxed{v_p = \frac{dp}{dt} = \frac{v_{max} s}{s + K_m}} \quad (9.44)$$

The reaction rate increases with increasing substrate concentration  $s$ , asymptotically approaching its maximum rate  $v_{max}$ , see figure 9.9. This implies that  $v_{max}$  is the maximal production rate and  $K_m$  gives substrate concentration at which the reaction rate is half of  $v_{max}$ . Thus it does not make sense to hope for a higher production rate and to increase  $s$  much beyond  $K_m$ .

Although very helpful, this analysis has some shortcoming. In particular, we can write an implicit solution for  $s$

$$\begin{aligned} s(t) + K_m \ln(s(t)) &= A - v_{max} t \quad \text{with } A \neq 0 \\ \Rightarrow c(t) &= \frac{e_0 s(t)}{K_m + s(t)} \end{aligned} \quad (9.45)$$

thus  $c(t)$  is not constant as assumed and in particular, it does not satisfy the initial condition  $c(0) = 0$ . This shows that this analysis is not consistent and needs to be improved. In particular, we have to understand in which sense it might be relevant after all.

## 9.6.2 Rigorous treatment

Our aim now is to find a general solution for the equations 9.40 for all times. Although this is not possible analytically, we can find solution for short and long times that together give the correct behaviour. For this purpose, we use perturbation analysis.



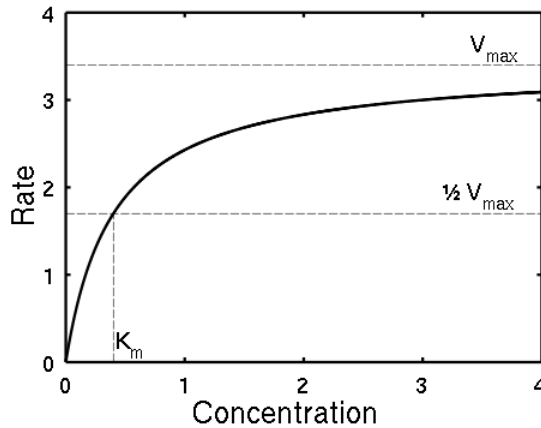


Figure 9.9: Michaelis-Menten kinetics. The reaction rate as a function of the substrate concentration, growing linearly with  $s$ , for small  $s$ , and then asymptotically approaching  $v_{max}$ . Source wikipedia.org

First we non-dimensionalize the ODE by defining non-dimensional quantities

$$\begin{aligned} \tau &= k_1 e_0 t \\ u(\tau) &= \frac{s(t)}{s_0} \leq 1 \\ v(\tau) &= \frac{c(t)}{e_0} \leq 1 \\ \lambda &= \frac{k_2}{k_1 s_0} \\ K &= \frac{k_m}{s_0} \\ \epsilon &= \frac{e_0}{s_0} \leq 1 \end{aligned}$$

We now have

$$\frac{du}{d\tau} = -u + (u + K - \lambda)v \tag{9.46}$$

$$\epsilon \frac{dv}{d\tau} = u - (u + K)v \tag{9.47}$$

with the initial conditions  $u(0) = 1$  and  $v(0) = 0$ . We note that  $u$  always decreases because  $K - \lambda = k_{-1}/(k_1 s_0) > 0$ .

We can analyze the equations qualitatively to see how the general solution will look like. For small times, we approximately have

$$\frac{du}{d\tau} = -u \tag{9.48}$$

$$\frac{dv}{d\tau} = \frac{1}{\epsilon} \tag{9.49}$$

thus substrate  $u$  decreases exponentially and complex  $v$  increases very fast. At  $v = u/(u + K)$ , the increase in  $v$  stops because now  $\dot{v} = 0$ . At this point,  $u$  still

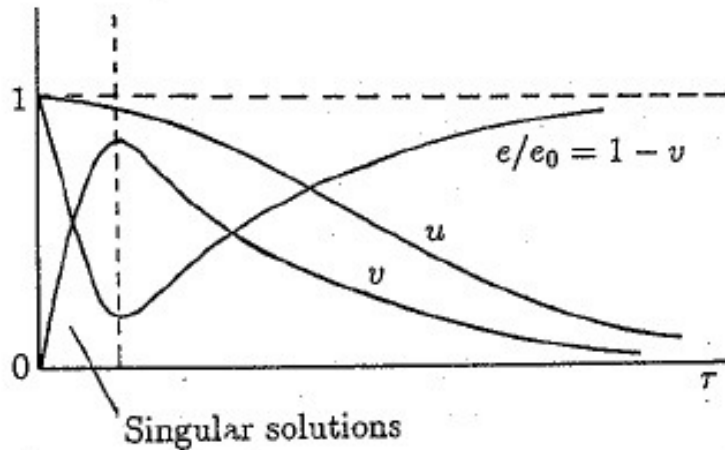


Figure 9.10: This diagram depicts the behaviour of the substrate  $u(\tau)$  and  $SE$  complex  $v(\tau)$  as a function of the nondimensional time. One can also see the progression of the concentration of the unbound enzyme  $\frac{e}{e_0}$ . Source: Mathematical biology book from J.D Murray

decreases because here  $\dot{u} = -\lambda u/(u + K)$  and  $\lambda$  is positive by definition. From there on, both  $u$  and  $v$  decrease. Thus the general evolution should look like sketched in figure 9.10.

We now use perturbation theory to derive an approximate solution. We use the small parameter  $\epsilon$  for a Taylor expansion:

$$u(\tau, \epsilon) = \sum_{n=0}^{\infty} \epsilon^n u_n(\tau)$$

$$v(\tau, \epsilon) = \sum_{n=0}^{\infty} \epsilon^n v_n(\tau)$$

To lowest order in  $\epsilon$  this gives

$$\begin{aligned} \frac{du_0}{d\tau} &= -u_0 + (u_0 + K - \lambda)v_0 \\ 0 &= u_0 - (u_0 + K)v_0 \\ \Rightarrow v_0 &= \frac{u_0}{u_0 + K} \\ \frac{du_0}{d\tau} &= -\frac{\lambda u_0}{u_0 + K} \\ \Rightarrow u_0(\tau) + K \ln[u_0(\tau)] &= 1 - \lambda\tau \end{aligned} \tag{9.50}$$

Thus this procedure gives us exactly the same result like the standard treatment. Although this solution could be improved systematically by going to higher order, this does not solve our problem that somehow our treatment becomes inconsistent again.

The solution to our problem is that we realize that in the perturbation scheme we make the strong assumption that the solutions are analytical for all times. However, this is not true for small times. We solve this problem by going from regular to singular perturbation theory. We now magnify the scale near the zero by introducing a new time scale  $\frac{\tau}{\epsilon} = \sigma$ . This allows us to look closely at the region around  $\tau = 0$ , because even small changes in  $\tau$  have large effects on the  $\sigma$  scale. We use the substitutions  $u(\tau, \epsilon) = U(\sigma, \epsilon)$  and  $v(\tau, \epsilon) = V(\sigma, \epsilon)$  to get

$$\begin{aligned}\frac{dU}{d\sigma} &= -\epsilon U + \epsilon(U + K - \lambda)V \\ \frac{dV}{d\sigma} &= U - (U + K)V\end{aligned}$$

We again approximate  $U(\sigma, \epsilon)$  and  $V(\sigma, \epsilon)$  by a Taylor expansion in  $\epsilon$  :

$$\begin{aligned}U(\sigma, \epsilon) &= \sum_{n=0}^{\infty} \epsilon^n U_n(\sigma) \\ V(\sigma, \epsilon) &= \sum_{n=0}^{\infty} \epsilon^n V_n(\sigma)\end{aligned}\tag{9.51}$$

For the dynamical equations we get in lowest order:

$$\begin{aligned}\frac{dU_0}{d\sigma} &= -\epsilon U_0 + \epsilon(U_0 + K - \lambda)V_0 \approx 0 \\ \Rightarrow U_0(\sigma) &= 1 \\ \frac{dV_0}{d\sigma} &= U_0 - (U_0 + K)V_0 \\ \Rightarrow V_0(\sigma) &= \frac{1 - \exp[-(1 + K)\sigma]}{1 + K}\end{aligned}$$

Thus the substrate concentration is constant, while the complex concentration first increases linearly and then saturates. This solution is valid for  $0 < \tau \ll 1$  (the so-called boundary layer), but not for all  $\tau$ . It is called singular or inner solution. In contrast, the solution obtained above for normal times it called the outer solution. If we compare the two solutions, we see that they are already matched:

$$\lim_{\sigma \rightarrow \infty} [U_0(\sigma), V_0(\sigma)] = [1, \frac{1}{1 + K}] = \lim_{\tau \rightarrow 0} [u_0(\tau), v_0(\tau)]$$

without the need to use higher orders. Together these both solutions give us the complete and correct time course as sketched in figure 9.10. This concludes our treatment of this problem, although in principle one could now proceed to higher orders in the Taylor expansion to improve on the lowest order solutions presented here.

## 9.7 Basics of non-linear dynamics

We now discuss how to analyze kinetic equations in a more systematic way. This field is called *dynamical systems* or *non-linear dynamics*. For an excellent

introduction into non-linear dynamics, we refer to the book by Steven Strogatz, "Nonlinear Dynamics and Chaos", Westview Press, December 2000.

In general, dynamical systems are described by a dynamical (differential) equation of the state vector  $\vec{x} = (x_1, \dots, x_n)$ :

$$\dot{\vec{x}} = \vec{f}(\vec{x}) = \begin{pmatrix} f_1(\vec{x}) \\ \vdots \\ f_n(\vec{x}) \end{pmatrix} \quad (9.52)$$

where the overdots denote differentiation with respect to the time  $t$ . The variables  $x_1, \dots, x_n$  might represent any species whose dynamics we are interested in, such as concentrations or population levels. The functions  $f_1(\vec{x}), \dots, f_n(\vec{x})$  are determined by the specific problem which we want to analyze.

The most general results of NLD are the following:

- For  $n = 1$ , the dynamical behaviour is determined by the fixed points. If they change, we have one out of four possible so-called *bifurcations*. Oscillations are not possible for  $n = 1$ .
- For  $n = 2$ , oscillations become possible. There are also a few more types of possible bifurcations.
- For  $N = 3$ , deterministic chaos becomes possible. All bifurcations can be mapped to the ones known from lower dimensions.

Although equation 9.52 looks like an overdamped equation, it is important to understand that also Newtonian systems can be written in this way. For example, the harmonic oscillator is described by the second-order differential equation:

$$m\ddot{x} + kx = 0$$

With the definition  $x_1 := x$  and  $x_2 := v = \dot{x}$ , we can rewrite the equation as follows:

$$\Rightarrow \dot{x}_1 = \dot{x} = x_2, \quad \dot{x}_2 = \ddot{x} = -\underbrace{\frac{k}{m}}_{\omega^2} \cdot x = -\omega^2 x_1$$

$$\Rightarrow \dot{\vec{x}} = \begin{pmatrix} 0 & 1 \\ -\omega^2 & 0 \end{pmatrix} \vec{x} = A\vec{x} \quad (9.53)$$

Thus, we end up with a linear version of our general dynamic equation. We also conclude that the harmonic oscillator is in fact a two-dimensional system. This is an example that oscillations become possible only in two dimensions.

The solutions of equation 9.52 can be visualized as trajectories flowing through an  $n$ -dimensional phase space with coordinates  $x_1, \dots, x_n$ . In general, non-linear dynamics deals with analyzing these flow properties, often in a graphical manner.

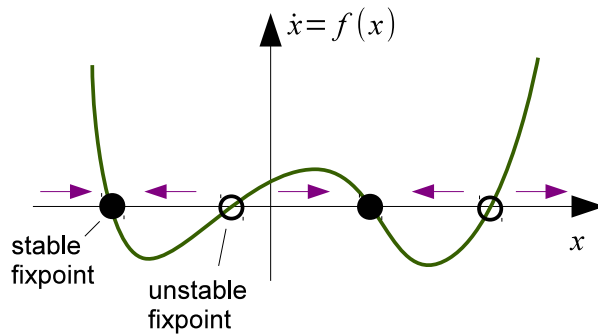


Figure 9.11: Phase portrait of an arbitrary function  $\dot{x} = f(x)$ . The pink arrows denote the direction of flow on a line. Fixed points ( $\dot{x} = 0$ ) in one dimension can either be stable (solid dot) or unstable (hollow dot), meaning that already small perturbations will result in a flow away from the unstable fixed point.

### 9.7.1 One-dimensional systems

We first restrict ourselves to  $n = 1$  dimension, i. e. with a single equation of the form  $\dot{x} = f(x)$ . In a so-called "phase portrait" we can visualize a "**flow on a line**": If  $\dot{x} > 0$ , the flow is in the positive  $x$ -direction, and if  $\dot{x} < 0$ , it is in the negative  $x$ -direction (figure 9.11). For  $\dot{x} = 0$  the system is in a steady state  $x^*$  which is often referred to as "fixed point".

It can also be seen in figure 9.11 that the system can evolve either to a stable steady state, stay at a fixed point (if it is unstable, this is only possible if there are no perturbations whatsoever) or explode. To determine whether we deal with a stable or an unstable fixed point, a "**linear stability analysis**" around the fixed point  $x = x^* + \eta$  can be performed:

$$\begin{aligned} \dot{\eta} = \dot{x} = f(x) &= f(x^* + \eta) = \underbrace{f(x^*)}_0 + \eta f'(x^*) + \mathcal{O}(\eta^2) \\ \Rightarrow \eta(t) &= \eta_0 e^{f'(x^*)t} \end{aligned}$$

$$f'(x^*) < 0 \Rightarrow \text{stable} \quad (9.54)$$

$$f'(x^*) > 0 \Rightarrow \text{unstable} \quad (9.55)$$

Also note the intrinsic time scale of the system,  $\tau = 1/f'(x^*)$ .

Examples:

#### 1. Logistic growth

The most prominent model of mathematical biology is the logistic growth model of a population size  $N(t)$ . This was suggested to describe the growth of human populations by Verhulst in 1838:

$$\dot{N} = rN\left(1 - \frac{N}{K}\right) \quad (9.56)$$

where  $N \geq 0$ . Here,  $r$  denotes the growth rate of the population and  $K$  is the carrying capacity which accounts for population-limiting effects such as

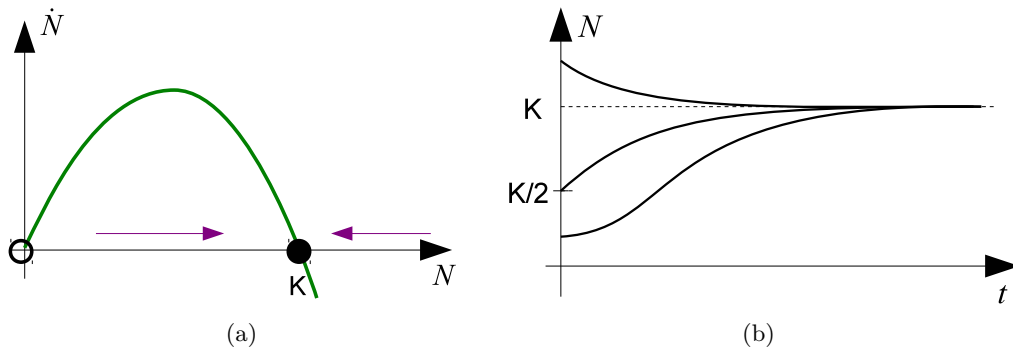


Figure 9.12: a.) Phase portrait of the logistic growth model (equation 9.56). The carrying capacity  $K$  denotes a stable fixed point. b.) The population always approaches  $K$  for large times. Note the qualitatively different behaviors for different initial values of  $N$ .

overcrowding and limited resources. The phase portrait is shown in figure 9.12a. To confirm analytically our graphical result that there is a stable fixed point at  $N^* = K$ , we can perform a linear stability analysis around this point:

$$f'(N^*) = r - \frac{2rN^*}{K} = -r > 0 \quad \checkmark$$

Hence, the carrying capacity  $K$  is approached by the population from any initial value  $N > 0$ , but in a qualitatively different manner (compare figure 9.12b, calculation not shown here).

## 2. Autocatalysis

An autocatalysis is a chemical reaction which exhibits a positive feedback to produce the species  $X$ :



With the law of mass action we can immediately identify the differential equation for the concentration of  $X$ :

$$\dot{x} = k_1 a x - k_{-1} x^2 \quad (9.58)$$

Thus we find that this equation is essentially the same as for logistic growth.

For a flow on a line, the trajectories can only increase, decrease or stay constant (compare figure 9.11), but they cannot cross themselves. Hence, no oscillations in a 1D system are possible. There are other ways to arrive at this conclusion. We can understand the first-order differential equation as an overdamped one-dimensional system and define a potential  $V(x)$  such that

$$\dot{x} = f(x) = -\frac{dV}{dx} \quad (9.59)$$

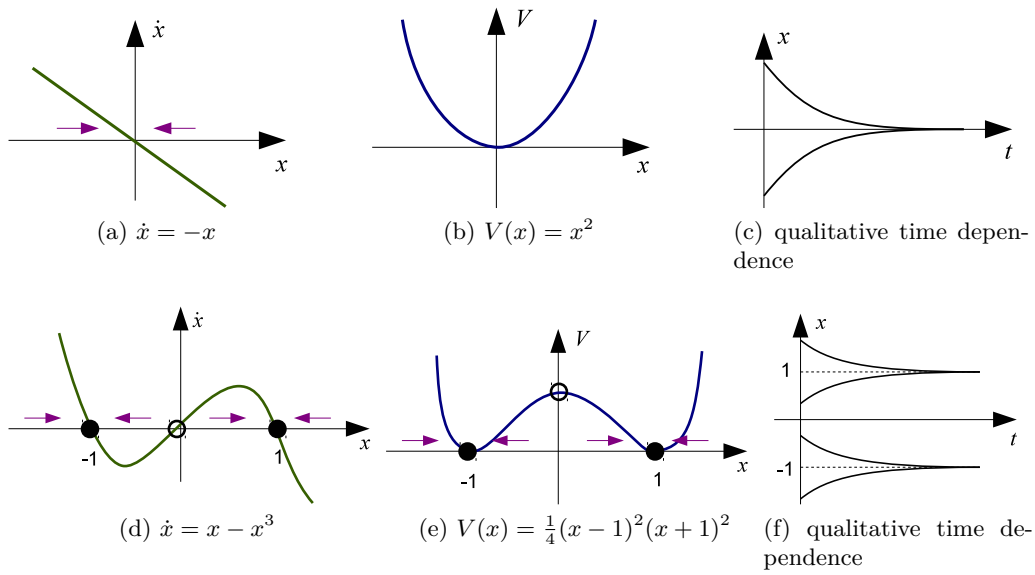


Figure 9.13: Phase portrait, potential and time evolution of a linear  $f(x)$  (upper panel) and a cubic  $f(x)$  (lower panel).

This integral always exists. We can now compute the derivative of  $V$  with respect to the time  $t$

$$\frac{dV}{dt} = \frac{dV}{dx} \cdot \frac{dx}{dt} = - \left( \frac{dV}{dx} \right)^2 \leq 0 \quad (9.60)$$

which implies that the system loses energy until it has reached a local minimum, i.e. a stable fixed point. To illustrate this, two examples are shown in figure 9.13. At any case, because the system comes to a halt, it cannot oscillate. This is different for  $n = 2$ , where energy is lost in one form but can be converted into another form.

## 9.7.2 Bifurcations

At first glance, the flow on the line seems to be a rather boring problem: With no oscillations, trajectories always end up in a stable fixed point or head out to infinity. However, as a function of model parameters, fixed points can be created or destroyed, or their stability can change. These qualitative changes in the system dynamics are called **bifurcations** and the parameter values at which they occur are so-called **bifurcation points**. Mathematical bifurcations usually represent some transition, instability or threshold in the physical model.

Bifurcations can be visualized in a **bifurcation diagram** which plots the fixed points  $x_i^*$  against the parameter  $r$  which is varied. Stable fixed points are usually depicted as solid curves whereas unstable fixed points are depicted as dotted lines. Note, that there can be several parameters  $r_i$ , leading to a multidimensional bifurcation diagram which then becomes increasingly complicated.

For  $n = 1$ , there are four types of bifurcations.

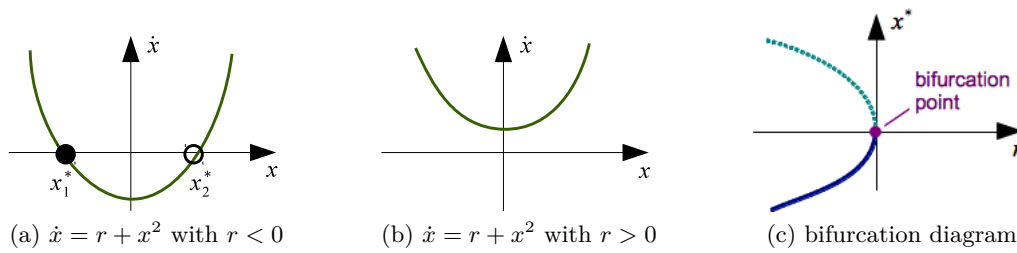


Figure 9.14: Example of a saddle-node bifurcation.

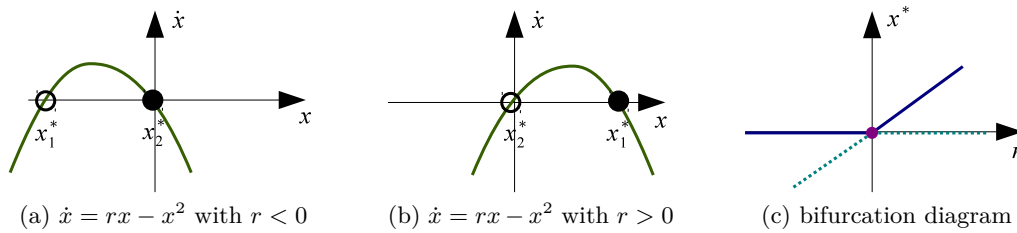


Figure 9.15: Example of a transcritical bifurcation.

### 9.7.2.1 Saddle-node bifurcation

The saddle-node bifurcation is the basic mechanism by which fixed points are **created** or **destroyed**. A typical example is shown in figure 9.14. With increasing  $r$ , the parabola is shifted in the positive  $\dot{x}$ -direction and the two fixed points  $x_1^*$  and  $x_2^*$  move closer to each other until they annihilate when  $r = 0$ . For  $r > 0$ , there is no fixed point at all and therefore no stable solution of the dynamic equation. Hence, the bifurcation point is located at  $r = 0$  (compare the bifurcation diagram in figure 9.14c).

### 9.7.2.2 Transcritical bifurcation

The transcritical bifurcation describes a **change in stability** of a fixed point. In the example shown in figure 9.15, the unstable fixed point  $x_1^* = r$  moves closer to the origin with increasing  $r$ . For  $r < 0$ , there is a stable fixed point  $x_2^* = 0$  at the origin. However, when  $r = 0$ , the fixed points "exchange their stability", meaning that for further increasing  $r > 0$  the fixed point  $x_2^*$  is unstable, whereas  $x_1^*$  is stable.

### 9.7.2.3 Supercritical pitchfork bifurcation

The pitchfork bifurcation is common in physical problems that exhibit inversion symmetry. The dynamic equation of our example in figure 9.16 is symmetric under the exchange  $x \rightarrow -x$ . For  $r < 0$ , there is only one fixed point  $x^* = 0$ . However, for  $r > 0$  two stable fixed points branch off symmetrically and the origin has become unstable. Note the bifurcation diagram (figure 9.16c) which



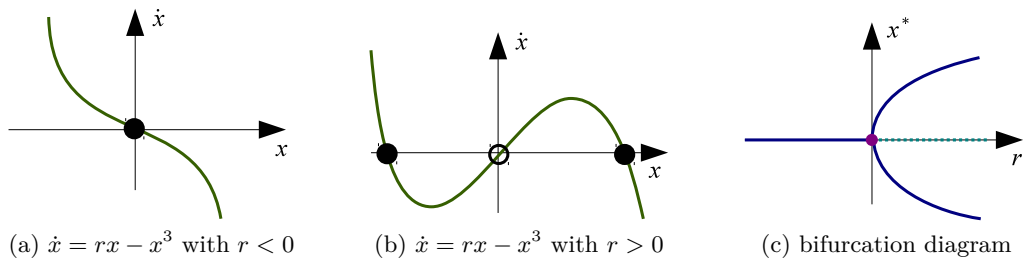


Figure 9.16: Example of a supercritical pitchfork bifurcation.

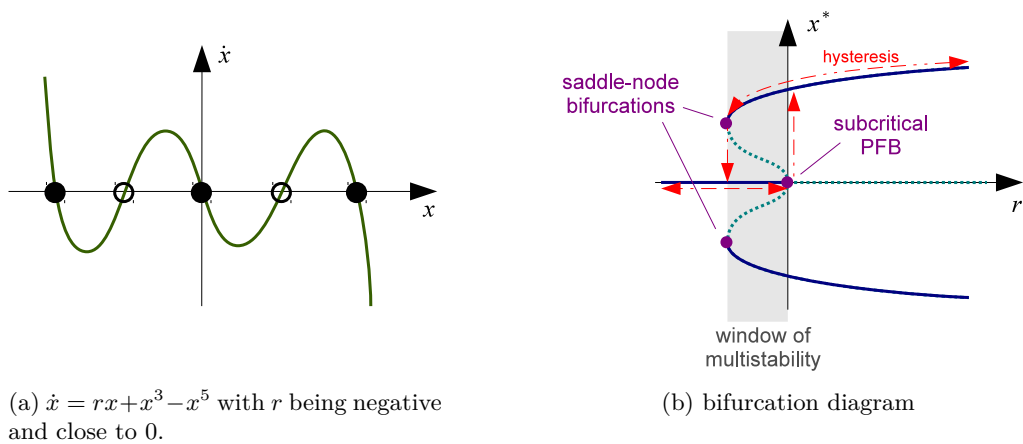


Figure 9.17: Example of a subcritical pitchfork bifurcation.

looks similar to a pitchfork, hence the name. An important physical example is the continuous (or second-order) phase transition in the Ising model.

#### 9.7.2.4 Subcritical pitchfork bifurcation

Actually, the subcritical pitchfork bifurcation is a pitchfork bifurcation of the form  $\dot{x} = rx + x^3$ . Since this leads to a blow-up  $x(t) \rightarrow \pm\infty$  for all  $r > 0$  and  $x_0 \neq 0$ , which is quite unpleasant for a real physical system, we add a stabilizing term  $-x^5$  to the dynamical equation (figure 9.17a).

In the resulting bifurcation diagram (figure 9.17b) we can observe two features which we have not encountered before: First, for  $r$  slightly smaller than 0, several qualitatively different stable fixed points exist at the same time, marking a "**window of multistability**". Secondly, the behavior of the system in this window depends on whether  $r$  was changed from very negative values or whether it was changed from positive values into the window. Transitions of the system between the possible steady states can only occur at the corresponding bifurcation points and are unidirectional. This lack of irreversibility is called "**hysteresis**".

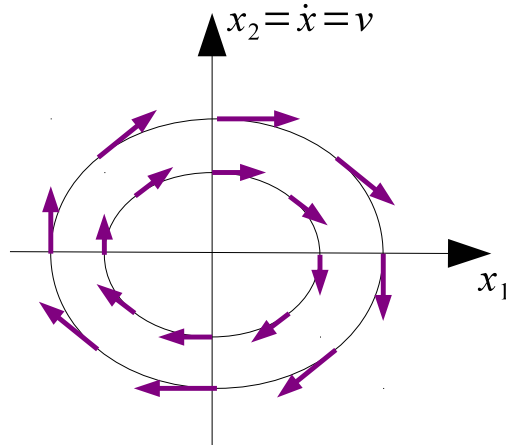


Figure 9.18: Phase plane trajectory of the harmonic oscillator. The closed orbit corresponds to a periodic motion. The amplitude of the periodic motion depends on the initial condition.

### 9.7.3 Two-dimensional systems

Instead of a "flow on a line" like we have seen for one-dimensional systems, in two dimensions we deal with a flow in the "phase plane" where oscillations become possible.

As an example, we again choose the harmonic oscillator

$$\dot{\vec{x}} = \begin{pmatrix} 0 & 1 \\ -\omega^2 & 0 \end{pmatrix} \vec{x} \quad (9.61)$$

and determine the shape of the orbit:

$$\begin{aligned} \frac{\dot{x}}{\dot{v}} &= \frac{v}{-\omega^2 x} \\ \Rightarrow -\omega^2 x dx &= v dv \\ \Rightarrow \frac{1}{2}v^2 + \frac{1}{2}\omega^2 x^2 &= \text{const} \end{aligned} \quad (9.62)$$

$$\Rightarrow \underbrace{\frac{1}{2}mv^2}_{\text{kinetic energy}} + \underbrace{\frac{1}{2}kx^2}_{\text{potential energy}} = \text{const} \quad (9.63)$$

We thus find that the system follows an elliptic path in the phase plane (equation 9.62, compare figure 9.18). Obviously the system is not overdamped as it is necessarily the case in 1D, since the energy of the system is conserved for all times (equation 9.63).

In biology, one often encounters oscillations. One out of many examples is the circadian rhythm which can be found in every single mammalian cell. However, such systems typically are non-linear in contrast to the linear harmonic oscillator, because linear systems have some disadvantages:

1. The amplitude depends on the initial conditions.

2. Perturbations stay small, but they are not corrected.
3. There is no feedback that can regulate the system.

In a noisy biological environment, these features would result in a non-functional system.

### Linear stability analysis

The flow-pattern we have observed for the harmonic oscillator is only one out of several flow patterns occurring in  $n = 2$ . Linear systems are the reference point for non-linear ones. We will now introduce a systematic classification of flow patterns in linear systems, and then expand this idea to non-linear ones:

$$\dot{x} = A \cdot \vec{x} \quad \text{with } A = \begin{pmatrix} a & b \\ c & d \end{pmatrix} \quad (9.64)$$

The well-known general solution of this linear ODE is:

$$\vec{x} = c_1 e^{\lambda_1 t} \vec{v}_1 + c_2 e^{\lambda_2 t} \vec{v}_2 \quad (9.65)$$

where  $\lambda_{1/2}$  are the eigenvalues of  $A$  and  $\vec{v}_{1/2}$  the corresponding eigenvectors. The eigenvalues are determined with the characteristic polynomial:

$$\begin{aligned} & (a - \lambda)(d - \lambda) - cb = 0 \\ \Rightarrow & \lambda^2 - \underbrace{(a + d)}_{=: \tau = \text{tr} A} \lambda + \underbrace{(ad - cb)}_{=: \Delta = \det A} = 0 \\ \Rightarrow & \lambda_{1/2} = \frac{\tau \pm \sqrt{\tau^2 - 4\Delta}}{2} \end{aligned} \quad (9.66)$$

For  $4\Delta > \tau^2$ , the eigenvalues are complex and the system oscillates. Hence,  $\Delta = \tau^2/4$  defines the boundary of the region where oscillations occur. Further analysis will result in six possible flow patterns which are illustrated in a phase diagram (figure 9.19).

As already mentioned, we can use our results of the linear system as a reference point for non-linear systems in a **linear stability analysis** similar to the one-dimensional case. Recall the dynamical equation:

$$\begin{pmatrix} \dot{x} \\ \dot{y} \end{pmatrix} = \begin{pmatrix} f(x, y) \\ g(x, y) \end{pmatrix}$$

Well-behaved non-linear systems can be expanded around their fixed points  $(x^*, y^*)$ : one first investigates the the two *nullclines* defined by  $\dot{x} = f(x, y) = 0$  and  $\dot{y} = g(x, y) = 0$  (figure 9.20). Secondly, one investigates their intersections which are the fixed points. We perform a *linear stability analysis* around them:

$$u := x - x^*, \quad v = y - y^*$$

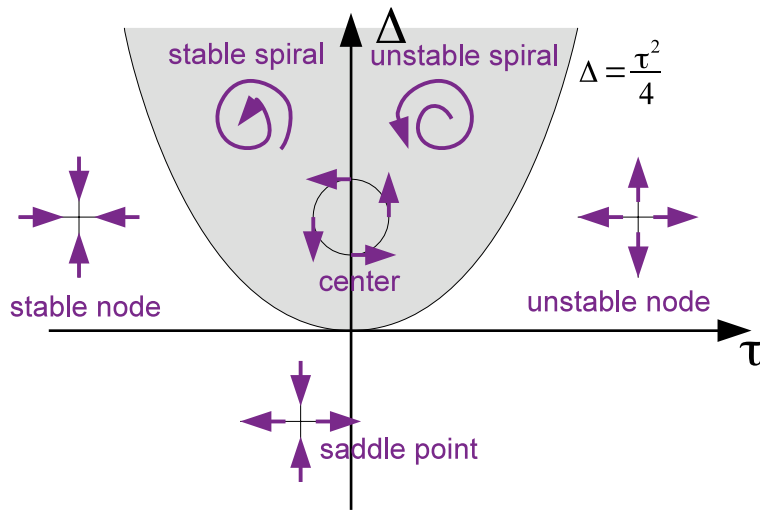


Figure 9.19: Different flow patterns for a linear 2D system. The gray area marks the area where oscillations occur in the system. Note that the center is unstable in regard to small perturbations.

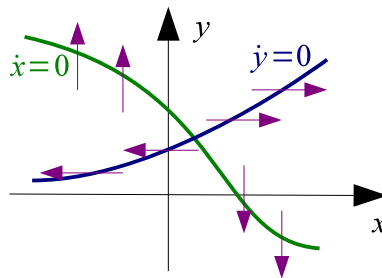


Figure 9.20: Nullclines of a two-dimensional system defined by  $\dot{x} = f(x, y) = 0$  and  $\dot{y} = g(x, y) = 0$ . On the nullclines, the flow is purely vertical and horizontal, respectively. The fixed point  $(x^*, y^*)$  is then given by their intersection.

$$\begin{aligned}
 \Rightarrow \dot{u} &= \dot{x} = f(x, y) = f(x^* + u, y^* + v) \\
 &= \underbrace{f(x^*, y^*)}_0 + \partial_x f(x^*, y^*)u + \partial_y f(x^*, y^*)v + \mathcal{O}(u^2, uv, v^2) \\
 \text{similar for } v \Rightarrow &\begin{pmatrix} \dot{u} \\ \dot{v} \end{pmatrix} = \underbrace{\begin{pmatrix} \partial_x f & \partial_y f \\ \partial_x g & \partial_y g \end{pmatrix}}_{=: A = J(x^*, y^*)} \cdot \begin{pmatrix} u \\ v \end{pmatrix} \quad (9.67)
 \end{aligned}$$

Now one can analyze the matrix  $A$  according to our procedure of the linear system above and thus classify the fixed points. Usually this is a good starting point for a full analysis of the non-linear system.

### 9.7.4 Stable limit cycles

In two dimensions, one can get oscillations. In addition, in non-linear systems a new class of oscillations are possible, the so-called stable limit cycles. As a

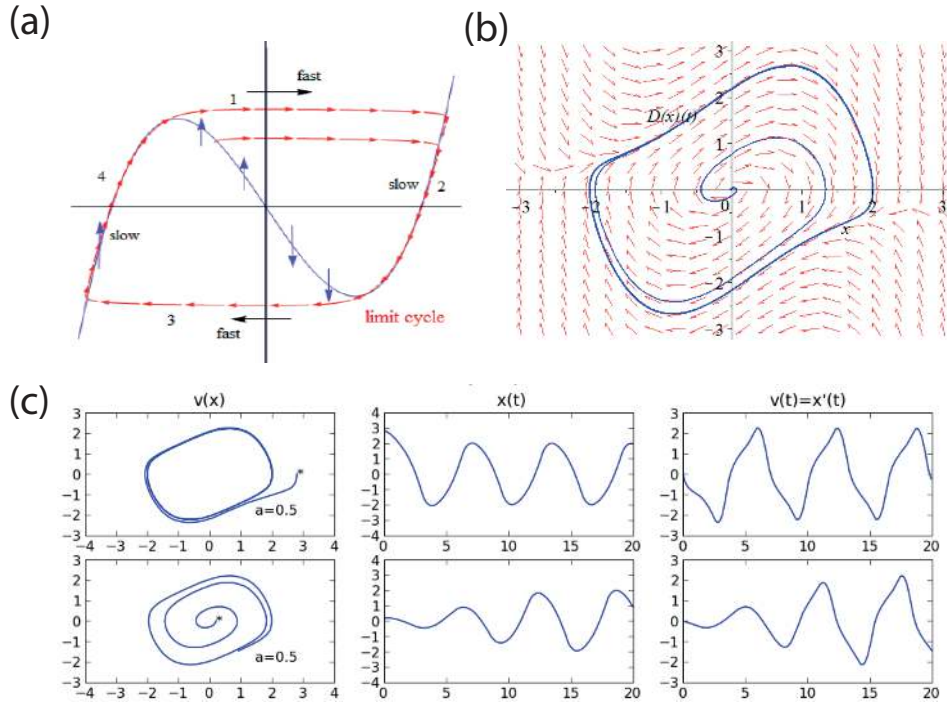


Figure 9.21: Van der Pol oscillator. (a) Flow in the  $(x, y)$ -phase plane: the system slowly follows the cubic nullcline and then quickly zips to the other side. (b) Flow in the  $(x, v)$ -phase plane. (c) Approach to the stable limit cycle from outside and inside. In both cases, we eventually end up with the sawtooth oscillations typical for the van der Pol oscillator.

paradigmatic example, we now discuss the van der Pol oscillator:

$$\ddot{x} + \mu(x^2 - 1)\dot{x} + x = 0 \quad (9.68)$$

Different from the harmonic oscillator, this one has negative damping at small amplitude and positive damping at large amplitude. Thus the oscillator is driven up by energy input if it relaxes and it is dampened if it is agitated. From this, an intermediate state of sustained oscillators is emerging with an amplitude that is independent of initial conditions.

We analyze this system in the regime  $\mu \gg 1$  according to Lienard. We rewrite it in the following way:

$$-x = \ddot{x} + \mu(x^2 - 1)\dot{x} = \frac{d}{dt}(\dot{x} + \mu F(x)) := \dot{w} \quad (9.69)$$

where we defined  $F(x) = (x^3/3 - x)$ . We therefore have a new set of dynamical equations

$$\dot{x} = w - \mu F(x), \quad \dot{w} = -x \quad (9.70)$$

We now define  $y := w/\mu$  and therefore get

$$\dot{x} = \mu(y - F(x)), \quad \dot{y} = -x/\mu \quad (9.71)$$

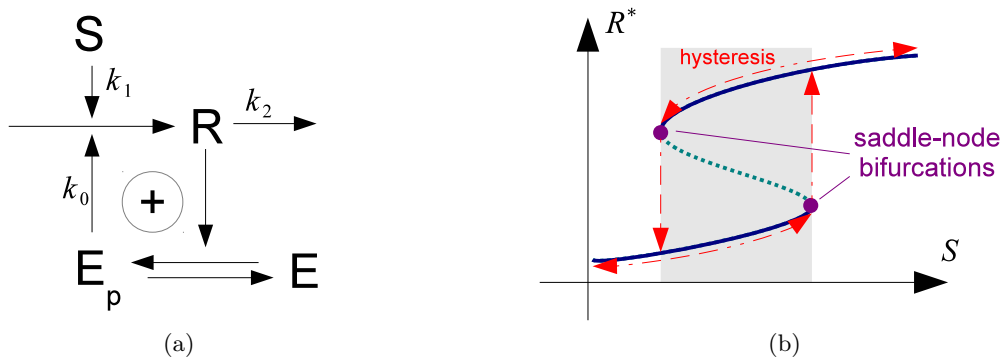


Figure 9.22: a.) A positive feedback loop in signal transduction. The signal  $S$  will be our bifurcation parameter. The response protein  $R$  acts as a kinase for the inactive enzyme  $E$ , i.e. it adds an inorganic phosphate to the enzyme to produce the active enzyme  $E_p$ . The latter can enhance the production of  $R$ . b.) Signal-response curve for the steady state response  $R^*$  in the form of a one-dimensional bifurcation diagram exhibiting bistability. In this example, bistability forms a reversible switch.

These equations are easy to understand: the nullclines are  $y = F(x)$  and  $x = 0$  and the steady state at  $(0, 0)$  is not stable because the Jacobian reads

$$A = \begin{pmatrix} -\mu(x^2 - 1) & \mu \\ -1/\mu & 0 \end{pmatrix} \quad (9.72)$$

thus we have  $\tau = \mu$  and  $\Delta = 1$  at  $(0, 0)$ . For small  $\mu$ , we have an unstable spiral, and for large  $\mu$ , we have an unstable node.

The flow in the  $(x, y)$ -plane can be understood as follows (compare figure 9.21). We start with an initial condition  $y - F(x) = O(1)$ . Then the velocity is fast in the  $x$ -direction ( $O(\mu)$ ) but slow in the  $y$ -direction ( $O(1/\mu)$ ). Thus it zips to the right side until it hits the cubic nullcline. If  $y - F(x) = O(1/\mu^2)$ , then both velocities become comparably small ( $O(1/\mu)$ ). The system now crosses the nullcline and slides along it until it reaches its extremum. Then it accelerates again in the horizontal direction and the second half of the cycle begins. Altogether we have a sequence of four parts (fast, slow, fast, slow). We are always driven to the same stable limit cycle independent of initial conditions. The resulting sawtooth-like pattern is typical for a *relaxation oscillator*, which slowly builds up some tension and then quickly relaxes it, compare figure 9.21.

## 9.8 Biological examples

### 9.8.1 Revisiting bistability

As we discussed above, positive feedback often leads to bistability and switch-like behaviour (figure 9.22a). The differential equation for the response  $R$  can be taken directly from the scheme:

$$\dot{R} = k_0 E_p + k_1 S - k_2 R \quad (9.73)$$

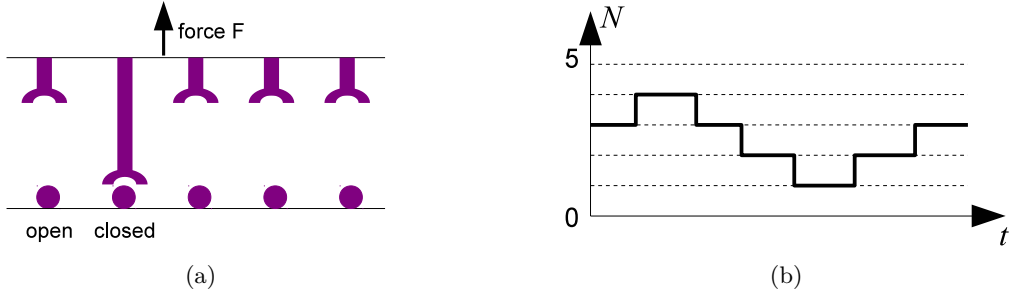


Figure 9.23: a.) Open and closed bonds of an adhesion cluster. b.) Possible trajectory of the number of closed bonds  $N$  in time for  $F = 0$ .

We now assume that  $E_p$  and  $E$  are in equilibrium, that  $E_p + E = E_{tot} = const$  and that the phosphorylation and dephosphorylation follow Michaelis-Menten kinetics.  $E_p^*$  can now be determined:

$$\dot{E}_p = \frac{k_1 R (E_{tot} - E_p)}{K_{m1} + (E_{tot} - E_p)} - \frac{k_2 E_p}{K_{m2} + E_p} \stackrel{!}{=} 0 \quad (9.74)$$

$$\Rightarrow k_1 R (E_{tot} - E_p^*) (K_{m2} + E_p^*) = k_2 E_p^* (K_{m1} + (E_{tot} - E_p^*))$$

$$\Rightarrow \frac{E_p^*}{E_{tot}} = G(k_1 R, k_2, \frac{K_{m1}}{E_{tot}}, \frac{K_{m2}}{E_{tot}}) \quad (9.75)$$

with<sup>2</sup>

$$G(u, v, J, K) = \frac{2uK}{B + \sqrt{B^2 - 4(v-u)uK}} \quad \text{Goldbeter-Koshland function} \quad (9.76)$$

$$B = (v - u) + vJ + uK$$

Though highly non-linear, the main equation (equation 9.73) is now one-dimensional and its steady-state solution shown in figure 9.22b. We see a window of bistability separated by two saddle-node bifurcations. This switch between high and low responses is a very important control element in biological systems.

## 9.8.2 Stability of an adhesion cluster

Another example for bifurcations in biological systems is the stability of an adhesion cluster under force (figure 9.23). Each of the  $N_t$  bonds in the cluster can either be open or closed. The number of closed bonds  $N(t)$  can be described by a dynamical equation:

$$\dot{N} = -k_{off} N + k_{on} (N_t - N) \quad (9.77)$$

$$= -k_0 e^{\frac{F}{F_0 \cdot N}} N + k_{on} (N_t - N) \quad (9.78)$$

with  $(N_t - N)$  denoting the number of open bonds and a force-dependent dissociation constant  $k_{off} = k_0 e^{\frac{F}{F_0 \cdot N}}$ . Hence, the force couples the bonds and makes the system non-linear.

<sup>2</sup>A Goldbeter and D E Koshland: An amplified sensitivity arising from covalent modification in biological systems, PNAS 1981

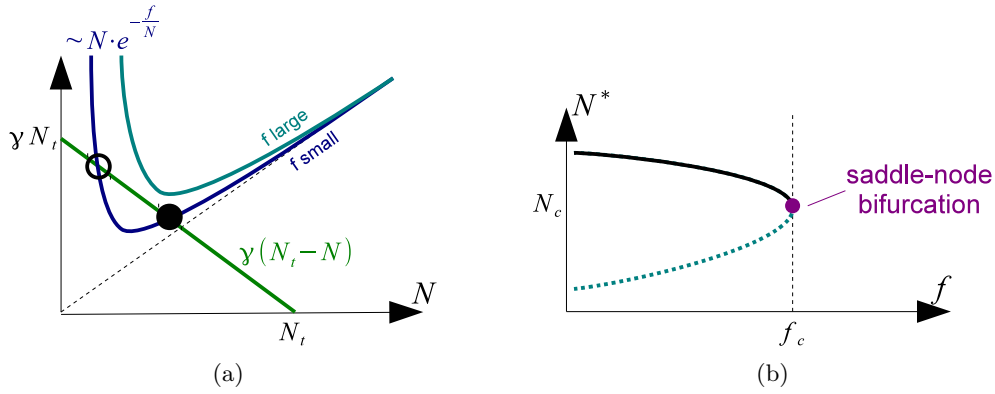


Figure 9.24: a.) Graphical solution of equation 9.80 for large and small  $f$ . Note, that for large  $f$  there is no stable solution. b.) Bifurcation diagram of the system. At the bifurcation point  $(f_c, N_c)$  the two fixed points collapse. This is a typical example for a saddle-node bifurcation.

If  $F = 0$ , we are dealing with a simple two-state process in which the bonds are decoupled ( $k_{off} = k_0$ ). In this case, the system is linear and the solution of equation 9.78 is simply an exponential relaxation to a steady state. For the steady-state value we get:

$$\dot{N} = 0 \Rightarrow k_0 N^* = k_{on}(N_t - N^*) \Rightarrow N^* = \frac{k_{on}}{k_{on} + k_0} N_t \quad (9.79)$$

If however  $F \neq 0$ , the system is non-linear and we observe a bifurcation as a function of  $F$ . Introducing the dimensionless quantities  $\tau = k_0 t$ ,  $f = F/F_0$  and  $\gamma = k_{on}/k_0$ , equation 9.78 reads:

$$\begin{aligned} \frac{dN}{d\tau} &= -e^{\frac{f}{N}} N + \gamma(N_t - N) \\ \stackrel{SS}{\Rightarrow} N e^{\frac{f}{N}} &= \gamma(N_t - N) \end{aligned} \quad (9.80)$$

This is visualized in figure 9.24, showing that a saddle-node bifurcation occurs as  $f$  is increased, thus a steady state only exists up to a critical force  $f_c$ .

We now compute the critical value for the bifurcation,  $f_c(\gamma)$ :

$$\text{equal values: } N_c e^{f_c/N_c} = \gamma(N_t - N_c) \quad (9.81)$$

$$\text{equal slopes: } e^{f_c/N_c} \left(1 - \frac{f_c}{N_c}\right) = -\gamma \quad | \cdot N_c \quad (9.82)$$

If we then insert equation 9.81 in equation 9.82 to get

$$\gamma = \frac{f_c}{N_t} e^{f_c/N_c} \quad (9.83)$$



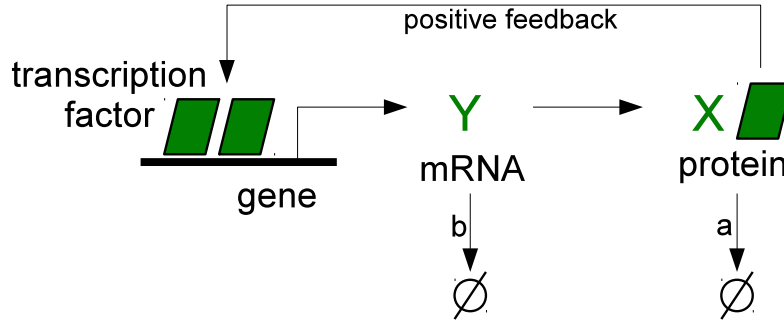


Figure 9.25: Sketch of a positive feedback loop implemented into a gene regulatory network. The gene is transcribed into mRNA ( $Y$ ) which is then translated into the protein  $X$ . The protein can form clusters of size 2 which then act as a transcription factor enhancing their own gene expression. Both mRNA and protein are subject to degradation processes within the cell.

Dividing equation 9.82 by equation 9.81 yields:

$$\begin{aligned}
 1 - \frac{f_c}{N_c} &= \frac{-N_c}{N_t - N_c} \\
 \Rightarrow f_c &= \frac{N_t N_c}{N_t - N_c} \\
 \Rightarrow \frac{f_c}{N_c} &= \frac{f_c}{N_t} + 1
 \end{aligned} \tag{9.84}$$

Now we insert equation 9.84 in equation 9.83:

$$\begin{aligned}
 \gamma &= \frac{f_c}{N_t} e^{(f_c/N_t + 1)} \\
 \Rightarrow \frac{\gamma}{e} &= \frac{f_c}{N_t} e^{f_c/N_t} \\
 \Rightarrow \boxed{\frac{f_c}{N_t} = \text{plog} \frac{\gamma}{e}}
 \end{aligned} \tag{9.85}$$

where  $x = \text{plog}(a)$  is the solution of  $xe^x = a$  (product logarithm). This solution tells us that rebinding  $\gamma$  creates a stability threshold  $f_c$  in force, which vanishes linearly with rebinding rate  $\gamma$ . For large  $\gamma$ , the relation becomes logarithmic.

### 9.8.3 Genetic switch

We now discuss an example for a saddle-node bifurcation in a two-dimensional biological system. Consider a model for a genetic control system as shown in figure 9.25 which forms a positive feedback loop.

Taking into account that the binding of the transcription factor to the DNA follows Michaelis-Menten kinetics, the corresponding dynamical equations can

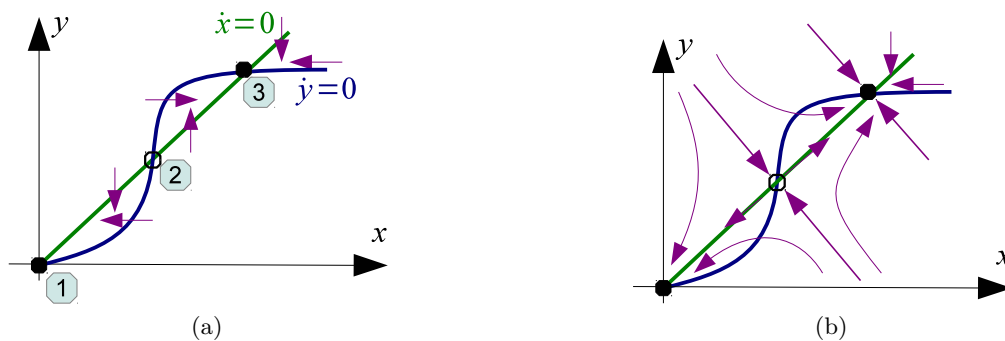


Figure 9.26: a.) Nullclines of the genetic switch model. The fixed points were numbered according to the text. The vector field is vertical on the line  $\dot{x} = 0$  and horizontal on the line  $\dot{y} = 0$ . The directions can be determined by noting the signs of  $\dot{x}$  and  $\dot{y}$ . b.) Phase portrait of the genetic switch.

immediately be formulated.

$$\dot{x} = y - ax \quad (9.86)$$

$$\dot{y} = \frac{x^2}{1+x^2} - by \quad (9.87)$$

The nullclines are then given by

$$y = ax \quad (9.88)$$

$$y = \frac{x^2}{b(1+x^2)} \quad (9.89)$$

and are shown in figure 9.26a denoting that there are at most three fixed points. Since the parameter  $a$  governs the slope of the curve  $\dot{x} = 0$ , the two fixed points ② and ③ collide and disappear as  $a$  increases. This behavior reminds us strongly of that of a saddle-node bifurcation in one-dimensional systems.

Now, the positions of the three fixed points are determined:

$$ax^* = \frac{x^{*2}}{b(1+x^{*2})} \Rightarrow x_1^* = 0 \quad (9.90)$$

$$\Rightarrow x_{2/3}^* = \frac{1 \pm \sqrt{1 - 4a^2b^2}}{2ab} \quad (9.91)$$

The fixed points ② and ③ collide if  $1 = 4a^2b^2$  which defines the critical parameter value  $a_c = 1/(2b)$ . At the bifurcation, the fixed point is given by  $x_{2/3}^* = 1$ . Hence,  $x_2^* < 1$  and  $x_3^* > 1$ .

In order to the types of the fixed points, we perform a linear stability analysis with a Jacobian:

$$A = \begin{pmatrix} -a & 1 \\ \frac{2x}{(1+x^2)^2} & -b \end{pmatrix}$$

For ①, we find for the determinant  $\Delta = ab > 0$  and for the trace  $\tau = a + b$  :

$$\Rightarrow \tau^2 - 4\Delta = (a + b)^2 - 4ab = (a - b)^2 > 0$$

Comparing this with figure 9.19, we know that ① is a stable node. For ② and ③ we get:

$$\begin{aligned} \Delta &= ab - \frac{2x^*}{(1 + x^{*2})^2} \\ \text{with } abx^* &= \frac{x^{*2}}{1 + x^{*2}} : &= ab - \frac{2ab}{1 + x^{*2}} \\ \Rightarrow \Delta &= ab \cdot \frac{x^{*2} - 1}{x^{*2} + 1} \end{aligned} \quad (9.92)$$

Since  $x_2^* < 0$ , we get  $\Delta < 0$  which classifies ② as a saddle point. On the other hand, ③ is a stable node, because with  $x_3^* > 1$  we now that  $0 < \Delta < ab$  and hence  $\tau^2 - 4\Delta > (a - b)^2 > 0$ . The phase portrait is plotted in figure 9.26b.

If  $a < a_C = 1/(2b)$ , or in other words, mRNA and protein degrade sufficiently slowly with  $ab < 1/2$ , then the system is bistable and acts like a genetic switch. Depending on the initial conditions, the gene is either "on" or "off". The stable manifold of the saddle acts like a threshold ("separative"), separating the two sinks of attraction.

In general, all four types of bifurcation discussed for  $n = 1$  can occur for  $n = 2$ . They keep their one-dimensional nature, with the flow in the extra dimension being essentially simple attraction or repulsion (example for "center manifold theory"). The example of the genetic switch shows this for a saddle-node bifurcation in  $n = 2$ .

### 9.8.4 Glycolysis oscillator

Every living cell needs energy in the form of ATP. In oxidation, this is produced from food sources such as glucose. One molecule of glucose ( $C_6H_{12}O_6$ ) can be used to produce up to 28 molecules of ATP. The biochemical process of breaking down sugar to obtain energy is called glycolysis. Since the production of ATP should adapt to its need, some kind of feedback has to be implemented into the pathway.

Indeed, glycolytic oscillations have been discovered in 1964 in yeast and muscle extracts (monitored by fluorescence of NADH, periods are 5 and 20 minutes, respectively). These oscillations are produced by the phosphofructokinase (PFK), whose activity is controlled by ATP/ADP (figure 9.27a). A simple mathematical model goes back to Sel'kov in 1968<sup>3</sup>. Inhibition by ATP and activation by ADP makes sure that the pathway becomes active only when needed. However, because ATP is also a substrate for PFK, this leads to an instability (figure 9.27b).

---

<sup>3</sup>E Sel'kov: "On the Mechanism of Single-Frequency Self-Oscillations in Glycolysis. I. A Simple Kinetic Model," Eur. J. Biochem. 4(1), 79-86, 1968.

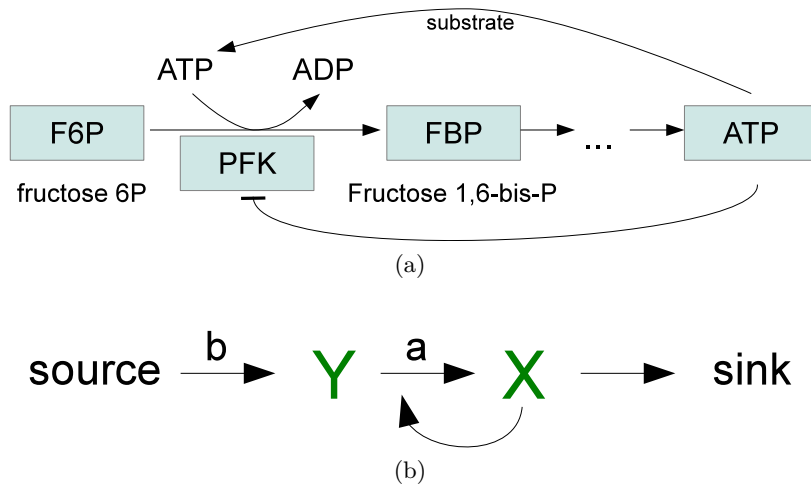


Figure 9.27: a.) Simplified scheme of the glycolysis pathway in a cell. Note, that ATP acts both as an inhibitor and an activator for its own production. b.) Simple model for  $x$  and  $y$  representing the conflicting role of ATP.

In dimensionless form, the corresponding dynamical equations (going back to Sel'kov) are:

$$\dot{x} = -x + ay + x^2y \quad (9.93)$$

$$\dot{y} = b - ay - x^2y \quad (9.94)$$

where  $x = [FBP], [ADP]$  and  $y = [F6P], [ATP]$ . The nullclines are given by

$$y = \frac{x}{a + x^2} \quad (9.95)$$

$$y = \frac{b}{a + x^2} \quad (9.96)$$

and are shown in figure 9.28a.

The only fixed point of this system,  $(b, \frac{b}{a+b^2})$ , has to be unstable for an oscillation. From a linear stability analysis we obtain:

$$A = \begin{pmatrix} -1 + 2xy & a + x^2 \\ -2xy & -(a + x^2) \end{pmatrix}$$

$$\text{at } \xrightarrow{\text{fixed}} \text{point} \quad \Delta = a + b^2 > 0 \quad (9.97)$$

$$\tau = -\frac{b^4 + (2a - 1)b^2 + (a + a^2)}{a + b^2} \stackrel{!}{>} 0 \quad (9.98)$$

$$\Rightarrow b = \frac{1}{2}(1 - 2a \pm \sqrt{1 - 8a}) \quad (9.99)$$

This defines a curve in  $(a, b)$ -space, as shown in figure 9.28b.

Due to the positive feedback,  $y$  is quickly consumed. Then the system breaks down and has to recover. In contrast to the linear system, there is only one

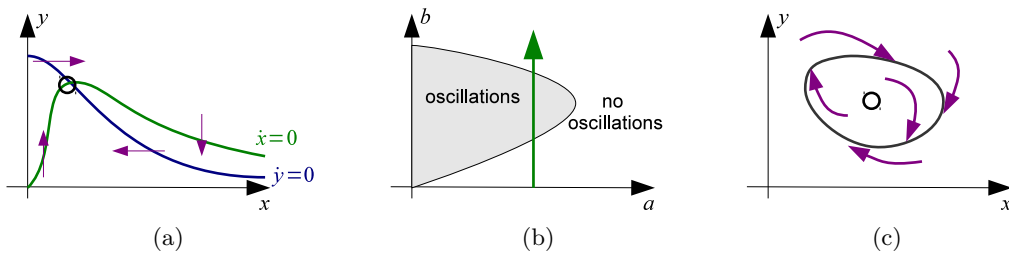


Figure 9.28: a.) Nullclines of the dynamical equations in the glycolysis oscillator. The direction of flow was determined by the signs of  $\dot{x}$  and  $\dot{y}$ . b.) Phase diagram of the system. The gray area marks the values  $(a, b)$  which lead to oscillations in the system (unstable fixed point), whereas outside this area the fixed point is stable and no oscillations occur. Varying  $b$  with  $a$  fixed will turn on and off the oscillations (green arrow) which is typical for a Hopf bifurcation. c.) Sketch of a stable limit cycle. For large  $t$ , every flow pattern in the phase plane will end up in this limit cycle, irrespective of its initial conditions.

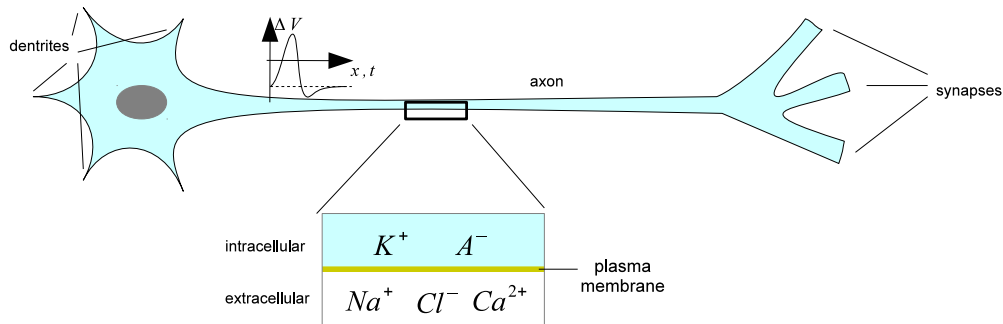


Figure 9.29: Sketch of a neuron with intra- and extracellular ionic composition ( $A^-$  stands for organic anions like nucleic acids). Signals of other nerve cells are received at the dendrites (passive cables) and are then passed along the axon (active cable) in form of an action potential with speed  $v \approx 10 - 100 \text{ m/s}$ . At the synapses, voltage-gated ion channels lead to  $Ca$ -influx, which in turn leads to vesicle fusion and neurotransmitter release. Neurotransmitters act as signals for the post-synaptic nerve cells. If an axon fires or not is determined at the axon hillock, where the input signals are summed up.

closed trajectory, a so-called **limit cycle** (figure 9.28c). Perturbations are counterbalanced and initial conditions do not matter. This motif is often encountered in biology. Note that in contrast to the bistable switch produced by autocatalysis, here autocatalysis leads to oscillations because there is an extra variable  $x$  that can be used up. Thus the same motif can lead to very different consequences depending on its context.

The glycolysis oscillator is an example for a so-called **Hopf bifurcation**. Varying the parameter  $b$  with  $a$  fixed, the oscillations can be switched on and off in a continuous manner. Hopf bifurcations also occur in other biological systems, e.g. for the active oscillator in our ears.

	intracellular (mM)	extracellular (mM)	Nernst potential (mV)
$K^+$	155	4	-98
$Na^+$	12	145	67
$Cl^-$	4	120	-90
$Ca^{2+}$	$10^{-4}$	1.5	130

Table 9.1: Ion concentration and the Nernst potential in a typical mammalian muscle cell. Since the Nernst potentials of the different ion species differ strongly, this ionic distribution is an out-of-equilibrium situation. Resting potentials of excitable cells are in the range of  $-50$  to  $-90$  mV.

## 9.9 Excitable membranes and action potentials

Neurons transmit signals along their axon as traveling waves called *action potentials* or *spikes*. This subject is part of electrophysiology, the most quantitative field in biology<sup>4</sup>. Other excitable cell types are e.g. muscle cells, neutrophils, or germ cells. The ionic composition of excitable cells is particularly important for the formation of an action potential. Typical ion concentrations for small ions within the cell are given in table 9.1.

With the Boltzmann equation we can give the probability of finding a monovalent positive ion on one side of the membrane with potential  $V$ . This in turn is proportional to its concentration  $c$ :

$$\begin{aligned}
 p &= \frac{1}{Z} \exp\left(-\frac{eV}{k_B T}\right) \sim c \\
 \Rightarrow \frac{c_1}{c_2} &= \exp\left(-\frac{e(V_1 - V_2)}{k_B T}\right) \\
 \Rightarrow \boxed{\Delta V = \underbrace{\frac{k_B T}{e}}_{25 \text{ mV}} \ln \frac{c_1}{c_2}} & \quad \text{Nernst potential} \quad (9.100)
 \end{aligned}$$

The resting potential in an excitable cell is typically  $\Delta V \approx -90$  mV which means that the potential inside is 90 mV lower than on the outside. Because the measured Nernst potentials for a typical ion composition (table 9.1) do not agree, the system is not in equilibrium. Especially the discrepancy between  $K^+$  and  $Na^+$  is striking, because chemically they are very similar. Also note the extreme concentration gradient of  $Ca^{2+}$ .

### 9.9.1 Channels and pumps

The non-equilibrium situation described above cannot be true for a plain lipid bilayer. In fact, ions have to be transported across the membrane to keep the system in non-equilibrium. Transport across the membrane can either be passive

<sup>4</sup>For a comprehensive overview, compare James Keener and James Sneyd, *Mathematical Physiology*, Springer, second edition 2009.

along the electrochemical gradient of the ions through open ion channels or active via so-called pumps. In the plasma membrane, there are numerous such membrane proteins fulfilling these functions. Of particular interest for the formation of an action potential are voltage-gated ion channels (for  $K^+$  and  $Na^+$ ) and the Na/K-pump (figure 9.30).

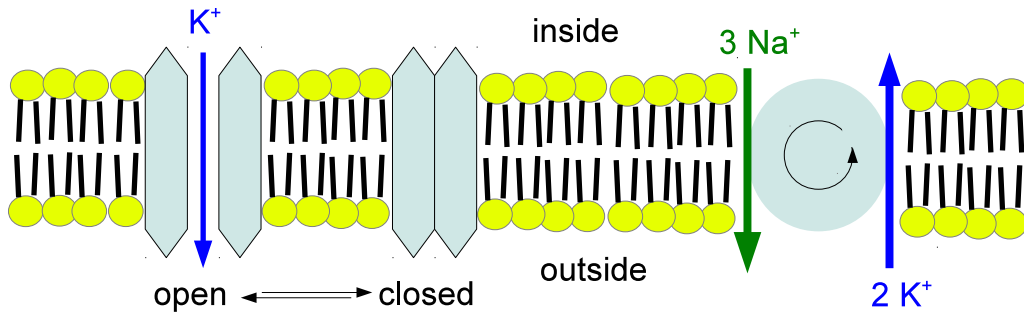


Figure 9.30: Schematic drawing of a membrane with a voltage-gated  $K^+$  channel and a Na/K-pump.

**Ion channels** can have two conformations: open and closed. The transition between these two conformations is called gating. For instance, voltage-gated  $Na^+$  channels in neurons are closed when the membrane is at the resting potential, but they open as the membrane potential becomes more positive. The probability of being open of this two-state system can be described by

$$p_{open} = \frac{e^{-\beta \cdot \Delta\epsilon}}{1 + e^{-\beta \cdot \Delta\epsilon}} \quad (9.101)$$

$$\Delta\epsilon = \Delta\epsilon_0 - qV : \quad = \frac{1}{1 + e^{\beta q(V^* - V)}} \quad (9.102)$$

where  $q = 12e$  is the effective charge,  $V^*$  is the threshold voltage (corresponding to  $V^* \approx -40 \text{ mV}$  for a neuron). A plot of equation 9.102 is given in figure 9.31. The equation implies that during an action potential (figure 9.31b) the  $Na^+$  channel is open, leading to a depolarization of the membrane. Today we know that neurons have more than 200 different ion channels. The standard book on the biophysics of ion channels is B. Hille, *Ionic channels of excitable membranes*, 3rd edition Sinauer 2001.

The resting potential  $\Delta V$  is maintained (and re-established after an action potential) mainly by an **ion pump**, the Na/K-ATPase (or simply Na/K-pump). Per molecule ATP consumed, it actively transports three  $Na^+$  out of the cell and two  $K^+$  into the cell. The net charge transport is then one positive charge that is transported from the inside to the outside. Hence, the outside becomes more positive and the inside more negative, leading to a negative resting potential.

## 9.9.2 Hodgkin-Huxley model of excitation

In 1952, Alan Hodgkin and Andrew Huxley published a series of five papers in *J. Physiol.* (some of them with their coworker Bernard Katz) summarizing years of

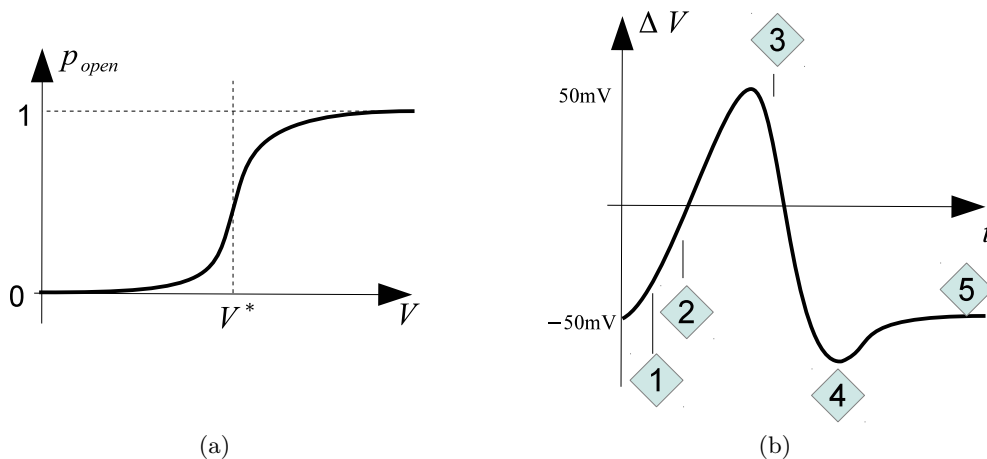


Figure 9.31: a.) Probability to be open for a voltage-gated ion channel following equation 9.102. The threshold potential is denoted at  $V^*$ . b.) Action potential of a nerve cell. 1: Threshold for opening of  $Na^+$  channels. 2:  $Na^{2+}$  channels open after  $0.5\text{ ms}$  and close  $2\text{ ms}$  later, leading to a "depolarization" of the membrane. 3:  $K^+$  channels open after  $2\text{ ms}$  and close several  $\text{ms}$  later, achieving a repolarisation. 4: Overshoot due to open  $K^+$  channels ("hyperpolarization"). 5: Resting state. Now the system needs some time to establish the initial state ("latency"). Similar depolarization waves, but with  $Ca^{2+}$ , are used to have all sarcomeres contracted simultaneously in a muscle.

theoretical work on action potentials in the squid giant axon, using the experimental data acquired in the squid summer season of 1949 at Plymouth, when scientific work had started again in post-war England. The Hodgkin-Huxley model is the most important mathematical model in biology and is still valid today. It is actually a four-dimensional non-linear dynamics model which they evaluated on hand-cranked computers. Without knowing about ion channels and pumps, they postulated exactly the corresponding mathematical structure. Experimentally, they used the new space clamp techniques (figure 9.32a) which allows for studying an action potential as a function of time without having to consider spatial effects. A few important historical milestones concerning excitability are summarized in table 9.2.

We now turn to the electrical properties of the axon, i.e. we express the biological system by an electric circuit (circuit diagram shown in figure 9.32b):

$$\begin{aligned}
 \text{lipid bilayer} &\rightarrow \text{capacitance } C \\
 \text{ion channels} &\rightarrow \text{resistors (time/voltage-dependent) } R_i = \frac{1}{g_i} \\
 &\quad g_i \text{ conductancies} \\
 \text{Nernst potentials} &\rightarrow \text{batteries (assumed to be constant) } V_i
 \end{aligned}$$

Recall that  $\Delta Q = C\Delta U$  and  $C/A = \mu\text{F} \cdot \text{cm}^{-2}$  for a lipid bilayer. The current components are given by  $I_i = g_i(\Delta V - V_i)$ . In the following back of the envelope calculation we will see that the Nernst potentials can indeed assumed to be



1952	Famous Hodgkin and Huxley papers: the dynamics of so-called <i>gates</i> produce temporal changes in conductivity
1960	Richard FitzHugh and later Nagumo et al. independently analyzed a reduced HH-model with phase plane analysis, leading to the standard NLD-model for action potentials
1963	Nobel prize for Hodgkin and Huxley (together with John Eccles, who worked on motorneuron synapses)
1991	Nobel prize for Erwin Neher and Bert Sakmann for the patch clamp technique: the molecular basis of an action potential could be demonstrated directly for the first time
2003	Nobel prize for Roderick MacKinnon for his work (Science 1998) on the structure of the $K^+$ channel, which in particular explained why $Na^+$ ions cannot pass
May 2012	Andrew Huxley dies at the age of 94; after his work on the action potential, he revolutionized muscle research (the sliding filament hypothesis from 1954 and the Huxley model for contraction from 1957 could have earned him a second Nobel prize)

Table 9.2: Important dates in the history of electrophysiology.

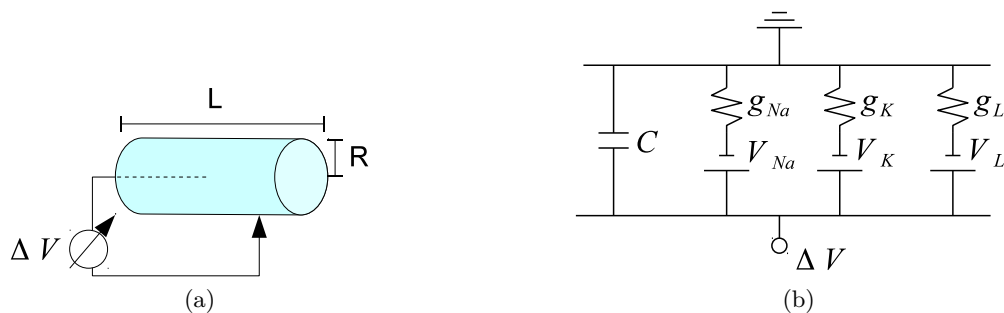


Figure 9.32: a.) Space clamp of the squid giant axon (here:  $R = 25 \mu m$ ) where an arbitrary potential can be clamped to the membrane. b.) Circuit diagram of an excitable membrane.  $g_i$  denotes the conductance and  $V_i$  denotes the Nernst potential of the respective ion species. Hodgkin and Huxley also introduced a third current component which they called  $L$  ("leakage").

constant. The charge transfer during depolarization is given by

$$\begin{aligned}\Delta Q &= \Delta V \cdot \frac{C}{A} \cdot (2\pi RL) \\ &= 100 \text{ mV} \cdot \frac{\mu F}{\text{cm}^2} \cdot 2\pi \cdot 25 \mu\text{m} \cdot L \\ &= 10^{10} \frac{e}{\text{cm}} \cdot L\end{aligned}$$

whereas the total charge inside the axon is

$$\begin{aligned}Q &= e \cdot c \cdot (\pi R^2 L) \\ &= e \cdot 100 \text{ mM} \cdot \pi (25 \mu\text{m})^2 \cdot L \\ &= 10^{15} \frac{e}{\text{cm}} \cdot L\end{aligned}$$

The relative change in charge  $\Delta Q/Q$  is in the order of  $10^{-5}$  which is a very small perturbation. Therefore, the Nernst potentials can well assumed to be constant. In their model, Hodgkin and Huxley also considered some leakage current component  $L$ . With Ohm's law ( $I = \dot{Q} = C \cdot \Delta \dot{V} = g\Delta V$ ) the first dynamical equation is given by

$$\Delta \dot{V} = -\frac{1}{C} [g_{Na}(\Delta V - V_{Na}) + g_K(\Delta V - V_K) + g_L(\Delta V - V_L)] \quad (9.103)$$

Note that this simple equation gives a stable fixed point and no interesting dynamics is to be expected except if the  $g_i$  have some dynamics by themselves. Hodgkin and Huxley realized for the first time that  $g_{Na}$  and  $g_K$  must have very different dynamics and came up with equations that gave a very good fit to their data.

At the core of their model is the assumption that some two-state process must lead to the breakdown of the conductance, suggesting a hyperbolic response. On the other hand, however, in their voltage clamp data they observed a sigmoidal response. They concluded that several two-state processes must be combined. They introduced three dynamic *gates*  $m$ ,  $h$  and  $n$  that together determine the conductancies:

$$g_{Na} = 120 m^3 h \quad (9.104)$$

$$g_K = 36 n^4 \quad (9.105)$$

$$g_L = 0.3 = \text{const.} \quad (9.106)$$

Here the exponents have been chosen simply from fits to the data. Each of the three gates is a two state process, where the transition rate from "closed" to "open" is given by  $\alpha_i$  and the transition rate from "open" to "closed" is given by  $\beta_i$ :

$$\dot{n} = \alpha_n(1 - n) - \beta_n n \quad (9.107)$$

$$\dot{m} = \alpha_m(1 - m) - \beta_m m \quad (9.108)$$

$$\dot{h} = \alpha_h(1 - h) - \beta_h h \quad (9.109)$$

The  $\alpha_i$  and  $\beta_i$  are phenomenologically determined functions of  $v = \Delta V$  but have the functional form of equation 9.102, which today we understand is appropriate for ion channels:

$$\begin{aligned}\alpha_m &= \frac{25 - v}{10 \cdot \left[ \exp\left(\frac{25-v}{10}\right) - 1 \right]} \\ \beta_m &= 4 \exp\left(\frac{-v}{18}\right) \\ \alpha_h &= \frac{7}{100} \exp\left(\frac{-v}{20}\right) \\ \beta_h &= \frac{1}{\exp\left(\frac{30-v}{10}\right) + 1} \\ \alpha_n &= \frac{10 - v}{100 \cdot \left[ \exp\left(\frac{10-v}{10}\right) - 1 \right]} \\ \beta_n &= \frac{125}{1000} \exp\left(\frac{-v}{80}\right)\end{aligned}$$

With equations 9.103 to 9.109, the HH-model is a NLD-model with the four variables  $\Delta V$ ,  $n$ ,  $m$  and  $h$ . A numerical solution for  $n$ ,  $m$  and  $h$  is shown in figure 9.33. The solution for  $\Delta V$  corresponds to a typical action potential (figure 9.31b) as observed experimentally. The HH-model was not only a perfect explanation of all the data they had measured, but it has stayed valid until today.

Before the gate  $h$  has recovered to its steady state, an additional stimulus does not evoke any substantial response, although the potential itself is close to its resting value. Therefore latency arises. This is another essential observation explained by the HH-model. Interestingly, this property also explains why the injection of a steady current can lead to oscillations. Such a current raises the resting potential above the threshold of an action potential. The axon fires but then has to recover before it fires again. Another way to make the HH-model oscillate is to immerse the axon in a bath of high extracellular  $K^+$ -ions. This raises the Nernst potential for  $K^+$  and therefore the resting potential. If it becomes superthreshold, oscillations start. Later we will see that these kinds of oscillations are very similar to the ones we obtain from the van der Pol oscillator.

### 9.9.3 The FitzHugh-Nagumo model

In the 1960s, Richard FitzHugh analyzed several reduced version of the the HH-model with phase-plane techniques. He started from the observation that the HH-model has two fast variables,  $m$  and  $v$  (the Na-channels activate quickly and the membrane potential changes quickly) and two slow variables  $n$  and  $h$  (K-channels are activated slowly and Na-channels are inactivated slowly). He first analyzed the fast phase plane and found that it shows bistability, which means that the system can switch from a resting to an excited state. On the long time scale,  $n$  starts to increase (K-channels open) and  $h$  starts to decrease (Na-channels

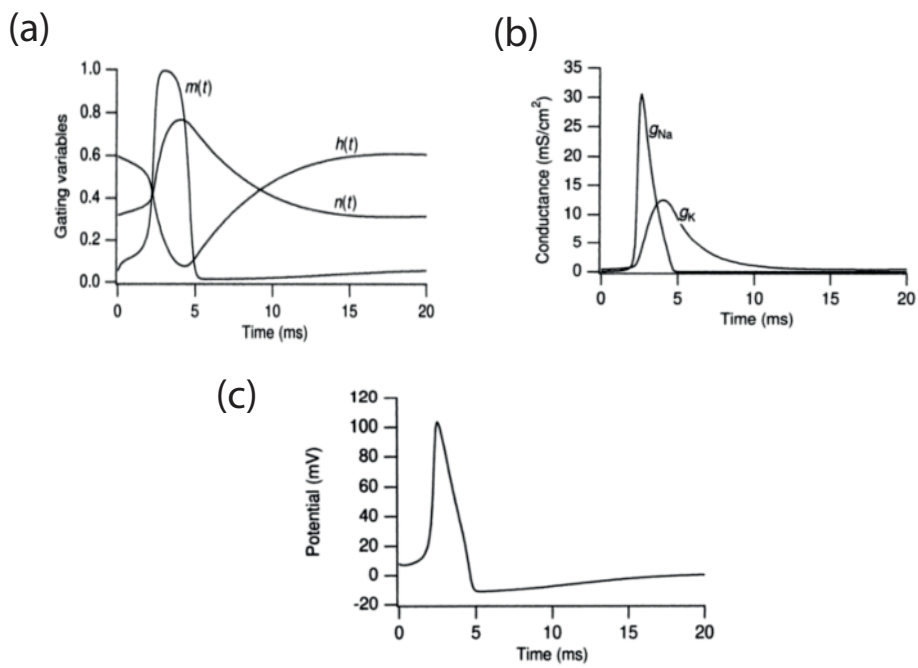


Figure 9.33: (a) Time dependence of the gates  $n$ ,  $m$  and  $h$  during an action potential. (b) Resulting time dependence of the conductancies. (c) Resulting action potential.  $\Delta V$  and  $m$  are fast variables, whereas  $n$  and  $h$  are slow variables. Taken from Keener and Sneyd.

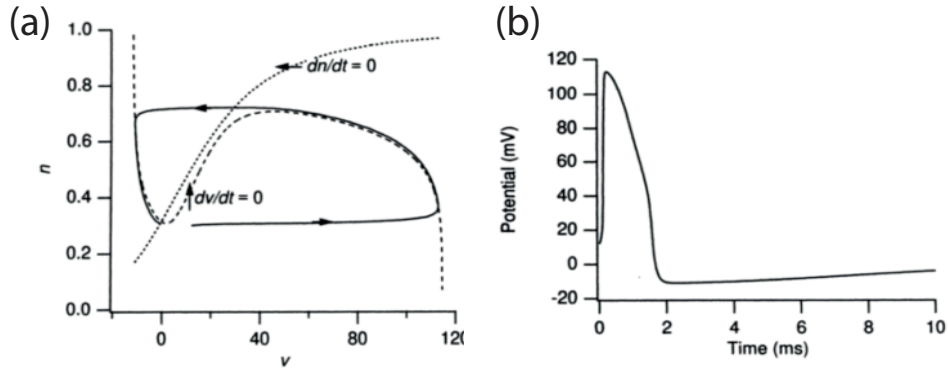


Figure 9.34: (a) Fast-slow phase plane of the Hodgkin-Huxley model. The FitzHugh-Nagumo model essentially has the same structure. (b) The resulting action potential. Taken from Keener and Sneyd.

close). This leads to the disappearance of the excited state through a saddle-node bifurcation and the system returns to the resting state.

FitzHugh next analyzed the fast-slow phase plane with  $v$  and  $n$ , which are called the excitation and recovery variables, respectively. He found that the  $v$ -nullcline has a cubic shape, that there is one fixed point and that the action potential is emerging as a long excursion away and back to the fixed point guided by the cubic nullcline, compare figure 9.34. This reduction of the HH-equations then motivated him to define an even more abstract model that later became to be known as the **FitzHugh-Nagumo model** (Nagumo and coworkers built this model as an electronic circuit and published in 1964). This model assumes two variables, one slow ( $w$ ) and one fast ( $v$ ). The fast (excitation) variable has a cubic nullcline and the slow (recovery) variable has a linear one. There is a single intersection which is assumed to be at the origin without loss of generality. Thus the model equations are

$$\epsilon \frac{dv}{dt} = v(1-v)(v-\alpha) - w + I_{app} \quad (9.110)$$

$$\frac{dw}{dt} = v - \gamma w \quad (9.111)$$

where  $I_{app}$  allows for an externally applied current,  $\epsilon \ll 1$  and  $0 < \alpha < 1$ . Typical values are  $\epsilon = 0.01$ ,  $\alpha = 0.1$  and  $\gamma = 0.5$ . The phase plane analysis then show that an excitation to a small value of  $v$  leads to a large excursion (action potential) leading to the steady state  $(0, 0)$ . If one injects a current  $I_{app} = 0.5$ , the fixed point becomes unstable and a stable limit cycle emerges through a Hopf bifurcation, thus the system becomes oscillatory (essentially it becomes a van der Pol oscillator). Thus this simple model reproduces the main features of the HH-model.

Interestingly, the HH- and FN-models have many more interesting features if studied for a time-dependent current  $I_{app}(t)$ . For example, one finds that the system does not start to spike if the current is increased slowly rather than in

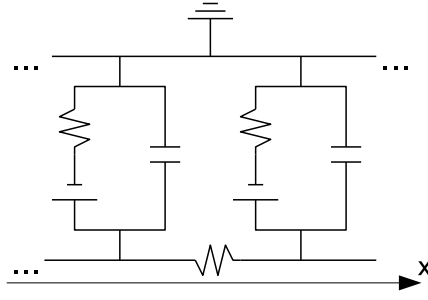


Figure 9.35: Extended electrical circuit diagram of an excitable membrane such as the squid giant axon.

a step-wise fashion. Thus it does not have a fixed threshold but goes super-threshold only if the current change is fast. Another interesting observation is that an inhibitory step (negative step function) triggers a spike at the end rather than at the start of the stimulation period. Thus the direction in which the current is changed matters.

#### 9.9.4 The cable equation

We now consider how an excitation propagates in space. From the electrical circuit diagram shown in figure 9.35, we can derive the cable equation. We first note that there are now different kinds of currents: there is a current  $I(x)$  flowing down the line, and there is a transverse current  $I_T(x)$  representing the leakage across the membrane. Note that the central mechanism here is the transverse current based on the ion channel dynamics as investigated in the space-clamp, and that this transverse current then leads to the longitudinal current which is the spatial propagation of an action potential. The longitudinal current is driven by a gradient in the potential and we assume a simple Ohmic relation:

$$V(x + \Delta x, t) - V(x, t) = -I(x, t)r dx \quad (9.112)$$

where  $r$  is the differential longitudinal resistance. We next note that the leakage current decreases the current along the line (Kirchhoff's balance of currents):

$$I(x + \Delta x, t) - I(x, t) = -I_T(x, t) dx \quad (9.113)$$

with  $I_T(x, t)$  having contributions both from the capacitance and the resistance:

$$I_T(x, t) = C \frac{dV(x, t)}{dt} + gV \quad (9.114)$$

Together we therefore get in the continuum limit

$$\frac{d^2 V(x, t)}{dx^2} = r \left( C \frac{dV(x, t)}{dt} + gV \right) \quad (9.115)$$

or with the decay length  $\lambda = \sqrt{1/(rg)}$  and the time constant  $\tau = C/g$ :

$$\lambda^2 \frac{d^2 V(x, t)}{dx^2} - \tau \frac{dV(x, t)}{dt} = V \quad (9.116)$$

This is the famous cable equation, a diffusion equation with damping, with a similar mathematical structures as the Schrödinger or Fokker-Planck equations. For a constant  $g$ , we deal with the passive cable equation that has been derived in 1855 by Lord Kelvin for the transatlantic cable. This equation applies to the dendrites.

For the axons, we have to use the active cable equation, where the damping is replaced by the dynamic equation of the HH-model

$$\lambda^2 \frac{d^2 V(x, t)}{dx^2} - \tau \frac{dV(x, t)}{dt} = \frac{g_{Na}}{g} (V - V_{Na}) + \frac{g_K}{g} (V - V_K) + \frac{g_L}{g} (V - V_L) \quad (9.117)$$

and supplemented by the three equations for the conductivities. It has been found already by Hodgkin and Huxley that such an equation allows for propagating wave. To mathematically analyze this equation, we can reduce this system to the bistable cable equation (in dimensionless form):

$$\frac{dV(x, t)}{dt} = \frac{d^2 V(x, t)}{dx^2} + f(V), \quad f(V) = -V(V - \alpha)(V - 1) \quad (9.118)$$

which has stable fixed points at  $V = 0$  (resting state) and  $V = 1$  (excited state) (for  $0 < \alpha < 1$ ). One can show that this equation has a traveling front solution with a tanh-shape. To get a traveling wave like the action potential, one has to add an relaxation process which brings the excited state back to the resting state.

If one specifies the cable equation for a cylindrical geometry with radius  $R$ , one notes that  $g$  and  $C$  both scale with  $R$  because they increase with the surface area, and  $r$  scales like  $1/R^2$  because it decreases with the volume. The propagation velocity therefore scales as  $\lambda/\tau \sim \sqrt{g/(rC^2)} \sim \sqrt{R}$ , as found experimentally. This explains why the squid has evolved a giant axon.

The active cable equation can also be extended to two and three dimensions. Then one not only gets propagating fronts and waves, but also e.g. spirals, which are self-sustained and do not propagate a signal. In the context of heart and muscle biology, such patterns are the sign of a pathophysiological situations (stroke, seizure).

### 9.9.5 Neuronal dynamics and neural networks

After having studied the elementary unit of the brain (the neuron and the action potential) in large detail, we now ask in which way many neurons work together in the brain, which has around  $10^{11}$  neurons and  $10^{14}$  synapses. Because such a large system cannot be simulated with all its details, we have to find abstract representations<sup>5</sup>. Such abstract models are increasingly simulated in neuromorphic hardware in order to emulate the amazing computational capabilities of the human brain (compare group of Karlheinz Meier at KIP).

---

<sup>5</sup>For a comprehensive introduction, see the books by Wulfram Gerstner and coworkers, *Neuronal Dynamics*, Cambridge University Press 2014, and by Peter Dayan and L.F. Abbott, *Theoretical Neurosciences*, MIT Press 2001.

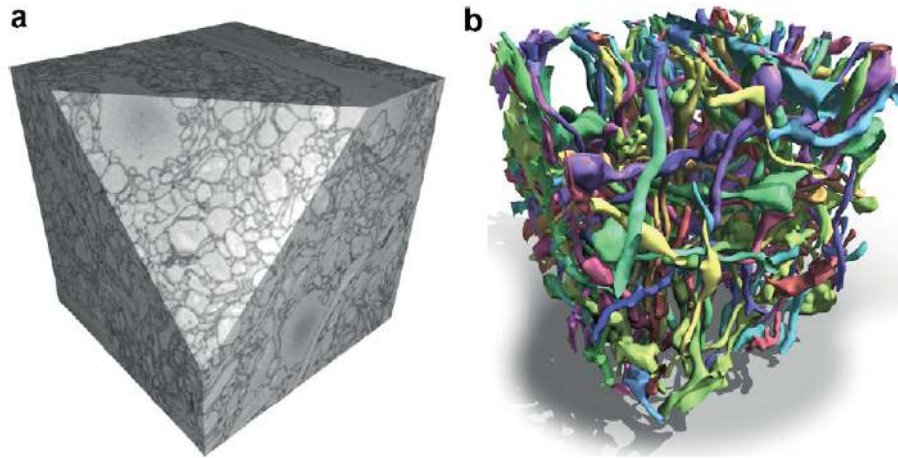


Figure 9.36: (a) Serial blockface scanning electron microscopy image of a part of a rabbit retina with  $512^3$  voxels (Denk group). (b) Image reconstruction based on a graphical model with supervoxels (Hamprecht group). From Bjoern Andres, *Medical Image Analysis 16*: 796-805 (2012). Such reconstructions should eventually provide a complete map of the synaptic connections between the neurons (connectome).

We first note that the way a neuron is built, it is clear how one has to connect it up into a network: dendrites collect the synaptic currents, they are summed up at the axon hillock, the axon might fire or not, and the resulting spike is distributed to the post-synaptic cells. The exact topology of the network depends on the part of the brain one is interested in and can be taken from experiments imaging the brain (e.g. with two-photon microscopy, serial blockface scanning electron microscopy or super-resolution microscopy, compare figure 9.36). We next note that the shape of an action potential is stereotyped (as described by the HH-model) and thus what seems to matter most is the timing of the spikes. A simple model which takes these considerations into account is the *leaky integrate-and-fire model* (LIF). For each neuron, we solve a dynamic equation for the membrane potential:

$$C \frac{dV}{dt} = -g(V - E) + I \quad (9.119)$$

but we disregard spatial aspects and do not include a relaxation variable. The first term is the ionic (leak) current and the second the input (synaptic) current. If a synaptic current arises, the voltage starts to rise. In the LIF, a spike is emitted if the potential crosses a given threshold from below. The potential then is reset (this replaces the dynamics of the relaxation variable) and can rise again (after a latency time). In this way, a spike train is generated in response to a constant input current. Typical values are 0.2 kHz for the frequency and 10 nA for the current.

As we have discussed above, the HH-model does not imply a fixed threshold, thus



the LIF is too simple in this regard. Moreover it results in a constant frequency under constant stimulation, while experimentally, the system adapts. In order to take these two issues into account, the *adaptive exponential integrate-and-fire model* (AdEx) has been suggested:

$$C \frac{dV}{dt} = -g(V - E) + g\Delta_T e^{(V - E_T)/\Delta_T} + I \quad (9.120)$$

$$\tau_w \frac{dw}{dt} = a(V - E) + b\tau_w \rho - w \quad (9.121)$$

The second term pushes the potential up once the value  $E_T$  is reached. In fact once this term dominates, the potential diverges in finite time and a spike is created. After spiking, the potential is reset and latency is implemented, as in LIF.  $w$  is an adaptation variable: it grows with the potential and with the spike train  $\rho$ , but relaxes on the time scale  $\tau_w$ . For constant stimulation, the spiking frequency therefore decreases (adaptation). The time constant  $\tau_w$  is of the order of hundreds of milliseconds. For  $a = b = \Delta_T = 0$ , we essentially recover the LIF-model.

A complete model for a neural network also needs a synaptic model. In the *current-based synaptic interaction model* (CUBA), a spike creates a typical current (e.g. the difference between two exponentials) that then is fed into LIF or AdEx models. Although CUBA-models are a natural choice for point neuron models such as LIF and AdEx, there is also physical justification for a *conductance-based synaptic interaction model* (COBA).

Synapses are also the place for learning and memory (plasticity) and therefore the synapse between neurons  $i$  and  $j$  gets a weight  $w_{ij}$  that has its own dynamics. For example, Hebb's rule states that synapses increase their weight if they are used frequently. With these rules, the neural networks is completely defined and can be trained for a certain function, e.g. automatic detection of handwriting or license plates.

## 9.10 Reaction-diffusion systems and the Turing instability

Naively, one might think that adding diffusion to a reaction system stabilizes it, but Alan Turing showed in 1952 that there exist diffusion-driven instabilities. Turing suggested that diffusion-driven instabilities might account for the spontaneous emergence of patterns in morphogenesis of animals (like the stripes of zebra or the spots of the leopard). Although it is hard to identify specific examples of Turing instabilities in development, it is clear that this concept is fundamental to understand pattern formation in many contexts. Here we introduce the main ideas and results of Turing. Recently his ideas have seen a renaissance, e.g. in the context of mechanochemical signaling (especially in the actin cytoskeleton) and newly discovered reaction-diffusion systems (like the bacterial Min-system). Turing investigated under which condition a reaction-diffusion system produces a heterogeneous spatial pattern. To answer this question, he considered a two-

dimensional system of the type:

$$\begin{aligned}\dot{A} &= F(A, B) + D_A \Delta A \\ \dot{B} &= G(A, B) + D_B \Delta B.\end{aligned}$$

A simple choice for the reaction part would be the activator-inhibitor model from Gierer and Meinhardt, where species A is autocatalytic and activates B, while B inhibits A. An even simpler choice is the activator-inhibitor model from Schnackenberg, where the autocatalytic species A is the inhibitor of B and B activates A. Both models form stripes in the Turing version and here we choose the second one because it is mathematically easier to analyse:

$$\begin{aligned}F &= k_1 - k_2 A + k_3 A^2 B \\ G &= k_4 - k_3 A^2 B.\end{aligned}$$

We first non-dimensionalize the system:

$$\begin{aligned}u &= A \left( \frac{k_3}{k_2} \right)^{1/2}, & v &= B \left( \frac{k_3}{k_2} \right)^{1/2}, \\ t &= \frac{D_A t}{L^2}, & x &= \frac{x}{L}, & d &= \frac{D_B}{D_A}, \\ a &= \frac{k_1}{k_2} \left( \frac{k_3}{k_2} \right)^{1/2}, & b &= \frac{k_4}{k_2} \left( \frac{k_3}{k_2} \right)^{1/2}, \\ \gamma &= \frac{L^2 k_2}{D_A}\end{aligned}$$

Note that the variables  $u$  and  $v$  are positive since they are concentrations of reactants. By introducing the variables above, the system is described as follows

$$\begin{aligned}\dot{u} &= \gamma \underbrace{(a - u + u^2 v)}_{=:f(u,v)} + \Delta u \\ \dot{v} &= \gamma \underbrace{(b - u^2 v)}_{=:f(u,v)} + d \Delta v\end{aligned}$$

with the ratio of the diffusion  $d$  and the relative strength of the reaction versus the diffusion terms  $\gamma$  which scales as  $\gamma \sim L^2$ .

We start with a linear stability analysis of the reaction part using  $\vec{W} = (u - u^*, v - v^*)$ . We denote the steady state with  $\vec{W}^* = (u^*, v^*)$  and a partial derivative with  $f_u = \frac{\partial f}{\partial u}$  etc. This yields

$$\dot{\vec{W}} = \gamma A \vec{W}$$

with the matrix

$$A = \begin{pmatrix} f_u & f_v \\ g_u & g_v \end{pmatrix} \Big|_{\vec{W}^*}.$$

Linear stability is guaranteed if the real part of the eigenvalues  $\lambda$  is smaller than zero,  $\text{Re } \lambda < 0$ . Thus, the trace of  $A$  is smaller than zero

$$\text{tr } A = f_u + g_v < 0 \tag{9.122}$$

and the determinant larger than zero

$$\det A = f_u g_v - f_v g_u > 0. \quad (9.123)$$

The  $u$ - and  $v$ - nullcline is given by setting  $f = 0$  and  $g = 0$ , respectively.

$$\begin{aligned} u\text{-nullcline: } v &= \frac{u-a}{u^2} \\ v\text{-nullcline: } v &= \frac{b}{u^2} \end{aligned}$$

For the steady state  $\vec{W}^* = (u^*, v^*)$ , we demand  $u^*$  and  $v^*$  to be positive for physical reasons.

$$\Rightarrow (u^*, v^*) = \left( a+b, \frac{b}{(a+b)^2} \right)$$

Thus, it is  $a+b > 0$  and  $b > 0$ .

$$\Rightarrow A = \begin{pmatrix} -1+2uv & u^2 \\ -2uv & -u^2 \end{pmatrix} \Big|_{\vec{W}^*} = \begin{pmatrix} \frac{b-a}{b+a} & (a+b)^2 \\ \frac{-2b}{a+b} & -(a+b)^2 \end{pmatrix} \quad \Rightarrow \quad \det A = (a+b)^2 > 0$$

We now turn to the full reaction-diffusion system and linearize it about the steady state

$$\begin{aligned} \dot{\vec{W}} &= \gamma A \vec{W} + D \Delta \vec{W} \\ \text{with } D &= \begin{pmatrix} 1 & 0 \\ 0 & d \end{pmatrix}. \end{aligned}$$

In order to obtain an ODE from this PDE, we use the solutions of the Helmholtz wave equation

$$\Delta \vec{W} + k^2 \vec{W} = 0$$

with no-flux boundary of size  $p$  in 1d, we have

$$\vec{W}_k(x) \sim \cos(k \cdot x)$$

with wavenumber  $k = \frac{n\pi}{p}$  and wavelength  $\lambda = \frac{2\pi}{k} = \frac{2p}{n}$  ( $n$  integer).

$$\begin{aligned} \Rightarrow \vec{W}(\vec{r}, t) &= \sum_k c_k \exp(\lambda t) \vec{W}_k(\vec{r}) \\ \Rightarrow \lambda \vec{W}_k &= \gamma A \vec{W}_k - D k^2 \vec{W}_k \end{aligned}$$

We now have to solve this eigenvalue problem. A Turing instability occurs if  $\text{Re } \lambda(k) > 0$ . Our side constraint is that the eigenvalue problem for  $D = 0$  (only reactions) is assumed to be stable, that is  $\text{Re } \lambda(k=0) < 0$ .

$$\Rightarrow 0 = \lambda^2 + \lambda[k^2(1+d) - \gamma \text{tr } A] + [dk^4 - \gamma(df_u + g_v)k^2 + \gamma^2 \det A].$$

We first note that the coefficient of  $\lambda$  is always positive because  $k^2(1+d) > 0$  and  $\text{tr } A < 0$  (for reasons of the stability of the reaction system). In order to get

an instability,  $\text{Re } \lambda > 0$ , the constant part has to be negative. Since the first and last terms are positive, this implies

$$df_u + g_v > 0 \quad \Rightarrow \quad d \neq 1. \quad (9.124)$$

This is the main result by Turing: An instability can occur if one component diffuses faster than the other. (9.124) is only a necessary, but not a sufficient condition. We require that the constant term as a function of  $k^2$  has a negative minimum.

$$\frac{(df_u + g_v)^2}{4d} > \det A = f_u g_v - f_v g_u \quad (9.125)$$

The critical wavenumber can be calculated to be

$$k_c = \gamma \left( \frac{\det A}{d_c} \right)^{1/2}$$

with the critical diffusion constant from

$$d_c^2 f_u^2 + 2(2f_v g_u - f_u g_v) d_c + g_v^2 = 0.$$

For  $d > d_c$ , we have a band of instable wavenumbers. The relation  $\lambda = \lambda(k^2)$  is called the *dispersion relation*. The maximum singles out the fastest growing mode. This one dominates the solution

$$\vec{W}(\vec{r}, t) = \sum_k c_k \exp(\lambda(k^2)t)$$

for large  $t$ . Note however, that in this case also non-linear effects will become important and thus will determine the final pattern.

In summary, we have found four conditions (9.122) - (9.125) for the Turing instability to occur. We now analyze the Schnackenberg-model in one spatial dimension. We already noted that  $a + b > 0$  and  $b > 0$  for the steady state to make sense. From the phase plane we see that  $f > 0$  for large  $u$  and  $f < 0$  for small  $u$ . Hence,  $f_u > 0$  around the steady state. Thus,  $b > a$ .

From condition (9.122) and (9.124), we now calculate that  $d > 1$  in this case (the activation  $B$  diffuses faster in this model). In general, the conditions (9.122)-(9.125) define a domain in  $(a, b, d)$ -space, the *Turing space*, in which the instabilities occurs. The structure of the matrix  $A$  tells us how this will happen: as  $u$  or  $v$  increases,  $u$  increases and  $v$  decreases. So, the two species will grow *out of phase*. If there is a fluctuation to a larger A-concentration, it would grow due to the autocatalytic feature. Locally this would inhibit B and it decreases strongly. However, because B is diffusing fast, it now is depleted from the environment and there A is not activated anymore. Therefore A goes down in the environment, whereas B is high. This is the basic mechanism for stripe formation.

In the Gierer-Meinhardt model, the two species grow *in phase*. When the autocatalytic species A grows, so does B, because A is the activator in this model. Now B diffuses out and suppressed A in the environment. This is an alternative mechanism for stripe formation.

The domain size  $p$  has to be large enough for a wavenumber  $k = \frac{n\pi}{p}$  to be within the range of the unstable wavenumbers ( $\gamma \sim L^2$ ):

$$\gamma L(a, b, d) < \left(\frac{n\pi}{p}\right)^2 < \gamma M(a, b, d)$$

where  $L$  and  $M$  can be calculated exactly. Typically, the mode which grows has  $n = 1$ . Whether the left or right solution occurs depends on the initial conditions. If the domain grows to double size, then  $\gamma$  changes by four ( $\gamma \sim L^2$ ).  $p$  stays the same because it is measured in units of  $L$ . Now, the mode  $n = 2$  behaves as shown in the following figures. On this way, a growing system will develop a 1D stripe pattern.